SYNTHESIS AND PHOTOPHYSICAL PROPERTIES OF LUMINESCENT SUPRAMOLECULAR SYSTEMS

Boyi Song

A Thesis Submitted for the Degree of MPhil
at the
University of St Andrews

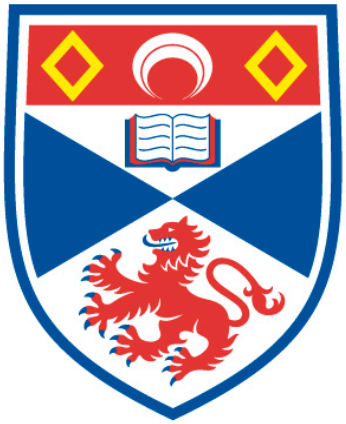

2018

Synthesis And Photophysical Properties Of Luminescent Supramolecular Systems

Boyi Song

University of St Andrews

This thesis is submitted in partial fulfilment for the degree of MPhil
at the
University of St Andrews

September 28th, 2017

1. Candidate's declarations:

I, Boyi Song hereby certify that this thesis, which is approximately 33000 words in length, has been written by me, and that it is the record of work carried out by me, or principally by myself in collaboration with others as acknowledged, and that it has not been submitted in any previous application for a higher degree.

I was admitted as a research student in October, 2014 and as a candidate for the degree of MPhil in September 2015; the higher study for which this is a record was carried out in the University of St Andrews between 2015 and 2017.

(*If you received assistance in writing from anyone other than your supervisor/s*):

I, Boyi Song received assistance in the writing of this thesis in respect of grammar, which was provided by Sandra Piai and Doreen du Boulay

Date……signature of candidate……

2. Supervisor's declaration:

I hereby certify that the candidate has fulfilled the conditions of the Resolution and Regulations appropriate for the degree of MPhil in the University of St Andrews and that the candidate is qualified to submit this thesis in application for that degree.

Date……..... signature of supervisor ……...

3. Permission for publication: (*to be signed by both candidate and supervisor*)

In submitting this thesis to the University of St Andrews I understand that I am giving permission for it to be made available for use in accordance with the regulations of the University Library for the time being in force, subject to any copyright vested in the work not being affected thereby. I also understand that the title and the abstract will be published, and that a copy of the work may be made and supplied to any bona fide library or research worker, that my thesis will be electronically accessible for personal or research use unless exempt by award of an embargo as requested below, and that the library has the right to migrate my thesis into new electronic forms as required to ensure continued access to the thesis. I have obtained any third-party copyright permissions that may be required in order to allow such access and migration, or have requested the appropriate embargo below.

The following is an agreed request by candidate and supervisor regarding the publication of this thesis:

PRINTED COPY
a) No embargo on print copy

b) Embargo on all or part of print copy for a period of **1**… year (maximum five) on the following ground(s):
    - Publication would be commercially damaging to the researcher, or to the supervisor, or the University
    - Publication would preclude future publication
    - Publication would be in breach of laws or ethics
c) Permanent or longer term embargo on all or part of print copy for a period of … years (the request will be referred to the Pro-Provost and permission will be granted only in exceptional circumstances).

Supporting statement for printed embargo request if greater than 2 years:

ELECTRONIC COPY

a) No embargo on electronic copy
b) Embargo on all or part of electronic copy for a period of **1**… year (maximum five) on the following ground(s):
    - Publication would be commercially damaging to the researcher, or to the supervisor, or the University
    - Publication would preclude future publication
    - Publication would be in breach of law or ethics
c) Permanent or longer term embargo on all or part of electronic copy for a period of … years (the request will be referred to the Pro-Provost and permission will be granted only in exceptional circumstances).

Supporting statement for electronic embargo request if greater than 2 years:

ABSTRACT AND TITLE EMBARGOES

An embargo on the full text copy of your thesis in the electronic and printed formats will be granted automatically in the first instance. This embargo includes the abstract and title except that the title will be used in the graduation booklet.

If you have selected an embargo option indicate below if you wish to allow the thesis abstract and/or title to be published. If you do not complete the section below the title and abstract will remain embargoed along with the text of the thesis.

a) I agree to the title and abstract being published **YES**/NO
b) I require an embargo on abstract YES/NO

c) I require an embargo on title YES/NO

Date……..…… signature of candidate ……

signature of supervisor ……

Please note initial embargos can be requested for a maximum of five years. An embargo on a thesis submitted to the Faculty of Science or Medicine is rarely granted for more than two years in the first instance, without good justification. The Library will not lift an embargo before confirming with the student and supervisor that they do not intend to request a continuation. In the absence of an agreed response from both student and supervisor, the Head of School will be consulted. Please note that the total period of an embargo, including any continuation, is not expected to exceed ten years.
Where part of a thesis is to be embargoed, please specify the part and the reason.

Acknowledgments

I would express my deepest thanks to my supervisor, Dr. Eli Zysman-Colman, for giving me the opportunity to undertake this fascinating research work here. His suggestions, helpfulness and enthusiasm have helped me a lot and improved my experimental skills during the projects.

I would like to thank Diego Rota Martir who helped me a lot with his vast knowledge of supramolecular chemistry and experimental experience. I thank Dr. Amlan Pal, where his daily effort kept our lab in good order and for providing me useful suggestions for complex synthesis. I thank Frauke Schibilla. She is a wonderful collaborator and did great self-assembly experiments for completing the project. I thank very much to Dr. Michael Yin Wong who gave me plenty of help with organic synthesis. I would thank David Hall who helped me a lot with the calculations involved in my projects. I would also thank Chenfei Li, Dongyang Chen, Jiyu Tian who helps me a lot in academics and daily life. I thank to all the rest of members in EZ-C group, especially Dr. Rajamalli Pachai Gounder, Adam Henwood, Clause Hierlinger, Laura Abad Galan, Deasan Lim, Nidhi Sharma, Ana, Neferu, Dr. Graeme Copley, Bryony Hockin, and Dr. Shiv Kumar. They provided a pleasurable and enjoyable environment during my stay in St. Andrews. Their suggestions and kind conversation helped me a lot and provided a pleasant and relaxed academic atmosphere.

I would thank Prof. Ifor Samuel for allowing me free reign of the use of his equipment. I thank Prof. Alexandra M. Z. Slawin and Dr. David B. Cordes for

their tremendous help on crystallography. I thank Prof. Bart Jan Ravoo's group, for their efforts on the collaborative project. I thank Prof. Denis Jacquemin and Dr. Daniel Escudero for their kind help of the calculations for optimisation of the supramolecular cage. I thank Mrs. Sylvia Williamson for her friendly help and allowing me to use the FT-IR.

I would finally thank all the Chemistry Department technical staff who contributed to the efforts of making this work possible.

Content

List of Figures

C(tcb), dark green; N, light blue; O, red; S, yellow; F, light green. Photocredit: P. J. Lusby et al. *J. Am. Chem. Soc.*, 2012, **134**, 19335.)

Figure **1.2.2.1.2** Ir (III) Metallo-Cryptophanes (**12** and **13**) and their building blocks (**9**, **10** and **11**) reported by Zysman-Colman et al. (Crystal structure of **12**: **10** and ppy ligands shown in green and grey, respectively. Photocredit: E. Zysman-Colman et al. *Chem. - A Eur. J.*, 2017, **23**, 6291. (**12**))

Figure **1.2.2.2.1** Ir-Cu supramolecular system reported by Hosseini (Crystal structure of **15** and **17**. Photocredit: C. Bronner et al. *Inorg. Chem.*, 2010, **49**, 8661 (**15**, up); C. Xu et al. *Chem. Commun.*,2015, **51**, 14787 (**17**, bottom))

Figure **1.2.2.2.2** Ir (III)-Pd (II) cages (**19** and **21**) and corresponding iridium complexes (**18** and **20**) reported by Zysman-Colman (Simulated structure of **19** (up) and **21** (bottom). Photocredit: D. Rota Martir et al. *Chem. - A Eur. J.*, 2017, **23**, 14359 (**19**, **21**))

Figure **1.2.2.2.3** Bipyramid configurations of Ir (0)-Zn (II) and Ir (0)-Co (II) reported by He et al. (Crystal structure of **24**, **25**, and **26**. **24**, **25**, C = gray, N = blue, Zn = green, Ir = pink, O = red, F = purple; **26**, C = gray, N = blue, Co = green, Ir = pink; Photocredit: X. Li et al. *Chem. Commun.*, 2016, **52**, 5105 (**24**, **25**); X. Li et al. *Chem. Commun.*, *Chem. Commun*., 2016, **52**, 9628-9631 (**26**))

Figure **1.2.2.2.4** Ir(III)-cation polymer reported by Sheu et. al. (Crystal structure of **28.** The 3D zinc-bridged structure exhibited open channels. Zn = green; **27** = blue and yellow; Ir = wine and cyan; O = red. Photocredit: M.-L. Ho et al. *Dalt. Trans.*, 2012, **41**, 2595)

Figure **1.2.2.3.1** Encapsulated **29** in MOFs (**31b**) and their building units (The 3D structure (**31b**) was calculated from the single crystal structure of unit (**31a**); C = grey, O = red, N = blue, Cl = green and Cd = orange. Photocredit: C.-Y. Sun et al. *Nat. Commun.*, 2013, **4**, 1–8, ESI)

Figure **1.2.2.3.2** Encapsulated **32** in self-assembled capsule (**34**) to afford protected emitters (**35**) (Simulated 3D structure of **34** and **35**. Photocredit: S. Horiuchi et al. *Nat. Commun.*, *Chem. - A Eur. J.*, 2016, **22**, 17534–17535)

Figure **1.2.2.4.1** Iridium based soft salts (**38** and **41**) and corresponding complexes (**36**, **37**, **39** and **40**)

Figure **1.3.1.1** Common cyclodextrins (**42**, α-CD; **43**, β-CD and **44**, γ-CD)

Figure **1.3.1.2** Chemical structure and configuration of hydrophobic functionalized cyclodextrin (**45**) and schematic representation of cyclodextrin vesicles (**46**) reported by Ravoo et. al. (Photocredit: B. J. Ravoo et al. *Chem. - A Eur. J.*, 2010, **16**, 2791)

Figure **1.4.1.1** Fluorescent Schiff-base macrocycles (**48** and **49**) applied as Hg (II) sensor and their reactant (**47**)

Figure **1.4.1.2** Fluorescent Schiff-base macrocycles (**50**) reported by Zhang et. al. with application on Cu (II) recognition.

Figure **1.4.1.3** Fluorescent Schiff-base macrocycles (**52**) reported by Zhu et al. applied as Zn (II) sensor and its aldehyde reactant (**51**).

Figure **1.4.2.1** Carbazole based conjugated macrocycles (**54**, **55** and **56**) and corresponding repeating units (**53**) (R=*n*-C_4H_9, *n*-$C_{16}H_{33}$)

suspension, 2mL H_2O and 10 μL metal salt solution were contained in each cuvette. λ_{ex}= 370 nm)

Figure **4.3.1.2** Emission spectra of **Mac-2** suspension with metal salt solutions (Air, at 298K. The theoretic concentration of **Mac-2** was $5*10^{-5}$ M, and the concentration of metal salt was $2.5*10^{-5}$ M in aqueous solution. 2mL **Mac-2** suspension, 2mL H_2O and 10 μL metal salt solution were contained in each cuvette. λ_{ex}= 370 nm)

Figure **4.3.1.3** Emission spectra of **Mac-3** suspension with metal salt solutions (Air, at 298K. The theoretic concentration of **Mac-3** was $5*10^{-5}$ M, and the concentration of metal salt was $2.5*10^{-5}$ M in aqueous solution. 2mL **Mac-3** suspension, 2mL H_2O and 10 μL metal salt solution were contained in each cuvette. λ_{ex}= 370 nm)

Figure **4.3.2.1** Emission spectra of **Mac-1** suspension with $FeCl_3$ solution in gradient concentrations (Air, at 298K. The theoretic concentration of **Mac-1** was $5*10^{-5}$ M, and the concentration of metal salt was $2.5*10^{-5}$ M in aqueous solution. 2mL **Mac-1** suspension and 2mL H_2O were contained in each cuvette with the gradual addition of metal salt solution. λ_{ex}= 370 nm)

Figure **4.3.2.2** Correlation between the emission intensity of **Mac-1** (λ=495 nm) and the logarithmic concentrations of metal cation (ln[Fe(III)]) in aqueous solution.

Figure **4.3.2.3** Emission spectra of **Mac-3** suspension with $FeCl_3$ solution in gradient concentrations (Air, at 298K. The theoretic concentration of **Mac-3** was

$5*10^{-5}$ M, and the concentration of metal salt was $2.5*10^{-5}$ M in aqueous solution. 2mL **Mac-3** suspension and 2mL H_2O were contained in each cuvette with the gradual addition of metal salt solution. λ_{ex}= 370 nm)

Figure **4.3.2.4** Correlation between the emission intensities of **Mac-3** (λ=488 nm) and the logarithmic concentrations of metal cation (ln[Fe(III)]) in aqueous solution.

Figure **4.3.2.5** Emission spectra of **Mac-3** suspension with $ZnCl_2$ solution in gradient concentrations (Air, at 298K. The theoretic concentration of **Mac-3** was $5*10^{-5}$ M, and the concentration of metal salt was $2.5*10^{-5}$ M in aqueous solution. 2mL **Mac-3** suspension and 2mL H_2O were contained in each cuvette with the gradual addition of metal salt solution. λ_{ex}= 370 nm)

Figure **4.3.2.6** Correlation between the emission intensities of **Mac-3** (λ=493 nm) and the logarithmic concentrations of metal cation (ln[Zn(II)]) in aqueous solution.

Figure **4.3.2.7** Emission spectra of **Mol-1** suspension with $FeCl_3$ solution in gradient concentrations (Air, at 298K. The theoretic concentration of **Mol-1** was $5*10^{-5}$ M, and the concentration of metal salt was $2.5*10^{-5}$ M in aqueous solution. 2mL **Mol-1** suspension and 2mL H_2O were contained in each cuvette with the gradual addition of metal salt solution. λ_{ex}= 370 nm)

Figure **4.3.2.8** Emission spectra of **Mol-2** suspension with $FeCl_3$ solution in gradient concentrations (Air, at 298K. The theoretic concentration of **Mol-2** was $5*10^{-5}$ M, and the concentration of metal salt was $2.5*10^{-5}$ M in aqueous solution.

2mL **MoI-2** suspension and 2mL H_2O were contained in each cuvette with the gradual addition of metal salt solution. λ_{ex}= 370 nm)

List of Tables

List of Schemes

Table of Abbreviations

ΔE_{ST}	Singlet-triplet energy gap
ΔE	HOMO-LUMO energy gap
ζ	Spin-orbit coupling constant
ε	Molar absorptivity
Φ_{PL}	Photoluminescence quantum yield (PLQY)
λ_{abs}	Absorption wavelength
λ_{PL}	Emission maximum of photoluminescence
τ	Emission lifetime
k_r	Radiative rate constant
k_{nr}	Non-radiative rate constant
n-BuLi	*n*-Butyllithium
^{3}MLCT	Metal-to-ligand charge transfer
^{3}LLCT	ligand-to-ligand charge transfer
ASAP-TOF	Atmospheric Solids Analysis Probe-time-of-flight mass spectrometry
ASAP-EI	Atmospheric Solids Analysis Probe-electron ionization mass spectrometry
bpy	2,2'-bipyridine
CDs	Cyclodextrins
CDV	Cyclodextrin vesicle
CDCB	Carbazolyl dicyanobenzene
CLSM	Confocal laser scanning microscope

COSY	correlation spectroscopy
CT	Charge transfer
CTV	Cyclotriveratrylene
CV	Cyclic voltammetry
DCM	Dichloromethane
DF	Delayed fluorescence
dFppy	2-(2,4-difluorophenyl)pyridine
DFT	Density functional theory
DMF	*N,N*-Dimethylformamide
DMSO	Dimethylsulfoxide
DOSY	Diffusion ordered spectroscopy
EA	Elemental analysis
EL	Electroluminescent or Electroluminescence
EQE	External quantum efficiency
ESI	Electrospray ionization
Et_2O	Diethyl ether
Fc^+/Fc	Ferrocene
FRET	Fluorescence resonance energy transfer
FT-IR	Fourier-transform infrared spectroscopy
H_2dcbpy	4,4′-dicarboxy-2,2′-bipyridine
HMBC	Heteronuclear multiple-bond correlation spectroscopy
HOMO	Highest occupied molecular orbital
HRMS	High-resolution mass spectrometry

HSQC	Heteronuclear single-quantum correlation spectroscopy
HUVEC	Human umbilical vein endothelial cells
I (I_0)	Emission intensity
ISC	Intersystem crossing
IC	Internal conversions
IQE	Internal quantum efficiency
iTMC	Ionic transition-metal complex
LDA	Lithium diisopropylamide
LC	Ligand-centered transition
LLCT	Ligand-to-ligand charge transfer
LTQ orbitrap	Linear trap quadropole orbitrap mass spectrometry
LUMO	Lowest unoccupied molecular orbital
MC	Metal-centered transition
MeCN	Acetonitrile
MeOH	Methanol
mesppy	4-mesityl-2-phenylpyridine
MLCT	Metal-to-ligand charge transfer
MOFs	Metal organic frameworks
NMR	Nuclear magnetic resonance
nr	Nonradiative
OLED	Organic light-emitting diode
PB 7.4 (buffer)	Phosphate buffer solution (0.1M, pH=7.4)
PF	Prompt fluorescence

PIC-TRZ	2-biphenyl-4,6-bis(12-phenylindolo [2,3-a]carbazole-11-yl)-1,3,5-triazine
PLQY/Φ	Photoluminescence quantum yield
PL	Photoluminescence or Photoluminescent
PMMA	Poly(methyl methacrylate)
ppy	2-phenylpyridine
Rf	Retardation factor
RISC	Reverse intersystem crossing
S_n	Excited singlet energy level
S_0	Ground state
S_1	The lowest excited singlet energy level
SCE	Saturated calomel electrode
SOC	Spin-orbit coupling
T_n	Excited triplet energy level
T_1	The lowest excited triplet energy level
TADF	Thermally activated delayed fluorescence
TBAF	Tetra-*n*-butylammonium fluoride
$TBAPF_6$	Tetrabutylammonium hexafluorophosphate
TCB	1,3,5-tricyanobenzene
TCE	Trichloroethylene
TCSPC	Time-correlated single photon counting
TDA	Tamm-Dancoff approximation
TD-DFT	Time-dependent density functional theory
THF	Tetrahydrofuran
TLC	Thin layer chromatography

TMS	Trimethylsilyl
UV	Ultraviolet
UV-vis	Ultraviolet–visible spectroscopy
XRD	X-ray diffraction

Abstract

Supramolecular chemistry has been developed in decades, and a large number of well-defined structures have been built by the utilizing of hydrogen bonds, coordination bonds and etc. However, the research on their photophysical properties is still rare. The high concentration of chromophores in supramolecular structures makes it possible to research the interactions between emitters in designed configurations, which is difficult to be achieved in traditional methods. Also, the localized luminescent units in individual sites of supramolecular systems can decrease the self-quenching of emitters theoretically, and their photoluminescence quantum yields (PLQYs) are expected to be improved.

This thesis focuses on synthesizing and exploring the photophysical properties of photoactive supramolecular systems, and contains work in three major areas. Firstly, a series of water soluble iridium complexes with terminal adamantyl groups were synthesized and used in the self-assembly with cyclodextrin vesicles (CDVs) through weak interactions. The effects on their photophysical properties brought by the interactions between CDV surface and iridium complexes were studied, as well as their potential application as bio-imaging probes. As expected, this group of iridium complexes showed enhanced emission intensity after being anchored to the CDV surface, and aggregated to perinuclear region in cell culture experiments. The second part involved the synthesis of an iridium complex based metalloligand, which was used to construct a supramolecular cage. The photophysical properties of both

metalloligand and coordination cage were explored. Even though the photophysical properties of supramolecular cage were not improved compared with its unit complex, this system provided a different configuration to a former supramolecular system which was built from similar metalloligands and published by our group. The final part is the study of a series of luminescent [2+2] Schiff-base macrocycles. These macrocycles were synthesized from carbazole based luminescent dialdehyde molecules, and the photophysical properties of building units and macrocycles were measured in solution and solid states. These macrocycles also exhibited specific recognitions to Fe (III) in aqueous systems as luminescent probes.

Indications of contributions

Chapter 2 is part of a collaborative project between Bart Jan Ravoo's group in Münster and Eli Zysman-Colman's group. The **Ir-0**, **Ir-3**, and **Ir-4**, were synthesized by me, and **Ir-1** was synthesized by Diego Rota Martir and me. **Ir-2** and 1-(2-(2-(2-(2-azidoethoxy)ethoxy)ethoxy)ethoxy)adamantane were synthesized and provided by Frauke Schibilla in Bart Jan Ravoo's group. The UV-vis absorption, emission spectra, PLQY and lifetime of **Ir-1** and **Ir-2** were measured by Frauke Schibilla. The UV-vis absorption, emission, PLQY and lifetime of **Ir-0**, **Ir-3** and **Ir-4** were measured by me, as well as the electrochemistry of all five complexes. The self-assembly experiments with cyclodextrin vesicles and related measurements including emission spectra, PLQY and lifetime were measured by Frauke Schibilla. The single crystal structures of **Ir-1'** and **Ir-2'** were obtained by Dr. David Cordes. The emission spectra of **Ir-1** and **Ir-2** in different solvents and cell culture experiments were measured by Frauke Schibilla. The results of cell culture experiments were provided by Frauke Schibilla, and I interpreted the result of the synthesis, characterization, and photophysics of the iridium complexes and their corresponding supramolecular systems in this thesis. I am the primary author of this text.

In chapter 3, the **Ir-5** and **$[(Ir\text{-}5)_6Pd_3](BF_4)_{12}$** were synthesized by me. Their ^1H DOSY NMR, UV-vis absorption, emission spectra, PLQY and lifetime in MeCN solution were measured by me. The HRMS (LC-ESI) of **$[(Ir\text{-}5)_6Pd_3](BF_4)_{12}$** was measured by Diego Rota Martir. The spin-coating of the 10 wt% PMMA doped

film was done by Diego Rota Martir, as well as the photophysical measurements for **Ir-5** and **[(Ir-5)$_6$Pd$_3$](BF$_4$)$_{12}$** in doped film (emission spectra, PLQY and lifetime). The single crystal structures of **Ir-5** were obtained by Dr. David Cordes. The geometry optimization of **[(Ir-5)$_6$Pd$_3$](BF$_4$)$_{12}$** was calculated by Prof. Denis Jacquemin and Dr. Daniel Escudero. I interpreted the results of the synthesis, characterization and photophysics in this thesis. I am the primary author of this text.

In chapter 4, the **Mo-0**, **Mo-1**, **Mol-2**, **Mac-0**, **Mac-1**, **Mac-2** and **Mac-3** were synthesized by me. Their FT-IR and photophysical properties including UV-vis absorption, emission spectra, PLQY and lifetime in DMF solution were measured by me, and their emission spectra and lifetime on bulk powder were measured by Chenfei Li. The spin-coating of **Mol-1** and **Mol-2** was done by Diego Rota Martir, as well as the measurement of their emission spectra, PLQY and lifetime in 10 wt% PMMA doped films. The variable temperature photophysical measurements of **Mol-1** and **Mol-2** in doped films, including emission spectra and lifetime from 77K to 298K were measured by Chenfei Li. The calculations of the geometry optimization and TDA of all compounds were done by me. The ion-recognition experiments and relative photophysical measurements were measured by me. I interpreted the results of the synthesis, characterization and photophysics in this thesis. I am the primary author of this text.

Chapter 1. Introduction

1.1 Basic Photoluminescence Processes and Mechanisms

Photoluminescence (PL) can be considered as the process of light emission from matter after the absorption of photons.[1] It is a common but important phenomenon that has been employed in photocatalysis,[2] bio-imaging,[3] metal recognition,[4] etc. In PL, most of the electrons stay in the singlet ground state. After absorbing photons, one electron is excited to a higher energy level (S_n) without changing the spin orientation.[5] According to Kasha's rule, the excited electrons decay to the lowest excited singlet energy level (S_1) quickly through non-radiative decay called internal conversion (IC), within a femtosecond timescale.[6] The electrons deactivate to the ground state through radiative decay (termed 'fluorescence') to give emissions or non-radiative decay without emissions. Generally, the inversion of spin orientation is prevented because of the spin selection rule. The effect of spin-orbital coupling (SOC)[7] brought by a heavy metal (such as Ir, Ru, Pt etc.) is able to relax the spin-forbidden nature of the radiative decay from the triplet state. Electrons transfer to the triplet excited state (T_1) through inter-system crossing (ISC), and their spin orientations are anti-parallel compared with before. The emission deactivation from the triplet excited state is called 'phosphorescence'.[8]

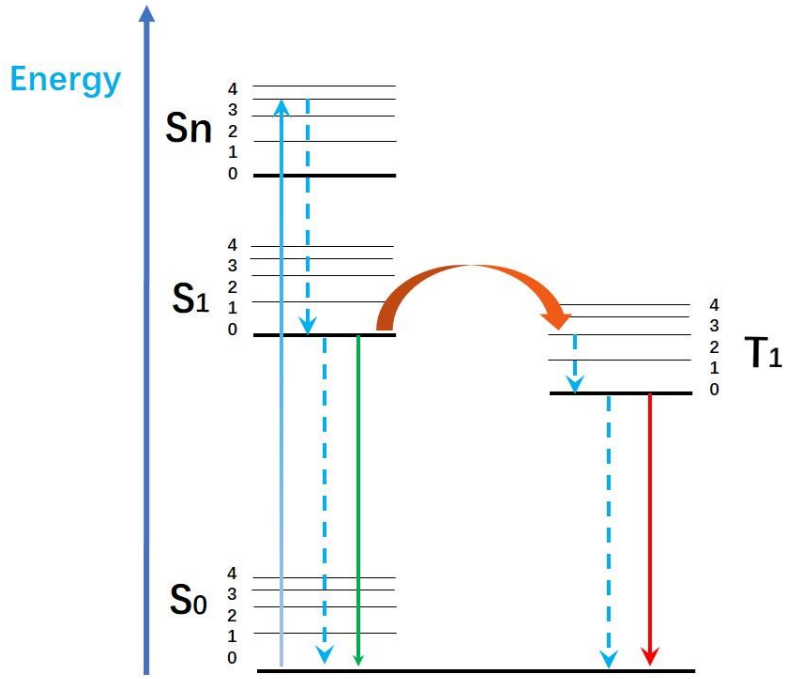

Figure 1.1: Jablonski diagram showing possible processes for photoluminescent molecules after absorbing external photons (blue arrow) to an excited singlet state (S_n): internal conversions (blue dashed arrows, IC), non-radiative decay (purple dash), fluorescence (green arrow), intersystem crossing (orange arrow, ISC), excited triplet states (T_n) and phosphorescence (red arrow).[9]

In photoluminescence, some parameters are always considered for calculation and valuing the photophysical properties of materials, including emission wavelength (λ_{PL}), photoluminescent quantum yield (PLQY), and lifetime (τ_{PL}).[10] Generally, the emission wavelength is the first considered parameter which is decided by the energy gap (ΔE) of the lowest unoccupied molecular orbital (LUMO) and the highest occupied molecular orbital (HOMO) according to $\Delta E = \frac{h}{\lambda}$ (*h* is the Planck constant), and reflects the emission colour. PLQY is

defined as the ratio of the number of emitted photons to absorbed photons.[10] It reflects the ability of emitters to convert the absorbed light energy to luminescence. Another important parameter is lifetime. It is the average time which the molecule spends on the excited state before decaying to the ground state.[1,10] Beside these three parameters which can be measured directedly, radiative decay constant (k_r) and non-radiative decay constant (k_{nr}) are two important calculated data which also bring important information of luminescent processes, $k_r=\Phi/\tau$, and $k_{nr}=1/\tau-k_r$.[10] The k_r is the rate of spontaneous emission of radiative, and the k_{nr} represents the rate of non-radiative decay processes, such as internal conversions. By analysing the k_r and k_{nr}, some factors affecting the photophysical properties of emitters can be explained. Also, the emission mechanisms can be analysed from the shapes of emission spectra to some extent. Theoretically, unstructured emission spectra which follow the Gaussian distribution in shape suggests the charge transfer mechanism of luminescence. In comparison, the structured emission spectra represent their localized emission mechanisms.

1.1.1 Pure organic phosphorescent materials

Intersystem crossing is generally forbidden because of the spin selection rule. It results those fluorescent emitters have 25% internal quantum efficiency (IQE) at most in devices, because only 25% electrically generated excitons locate on

singlet excited state statistically. In comparison, phosphorescent emission utilizes excitons on triplet state and improves the theoretical IQE to 75%.[11] However, in pure organic systems, the design of phosphorescent molecules is still a challenge. In 2016, Zhao et al. reported a feasible design solution for pure organic phosphorescent materials, and a group of molecules were synthesized (**1 a-c,** Figure 1.1.1.1).[11] According to their results, atoms with spare n orbitals are necessary to provide efficient SOC and improve intersystem crossing efficiency. Also, the T_1 state should be close in energy to the (π, π^*) state for a long lifetime. The final condition was that the energy gap between S_1 and T_1 ($\Delta E_{st}=S_1-T_1$) should be higher than 0.6 eV to block reverse intersystem crossing. If the ΔE_{st} were too small, the thermally activated delayed fluorescence (TADF) would strengthen and reduce the phosphorescence.

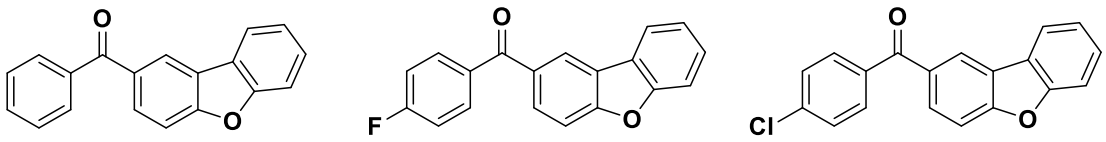

τ_{PL}=232 ms
Φ_{PL}=34.5%
1a

τ_{PL}=110 ms
Φ_{PL}=6.5%
1b

τ_{PL}=44 ms
Φ_{PL}=36.0%
1c

Figure 1.1.1.1 Chemical structures of pure organic phosphorescent molecules, **1a**, **1b** and **1c**. (Photophysical properties were measured in crystalline state)[11]

1.1.2 Pure organic thermally activated delayed Fluorescence (TADF) materials

TADF molecules are considered as the next generation of optoelectronic materials because they have the potential to achieve 100% internal quantum efficiency in devices, similar to heavy metal phosphorescent complexes but at a lower price and toxicity.

The emission mechanism of TADF (Figure 1.1.2.1) is somewhat similar to the fluorescence which has been stated as Figure 1.1 at the beginning of this chapter. However, the energy gap between S_1 and T_1 should be less than 0.2 eV. With such a small gap, the excited electrons in the triplet state can transfer to the corresponding singlet state through reverse intersystem crossing (RISC). There will be at least two components of the emission decay. The directly formed excitons jump back to the ground state quickly as fluorescence, which is referred to as prompt fluorescence in the process. At the same time, the electrons in the excited triplet state transfer to the excited singlet state firstly, and then relax to the S_0 through radiative decay process. Because the RISC is much slower than the prompt fluorescence process, this emission decay is longer, usually within the microsecond regime,[12] and is called the delayed fluorescence.

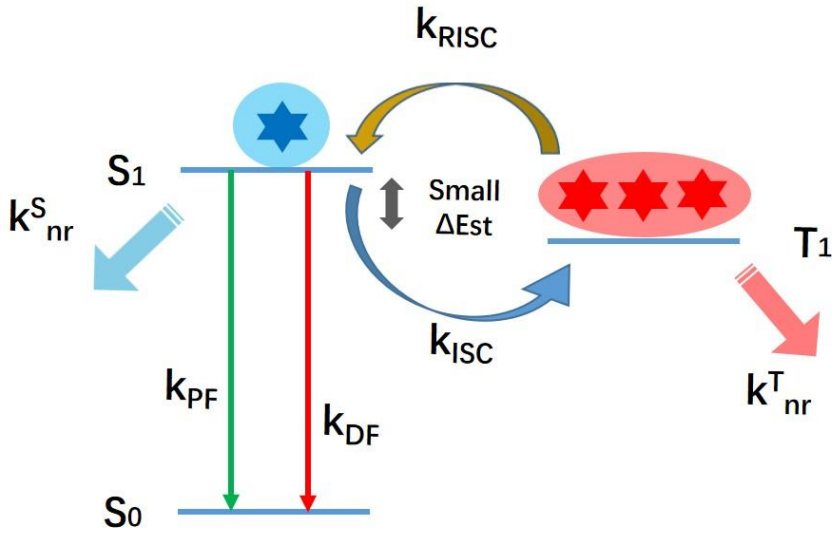

Figure 1.1.2.1: Electroluminescent mechanism for TADF molecules from an excited triplet state (T_1) to singlet state (S_1) and ground state (S_0): PF = prompt fluorescence; DF = delayed fluorescence; ISC = intersystem crossing; RISC = reverse intersystem crossing; ΔE_{ST} = the energy difference between the first excited singlet and triplet states; nr = nonradiative.

The TADF phenomenon was firstly observed in 1961. Eosin showed delayed fluorescence in ethanol at 70 ^oC, and its mechanism was also researched.[13] Interestingly, the development of TADF materials started from organometallics especially heavy metal based complexes. In 2008, Yersin and Monkowius published a patent with multinuclear complexes showed TADF properties, and applied in OLEDs.[14] Another tin (IV) based porphyrin followed in 2009 which was reported by Adachi et al.[15] However, these organometallic TADF molecules did not perform high efficiency in OLED devices. In 2011, the first pure organic TADF emitter was reported by Adachi as PIC-TRZ (**2**, Figure

1.1.2.2).[16] This molecule exhibited an external quantum efficiency (EQE) of 5.3%, which is very close to the maximum EQE of traditional fluorescent materials. The really intense research exploring pure organic TADF materials came in 2012, when CDCBs (**3**, Figure 1.1.2.2) was reported by the same group.[17] These donor-bridge-acceptor structures had highly twisted donor carbazole to the main acceptor plane to reduce the overlap of HOMO and LUMO for smaller ΔE_{st}. This material (**3**, Figure 1.1.2.2) had an EQE of 19.3%,[17] which was much higher than traditional fluorescent materials, where the theoretical maximum is 5%. From that time onwards, TADF became a very productive area and more than 400 reports have been published to date.

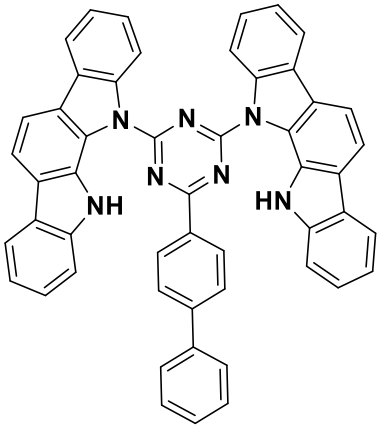

2

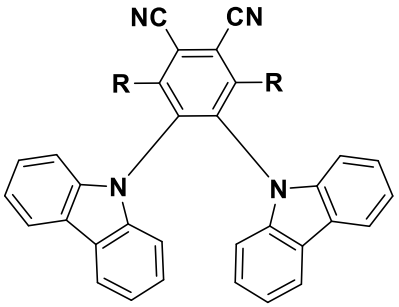

3

Figure 1.1.2.2 TADF molecules (**2** and **3**) reported by Adachi et. al.[16,17]

1.2 Photoactive iridium complexes in supramolecular structures

1.2.1 Photoactive metallosupramolecular cages

Beside the TADF molecules, ionic transition metal complexes (iTMC) are also researched widely as luminescent materials with theoretical IQE of 100%. Because their heavy metal effects relax the spin-forbidden nature, the excitons generated on singlet excited state can transfer to the triplet excited state and deactive to the ground state as phosphorescence.[8] Because these iTMCs also have relatively stable configurations and easy decorated ligands, they act as common blocks and linkers in supramolecular systems. Metallo-coordination cages, for example, are assembled from metal ions and multidentate ligands or complexes with spare coordination sites, have been attracting attention in supramolecular chemistry for the last three decades.[18] Their closed pseudo-spherical geometry with a hollow interior makes them suitable for applications as host and nanoscale vessels.[19]

The first metallo-coordination cage was reported by Saalfrank and co-workers in 1988.[20] By using metal ions (including Zn (II), Mn (II), Co (II), and Ni (II)) and ketone based bridge ligand, a M_4L_6 (M= metal, L= ligands) tetrahedral cage with metal vertexes and ligand edges was built (**4**, Figure1.2.1.1). After three decades of development, in 2016, Fujita published a giant $M_{30}L_{60}$ cage

synthesized from bent ligands and Pd (II) which has a planar coordination configuration (**5**, Figure 1.2.1.1).[21] Nowadays, developing applications for metallo-coordination systems is a hot topic and their luminescent properties are of considerable interest.[22,23] The luminescent coordination system is self-assembled by a large number of chromophores or photoactive blocks surrounding a bound molecule, and the excited states of cages and guests can be interacted by high local chromophores, which is very difficult to be achieved through other methods.

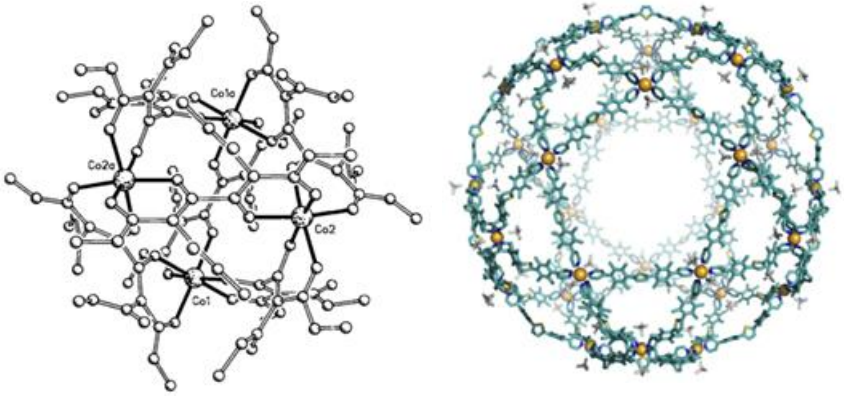

4 **5**

Figure 1.2.1.1 The first reported metallo-coordination cage (**4**), and $M_{30}L_{60}$ cage (**5**) published by Fujita et al. (Photocredit: J. Davies et al. *Angew. Chemie Int. Ed. English* 1990, **29**, 312 (**4**, left); D. Fujita et al. *Chem*, 2016, **1**, 97 (**5**, right))[18,21]

1.2.2 Photoactive iridium complexes based supramolecular systems

Some luminescent cage-like structures have been reported, mostly used pure organic ligands to coordinate with labile ions, such as Ru (II)[24] and Pd (II).[25] However, there are only a few examples using luminescent organometallic complexes as blocks for building coordination supramolecular cages. Among them, iridium complex-based supramolecular systems are rarer.[26] According to the literature, photoactive iridium complexes base supramolecular systems can be classified as single metal coordination cages, heterometal coordination cages, Ir (III) encapsulated systems and soft salts.

1.2.2.1 Single metal coordination cage

In single metal coordination systems, Ir (III) was linked by organic ligands to form well defined structures. Generally, cyclometalating iridium dimers were used to coordinate with pure organic ligands through Ir-N bonds and this kind of supramolecular cages provides two examples of obtaining enhanced emissions compared to their analogue complexes.

In 2012, Lusby et al. published an octahedral cage composed of iridium complexes (**7**, Figure 1.2.2.1.1).[27] Six homochiral $[Ir(ppy)_2]^{2+}$ (ppyH= 2-phenylpyridine) occupied the vertices and were linked by four 1,3,5-

tricyanobenzene (**TCB, 6,** Figure 1.2.2.1.1) on the faces. The cage's photophysical properties were compared to a reference structure as $[Ir(ppy)_2(PhCN)_2]OTf$ (525 nm, Φ_{PL}=1 %, in TCE) (**8**, Figure 1.2.2.1.1). The formation of the cage introduced a red-shift (λ_{PL}= 575 nm) and broader emission spectra. Also, the PLQY of the cage compound increased to 4% in TCE, and showed less sensitivity to oxygen.

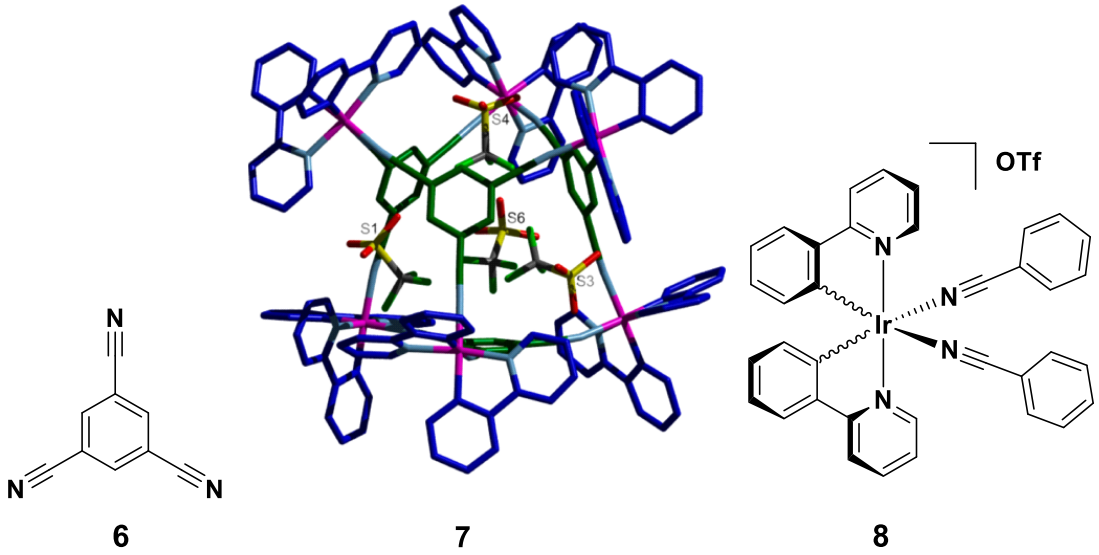

6 **7** **8**

Figure 1.2.2.1.1 Octahedral chiral Ir (III) cage (**7**), its building unit (**6**), and reference complex (**8**) for photophysical measurements reported by Lusby et. al. (X-ray crystal structures of **7**. Colour code: Ir, magenta; C(ppy), dark blue; C(tcb), dark green; N, light blue; O, red; S, yellow; F, light green. Photocredit: P. J. Lusby et al. *J. Am. Chem. Soc.*, 2012, **134**, 19335.)[27]

Another example is homochiral Ir (III) metallo-cryptophanes (**12, 13**, Figure 1.2.2.1.2) published by Zysman-Colman et al. in 2017.[26] The rac-$[Ir(ppy)_2(NCMe)_2]^+$ (**9**, Figure 1.2.2.1.2) was used as a precursor to coordinate

with the cyclotriveratrylene (**CTV**) derivatives (**10**, **11,** Figure 1.2.2.1.2) to afford a 3D $[\{Ir(ppy)_2\}_3(L)_2]^{3+}$ cage through Ir-N (pyridyl) bonds. Because the ligand had a chiral tripodal form, the products showed homochirality after assembling with $[Ir(ppy)_2Cl]_2$ enantiomers. By comparing cage **12** to its analogue complex (**$[Ir(ppy)_2(4\text{-}pyCO_2Et)_2]^+$**), the **12** had a red shift from 560 nm to 603 nm in DCM, and its PLQY slightly decreased to 1%. However, the emission lifetime of cage **12** increased and was found to be biexponential to 59 ns (0.7) and 129 ns (0.3) compared with the analogue complex (56 ns, [**$Ir(ppy)_2(4\text{-}pyCO_2Et)_2]^+$**).[28] Cage **13** changed the ketone to methylene on the **CTV** derivatives. With this modification, the emission spectra of cage **13** was more structured in DCM and blue shifted to 516 nm compared to cage **12**. Because the synthesis of its analogous mononuclear complex was unsuccessful, there was no direct comparison between cage **13** and its corresponding complex, even though cage **13** showed higher PLQY at 15% and longer emission lifetimes (523ns [0.4], 887 ns [0.6], contribution of component in brackets) than the others in DCM solution.

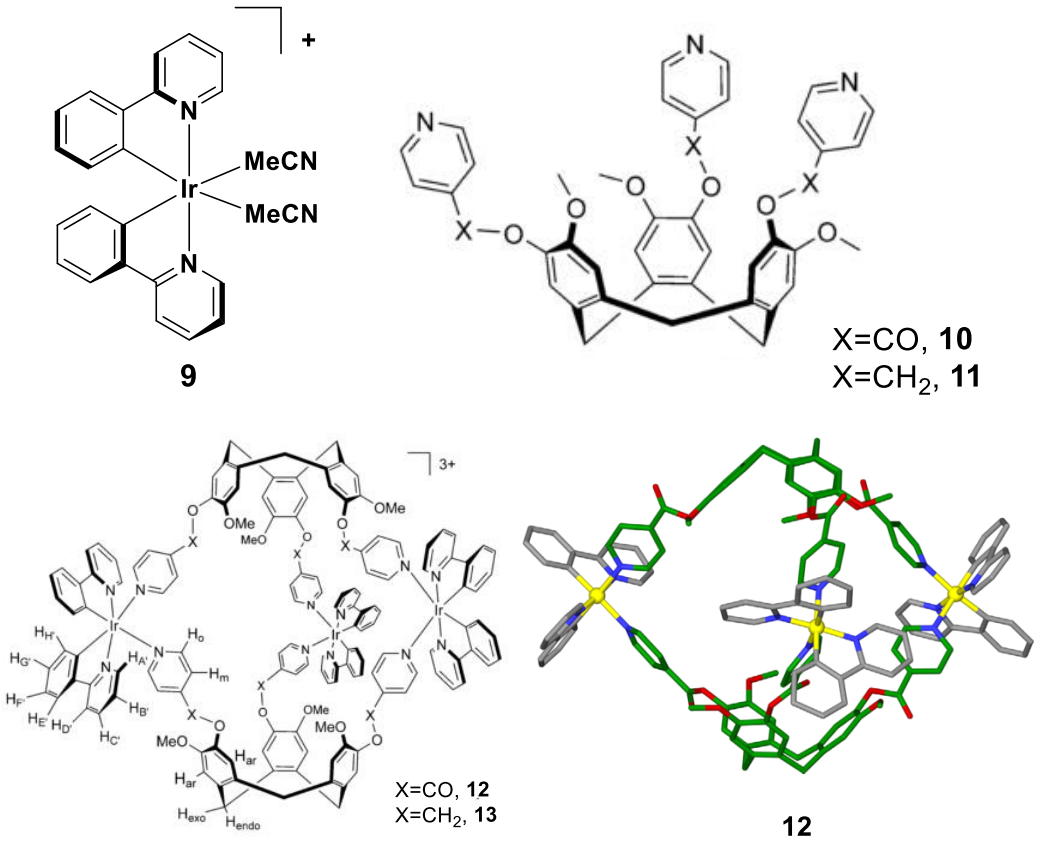

Figure 1.2.2.1.2 Ir (III) Metallo-Cryptophanes (**12** and **13**) and their building blocks (**9**, **10** and **11**) reported by Zysman-Colman et al. (Crystal structure of **12**: **10** and ppy ligands shown in green and grey, respectively. Photocredit: E. Zysman-Colman et al. *Chem. - A Eur. J.*, 2017, **23**, 6291. (**12**))[26]

1.2.2.2 Heterometal coordination system

There are a few examples using $[Ir(C^N)_2(N^N)]^+$ or $Ir(C^N)_3$ complexes as building blocks for supramolecular systems. In these systems, the iridium complex works as an unit to self-assemble with other metal cations, including Cu (I), Cu (II), Zn (II), Cd (II), Co (II), Ni (II) and Pd (II) to produce well-defined

structures. The other metals work as linkers to bond the iridium complexes together and adjust the geometry by their coordination configurations.

Cu (II) was used to self-assemble with iridium complexes containing pendant binding sites because of its planar configuration and good chemical stability. In 2010, Hosseini published an Ir(III)-Cu(II) supramolecule with paddlewheel structure (**15**, Figure 1.2.2.2.1).[29] Two Cu (II) were located in the centres of two parallel planes, and each one was connected to four iridium complexes (**14**, Figure 1.2.2.2.1) lying on the same plane through Cu-O (carboxylic acid) bonds. Unfortunately, this supramolecule had poor solubility in common organic solvents, and decomposition happened in its DMF solution. Single crystal XRD (**15**, Figure 1.2.2.2.1) was used to demonstrate its structure, but no further solution investigation could be carried out. Cu (I) is also a common cation for building complexes owing to its promising photophysical properties. In 2015, Hosseini et. al. reported another Ir(III)-Cu(I) supramolecular structure that made a grid coordination network.[30] The $[Cu(CH_3CN)_4](BF_4)$ solution slowly diffused to racemic iridium complex (**16**, Figure 1.2.2.2.1) solution and afforded a grid-type network (**17**, Figure 1.2.2.2.1) with Cu (I) on vertices and iridium complexes on edges. Before self-assembling, the iridium complexes (**16**) exhibited red emissions at 677 nm and 3% PLQY in the solid state (λ_{PL}=695 nm in THF solution). However, the grid structure (**17**) showed no emission.[30]

According to the literature, **17** was unstable in air because of the oxidation of Cu (I) as well as the desolvation and collapse of its architecture.

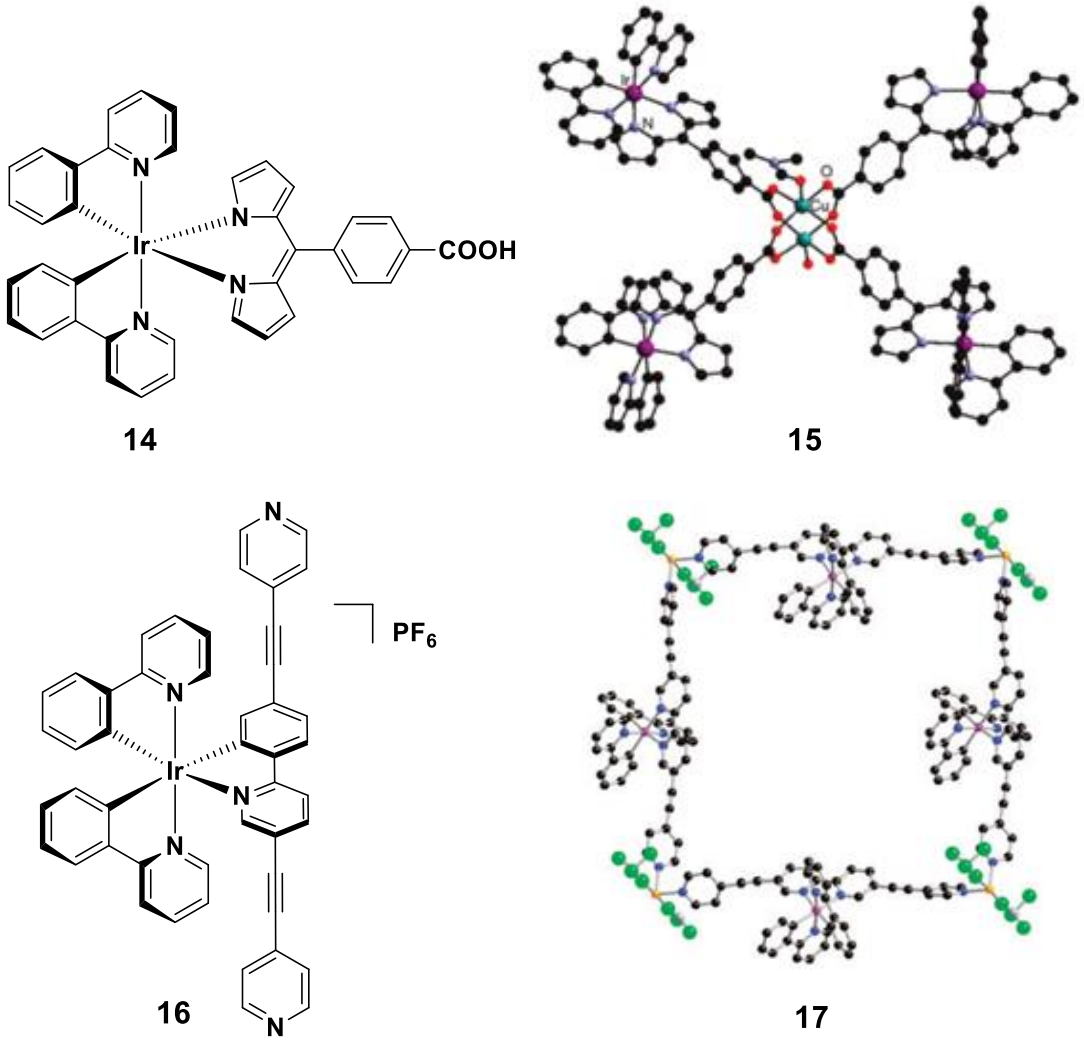

Figure 1.2.2.2.1 Ir-Cu supramolecular system reported by Hosseini (Crystal structure of **15** and **17**. Photocredit: C. Bronner et al. *Inorg. Chem.*, 2010, **49**, 8661 (**15**, up); C. Xu et al. *Chem. Commun.*,2015, **51**, 14787 (**17**, bottom))[29,30]

The ancillary ligand with terminal pyridyl was also used in Ir (III)-Pd (II) supramolecular systems. In 2017, Zysman-Colman et al. published the homochiral emissive $[Ir_8Pd_4]^{16+}$ cages (**19**, **21**, Figure 1.2.2.2.2) with pseudo

spherical geometry.[31] The iridium dimer enantiomers were separated into **Λ** and **Δ** components with the assistance of L-Serine.[27,31] Adjacent Pd (II) coordinated with double-bridge iridium complexes (**18**, **20**) through Pd-N(pyridyl) bonds to form a crown like structure. The ppy (**18**, Figure 1.2.2.2.2) and dFppy (2-(2,4-difluorophenyl)pyridine) (**20**, Figure 1.2.2.2.2) were used as cyclometalating ligands to tune the photophysical properties of the cage. After the self-assembly, all Ir (III)-Pd (II) cages exhibited red-shift emission wavelengths, decreased PLQY, and shorter lifetime in DCM solution. This situation could be interpreted as the coordination with Pd (II), which worked as Lewis acid and stabilized the LUMO of iridium complexes, leading a smaller energy gap. Host-guest interactions between these cages and complex **22** (blue emission, Figure 1.2.2.2.2) were researched, and suggested the possibility of producing white emission materials through energy transfer between guest and host.[31]

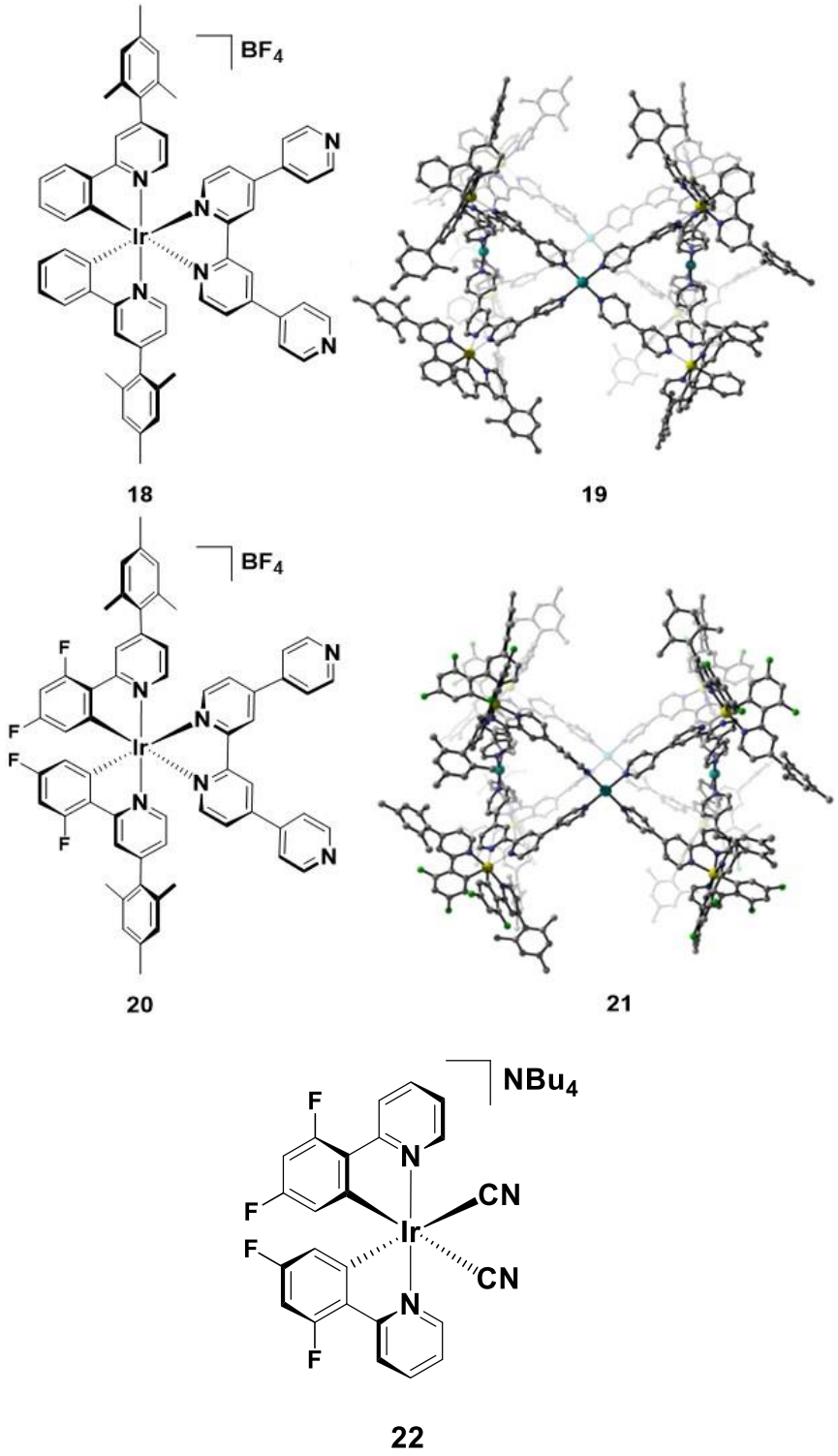

Figure 1.2.2.2.2 Ir (III)-Pd (II) cages (**19** and **21**) and corresponding iridium complexes (**18** and **20**) reported by Zysman-Colman (Simulated structure of **19** (up) and **21** (bottom). Photocredit: D. Rota Martir et al. *Chem. - A Eur. J.*, 2017, **23**, 14359 (**19**, **21**))[31]

Beside the terminal pyridyl metalloligands, the primary amine decorated ligands are another choice to link iridium complexes and transition metal atoms. In 2016, He and et al. built an Ir (III)-Zn (II) supramolecular system (**24**, Figure 1.2.2.2.3) through a one pot reaction.[32] Iridium complex (**23**, Figure 1.2.2.2.3), 2-formylpyridine, and $Zn(BF_4)_2 \cdot 6H_2O$ self-assembled in MeCN solution to form a bipyramidal geometry with two iridium complexes and three Zn (II) (**24**, Figure 1.2.2.2.3). In this system, the two iridium atoms were located on two opposing vertices, and three Zn (II) were located on the vertices of a planar triangle and coordinated with spare nitrogen atoms on the ligands. This Ir (III)-Zn(II) had emission maxima at 508 nm in degassed MeCN and potential applications on CO_2 fixation. The three Zn (II) were buried in the cavity with free coordination sites and the CO_2 could be converted to CO_3^{2-} and bonded to them (**25**, Figure 1.2.2.2.3). With the fixation of CO_2 in the cavity, the emission intensity of Ir (III)-Zn (II) cage decreased rapidly without shifts in the emission energy. SO_2 could also be encapsulated as SO_3^{2-} with the same observations as CO_2. In 2016, Co (II) was introduced to the same system by He et al. as a new metal cation (**26**, Figure 1.2.2.2.3),[33] and the new cage exhibited efficient photocatalytic ability on α-trichloromethylation of 2-acylpyridines under visible light.

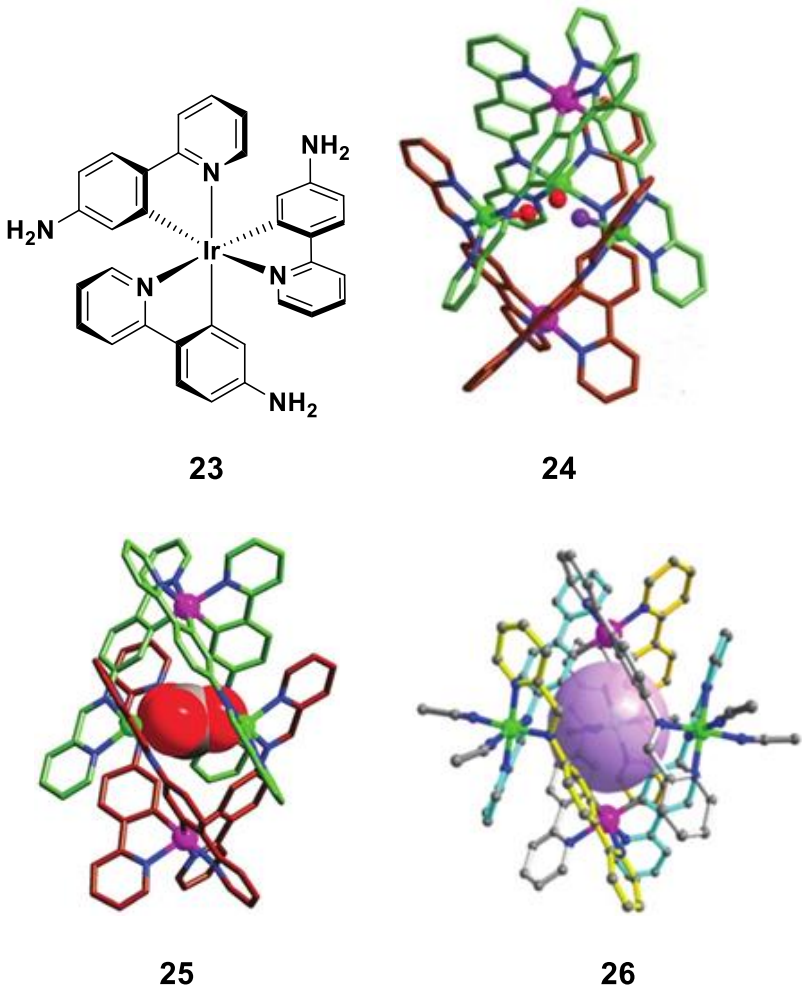

Figure 1.2.2.2.3 Bipyramid configurations of Ir (0)-Zn (II) and Ir (0)-Co (II) reported by He et al. (Crystal structure of **24**, **25**, and **26**. **24**, **25**, C = gray, N = blue, Zn = green, Ir = pink, O = red, F = purple; **26**, C = gray, N = blue, Co = green, Ir = pink; Photocredit: X. Li et al. *Chem. Commun.*, 2016, **52**, 5105 (**24**, **25**); X. Li et al. *Chem. Commun.*, *Chem. Commun*., 2016, **52**, 9628-9631 (**26**))[32,33]

Apart from individual supramolecular systems, extended polymer networks were set up by coordinating carboxyl decorated Iridium complexes with other metal cations, such as Zn (II), Cd (II), Co (II), and Ni (II). In 2012, Sheu et al.

reported a series of iridium complex based coordination polymers.[34] The iridium complex (**27**, Figure 1.2.2.2.4) using H_2dcbpy (H_2dcbpy = 4,4′-dicarboxy-2,2′-bipyridine) as an ancillary ligand acted as a bridge ligand linking the other cations to afford a porous structure (**28**, Figure 1.2.2.2.4). After the formation of polymers, ^{3}MLCT emission was retained. By comparing with the parent complex (**27**, Figure 1.2.2.2.4, λ_{PL}= 613 nm in solid state), these polymers showed slight changes in emission wavelengths, from 587 nm (Cd (II)) to 613 nm (Zn (II)) in the single crystal state, and also in their PLQYs. Even though Zn (II) polymer did not have an emission wavelength shift like the reference complex, its PLQY increased to 27.4% in comparison to complex **27** (Φ_{PL}=17.8%). For the other Ir(III)-cation polymers, Cd (II) had slightly enhanced PLQY, but the polymers with Ni (II) and Co (II) decreased to 1~2%, which was quenched by metal cations. Besides, these Ir (III)-cation polymers showed great sensitivity to oxygen as well as quick response and high reversibility.[34] Because of these special properties, they had potential applications as oxygen sensors.

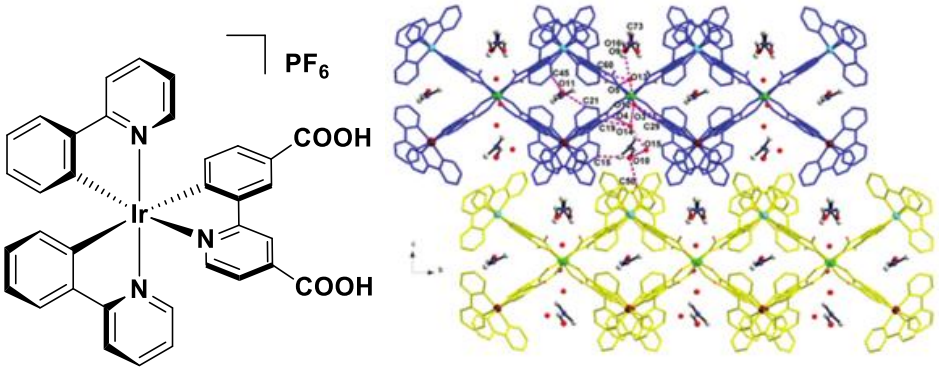

27 **28**

Figure 1.2.2.2.4 Ir(III)-cation polymer reported by Sheu et. al. (Crystal structure of **28.** The 3D zinc-bridged structure exhibited open channels. Zn = green; **27** = blue and yellow; Ir = wine and cyan; O = red. Photocredit: M.-L. Ho et al. *Dalt. Trans.*, 2012, **41**, 2595)[34]

1.2.2.3 Ir (III) encapsulated system

Iridium complexes can not only be used to build host systems as blocks, but also act as guests in some porous structures such as MOFs and capsules. The rigid environment and protection from oxygen can bring some changes to their photophysical properties and enhance their PLQY at the same time.

In 2013, Wang et. al. reported a MOF system (**31**, Figure 1.2.2.3.1) encapsulating $[Ir(ppy)_2(bpy)]PF_6$ (**29**, Figure 1.2.2.3.1) to produce white-light emission.[35] 2,4,6-tris(2,5-dicarboxylphenyl-amino)-1,3,5-triazine (**30**, Figure 1.2.2.3.1) was used as the organic units to build highly porous blue emitting MOF with Cd (II) (λ_{PL}= 425 nm, Φ_{PL}= 15.1%, τ= 0.84 ns, in solid state). Complex

29 (λ_{PL}= 587 nm, Φ_{PL}= 34%, τ= 430 ns, in film)[36] was loaded in the 3D mesoporous anionic MOFs and bonded in cavities. After the encapsulation, there were two emission wavelengths at 425 nm and 530 nm. The signal at 425 nm is characterized by the blue emission of MOF, and the 530 nm peak was contributed by the encapsulated complex **29**, even though there was a blue shift compared with the reference complex in the solid state. This phenomenon could be explained as the effect of a rigid environment, which was reported as the 'rigidchromic effect'.[35,37] Complex **29** occupied the porous structure with 8.8 wt% after soaking for 10 days, and the PLQY of **29**@**31** was enhanced to 28.7% compared with MOF **31,** with bright white lights. The lifetime of **29**@**31** at 425 nm was 0.75 ns (λ_{PL}= 370nm), which was much shorter than complex **29**, but similar to MOF **31**, confirming there was no energy transfer between complex **29** and MOF **31**.

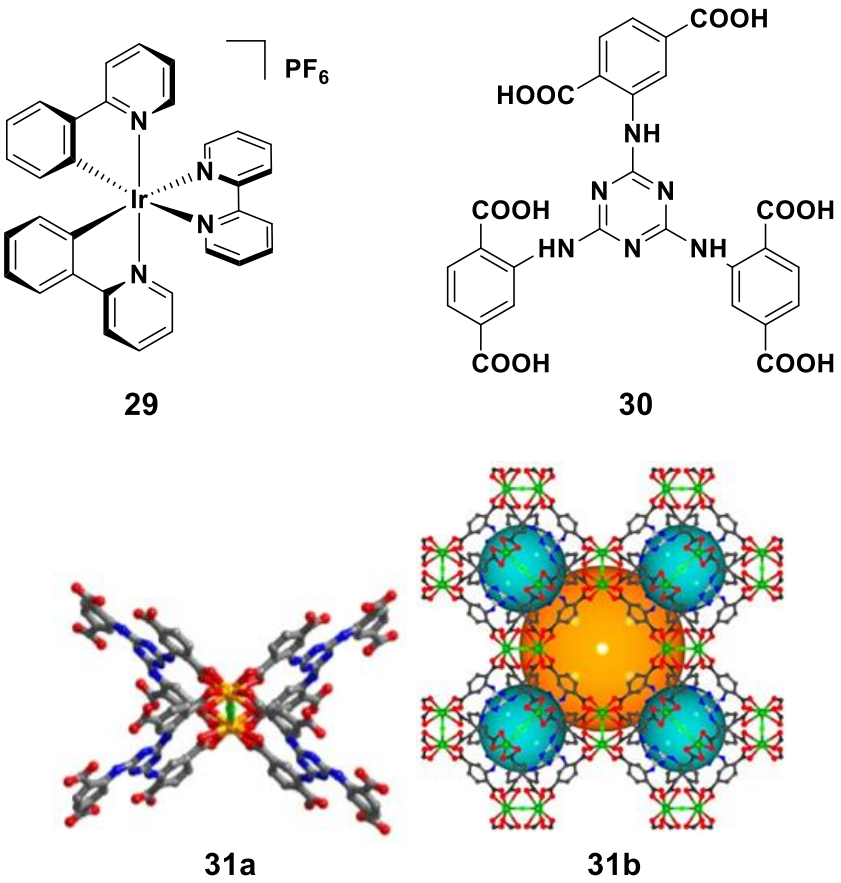

Figure 1.2.2.3.1 Encapsulated **29** in MOFs (**31b**) and their building units (The 3D structure (**31b**) was calculated from the single crystal structure of unit (**31a**); C = grey, O = red, N = blue, Cl = green and Cd = orange. Photocredit: C.-Y. Sun et al. *Nat. Commun.*, 2013, **4**, 1–8, ESI)[35]

Beside MOFs, iridium complexes were encapsulated by self-assembled organic capsules. In 2016, Umakoshi published a hexameric self-assembled capsule (**34**, Figure 1.2.2.3.2) with wrapped $[Ir(ppy)_2(bpy)]Cl$ (**32**, Figure 1.2.2.3.2).[38] This capsule self-assembled from resorcin[4]arene (**33**, Figure 1.2.2.3.2) with sixty hydrogen bonds, and the cation-π interactions between the host and complex **32** stabilized the host-guest system. After the encapsulation

(4 equivalents of **33**), the emission of complex **32** blue shifted to 582 nm in chloroform compared with free complexes (λ_{PL}= 609 nm in chloroform), which was attributed to the 'rigidchromic effect'[35,37] as the MOF system stated before. Also, the encapsulated complex (**35**, Figure 1.2.2.3.2) had enhanced PLQY to 32% compared with **32** (Φ_{PL}= 20%), and its lifetime increased from 420 ns to 860 ns. With the addition of a large amount of **33**, the PLQY and lifetime were improved further to 42% and 990 ns, respectively. This phenomenon could be explained by the reversible self-assembly of capsules. The high concentration of **33** pushed the chemical equilibrium and ensured that all complex **32** were encapsulated. The rigid capsule protected the iridium complex from the oxygen quenching, with the assistance of weaker vibrational quenching, **35** had higher PLQY and a longer lifetime.[38]

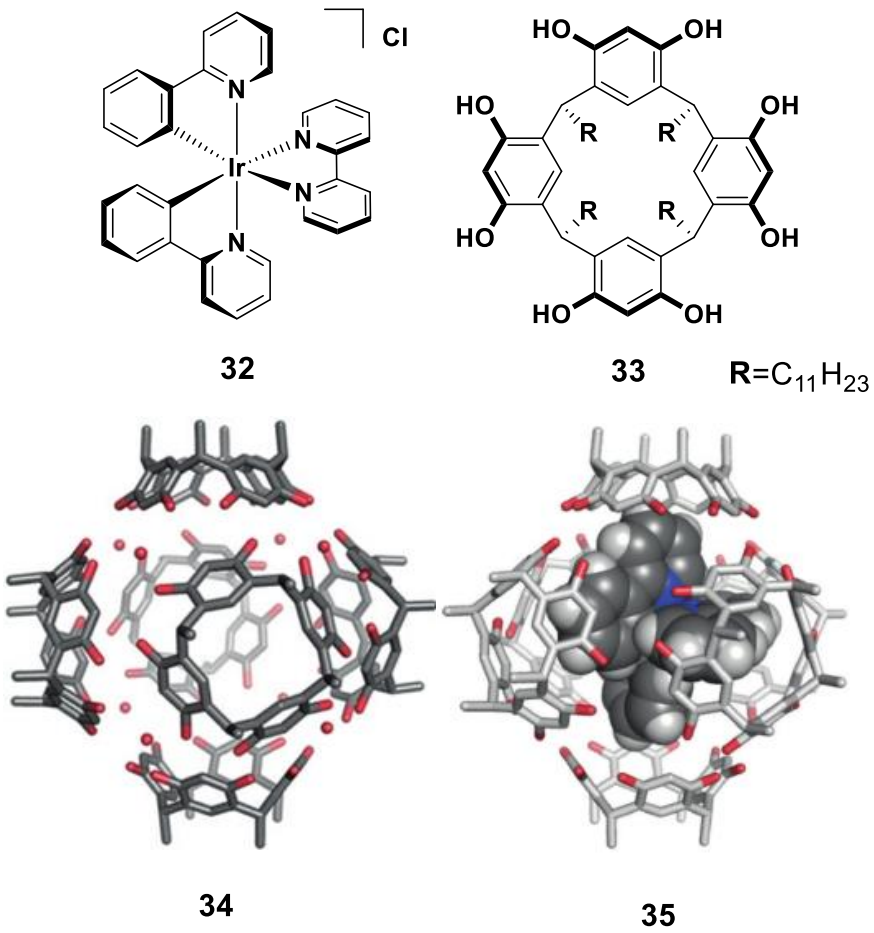

Figure 1.2.2.3.2 Encapsulated **32** in self-assembled capsule (**34**) to afford protected emitters (**35**) (Simulated 3D structure of **34** and **35**. Photocredit: S. Horiuchi et al. *Nat. Commun.*, *Chem. - A Eur. J.*, 2016, **22**, 17534–17535)[38]

1.2.2.4 Ir (III) soft salts

Soft salts are ionic materials composed of organometallic components with opposite charges instead of halide, alkali metal, and other ions as counterions. These systems have porous networks in solid state and the ions are mainly bonded via electrostatic forces.[39,40]

In 2010, Thompson et al. reported a group of iridium soft salts.[39] By comparing their photophysical properties with their corresponding complexes, the soft salts (**38,** Figure 1.2.2.4.1 is an example) showed dual emissions (λ_{PL}=456 nm, 572 nm, in MeCN), which were dependent on their two components (**36**, λ_{PL}=458 nm, and **37**, λ_{PL}=572 ns, Figure 1.2.2.4.1). This characterization made colour tuning easy through the modification of each part. Because the Dexter energy transfer happened between ions in soft salts, the lifetime of the high energy partner complex markedly decreased as a result of quenching (**36**, 36.7μs to 8.6 μs), but the lifetime of the low energy partner complex was not affected (**37**, 3.4 μs to 3.1 μs). Similarly, the PLQY of soft salts (**38**, Φ_{PL}= 74%) matched the PLQY of the components which had relatively longer wavelengths (**36**, 458 nm, 38%; **37**, 572 nm, 78%). In 2014, another iridium complex based soft salt was published by Zysman-Colman.[40] This soft salt (**41**, Figure 1.2.2.4.1) was constituted by one Ru (II) cationic complex (**40**, Figure 1.2.2.4.1) and two Ir (III) anionic complexes (**39**, Figure 1.2.2.4.1). Compared with the corresponding free complexes, this soft salt retained the luminescent features of both components. Specifically, the change in the concentration and solvents could modulate the relative emission intensity from two organometallic ions, and tune the emission colour from blue-green to orange-red, including white light.

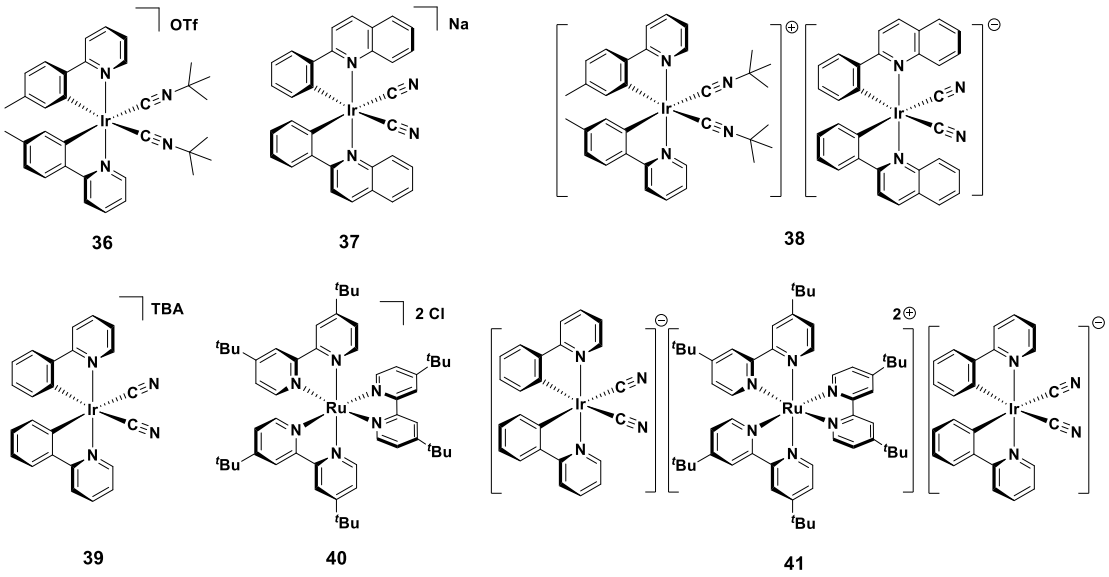

Figure 1.2.2.4.1 Iridium based soft salts (**38** and **41**) and corresponding complexes (**36**, **37**, **39** and **40**)[39,40]

1.3 Adamantane and cyclodextrin vesicles

1.3.1 Cyclodextrins

Beside coordination bonds, weak host-guest interactions such as hydrogen bonds and Van der Waals' force are also used to build supramolecular systems. Among the host structures, cyclodextrins (CDs) are well-known cyclic oligosaccharides with good chemical stability. They have been used for drug delivery,[41] molecular switches,[42] energy conversion and storage.[43] The widely used cyclodextrins can be classified into three types: α-cyclohexaamylose (α-CD, **42**. Figure 1.3.1.1), β-cycloheptaamylose (β-CD, **43**, Figure 1.3.1.1), and γ-cyclooctaamylose (γ-CD, **44**, Figure 1.3.1.1) formed by 6, 7, and 8 glucose

units, respectively. It is difficult to synthesise cyclodextrins containing units less than 6 because of high ring tension.

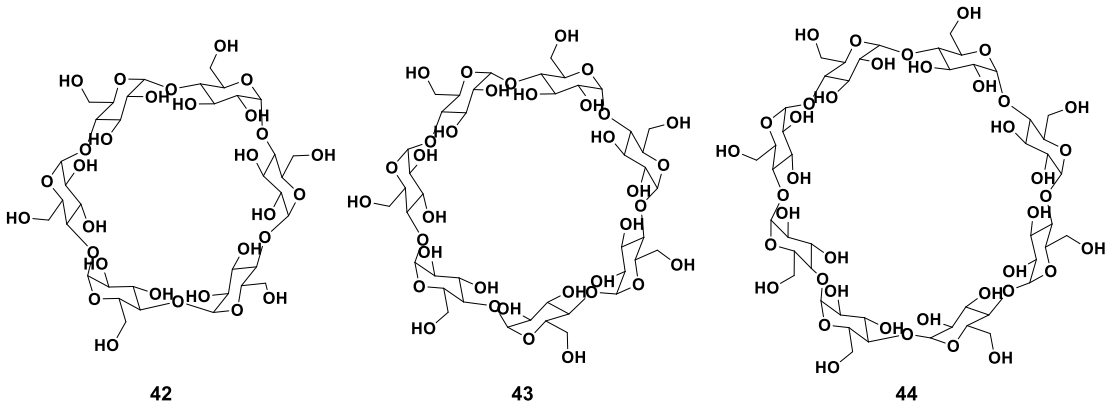

42 43 44

Figure 1.3.1.1 Common cyclodextrins (**42**, α-CD; **43**, β-CD and **44**, γ-CD)

Cyclodextrin vesicles (CDVs) are spherical models with bilayer structures for biological cell membranes.[44] They can be prepared from amphiphilic cyclodextrin derivatives in aqueous systems through the self-assembly process. In 2000, the Ravoo group first synthesized surface active cyclodextrins and the corresponding vesicle systems.[45] By decorating cyclodextrins with hydrophobic functional groups (**45**, Figure 1.3.1.2), the vesicles formed with the hydrophilic surface and hydrophobic core in aqueous solution. Importantly, CDVs have similar properties to natural membranes which bring broad applications for drug delivery,[46] smart materials,[47] and bio-recognitions (**46**, Figure 1.3.1.2).[48]

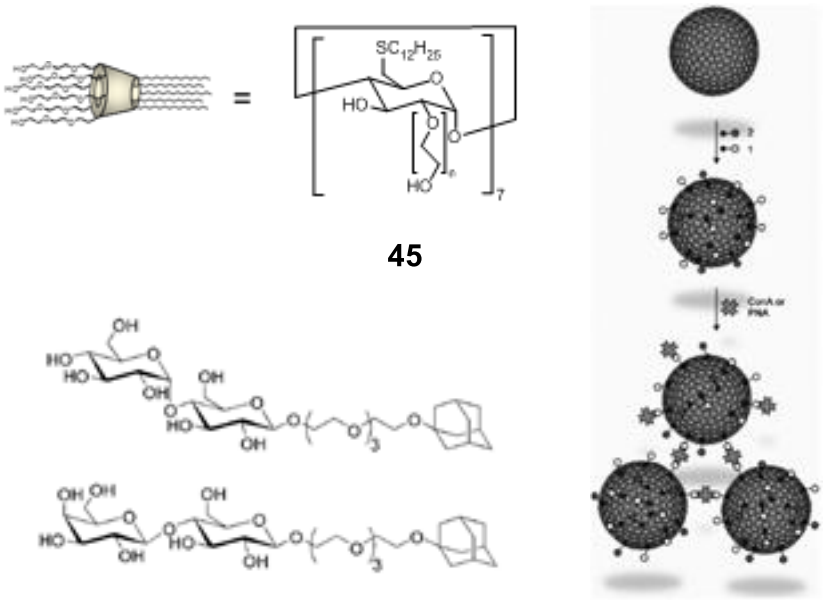

Figure 1.3.1.2 Chemical structure and configuration of hydrophobic functionalized cyclodextrin (**45**) and schematic representation of cyclodextrin vesicles (**46**) reported by Ravoo et. al. (Photocredit: B. J. Ravoo et al. *Chem. - A Eur. J.*, 2010, **16**, 2791)[48]

1.3.2 Molecular recognition between cyclodextrins and adamantanes

The β-cyclodextrin and adamantane are a classical pair of recognition system. Because the size and shape of adamantane are suitable to fit into the cavity of β-cyclodextrin, these two molecules can bond specifically through host-guest interactions. Also, the multiple substitution sites on each component make it easy to modulate their properties.

The β-cyclodextrin-adamantane system can be used for drug delivery. In 2014, Zhao and co-workers reported supramolecular nanoparticle carriers built from functionalized cyclodextrin and adamantane.[49] With the guidance of folic acid, this self-assembled nanoparticle system delivered an anti-cancer drug to specifically targeted cells.

Proteins can also be decorated on the surface of cyclodextrin vesicles through the specific recognition of adamantane.[50] Proteins are linked to adamantane through a long poly(ethylene glycol) chain. This functionalized guest is able to bond to the surface of CDVs through host-guest interactions. With the assistance of polyvalent bonds, the protein can remain on the surface of polymersomes.

1.4 Photoactive macrocyclic structures

1.4.1 Photoactive Schiff-base macrocyclic structures

In supramolecular systems, the structures built through covalent bonds can be much more stable than those based on weak interactions. Because covalent bonds not only have much higher bond energy than hydrogen bonds and Van der Waals' force, but also have good directionality, leading to more rigid configurations. Also, charge transfer can be achieved in conjugated structures which are also set up by covalent bonds with great significance in photoactive

applications. Among covalent bond based structures, Schiff-base macrocycles makes up a large group of macrocyclic structures which keep attracting intentions as ligands[51] and sensors.[52,53,54] It is one of the earliest synthesized macrocyclic structures in the world,[55] which can be modified by different functional groups on both aldehyde and amine precursors.

Even though hundreds of conjugated Schiff-base macrocycles have been published, there is little research on their photophysical properties. In 2005, Li et al. reported a series of luminescent Schiff-base macrocycles (**48**, **49**, Figure 1.4.1.1) synthesized from quinoxaline (**47**, Figure 1.4.1.1),[52] and characterized their photophysical properties in a 0.2 M NaOAc–HOAc buffer solution. In this buffer solution, both macrocycles (**48**, **49**, Figure 1.4.1.1) had green emissions at 507 nm and similar PLQY of 0.6%, 0.7%, respectively. Moreover, this group of macrocycles exhibited high sensitivity to Hg (II) in aqueous solution, and their emission intensities decreased linearly with the incremental Hg (II) concentration.

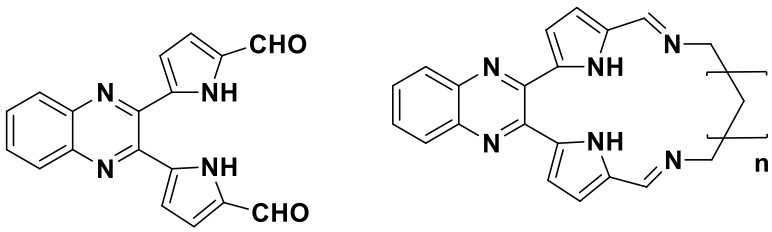

47

n=1, **48**
n=2, **49**

Figure 1.4.1.1 Fluorescent Schiff-base macrocycles (**48** and **49**) applied as Hg (II) sensor and their reactant (**47**)[52]

Another example is a tetraphenylethylene Schiff-base macrocycle (**51**, Figure 1.4.1.2) published by Zheng et al. in 2014.[54] This [2+2] compound had emission maxima at 595 nm in THF, and its emission intensity could be dramatically increased because of aggregation-induced emission (AIE). Macrocycle **51** also showed selective recognition for Cu (II) in THF:H_2O= 1:9 (v/v) suspension, and the PLQY decreased from 8.4% to 0.2% by quenching with the addition of 2 equivalents of Cu (II).

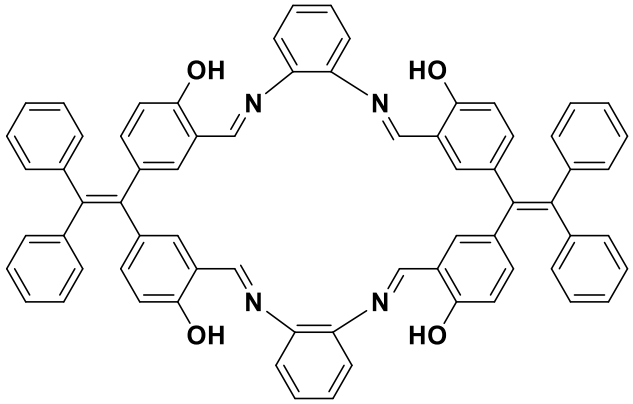

50

Figure 1.4.1.2 Fluorescent Schiff-base macrocycles (**50**) reported by Zhang et. al. with application on Cu (II) recognition.[54]

Another photoactive [2+2] macrocycle (**52**, Figure 1.4.1.3) was published by Zhu et al. in 2012.[53] This structure was built from a binaphthol derivative (**51**, Figure 1.4.1.3) and (*R,R*)-1,2-diaminocyclohexane in THF solution, and represented high selectivity to Zn (II) in MeCN. With the addition of Zn (II) solution, the emission peak at 370 nm gradually disappeared and formed a new enhanced peak at 470 nm.

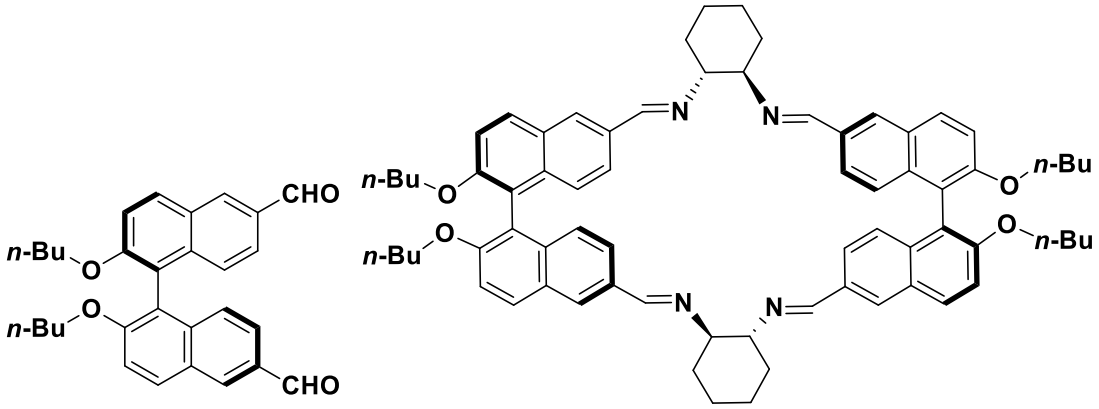

51 **52**

Figure 1.4.1.3. Fluorescent Schiff-base macrocycles (**52**) reported by Zhu et al. applied as Zn (II) sensor and its aldehyde reactant (**51**).[53]

1.4.2 Photoactive carbazole based macrocyclic structures

Carbazole is an electron rich fragment in photoelectrical materials. It has a rigid planar structure with multiple substitution sites. In macrocyclic systems, carbazole derivatives can be used as repeating units to build optical macrocycles with functionalization.[56,57]

In 2006, a series of carbazole based conjugated macrocycles (**54**, **56**, Figure 1.4.2.1) were reported by Zhu et al.[56] In these macrocycles, carbazoles were located on the vertices and linked by diethynyl groups. Three (**54**) and four (**56**) repeating units were contained in macrocycles respectively, and long alkyl chain substituted the *N*-H on carbazoles to improve their solubility in organic solvents. The UV-vis absorption was measured in DCM to analyse the effect of

extending the π conjugation length. According to the results, both macrocycles showed a red shift in the UV spectra compared with their precursors, especially for **54**, which was bathochromically shifted by 59 nm compared with the mono carbazole unit (**53**, Figure 1.4.2.1). However, with the extension of the conjugated system, the red shift changed less. From the emission spectra, the mono-carbazole unit (**53**) had dual emissions at 366 nm and 385 nm in DCM, and the precursor with two carbazoles (**55**, Figure 1.4.2.1) had one main emission at 431 nm and two shoulders at 384 nm and 408 nm, respectively. Compared with the precursors, the formation of macrocycles (**54**, **56**) brought further red shifts. Both macrocycles (**54**, **56**) had one main peak at 440 nm and two shoulders at 425 nm and 428 nm. In the same year, the nanofiber structure of **56** was observed by Zang et al. through atomic force microscopy (AFM).[58] Its photophysical properties in solution and nanofiber aggregations were researched. Compared to solution, both absorption and emission spectra showed an obvious red shift in the solid state and the emission curve became broader, which was characteristic of the $\pi-\pi^*$ stacking aggregation of **56** in the nanofibers.

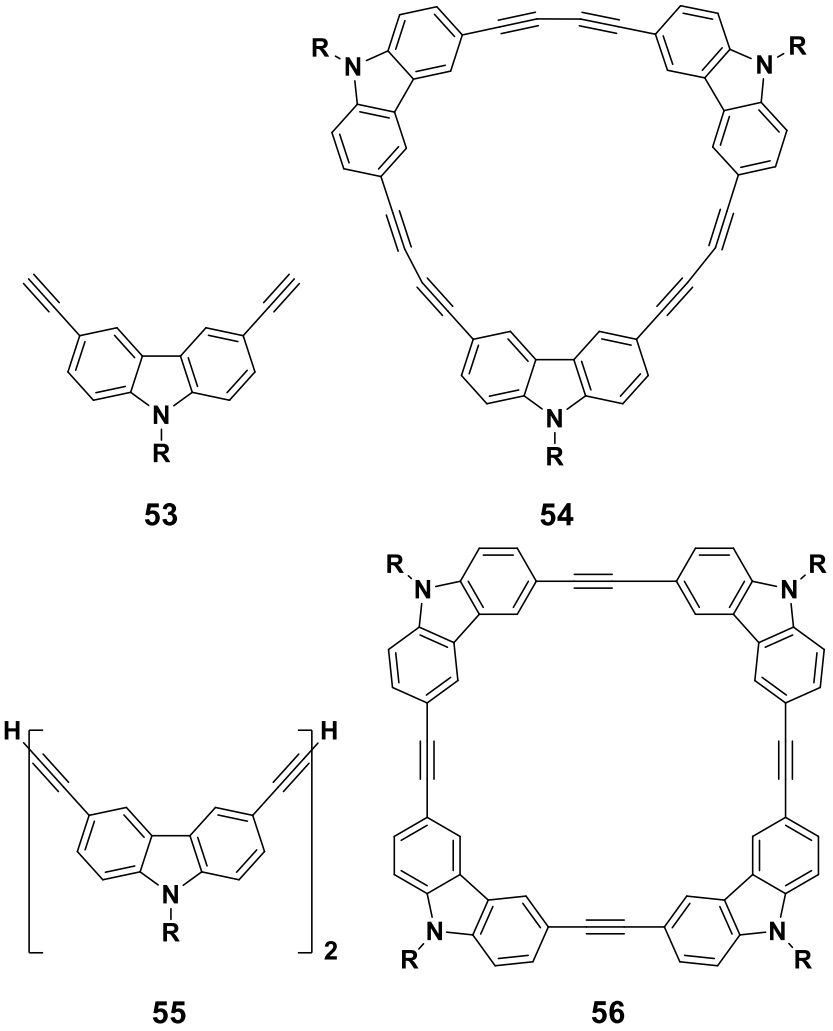

Figure 1.4.2.1 Carbazole based conjugated macrocycles (**54**, **55** and **56**) and corresponding repeating units (**53**) (R=*n*-C_4H_9, *n*-$C_{16}H_{33}$).[56,58]

Another example is a giant carbazole based macrocycle (**57**, Figure 1.4.2.2) published by Müllen in 2006 through template effect.[57] This polycarbazole macrocycle was prepared with the help of **58** and hydroxyl groups on the nitrogen of carbazole. Dissimilar to the carbazole-alkynyl system, the direct linking carbazoles had a blue-shift absorption from 390 nm to 363 nm compared with the linear polymer template in DCM solution. The strongly twisted successive carbazole could be the reason. Because of the steric hindrance, all

carbazoles on the macrocycle are linked in a cis fashion. However, the emission spectra of this macrocycle and linear poly(2,7-carbazole) were similar (λ_{PL}= 420 nm in DCM), which represented their similar geometries in the excited state.[57]

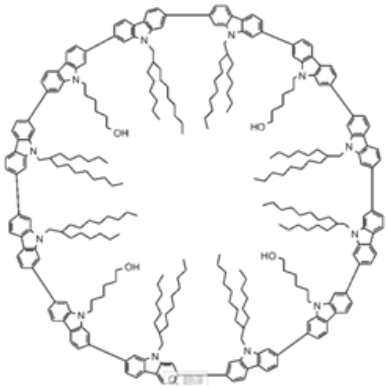

57

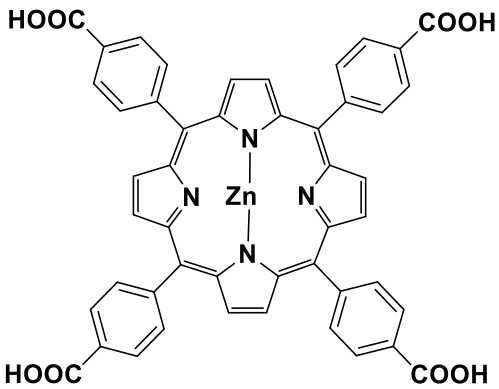

58

Figure 1.4.2.2 A giant carbazole based macrocycle (**57**) and its synthetic template (**58**) reported by Müllen et al.[57]

1.5 Overall objectives

Luminescent materials have been playing important roles in many areas including lighting, displaying, sensing, etc. The photophysical theory exhibits that the excited emitting molecules can be affected by each other, and their PLQYs are generally decreased because of the self-quenching. It is not easy to localize the luminescent molecules on predesigned distances and configurations for exploring the interactions between chromophores through traditional methods. With the assistance of building supramolecular systems, luminescent units can be settled on designed positions, and their photophysical

properties can be researched and cross-compared with individual units to enrich the photophsycial theory and guide the design of luminescent materials. By analysing the literatures stated upward, the supramolecular structures built by iridium complexes and transition metals through coordination bonds represented red-shift emissions and decreased PLQYs compared with the initial emitters generally, which was due to the metal cations acting as linkers and Lewis acids. In this thesis, an iridium complex with extended terminal pyridyl ligand was designed and reported in the Chapter 3 to explore how its photophysical properties will be affected by building supramolecular cage with Pd (II), and can the PLQY be improved by increasing the distance between Ir (III) and Pd (II) atoms. Beside the coordination supramolecular systems, all the encapsulated iridium complexes exhibited enhanced PLQYs, because the emitters were protected from the oxygen quenching and self-quenching. Weak interactions were utilized to build iridium complexes based supramolecular systems in the Chapter 2. The complexes were decorated by terminal adamantly and self-assembled with CDVs to be separated and anchored on a relatively rigid surface. It can provide an easier method to improve the photophsyical properties of iridium complexes compared with the encapsulation. Also, because CDVs can be uptaken by cells, this luminescent supramolecular system was applied on bio-imaging, which provided an idea to utilize highly emitting hydrophobic molecules in biological probes. Covalent bonds based supramolecules have obviously different properties compared with the former

two systems. The high bond energy makes the structure rigid, and the conjugated system exhibits satisfied electron transition properties which represented as red-shift emission maxima compared with the scaffold. Schiff-base macrocycles in Chapter 4 were synthesized from a group of dialdehyde carbazole derivatives which were expected to be fluorescent, phosphorescent and TADF molecules through solvent thermal method. The [2+2] macrocycles were all linked by alkyl chains to keep the photophysical properties of each chromophore and to improve their solubility in solvents. The photophysical of carbazole derivatives and macrocycles were measured and cross compared in solution and solid state for analysing the impact of condensation, *N*-substitutions, and close chromophores. Apart from the changes of photophysical properties, these macrocycles exhibited specific recognitions to Fe (III) in aqueous solution, which can be applied as luminescent ironic probes.

Chapter 2. Exploring the optoelectronic properties of iridium complexes assembled with cyclodextrin vesicles

2.1 Objective

Organometallic complexes have been used widely as oxygen sensors[59], lighting devices[60], and biological probes[61] because their emission colour can be easily tuned and they typically possess high photoluminescence quantum yields (PLQY)[59]. Most of the research in this area has focused on using different ligands to improve the photophysical properties of these complexes.[59,62] Among the large family of heavy metal complexes, iridium complexes exhibit superior photophysical properties because of their high Spin-Orbital Coupling (SOC), which enhances the intersystem crossing.[63] Most iridium complexes have good solubility in organic solvents, such as dichloromethane (DCM), acetonitrile (MeCN), and methanol (MeOH), but not in water. Biological probes need to be soluble in water as living bodies are characterized by an aqueous environment. In aqueous solution, cells can capture the surrounding luminescent molecules and transfer them inside through energy-dependent pathway such as endocytosis primarily and energy independent pathway (passive diffusion etc.).[64,65] These captured molecules will aggregate in certain region of the cell through the interactions with subcellular units. With the external excited light, the luminescent molecules can provide information of the cellular morphology,

cytolergy, subcellular structures such as mitochondria, etc.[64] After Ruthenium (II) complexes have been applied in sensing[66] and bio-labeling,[67] iridium complexes were later developed in this area and attracted much attention.[68] Compared with Ruthenium (II) complexes, iridium (III) complexes have advantages of: 1) higher PLQY at room temperature; 2) broader tunable spectra from the near infrared to near-UV region; 3) larger Stokes shifts, which could avoid the excitation beam and inner filter effects; 4) multiple choices for decorating molecules and adjusting their properties.[69] Even though Iridium complexes exhibit above advantages on bio-imaging, most of them are hydrophobic. In order to use these complexes in aqueous systems and be transferred through the membrane, a variety of decorations have to be used to improve their solubility in water. 1) Charged ligands. Q. Li et al. published complex **59** (Figure 2.1.1) as a water-soluble phosphorescent probe for bisulfite and cyanide recognition, where iodide was the counterion.[70] 2) Decorated ligands with hydrophilic functional groups. In 2015, a series of water-soluble complexes (**60-63,** Figure 2.1.1) using ethylenediamine as the ancillary ligand and hydrophilic decorated cyclometalating ligands was reported[71]. Chloride and lithium were used as counterions for these complexes to increase their water solubility. 3) Coated iridium complexes with water-soluble polymers. H. Shi and collaborators published an iridium complex (**64,** Figure 2.1.1) composed of conjugated polymer (**65,** Figure 2.1.1) that have opposite charges and efficient

spectra overlap for fluorescence resonance energy transfer (FRET) in aqueous solutions for Hg (II) detection.[72]

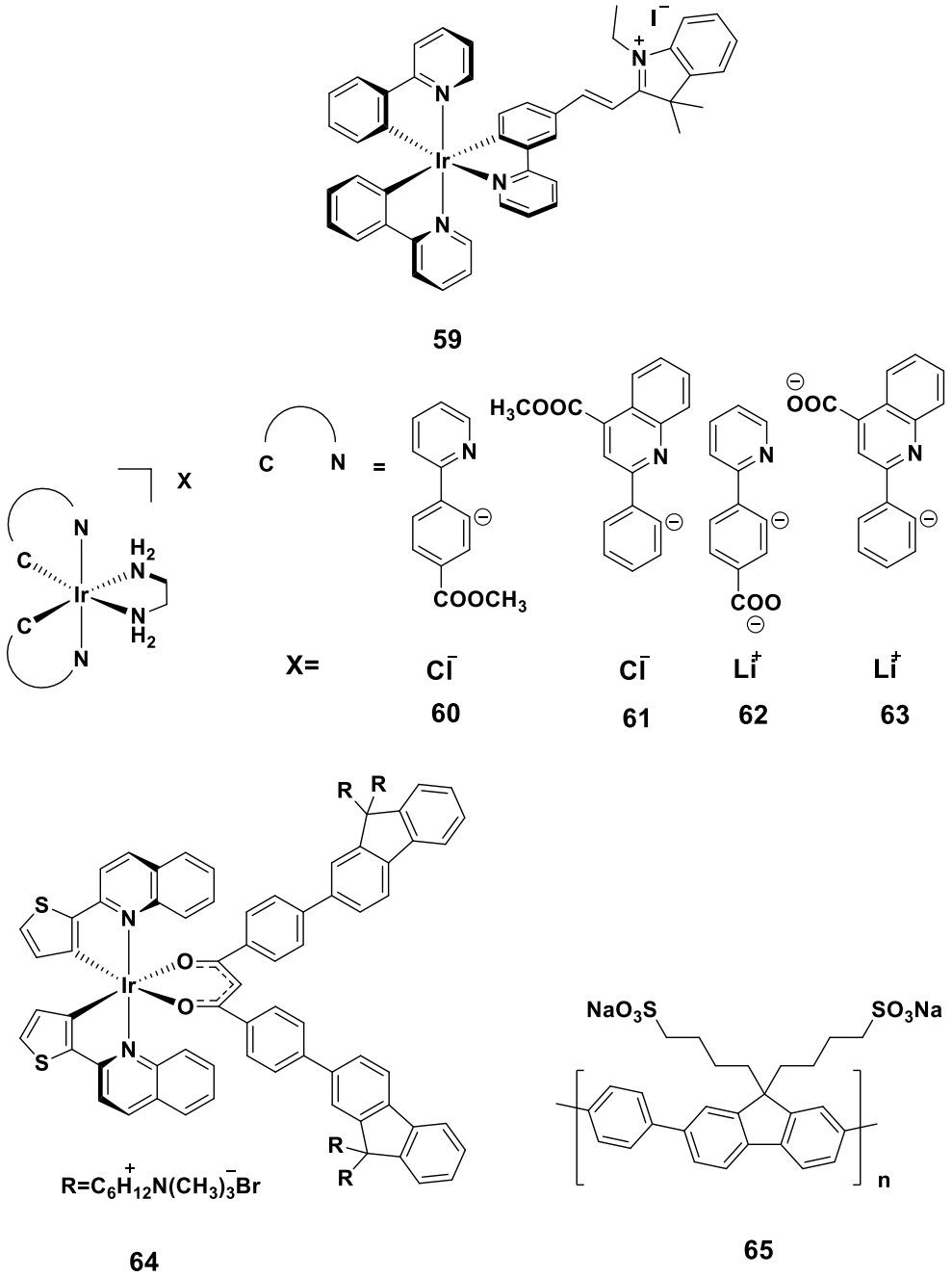

Figure 2.1.1 Water soluble iridium complexes (**59**-**65**) applied as luminescent sensors with 1) Charged ligands (**59**)[70]; 2) Decorated ligands with hydrophilic functional groups (**60**-**63**)[71]; 3) Coated by water-soluble polymers (**64**, **65**)[72].

In this project, the 2,2′-bipyridine was decorated on position four with polyether chains as the ancillary ligand and a chloride ion was chosen as the anion to enhance the solubility of the complex in water. A group of water-soluble iridium complexes decorated with adamantyl groups (**Ir-1** to **Ir-4,** Figure 2.1.2) were synthesized. The adamantyl groups were targeted as recognition units for cyclodextrin vesicles (CDVs) in order to explore the host-guest interactions between the iridium complexes and the CDVs in water, with a view to their use in bio-imaging.

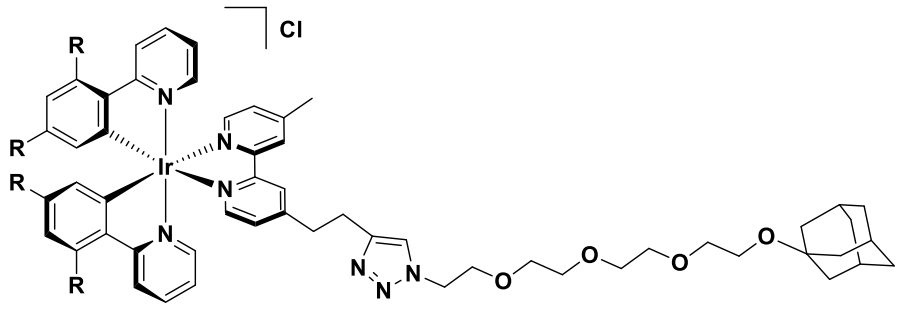

Ir-1: R=H
Ir-2: R=F

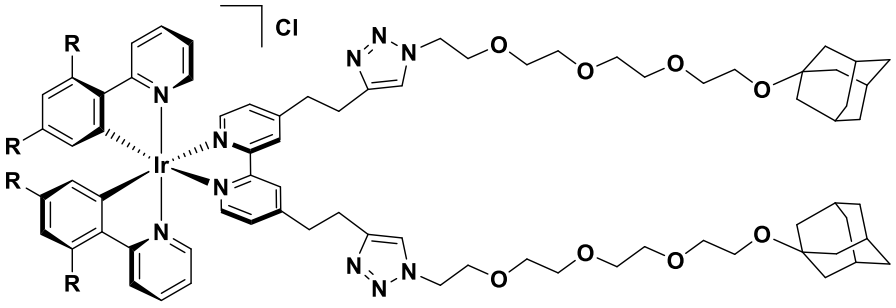

Ir-3: R=H
Ir-4: R=F

Figure 2.1.2 Iridium complexes designed and synthesized in the project (**Ir-1** to **Ir-4**)

Adamantane and cyclodextrin vesicles (CDV) are one of the classical and most popular pairs of molecular recognition systems[73]. The compatible size of host and guest results in strong binding, which can also be used to stimulate the membrane transportation.[74]

The PLQY of iridium complexes can be decreased as a result of aggregation phenomenon leading to self-quenching. However, after assembling with CDVs, the decorated iridium complexes will be isolated on the surface of CDVs as a localized and somewhat rigidified environment to improve their PLQYs and obtain longer lifetime. Because CDVs can be taken up by cells,[75] these compounds were also used for bio-sensing and bio-imaging. Photophysical measurements of both the iridium complexes and the complexes assembled with the CDVs were investigated by emission spectroscopy.

2.2 Results and discussion

2.2.1 Synthesis

The precursor of mono-substituted ancillary ligand (**66**, Figure 2.2.1.2) was synthesized by using LDA to deprotonate one of the methyl groups of 4,4′-dimethyl-2,2′-bipyridine, and coupled with (3-bromoprop-1-yn-1-yl)trimethylsilane (Scheme 2.2.1.1). Dry THF was used as the solvent and all the flasks used in this reaction were dry and protected by an inert atmosphere.

LDA was prepared from *n*-butyllithium and diisopropylamine at -78 ^{o}C in anhydrous THF for 30 min. After dissolving 4,4′-dimethyl-2,2′-bipyridine in anhydrous THF under -78 ^{o}C for 15 min, 1 equivalent of LDA was added dropwise to the solution. The mixture was stirred at -78 ^{o}C for 30 minutes, and 1.2 equivalents of commercial (3-bromoprop-1-yn-1-yl)trimethylsilane was then added to the mixture. After one hour of being stirred, the solution was raised to room temperature and stirred overnight. The yield of this reaction was 50%, and it was important to add the LDA (1 equivalent) slowly to the reaction mixture to make sure that only one methyl was deprotonated.

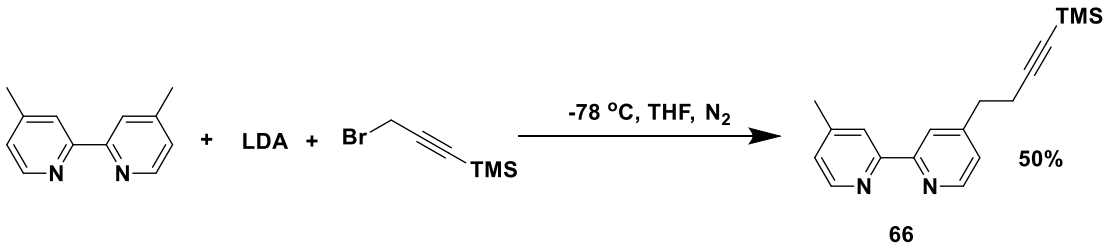

Scheme 2.2.1.1: LDA reaction for synthesizing the precursor of mono-substituted N^N ligand (**66**)

The deprotection of the terminal TMS-alkynyl was done by using potassium carbonate (Scheme 2.2.1.2) to afford the mono-substituted N^N ligand (**66'**). This reaction took 4 hours and afforded a clean product simply by extracting the mixtures with dichloromethane. ^{1}H NMR was used to monitor the progress of the reaction. Instead of one single peak integrating 9 at 0.13 ppm, one triplet

peak at 2.02 ppm integrating 1 showed the signal of terminal alkynyl (Figure 2.2.1.1).

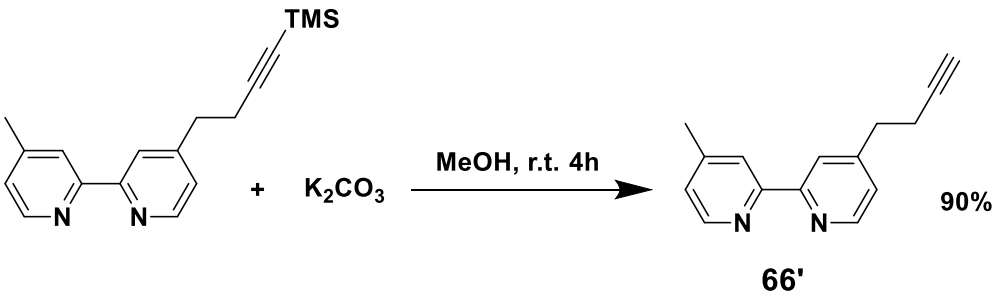

Scheme 2.2.1.2: Deprotection to obtain ligand **66'**

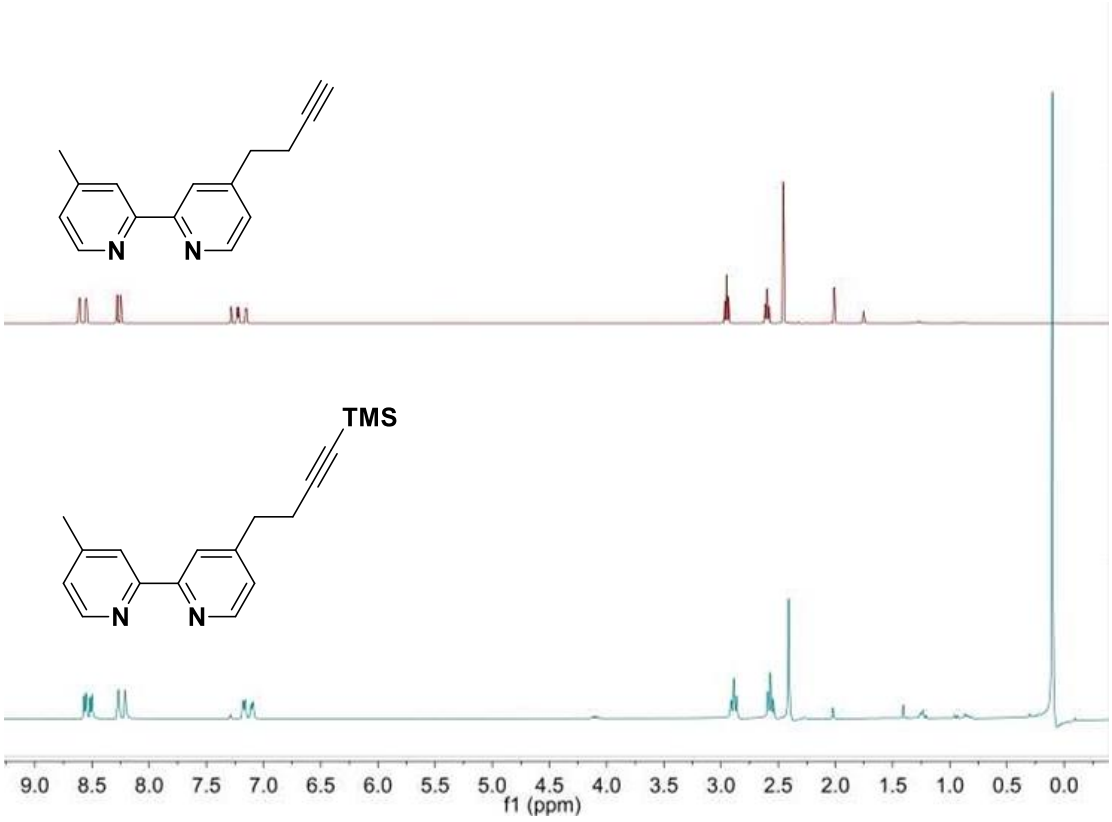

Figure 2.2.1.1 ^{1}H NMR of **66'** (up) and **66** (bottom) for monitoring the deprotection process

The first C^N ligand was 2-phenylpyridine (ppy), and it is commercially available. The ligand 2-(2,4-difluorophenyl)pyridine (dFppy, **67**, Figure 2.2.1.3) was prepared using a Suzuki-Miyaura palladium catalyzed cross-coupling reaction (Scheme 2.2.1.3). The commercial 2-bromopyridine and (2,4-difluorophenyl)boronic acid were dissolved in THF/water (v/v) =4:1, and 6 equivalents of potassium carbonate was added to the solution. $Pd(PPh_3)_4$ was used as the catalyst, which is very sensitive to oxygen. Therefore, this reaction was strictly conducted in a nitrogen atmosphere. After purification by column chromatography, a light yellow oil was obtained and the yield was as high as 74%.

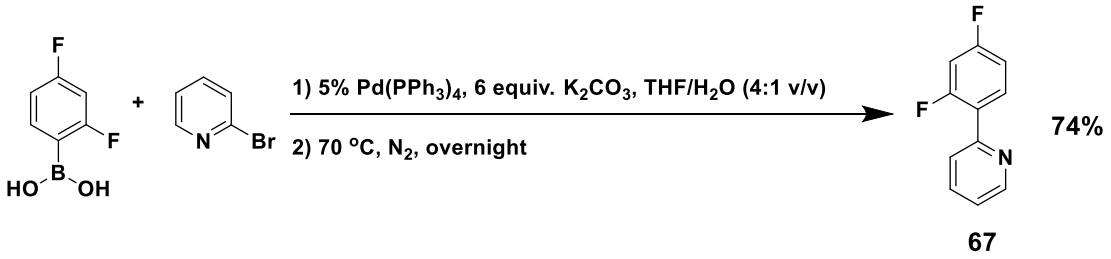

Scheme 2.2.1.3 Synthesis of dFppy C^N ligand (**67**)

After obtaining the ligand **67**, μ-dichloro-bridged iridium dimers were synthesized following a previously reported method.[76] The mixture of $IrCl_3 \cdot 3H_2O$, ligand **67** and 2-ethoxyethanol was degassed for 15 min and heated to 120 °C overnight (Scheme 2.2.1.4). After cooling the suspension to room temperature, its suspension was filtered, and the residue was washed with water and non-polar organic solvents such as diethyl ether and hexane, generating for the

iridium dimers a good yield for both the dimers bearing ppy and dFppy cyclometalating ligands.

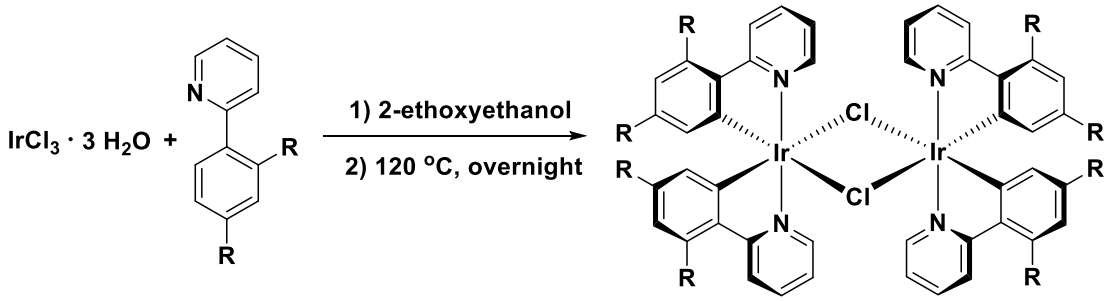

ppy, R=H
67, R=F

68, R=H, **77%**
69, R=F, **91%**

Scheme 2.2.1.4 Preparation for μ-dichloro-bridged iridium dimers [**ppy** (**68**, R=H), **dFppy** (**69**, R=F)]

The complexation was carried out employing the general procedure used in the Zysman-Colman Group.[76] The μ-dichloro-bridged iridium dimer (**68**, **69**) and ligand **66'** were added to the mixture of DCM and methanol (v/v=1:1), after being degassed with nitrogen for 15 min. This reaction mixture was heated to 55 °C overnight (Scheme 2.2.1.5). The μ-dichloro-bridged iridium dimer reacted with the ancillary ligand, cleaving the chloride bridges. The charge of these complexes (**Ir-1'**, **Ir-2'**, Scheme 2.2.1.5) was balanced by a chloride anion. Their structures were characterized by ^{1}H NMR, 2D COSY, HMBC, HMQC, XRD and HRMS. The peak at 2.06 ppm shows the terminal alkynyl resonance, which was not very sensitive to the formation of the complex.

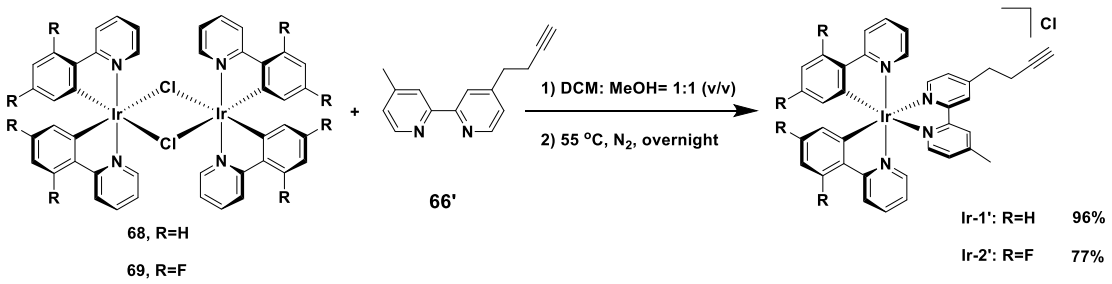

Scheme 2.2.1.5. Complexation for iridium complex precursor with mono-sbustituted N^N ligand (I**r-1'** and **Ir-2'**)

The synthesis of the disubstituted N^N ligand (**70**, Figure 2.2.1.6) was similar to the monosubstituted one, but used 2.5 equivalents of LDA and (3-bromoprop-1-yn-1-yl) trimethylsilane to improve its yield (Scheme 2.2.1.6-i). The C^N ligands were ppy and dFppy, respectively, and the μ-dichloro-bridged iridium dimers were also synthesized from $IrCl_3{\cdot}3H_2O$ in 2-ethoxyethanol. Complexation was carried out by using the iridium dimer (**68**, **69**) and the N^N TMS-protected ligand (**70**, Scheme 2.2.1.6-ii). ^{1}H NMR, 2D COSY, HMBC, HMQC, XRD and HRMS were used to characterize their structures. The peak at 0.04 ppm integrating for 9 represents the TMS group. The same conditions were used for deprotection as for the monosubstituted iridium complexes (Scheme 2.2.1.6-iii). After removing the solvent, the crude mixture appeared as a black oil and ^{1}H NMR was used to characterize the mixture. The single peak at 0.04 ppm disappeared and a new peak at 2.06 ppm showed the proton on the terminal alkynye. The crude product was redissolved in DCM and extracted

with water three times. Organic portions were collected and dried by anhydrous sodium sulfate. After evaporation, this product was used for the next step reaction without further purification.

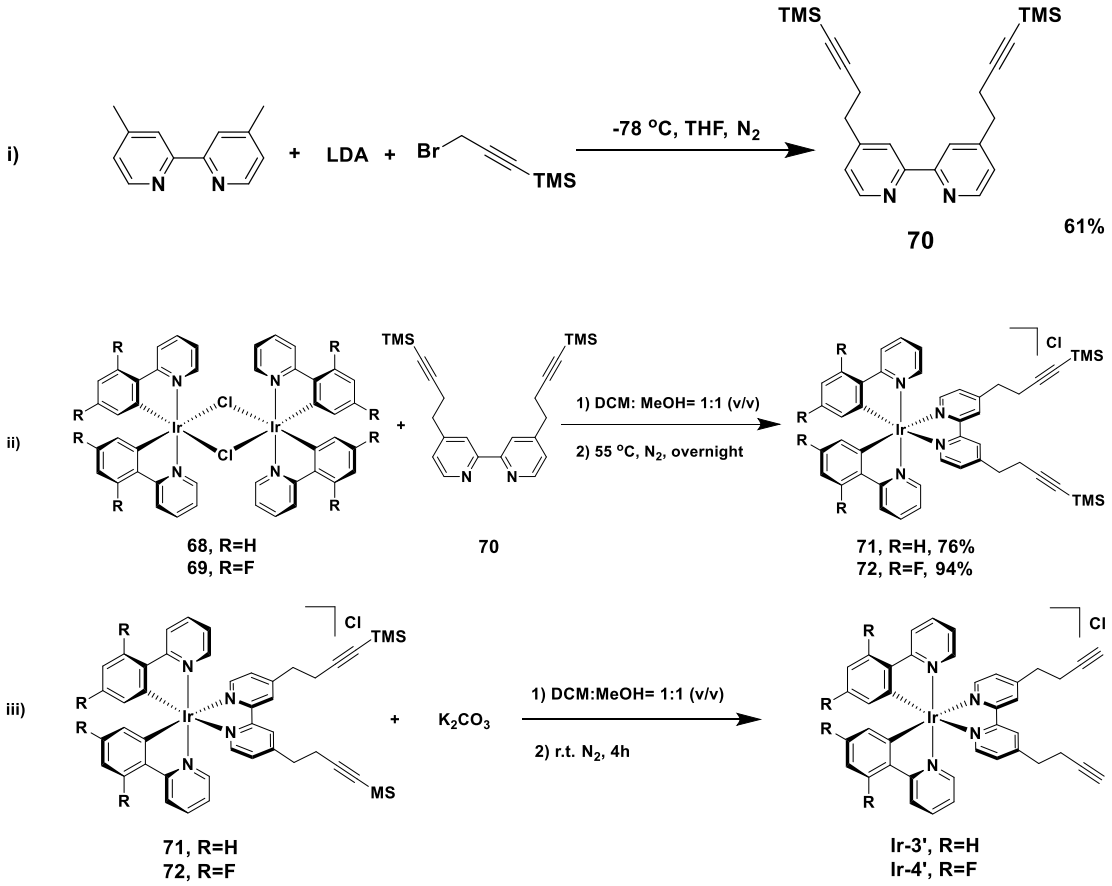

Scheme 2.2.1.6 The synthetic route of di-substituted iridium complex precursors (**Ir-3**' and **Ir-4**')

The click reaction conditions for both families of iridium complexes were the same. The precursor iridium complexes (**Ir-1'**, **Ir-2'**, **Ir-3'**, and **Ir-4'**) and 1-(2-(2-(2-(2-azidoethoxy)ethoxy)ethoxy) ethoxy)adamantane which was provided by Frauke Schibilla from University of Münster, were added to the mixture of

methanol and water (v/v= 1:1). Copper sulfate and sodium ascorbate were used to generate the Cu(I) catalyst (Scheme 2.2.1.7). Because these precursor iridium complexes are not very soluble in methanol, several drops of THF were added to obtain a homogeneous reaction system. The solution was degassed for 15 minutes and reacted in an inert atmosphere for 2-3 days at room temperature. Before stopping the reaction, ^{1}H NMR was used to characterize the mixture. The reaction could be stopped when the peak at 2.02 ppm, which represented the terminal alkyne, had disappeared.

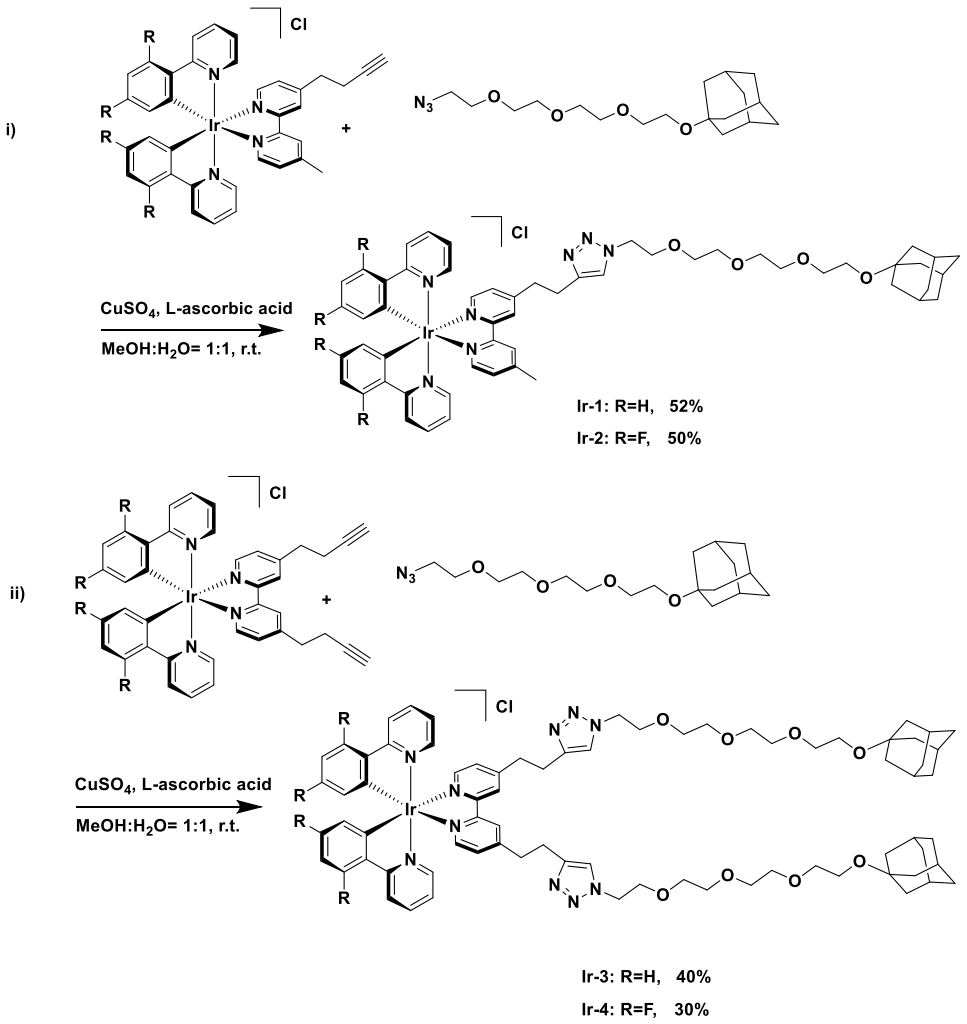

Scheme 2.2.1.7. Click reaction for attaching adamantane to iridium complexes (**Ir-1**, **Ir-2**, **Ir-3** and **Ir-4**)

These target iridium complexes have good solubility in water, so extraction with DCM could decrease their yield. Reduced pressure distillation and short silica chromatography columns were used for purification. These complexes could dissolve in most solvents, such as DCM, MeCN, MeOH and H_2O. The presence of the long polyether chain made it difficult to obtain crystals with a suitable quality for a single crystal XRD, but ^1H NMR, 2D COSY, HSQC, HMBC and HRMS were used to characterize their structures.

Ir-0 was chosen as the reference complex to compare and contrast their photophysical properties and bio-imaging tests. **Ir-0** was synthesized using the general complexation methods stated before (Scheme 2.2.1.8), and purified by a short silica chromatography column.

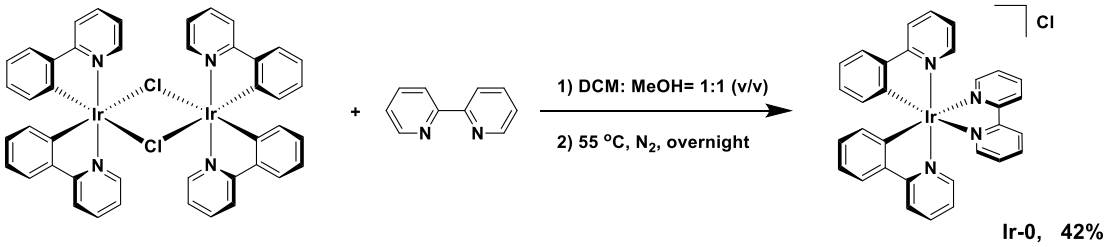

Scheme 2.2.1.8 Preparation for template iridium complex (**Ir-0**)

2.2.2 Molecular structure

Each unit cell in the structure of **Ir-2'** contains the iridium complex with one chloride anion. The near-octahedral geometry is similar to the other $[Ir(ppy)_2(bpy)]^+$ based complexes.[36] The bond length of C2-C41 (1.19(1) Å) and bond angle of C2-C41-C39 (176(1)^o) shows that the triple bond is maintained and is consistent with the ^{1}H NMR, 2D-COSY, HMBC, HMQC, and HRMS data. The Ir-N(ppy) (2.301(5) and 2.305(5) Å), Ir-N(bpy) (2.121(5) and 2.124(6) Å) are not much affected by extended alkyl groups and similar to $[Ir(ppy)_2(bpy)]^+$.[36] **Ir-1'** had the same situation, but the terminal triplet bond missed because its terminal alkynyl group exhibited disorderly in XRD measurement**.** The bond length and angles between the iridium centre and ligands are similar to **Ir-2'**,

and not much affected. With the support of HRMS and ^{1}H NMR, this triplet bond was also confirmed.

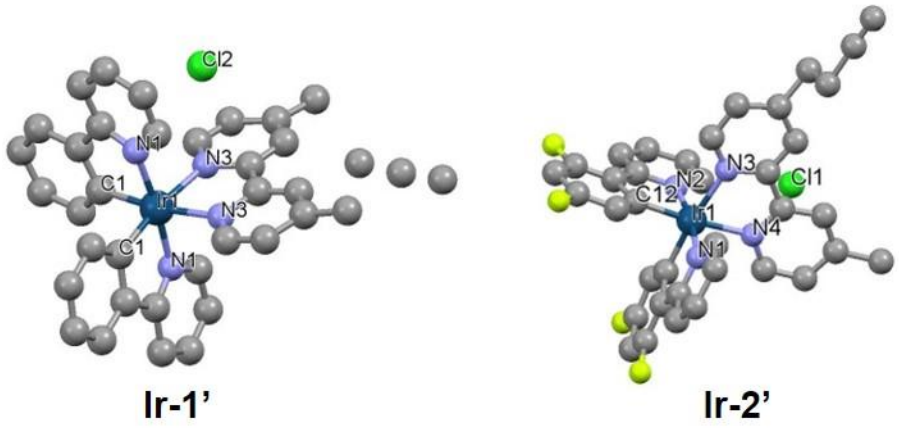

Figure 2.2.2.1 Single crystal structure for **Ir-1'** and **Ir-2'** (the grey balls represent carbon atoms, the deep blue ones are iridium atoms, the light blue are nitrogen, the yellow are fluorine and the green are chloride atoms. Hydrogen atoms and solvent molecules are omitted for clarity)

2.2.3 Electrochemistry

Cyclic voltammograms (CV) were recorded for all five complexes in MeCN with 0.1 M $TBAPF_6$ (tetrabutylammonium hexafluorophosphate) as the supporting electrolyte, and referenced with the ferrocene/ferrocenium couple. **Ir-1** to **Ir-4** showed an irreversible oxidation at 1.0 V. These peaks represented the oxidation of 1,2,3-triazole, similar to the values found in the literature.[77,78] **Ir-0**, **Ir-1** and **Ir-3** had analogous waves at 1.3 V, and these were the signals of the Ir(III)/Ir(IV) couple and oxidation of ppy in the complexes. By comparison, the

similar peaks in **Ir-2** and **Ir-4** were pushed to a higher oxidation potential at 1.65 V, which was caused by the fluorine atoms on C^N ligands stabilizing their HOMO. All these five peaks were reversible.

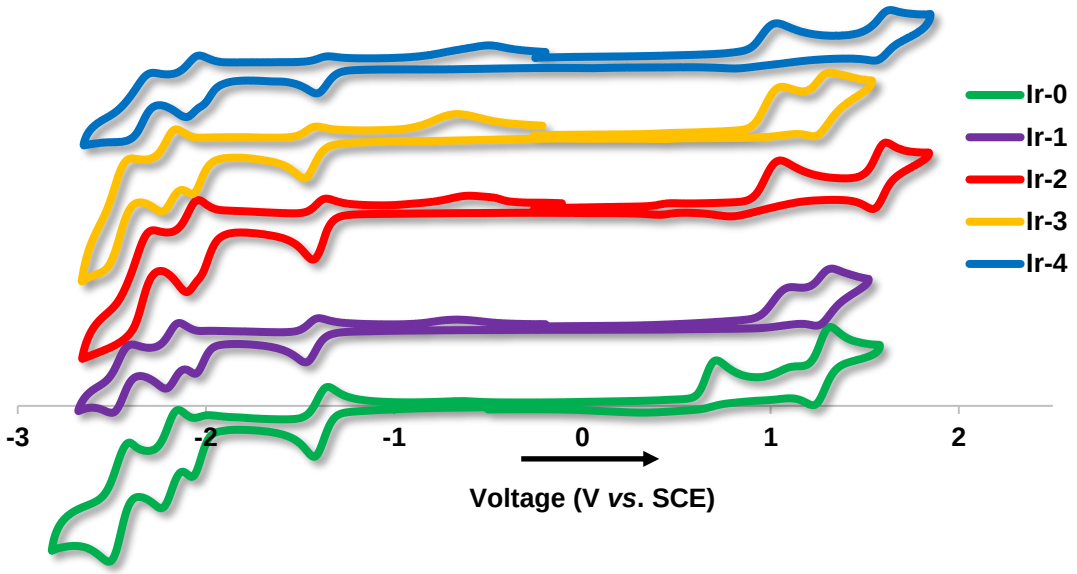

Figure 2.2.3.1 Cyclic Voltammetry of **Ir-0-4** in MeCN solution, reported versus SCE (Fc/Fc^+ = 0.38 V in MeCN).[79] Scan rates were at 100 mV s^{-1} and were in the positive scan direction.

For reduction, **Ir-1** to **Ir-4** showed irreversible peaks at -1.3 V, except **Ir-0**. This wave was assigned to the reduction of N^N ligands. The waves at about -2.0 V, which represented the C^N ligands, were also separated into two groups. **Ir-1** and **Ir-3** were pushed to more negative potential at -2.2 V because they do not have fluorine on the C^N ligand to stabilize the orbitals, compared with **Ir-2** and

Ir-4 at 2.0 V. From the electrochemical data, these complexes gave the expected results, and had similar reduction potentials, which should be mainly affected by ancillary ligands.

2.2.4 Photophysical properties

The absorption spectra of all five iridium complexes in MeCN were recorded. According to the literature[80], bands under 340 nm are assigned as ligand-centred transitions (LC). Bands between 340 and 500 nm are associated with a mixture of metal-to-ligand charge transfer (^{1}MLCT) and ligand-to-ligand charge transfer (^{1} LLCT) between the phenyl rings on C^N ligand and ancillary ligand.[62] As shown in Figure 2.2.4.1, **Ir-0**, **Ir-1** and **Ir-3** have very similar absorption spectral profiles in MeCN, but different extinction coefficients. The mono-substitution (**Ir-1**) showed the highest molar absorptivity, and the non-decoration template (**Ir-0**) was the lowest. **Ir-2** and **Ir-4** also have similar spectral shapes, but their absorbance had an opposite tendency. The di-substituted iridium complex (**Ir-4**) had higher molar absorptivity than **Ir-2**. By comparing these two groups, **Ir-2** and **Ir-4** were blue shifted compared with the other two complexes, which was due to the stabilization of HOMO. The two decorated ppy based iridium complexes exhibited higher molar absorptivity in MeCN.

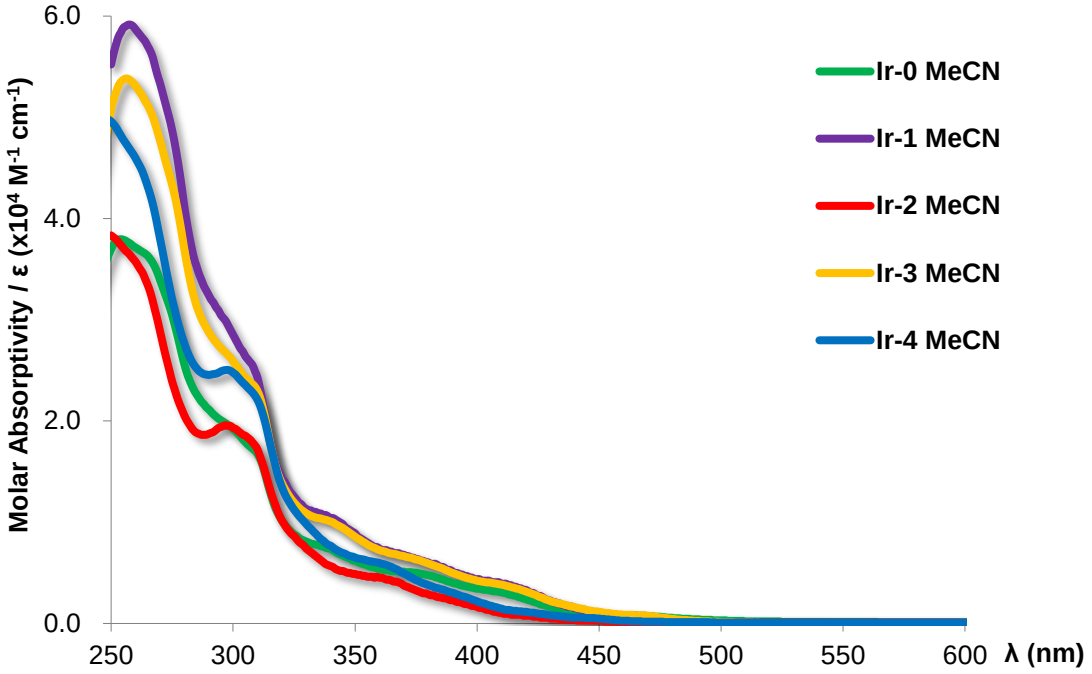

Figure 2.2.4.1 Molar absorptivity spectra of **Ir-0** to **Ir-4** in MeCN solution.

Because all the self-assembly experiments were run in aqueous solution, PB 7.4 buffer (Phosphate buffer solution, pH=7.4) was chosen as the other solvent for the photophysical measurements. From the absorbance spectra, the change in solvent had little influence, but both their molar absorptivity decreased, especially for **Ir-1**. After changing the solvent to PB 7.4 from MeCN, the absorbance of **Ir-1** and **Ir-2** decreased to a similar intensity.

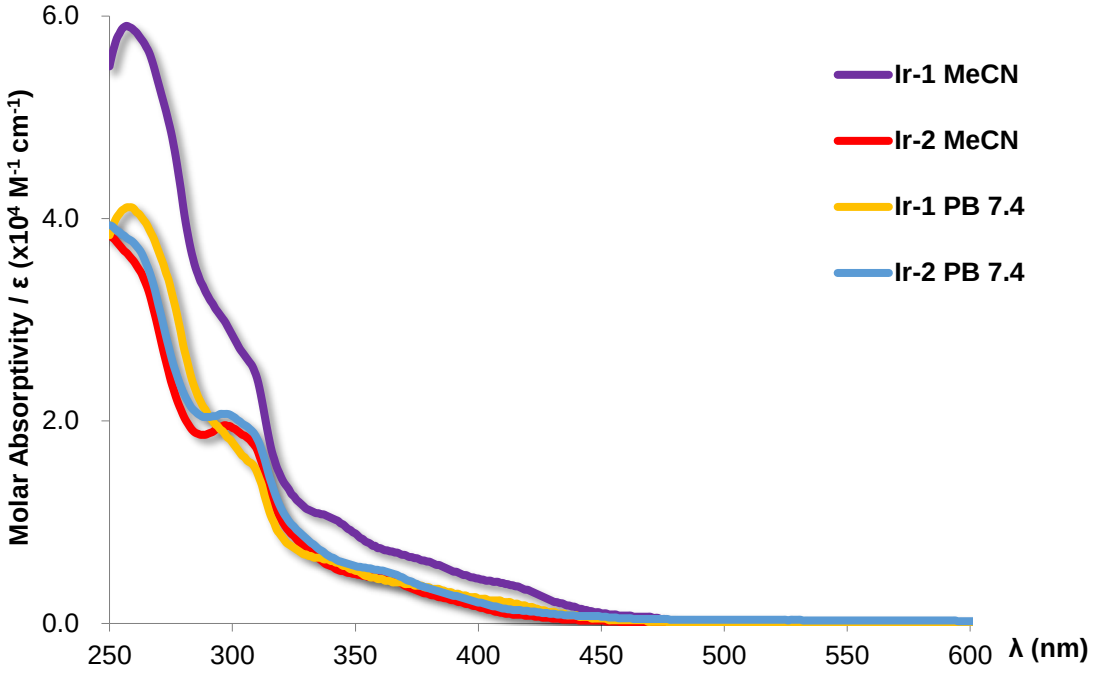

Figure 2.2.4.2 Molar absorptivity spectra of **Ir-1** and **Ir-2** in MeCN and PB 7.4 solution.

These five iridium complexes can be divided into three groups according to their structures and emission wavelengths. **Ir-1** and **Ir-3** have almost the same emission maxima at 575 nm and similar shape of spectra, so the emission colour of ppy based mono-substituted iridium complexes and di-substituted compounds were the same. As mentioned before, the designed broken conjugated link between the main body of iridium complex and the extended part minimized the influence on their photophysical properties. The same situation also took place in complexes using dFppy as cyclometalating ligands, **Ir-2** and **Ir-4** emitting at 515 nm. The 60 nm blue-shift was brought by the

difluoro functional groups on ppy ligand, which stabilized their HOMO and increase the energy of the triplet state. The parent template **Ir-0** had emission maxima at 589 nm, which was a little longer than **Ir-1** and **Ir-3**. This could be because of the methyl group in position four of bpy of **Ir-1** and **Ir-3**. The methyl groups are inductive donors on the bpy, and slightly destabilized their LUMO, and produced a larger band gap compared with $[Ir(ppy)_2(bpy)]Cl$.

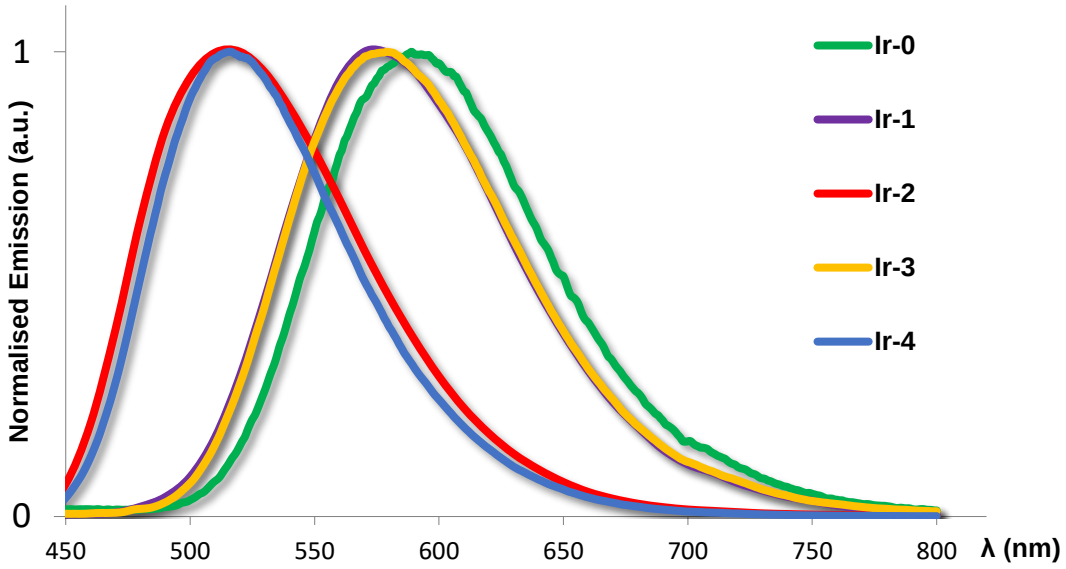

Figure 2.2.4.3 Normalized emission spectra of **Ir-0** to **Ir-4** in degassed MeCN (λ_{ex}=370 nm)

Generally, PLQY decreases with the increase in wavelength, which means green emitters generally have higher PLQY, but decreases when they are tuned to yellow and red. This phenomenon can be explained by the energy gap law. The small emission energy gap (tuning toward red emission) increases the non-

radiative decay because the vibrational modes in the ground state can easily couple with those in an excited state. By contrast, with a large emission energy gap towards blue, the destabilization of ^{3}MC along with ^{3}LC leads to the efficient quenching of emissions.[4,81]

Compared with **Ir-0**, which had PLQY as 11.3% in degassed MeCN, the ppy based iridium complexes (**Ir-1** and **Ir-3**) had the opposite results (Table 2.2.4.1). The mono-substitution complex (**Ir-1**) had much higher PLQY as 34.6%, but the di-substitution structure (**Ir-3**) decreased to 7.9%. According to the energy gap law, when the emission colour is tuned from yellow to green, their PLQY increases. By comparing the dFppy based complex with the ppy based group, both mono-substituted and di-substituted complexes had improved PLQY respectively. **Ir-2** had the highest PLQY as 62.8%, and **Ir-4** also increased to 23.6% from 7.9% (**Ir-3**)

For lifetime, **Ir-0** was 728 ns in MeCN (Table 2.2.4.1). After decoration of the bpy, the mono-substitution complex (**Ir-1**) had a shorter lifetime as 475 ns. However, the lifetime of di-substituted complex (**Ir-3**) increased to 717 ns. **Ir-4** (τ=1496 ns) also had a longer lifetime than **Ir-2** (τ=1310 ns), indicating that di-substituted iridium complexes tended to have a longer lifetime than the corresponding mono-substituted structures in this group. The effect of fluorine

on cyclometalating ligands increased their lifetimes dramatically.[82] Compared with **Ir-1**, the fluorine decorated iridium complex (**Ir-2**) had a much longer lifetime as 1310 ns. The same situation also occurred with the di-substituted complexes, and the **Ir-4** had the longest lifetime within the group as 1496 ns.

By using the lifetime and PLQY, k_r (radiative decay constant) and k_{nr} (non-radiative decay constant) can be calculated, as shown in the Table 2.2.4.1. From the literature[83], $k_r = \Phi / \tau$, and $k_{nr} = 1/\tau - k_r$. More efficient luminescent processes have larger k_r and smaller k_{nr}. According to the calculation results, **Ir-0**, **Ir-1**, and **Ir-3** had very close k_{nr}, and **Ir-1** had the highest k_r, as it had the highest solution based PLQY within this group. **Ir-2** had relatively low k_r and k_{nr}, but it was the only complex that had higher k_r than k_{nr}. By comparison, mono-substituted complexes had relatively higher k_r, but the k_{nr} was affected mainly by the functional groups on cyclometalating ligands.

Table 2.2.4.1 Redox data, emission wavelength, PLQY, and lifetimes of the **Ir 0-4** in MeCN

Compound	E^{OX} [a] /mV	Emission [b] λ_{PL} /nm	PLQY [b,c] (%)	Lifetime [d] τ_{PL}/ns	k_r [e] $10^5 s^{-1}$	k_{nr} [f] $10^5 s^{-1}$
Ir-0	1.2	589	11.3	728	1.55	12.18
Ir-1	1.3	575	34.6	475	7.28	13.77
Ir-2	1.6	515	62.8	1310	4.79	2.84
Ir-3	1.3	579	7.9	717	1.10	12.85
Ir-4	1.6	516	23.6	1496	1.58	5.11

[a] 0.1M $[n\text{-}Bu_4N]PF_6$ was used as the supporting electrolyte and redox data was measured vs SCE in MeCN at room temperature at a scan rate of 100 mV s^{-1}. Glassy-carbon electrode was used as the working electrode, silver wire was the pseudoreference electrode, Pt wire was the counter electrode, and Fc/Fc^+ was the internal reference (0.38V vs SCE)[84]. [b] Measurements in degassed MeCN at 298 K, λ_{ex}=370 nm. [c] Quinine sulfate was employed as the external reference (Φ_{PL} = 54.6% in 0.5 M H_2SO_4 at 298 K)[85]. [e] $k_r=\Phi/\tau$. [d] Measurements in degassed MeCN at 298 K, λ_{ex}=378 nm [f] $k_{nr}=1/\tau-k_r$.

The photophysical properties both in MeCN and PB 7.4 were measured and compared. As shown in Figure 2.2.4.4, **Ir-1**, for example, had the same absorption in both solvents, but there was a red shift for emission spectra in PB

7.4. This phenomenon could be brought by the different polarity of the solvents, and the same happened on **Ir-2**. Both **Ir-1** and **Ir-2** had 10 nm red shift in PB 7.4 compared to MeCN.[86]

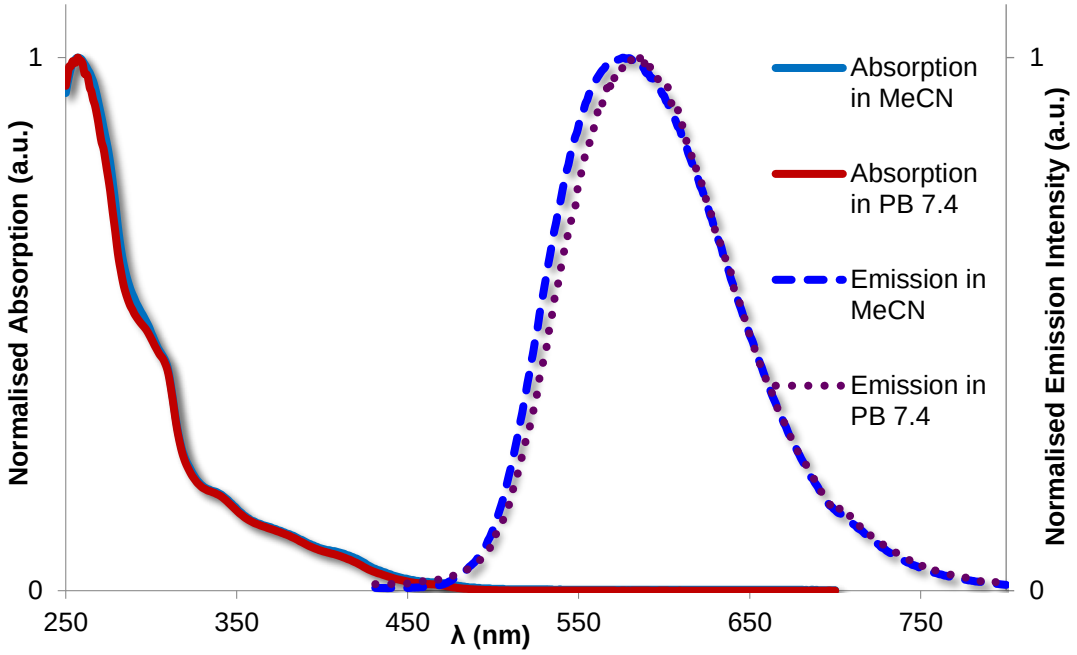

Figure 2.2.4.4 Normalized absorption and emission spectra of **Ir-1** in MeCN and PB 7.4 (λ_{ex}=370 nm)

Although the emission wavelengths did not change a lot in aqueous solutions, their PLQY and lifetime decreased dramatically. **Ir-1** had only 3.5% PLQY in PB 7.4 (Table 2.2.4.2) compared with 34.6% in MeCN, and **Ir-2** decreased to 14.8% from 62.8%. From the calculated k_r and $k_{nr,}$ it was found that both complexes had smaller radiative decay rate constants, and much higher non-radiative decay rate constants, especially for **Ir-1**, which had 10 times higher k_{nr}

compared with MeCN solution.[86] However, the expected emission wavelength and suitable PLQY were maintained, and these properties could support further research into self-assembled processes with CDV and applications for bio-imaging.

Table 2.2.4.2 Emission wavelength, PLQY, and lifetimes of **Ir-1** and **Ir-2** recorded in degassed PB 7.4

Compound	Emission λ_{pl} /nm [a]	PLQY (%) [a,b]	Lifetime τ_{pl}/ns [c]	k_r, $10^5 s^{-1}$ [d]	k_{nr}, $10^5 s^{-1}$ [e]
Ir-1	585	3.5	73	4.79	132.19
Ir-2	525	14.8	459	3.22	18.56

[a] Measurements in degassed PB 7.4 at 298 K, λ_{ex}=370 nm. [b] Quinine sulfate employed as the external reference (Φ_{PL} = 54.6% in 0.5 M H_2SO_4 at 298 K)[85]. [c] Measurements in degassed PB 7.4 at 298 K, λ_{ex}=378 nm [d] $k_r=\Phi/\tau$. [e] $k_{nr}=1/\tau-k_r$.

These iridium complexes also showed obvious solvent effects. Because their structures were combined with hydrophilic and hydrophobic groups, they had good solubility in most solvents, excluding very non-polar solvents such as hexane and diethyl ether. The emission wavelengths and intensities changed

a lot when these iridium complexes were added to different solvents, from toluene to DCM. As shown in the emission spectra (Figure 2.2.4.5) and Table 2.2.4.3, with the increase of solvent polarity, emission colour ranged from yellow to orange for **Ir-1**, and from blue to green for **Ir-2**, and both had the highest emission intensity in DCM.

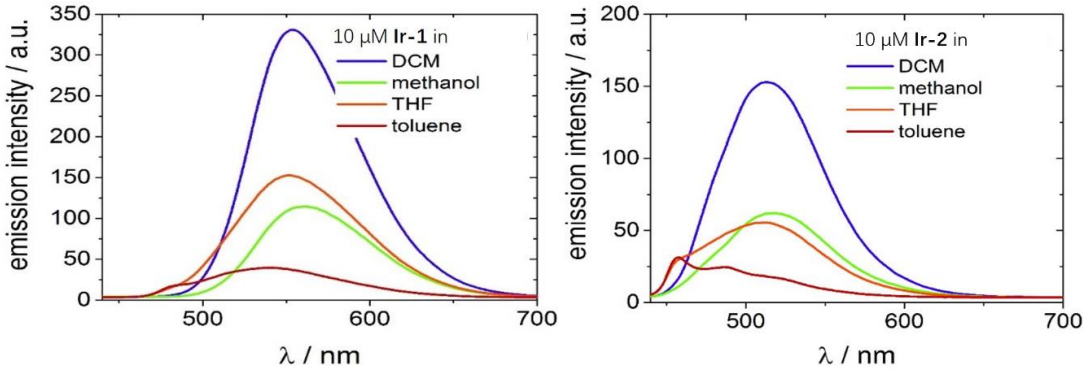

Figure 2.2.4.5 Solvent effect: emission spectra of **Ir-1** and **Ir-2** in DCM, MeOH, THF and toluene (Measured by Frauke Schibilla in University of Münster) (λ_{ex}=370 nm)

Table 2.2.4.3 Emission wavelength of **Ir-1** and **Ir-2** recorded in solvents

Solvents	Emission wavelength λ_{PL} /nm [a]	
	Ir-1	**Ir-2**
toluene	539	486
THF	551	514
DCM	554	513
MeOH	562	518

[a] Measurements in degassed solvents at 298 K containing 10 μM complexes, λ_{ex}=370 nm.

2.2.5 Self-assembled experiments between Ir (III) complexes and CDVs

Ir-1 to **Ir-4** were used as guests to self-assemble with CDV in aqueous solutions. Emission intensity and lifetime were used as the main parameters for characterization. With the addition of β-CDV to **Ir-1** solution ($c_{\mathbf{Ir\text{-}1}}$=10 μM), the emission spectra kept blue shifting and the emission intensity kept rising until 1 equivalent of β-CDV to **Ir-1** was added (Figure 2.2.5.1). However, for **Ir-2**, not only did the emission wavelengths and intensity change, the shape of the emission spectra also became splitting into two peaks. The emission profiles changed completely from one to two peaks when the addition of β-CDV was 1 equivalent to **Ir-2** in solution. This phenomenon could be explained by the change of emission mechanism from CT to LC. Moreover, the emission peak did not split much, and the resolved vibrational structure was observed. With the addition of more than 1 equivalent of β-CDV to iridium complexes to the reaction systems, those complexes were attached to the surface of CDVs through host-guest interactions, and the emission intensity increased continuously, even though the increase rate of emission intensity was affected less with the addition of β-CDV.

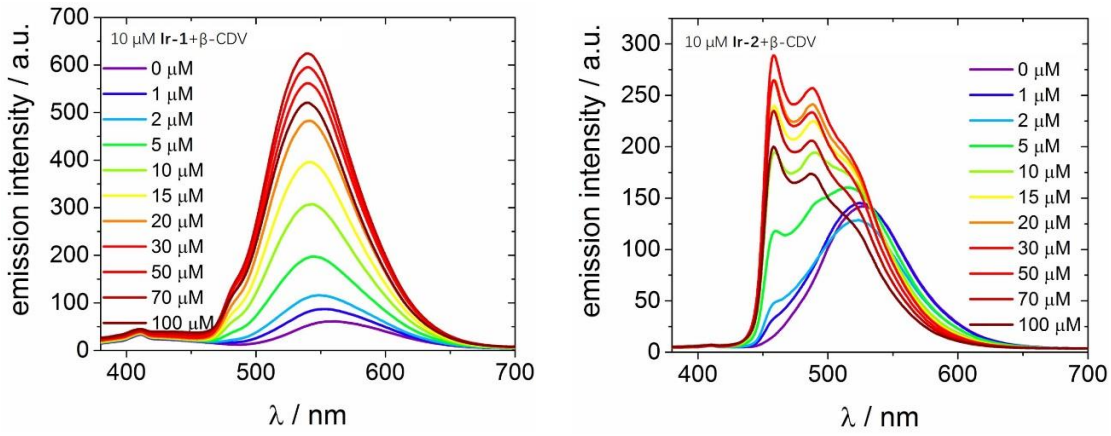

Figure 2.2.5.1 Emission spectra of **Ir-1** and **Ir-2** with added different concentrations of CDV in PB 7.4 (λ_{ex}=370 nm)

Lifetime also had large changes after the assembly of **Ir-1**, **Ir-2** and β-CDV. After recognition in PB 7.4 solution, the host-guest interactions brought about a very long lifetime that was biexponential in origin. However, there was a component with a short lifetime. By comparing the **Ir-1** (73 ns) and **Ir-2** (459 ns), this short component was attributed to free iridium complexes in solution. Based on this discovery, **Ir-3** and **Ir-4** with di-substituted adamantane were designed and synthesized to obtain stronger binding to CDVs.

Table 2.2.5.1 Lifetime of **Ir-1** and **Ir-2** with addition of β-CDVs [a]

lifetime	**Ir-1**	**Ir-1**+β-CDV	**Ir-2**	**Ir-2**+β-CDV
τ_1 / ns	73	506.8 (79%)	459	1031.1 (69%)
τ_2 / ns	-	75.3 (21%)	-	404.8 (31%)

[a] Measurements in degassed PB 7.4 at 298 K containing 10 μM of compounds, λ_{ex}=378 nm.

The measurement for self-assembly between iridium complexes and CDVs showed the presence of both bound and unbound iridium complexes to the CDVs. In order to improve the strength of the self-assembly, di-substituted adamantanes decorated iridium complexes (**Ir-3** and **Ir-4**) were synthesized, which were expected to bind more strongly with the CDVs. The self-assembly experiments showed similar changes of the emission intensities to the mono-substituted system (Figure 2.2.5.2).

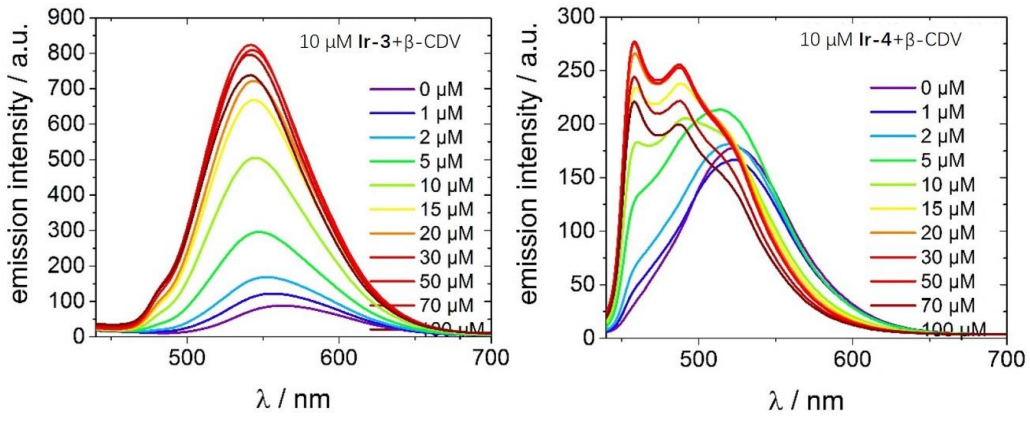

Figure 2.2.5.2 Emission spectra of **Ir-3** and **Ir-4** with added different concentrations of CDV in PB 7.4. (λ_{ex}=370 nm)

2.2.6 Cellular uptake studies of self-assembled system

Cell culture experiments were tested by Confocal Laser Scanning Microscope (CLSM) to evaluate the cell membrane transportation of complexes decorated on CDVs. As shown in Figure 2.2.6.2, the CDVs were transported into cells and localized in perinuclear regions, forming green luminescent rings surrounding the nuclei and negligible nuclear emission. Some of the literature has described cyclometalated iridium complexes as probes for perinuclear region such as complex **73**[87] and **74**[88] (Figure 2.2.6.1), but used a large conjugated system. According to the literature, complex **73** had emission maxima at 594 nm and a weak peak at 644 nm in MeCN. It had a long lifetime as 3.75 μs and low PLQY as 10%.[87] Complex **74** was reported by Lo et al. in 2013.[88] It had emission maxima at 564 nm and a shoulder peak at 595 nm. Similar to **73**, complex **74** had low PLQY as 8.2% in MeCN but a relatively short lifetime as 0.63 μs. Both **73** and **74** had efficient uptake and localization in the perinuclear region. The nuclei was surrounded by a luminescent ring indicating the negligible nuclei uptake of these complexes.[87, 88] In this project, **Ir-1** and **Ir-2** had much higher PLQY than those two reported complexes in MeCN ($\Phi_{PL\text{-}1}$=34.6%,$\Phi_{PL\text{-}2}$=62.8%), and achieved colour tuning from 575 nm to 515 nm by decorating their cyclometalating ligands. The more efficient emission reduced the concentration of probes to 1.25 μM in experiments from 5 μM as the reported structures (**73**)[87]. More importantly, from the cellar uptake experiments, it could be observed that only the complexes assembled with CDVs transferred the cell membrane, and

there was almost no emission in blank experiments, which represented no cellular uptake of the iridium complexes without CDVs.

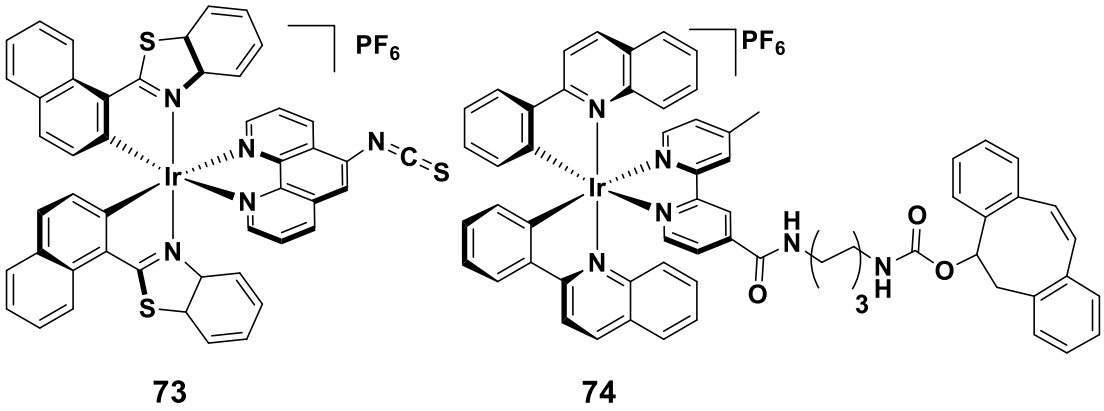

73 **74**

Figure 2.2.6.1 Iridium complex based luminescent probes for bio-imaging in perinuclear region (**73**, **74**)[87, 88]

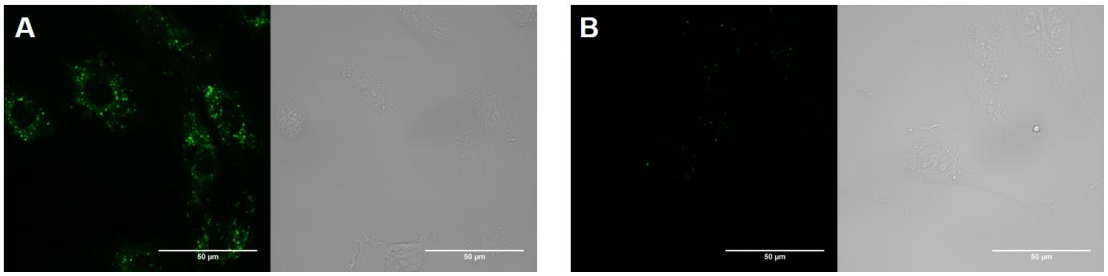

Figure 2.2.6.2 CLSM images for cellular uptake of **Ir-1** with CDVs (A) and without CDVs (B) (Fluorescence image on the left and brightfield image on the right of each panel, scale in images: 50 μm). HUVEC cells were transfected by Mito-RFP for 24h and incubated 90 minutes with **Ir-1** as 1.25 μM and CDVs as 3.75 μM in medium, followed by washing and the images were taken after 16 hours.

2.3 Conclusion

In this project, three families of iridium complexes decorated either with one adamantane or two adamantane groups were synthesized as part of a collaborative project with the Ravoo group in Münster. As designed, the absence of electronic conjugation between the adamantyl moiety and the iridium chromophore minimized the change of emission wavelength compared to the reference complex (**Ir-0)**. Polyether chains were used to link adamantyl groups to the iridium complexes, which were all charged and isolated as their chloride salts. The four decorated iridium complexes were soluble in water. ^{1}H and 2D NMR, HRMS and XRD were used to characterize their structures. Cyclic voltammetry, UV-vis absorption, emission spectra, PLQY, and emission lifetime were used to test their photophysical properties. The mono-substituted complexes showed increased PLQY, compared to the di-substituted analogues due to lower non-radiative decay constants. In PB 7.4 solution, all the complexes suffered stronger quenching. After the self-assembly of the adamantane-functionalized iridium complexes with CDVs, the assembly showed improved emission intensity and lifetime. With the addition of CDVs to 1 equivalent to complexes, their emissions blue-shifted with longer lifetimes. Cellular transportation experiments were tested and the CDVs decorated complexes showed localization in perinuclear regions under CLSM. Control experiments used **Ir-0** as the emitter, which, as expected, showed poor uptake

into the cell. According to the results, **Ir-1** to **Ir-4** could be applied to bio-probes and bio-imaging areas.

Chapter 3. Exploring the self-assembly of iridium(III) complexes into phosphorescent supramolecular iridium cages

3.1 Objective

Metallo-supramolecular chemistry plays an important role in developing novel supramolecular systems with functional properties. Different metals provide different binding sites and configurations, which can be used to prepare a broad variety of supramolecular structures such as coordination grids and networks[89,90], macrocycles,[91,92] polymers,[93,94] and capsules and cages.[95,96] These supramolecular structures have predominantly found applications in sensing,[97,98] gas storage and purification[99,100] and catalysis.[101,102]

Metallo-supramolecular cages have been developed for decades, and a variety geometries were built, such as tetrahedron,[103] octahedron,[104] cube[105], cuboctahedron,[106] and spherical structures.[107] In 2006, Fujita and co-workers reported interesting examples of tetrahedron cages (**75**, Figure 3.1.1) constructed from 2,4,6-tris(4-pyridyl)-triazine (tpt) and Pd (II) complexes.[108] A good example of cubic geometry was published by Yang et. al. in 2003 as a metal cyanide cage where four $\{Co(H_2O)_3(CN)_3\}$ were assembled with four $\{Co(tach)(CN)_3\}$ linked by cobalt ions to afford the cubic configuration (**76**,

Figure 3.1.1).[109] In this system, the cyano ligand bridged adjacent Co (III) and Ni (II) located on the vertexes of the cube. As cobalt ions provide octahedral coordination configuration, the angles between two adjacent edges were all near to 90^{o}. Rhombic dodecahedron is subgroup of polyhedral structures close to spherical geometry. In 2002, D.K. Chand and co-workers built a rhombic dodecahedral structure by using 1,3,5-tris(4-pyridylmethyl)benzene as ligand scaffold and Pd (II) (**77**, Figure 3.1.1).[110] This sphere was obtained by combining six square planar Pd (II) centres with eight bridging ligands. The configuration of this ligand is very important to achieve this particular structure. Indeed, 1,3,5-tris(4-pyridylmethyl)benzene has an angle of 60^{o}, which is adequate to form the observed topology.[111]

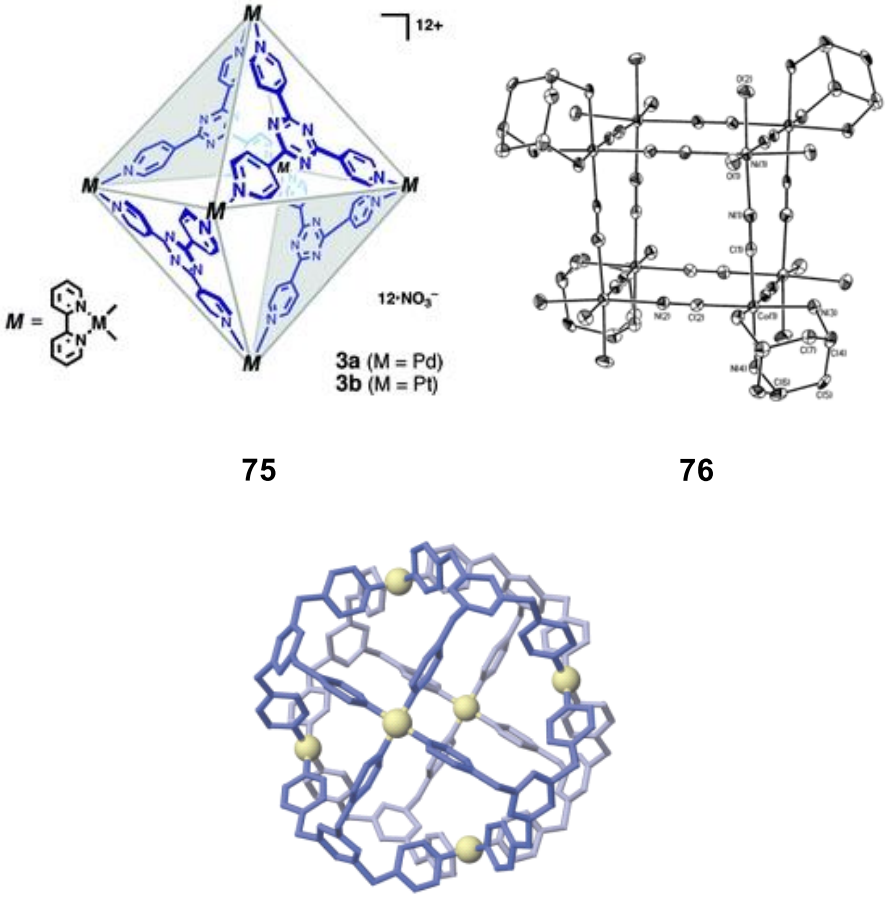

75 **76**

77

Figure 3.1.1 Metallo-supramolecular systems: tetrahedron cages published by Fujita et al. (**75**)[108]; cyano ligand bridged cubic cage (**76**)[109]; Pd linked rhombic dodecahedral cage (**77**)[110] (Photocredit: V. Maurizot et al. *Dalt. Trans.*, 2006, **0**, 2751 (**75**); J. Y. Yang et al. *Inorg. Chem.*, 2003, **42**, 1410 (**76**); D. K. Chand et al. *Chem. Commun.*, 2002, **117**, 2487 (**77**))

Among these 3D cage structures, cages of stoichiometry M_nL_{2n} are the most reported. To form these structures, square planar metal ions as vertices and rigid bent ligand as edges are required.[112] M_nL_{2n} based structures were firstly reported by M. Fujita and co-workers.[113] The most thermodynamically stable

polyhedral structures reported to date have n values of 6,[114] 12,[106] 24,[112] and 30[21] (Figure 3.1.2).

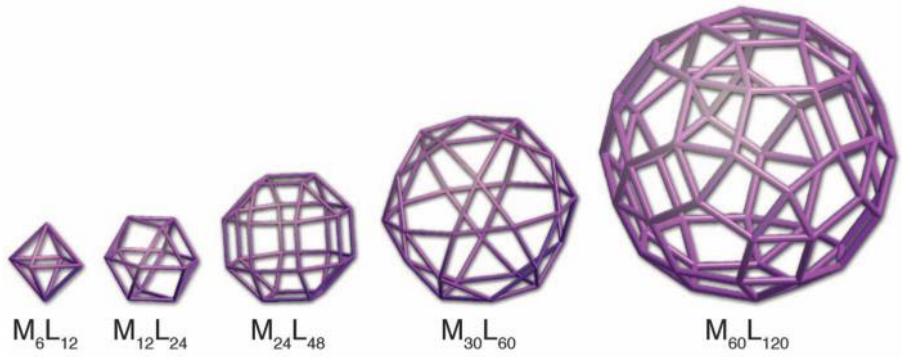

Figure 3.1.2. Topological configurations of spherical supramolecular M_nL_{2n} cages[112](Photocredit: Q.-F. Sun et al. *Science.*, 2010, **328**, 1145)

The structures with n=12 (**78**, Figure 3.1.3) and 24 (**79**, Figure 3.1.3) were reported by Fujita et. al. in 2010 using Pd (II) and a bent ligand bearing terminal 4-pyridyls as the coordinating vector to coordinate with Pd (II).[112] In 2016, M. Fujita et. al. reported the largest M_nL_{2n} system with n=30 (**5**, Figure 3.1.4) which had a diameter of 8.2 nm and a cavity that was large enough to encapsulate proteins.[21] The ligands were extended with linear fragments such as phenyl. Other ligands adequate for forming M_nL_{2n} structures are also reported (**80**, **81**,Figure 3.1.5).[115] Terminal 4-pyridyl is nowadays a popular strategy to assemble bent ligands with Pd (II) and often, alkynyl groups have been used to extend the coordinating vectors of the ligands (**80**, **81**,Figure 3.1.5).[115,116]

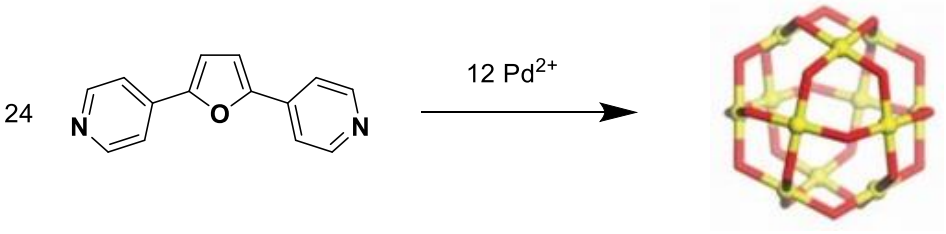

78

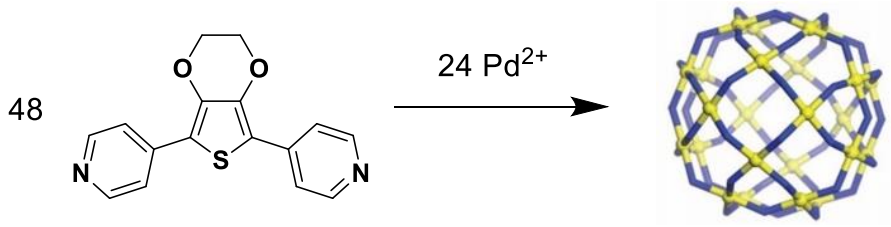

79

Figure 3.1.3 The schematic presentations of the synthesis of $M_{12}L_{24}$ (**78**) and $M_{24}L_{48}$ (**79**) structures from bent ligands and Pd (II) [112] (Photocredit: Q.-F. Sun et al. *Science.*, 2010, **328**, 1145)

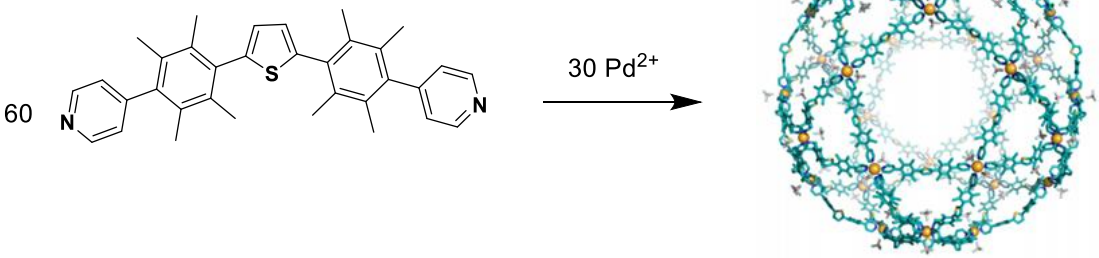

5

Figure 3.1.4. Schematic presentation of the synthesis of $M_{30}L_{60}$ (**5**) reported by Fujita et.al.[21] (Photocredit: D. Fujita et al. *Chem*, 2016, **1**, 97)

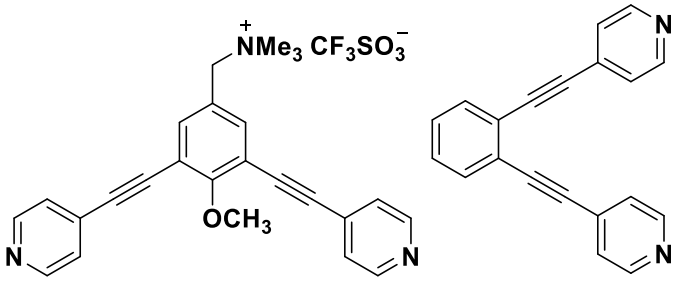

80 **81**

Figure 3.1.5 Alkynyl extended ligands for M_nL_{2n} cages (**80**, **81**)[115,116]

Most of iridium complexes emit through the mixture of ^{3}MLCT and ^{3}LLCT. Their triplet emissions are sensitive to triplet-triplet quenching and annihilation.[117] Small molecules can quench the excited iridium complexes significantly. Therefore, the design of iridium complexes that can be protected by intra-molecular self-organised fragments from small quenchers can be a promising method to maintain a high PLQY.[118] 2,2'-Bipyridine (bpy) is a common ancillary ligand for iridium complexes. It is rigid as bidentate ligand to coordinate with Ir (III). The functionalization of the bpy scaffold with terminal pyridyl units can result in a promising ligand that can be used as both ancillary ligand for Ir(III) complexes and coordinating vector for self-assembly with Pd (II). Following this approach, M_nL_{2n} type supramolecular cages (**19, 21**) by using metalloligand (**18, 20**) (Figure 3.1.6) to coordinate with Pd (II) through Pd-N (pyridyl) coordination have been reported by Diego Rota Martir in our group (Figure 3.1.6).[31]

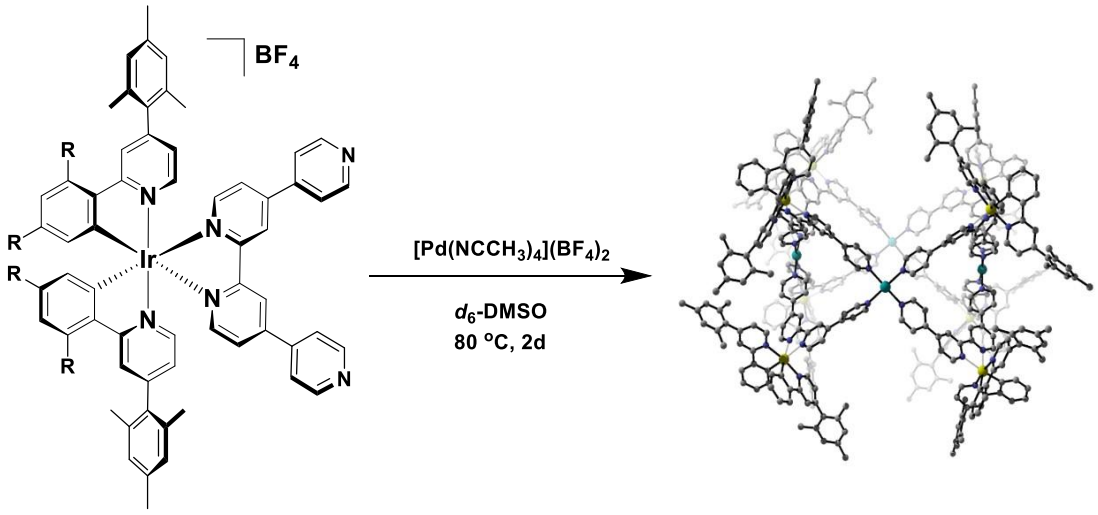

R=H, Λ, Δ–**Ir** **18**
R=F, Λ, Δ–**FIr** **20**

R=H, Λ, Δ–[Ir_8Pd_4]$^{16+}$ **19**
R=F, Λ, Δ–[FIr_8Pd_4]$^{16+}$ **21**

Figure 3.1.6 M_nL_{2n} molecular cage (**19, 21**) synthesized from iridium complex (**18, 20**) containing terminal pyridyl ancillary ligand by Diego Rota Martir[31] (Calculated structure is shown on right (**19, 21**) (Photocredit: D. Rota Martir et al. *Chem. Eur.J.* 2017, **23**,14359))

In the present work, an alkynyl spacer was added between the bpy core and the distal 4-pyridyl units to obtain a longer distance between the Pd (II) centres and the iridium core. This approach may result in reducing the emission quenching of the iridium chromophores due to close interaction with palladium ions and therefore, it may give rise to a brighter cage compared to the one previously reported by our group. In the designed ligand, the conjugated system was kept and extended linearly (**82**, Figure 3.1.7). With large highly conjugated system, such as the cage targeted in this work and other iridium cages reported (**12**, **17**, Figure 3.1.7), the emission of the iridium chromophores assembled in the cage structure are expected to be red-shifted compared to the

corresponding metalloligand with a reduced PLQY and shorted phosphorescent lifetime.[26,30]

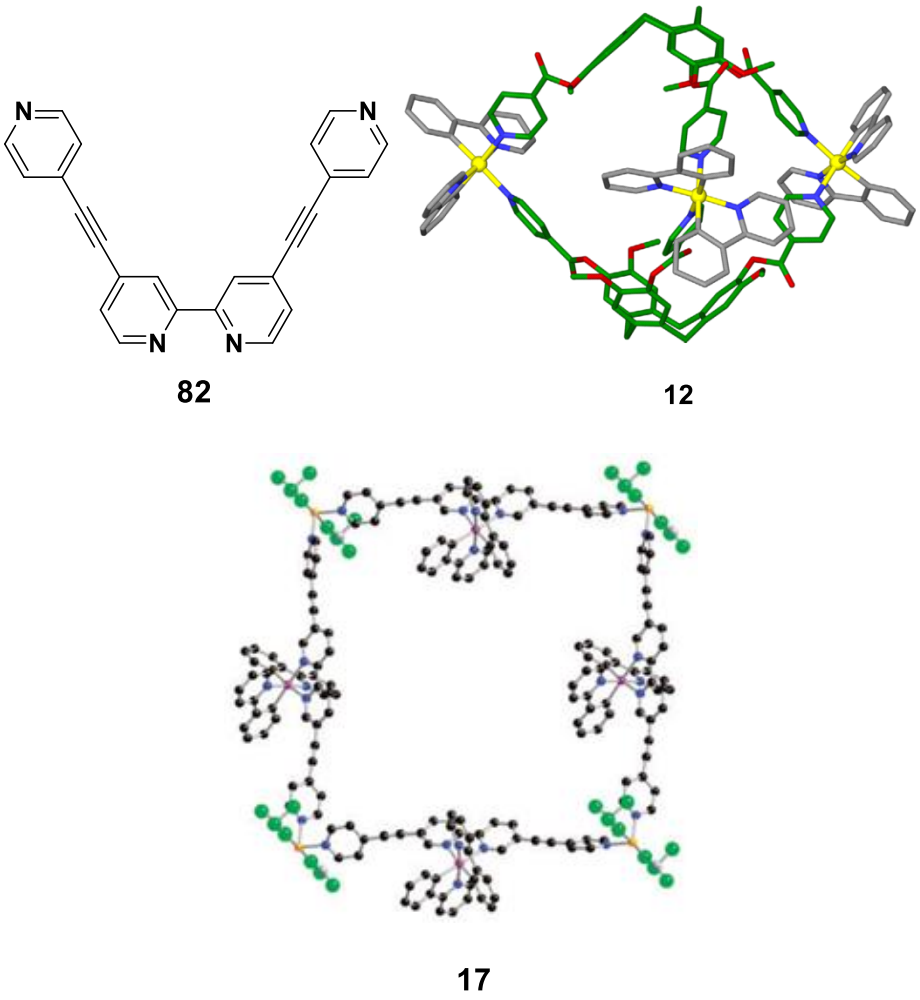

Figure 3.1.7 Designed terminal pyridyl ancillary ligand for iridium complex applied in building supramolecular cages (**85**); reported Iridium complex based supramolecular cages (**12**, **17**) (Crystal structure of **12** and **17**. Photocredit: E. Zysman-Colman et al. *Chem. - A Eur. J.*, 2017, **23**, 6291. (**12**); C. Xu et al. *Chem. Commun.*,2015, **51**, 14787 (**17**))[26,30]

3.2 Results and discussion

3.2.1 Synthesis

The 4,4'-bis(pyridin-4-ylethynyl)-2,2'-bipyridine (**82**, Scheme 3.2.1.1) was synthesized from 4,4'-dibromo-2,2'-bipyridine (**86**, Scheme 3.2.1.1) by two steps of Sonogashira reaction, and the compound **86** was prepared from 2,2'-bipyridine. Because the 4 and 4' positions of bpy have relatively low reaction activity, oxidation was the first step to activate those points. Acetic acid was used as the solvent and hydrogen peroxide was the oxidant to prepare compound **83** (Scheme 3.2.1.1), and the product was purified by recrystallization from ethanol and water. After the oxidation, concentrated sulfuric acid and nitric acid were added to **83** for nitration. While adding sulfuric acid, an ice bath and a dropping funnel were used for avoiding overheat. Concentrated nitric acid was subsequently added. The reaction system was then raised to room temperature and heated to 100 ^{o}C for 3 days. Because both acid and the product were mixed and have good aqueous solubility, the reaction mixture was poured into a mixture of liquid nitrogen and crushed ice to force the precipitation. At low temperature a light yellow suspension (**84**, Scheme 3.2.1.1) was obtained and collected by filtration. Bromination followed the nitration. Acetyl bromide was used as bromination reagent in acetic acid. The mixture was refluxed overnight, and it was subsequently neutralized by saturated sodium hydroxide and extracted by DCM to afford **85** (Scheme

3.2.1.1). The reduction of **85** was run in MeCN with PBr_3 as the last step. The mixture was heated to 90 ^oC overnight under inert atmosphere. After the neutralization, the aqueous solution was extracted by DCM to obtain crude product. Recrystallization from boiling ethanol and water could afford pure compound **86** (Scheme 3.2.1.1).

Two steps of Sonogashira reactions starting with **86** were carried out (Scheme 3.2.1.1).[96,119] For these two reactions, anhydrous and oxygen free conditions were necessary, and THF was the solvent. The first reaction was left overnight and monitored by TLC. The reaction was stopped when compound **86** was completely reacted, and the mixture was extracted by DCM and purified through silica column chromatography to afford off-white solid (**87**, Scheme 3.2.1.1) with a yield of 66%. The second Sonogashira reaction was combined with the deprotection of the TMS group. Tetrabutylammonium fluoride (TBAF) and compound **87** was stirred in THF solution for 0.5 h, and 4-bromopyridine was added following the same reaction condition used for the first Sonogashira reaction. TLC was also needed for monitoring the progress of the reaction. Column chromatography was not suitable for this purification because of the poor solubility of ligand **80**. After removing THF, the residue was triturated, sonicated and washed with water, ethyl acetate, DCM and cold ethanol to afford pink solid. The purified ligand **80** was checked by ^1H NMR and HRMS, and the result matched the expected structure.[119]

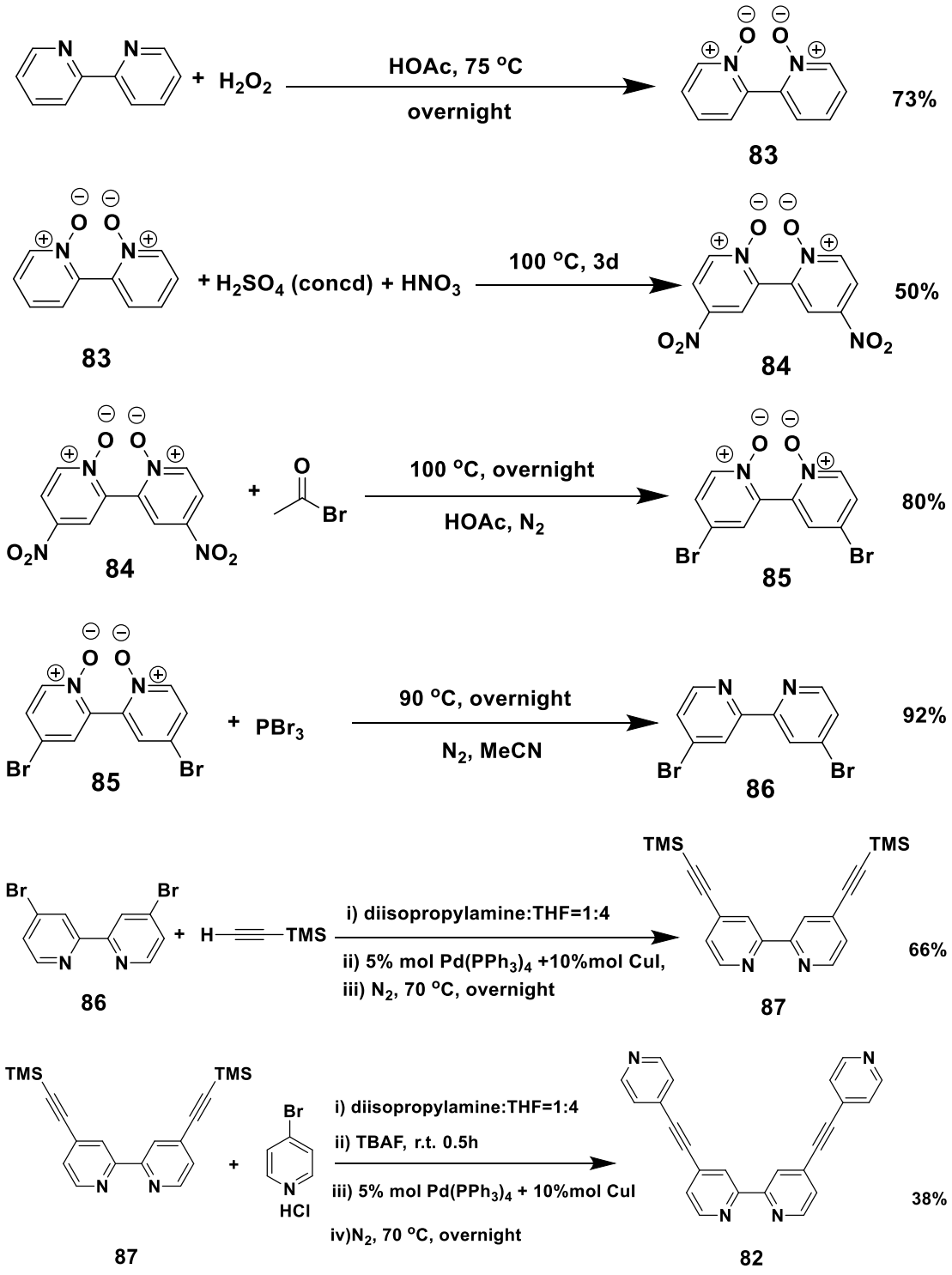

Scheme 3.2.1.1 Synthetic route of N^N ligand **82** from 2,2'-bipyridine [96,119-120]

The 4-mesityl-2-phenylpyridine (mesppy, **88**, Scheme 3.2.1.2) was chosen as the cyclometalating ligand, which is similar to the ligand (**18**, **20**, Scheme 3.1.5) used for the iridium cages reported by Diego Rota Martir.[31] Ligand **88** was synthesized through two steps of Suzuki-Miyaura palladium catalysed cross-coupling reaction following the reported conditions.[76]

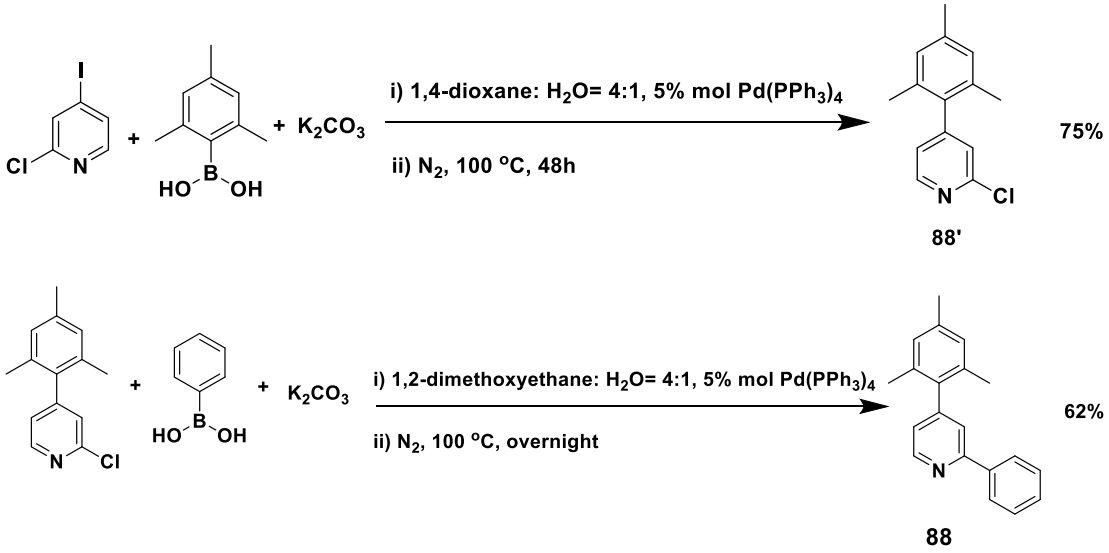

Scheme 3.2.1.2 Synthetic route of cyclometalating ligand **88**[76]

After obtaining the cyclometalating ligand **88**, it was coordinated with $IrCl_3 \cdot 3H_2O$ in 2-ethoxyethanol to afford μ-dichloro-bridged iridium dimer (**89**, Scheme 3.2.1.3). The mixture was heated to 120 °C for overnight before the yellow precipitate was filtered and washed by water and non-polar organic solvents, such as hexane and cold diethyl ether. ^{1}H NMR was used for comparing with literature and confirmed that the complex was made with high purity.[76]

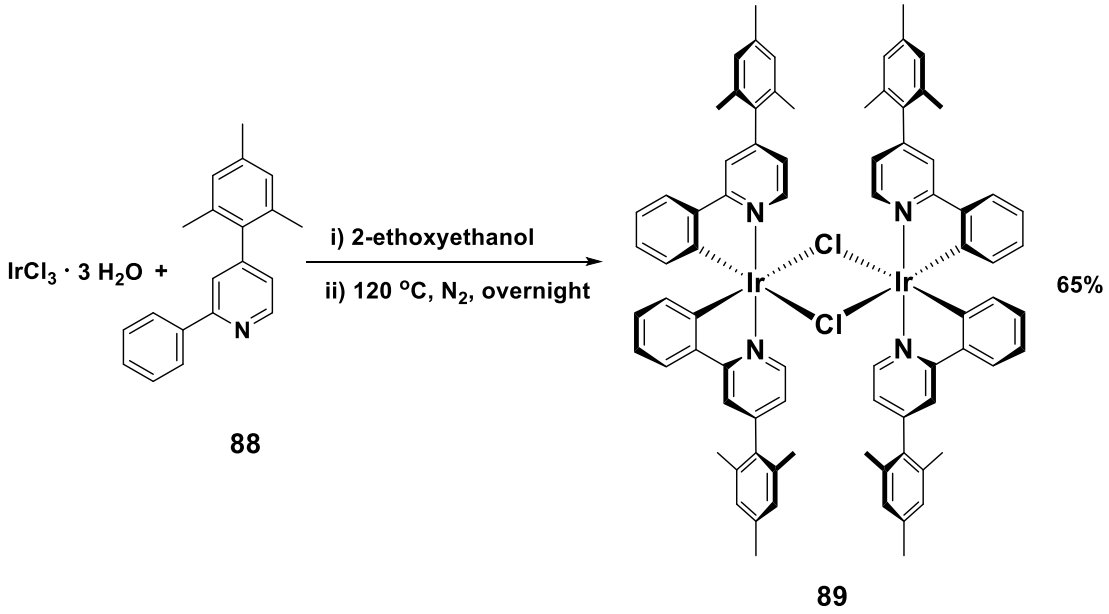

Scheme 3.2.1.3 Synthesis for μ-dichloro-bridged iridium dimer (**89**)

Unlike the complexation condition in Chapter 2, 2-methoxyethanol was used as solvent in this complexation to obtain higher reaction temperature (Scheme 3.2.2.4). Because ligand **82** has four coordination sites, thermodynamic equilibrium should be considered. For this complexation, the reaction time could not be too long. This reaction was left for two days at the beginning, however, a side product as a dark red solid was formed after 16 h. In order to improve the yield, this complexation was left for a shorter time compared with normal overnight reactions, and purified through short silica column chromatography. KBF_4 was then used to charge this iridium complex with tetrafluoroborate in DCM/MeOH (v/v=1:1) solution. Single crystals suitable for X-ray diffraction of the complex **Ir-5** (Scheme 3.2.1.4) were prepared by vapour diffusion method of Et_2O into DCM solution of **Ir-5**.

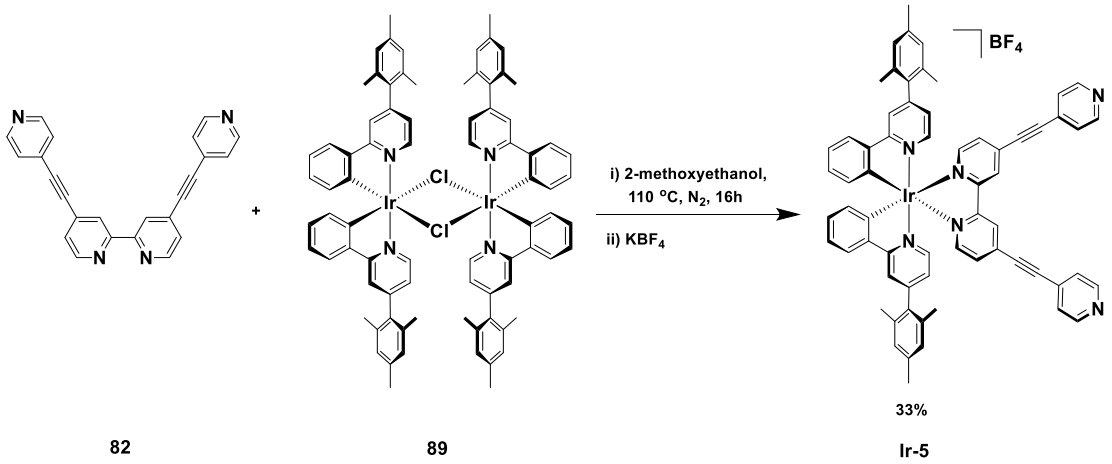

82 89 Ir-5

Scheme 3.2.1.4 Complexation for **Ir-5** synthesis

$[Pd(NCCH_3)_4](BF_4)_2$ and **Ir-5** were used to prepare supramolecular system (Scheme 3.2.1.5). According to the literature,[112] the ratio of equivalents of palladium and iridium complexes in this system would not affect the geometries and combinations of supramolecular cages. In order to improve the yield of the cage, 1 equivalent of **Ir-5** and 3 equivalents of $[Pd(NCCH_3)_4](BF_4)_2$ were added to d_6-DMSO. This reaction was monitored by ^{1}H NMR. ^{1}H DOSY NMR was also used to analyse and compare the diffusion coefficients of **Ir-5** and of the assembled product. The solution was heated to 80 °C for overnight, and aliquots were analysed by high resolution ESI mass spectrometry to obtain information about the structural composition of the assembly. After confirming the formation of giant systems, the solution was filtered through zeolite to get rid of the decomposed palladium that was formed, and then the solution was dropped into saturated NH_4PF_6 solution in methanol at 0 °C. Some dark brown

precipitate formed and was collected by filtration to obtain the **[(Ir-5)$_6$Pd$_3$](BF$_4$)$_{12}$** cage as its hexafluorophosphate salt.

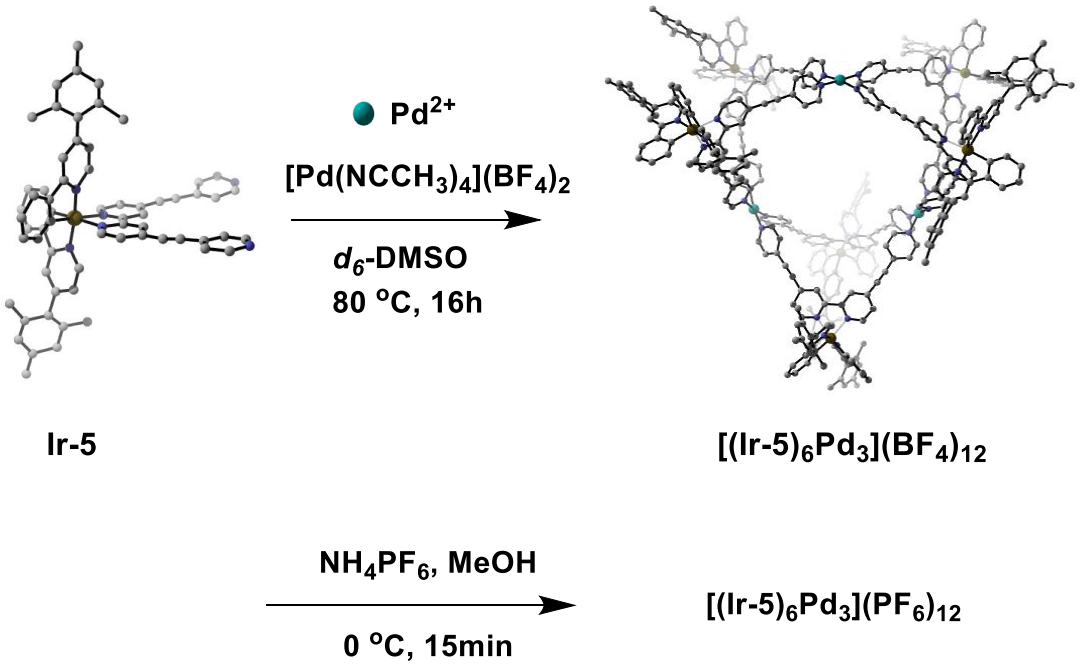

Scheme 3.2.1.5: Self-assembly for **[(Ir-5)$_6$Pd$_3$](BF$_4$)$_{12}$** cage (supramolecular cage on right was simulated structure obtained from calculation result)

3.2.2 Characterization

The primary characterization of **Ir-5** was achieved by NMR spectroscopy and mass spectrometry. ^{1}H NMR and 2D NMR including COSY, HSQC and HMBC were measured to prove its structure. The result of HRMS (LTQ Orbitrap) also matched the desired complex. The single crystal of **Ir-5** was prepared by vapour diffusion method of Et_2O into DCM solution of **Ir-5** and tested by single crystal X-ray diffraction. From the XRD result (Figure 3.2.2.1), its structure could be observed and analysed directly.

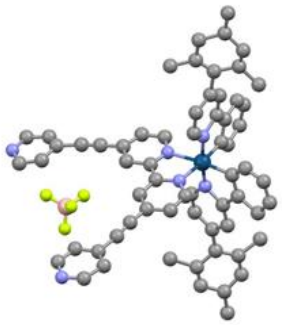

Ir-5

Figure 3.2.2.1: Single crystal structure of **Ir-5** (The grey balls represent carbon atoms, the deep blue ones are iridium atoms, the light blue are nitrogen, the yellow are fluorine and the green are chloride atoms. Hydrogen atoms and solvent molecules are omitted for clarity)

^{1}H DOSY NMR was used to analyse and compare the difference in sizes between **Ir-5** and **[(Ir-5)$_6$Pd$_3$](PF$_6$)$_{12}$**. Diffusion-ordered spectroscopy (DOSY) can separate the NMR signals of different species according to their diffusion coefficient.[22] It is a useful test facility in analysing supramolecular synthesis. Through the Stokes-Einstein Equation $D=\frac{kT}{6\pi\eta r}$,[121,122] it can be analysed that under the same conditions, larger systems have lower diffusion coefficients, which also reflect on the positions of signals in DOSY spectra. The corresponding diffusion coefficients can also be calculated through the software. In this project, the **Ir-5** gave blue signal in the Figure 3.2.2.2, and **[(Ir-5)$_6$Pd$_3$](BF$_4$)$_{12}$** was the red spectra. Because the red signal moved slower than the other, it showed that a larger system was formed after the self-assembly process. By using analytical software (Top-spin and Dynamic centre), their

coefficients were obtained as $D_{\mathbf{Ir\text{-}5}}$=1.7 x 10^{-10} m^2/s, and $D_{\mathbf{[(Ir\text{-}5)_6Pd_3](BF_4)_{12}}}$=8.8 x 10^{-11} m^2/s. The hydrodynamic radii of **Ir-5** and **$[(Ir\text{-}5)_6Pd_3](BF_4)_{12}$** can be calculated as $r_{S\ \mathbf{Ir\text{-}5}}$=0.64 nm and $r_{S\ \mathbf{[(Ir\text{-}5)_6Pd_3](BF_4)_{12}}}$=1.24 nm, respectively.

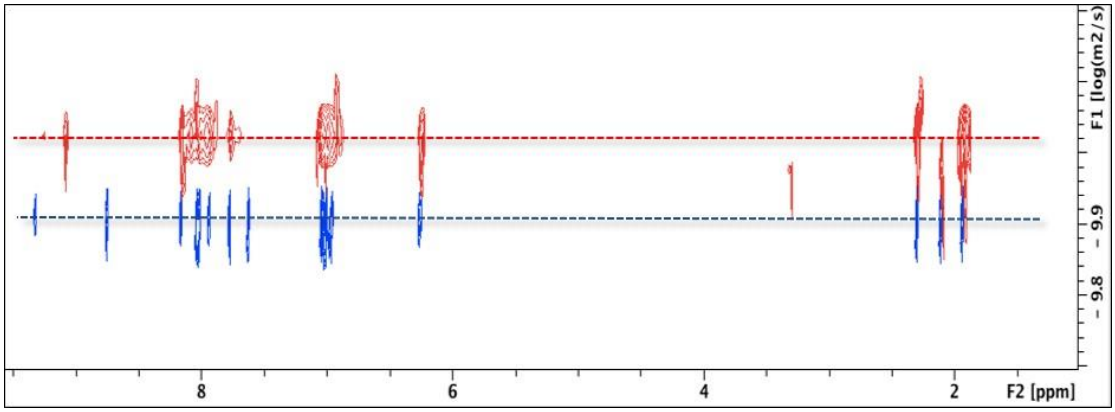

Figure 3.2.2.2: ^{1}H DOSY NMR–d_6-DMSO (blue signals showed the migration rate of **Ir-5**, ns=15, D20=0.1, P30=2300; red signals showed the migration rate of **$[(Ir\text{-}5)_6Pd_3](BF_4)_{12}$**, ns=16, D20=0.4, P30=1000)

HR-ESI-MS was used to analyse the structure of the obtained cage. By comparing the measured molecular weight and **Ir-5**, the combination of this supramolecule was confirmed as six **Ir-5** and three Pd (II). The isotopically resolved peaks of **$\{[(Ir\text{-}5)_6Pd_3](BF_4)_n\}^{n+}$** (n=4-7) were observed at m/z =1896.4959, 1499.7959, 1235.3292, and 1046.4244 which are assigned to **$\{[(Ir\text{-}5)_6Pd_3](BF_4)_4\}^{4+}$**, **$\{[(Ir\text{-}5)_6Pd_3](BF_4)_5\}^{5+}$** (Figure 3.2.2.3), **$\{[(Ir\text{-}5)_6Pd_3](BF_4)_6\}^{6+}$**, and **$\{[(Ir\text{-}5)_6Pd_3](BF_4)_7\}^{7+}$** respectively, and closely matched simulated spectra. (Figure **S80**-**S83**). However, the HR-ESI-MS also showed some other ions after the main peak. Through the MS/MS, the combination was

Ir-5, Pd (II) and the other iridium complex, which should be further purified in future work.

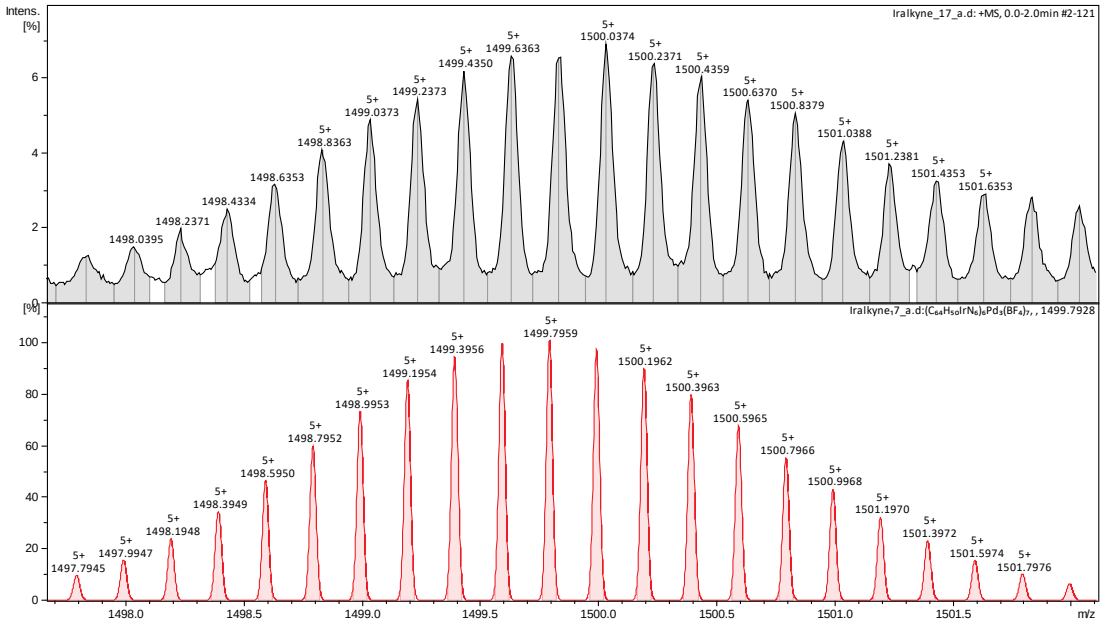

Figure 3.2.2.3. The HR-ESI-MS representing the state of **[(Ir-5)$_6$Pd$_3$](BF$_4$)$_7$**$^{5+}$

Calculations were run to show the geometry of this Ir-Pd structure. From the calculation result, it showed that Pd (II) localized on the point of a triangle, and adjacent Pd (II) were doubly bridged by **Ir-5.** Because Pd (II) provides square planar coordination geometry, **[(Ir-5)$_6$Pd$_3$](BF$_4$)$_{12}$** showed a crown like structure with a triangular shape. From the simulated structure, the radii of **[(Ir-5)$_6$Pd$_3$](BF$_4$)$_{12}$** can be obtained as 1.51 nm, which was a litter longer than the bond length calculated from its ^{1}H DOSY NMR, but it can be reasonable because the structures with large channel in the middle can exhibit relatively higher diffraction coefficients compared with perfect spherical structures.

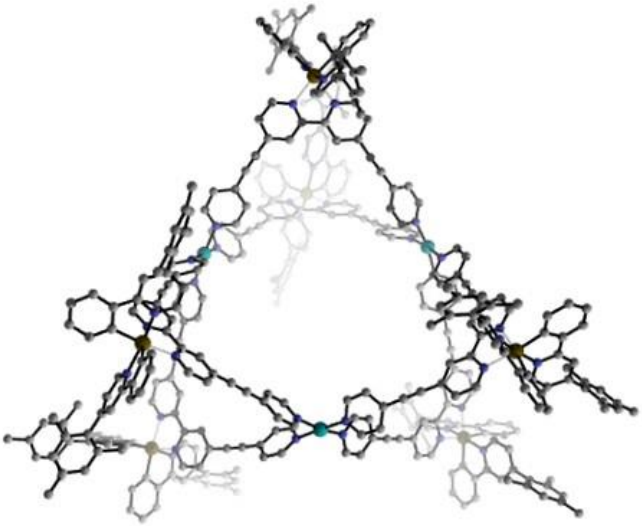

Figure 3.2.2.4: The calculated structure of **[(Ir-5)$_6$Pd$_3$](BF$_4$)$_{12}$** (The simulation of **[(Ir-5)$_6$Pd$_3$](BF$_4$)$_{12}$** based on the single crystal data of **Ir-5**)

A similar supramolecular structure was published by Fujita et. al. in 2007 (**90(a)**, Figure 3.2.2.5).[116] By comparing the ligand **82** with **81**, they had similar topologies, as well as similar bond length and angle. Pd (II) was used as the linker in both systems, and therefore, their assemblies resulted in similar geometries. Because of the similar ligand and same metal centre, **[(Ir-5)$_6$Pd$_3$](BF$_4$)$_{12}$** exhibited the same geometry as **90(a)**.

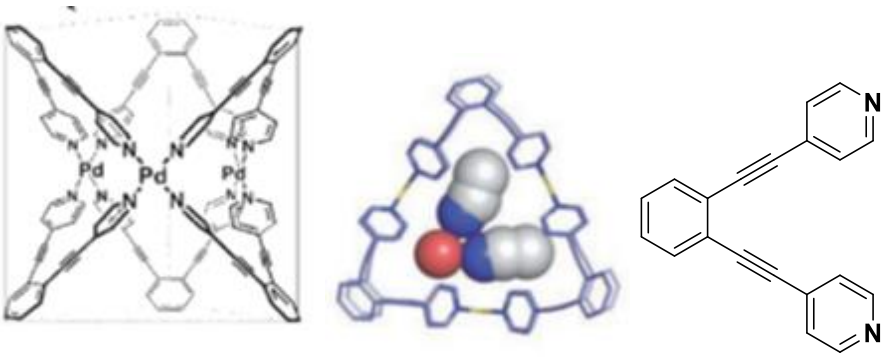

Figure 3.2.2.5 Supramolecular cage (**90**) self-assembled from extend pyridine ligand (**81**) and Pd^{2+} reported by Fujita et al. (**90a**. Chemical structure of **90** ($[(Pd)_3(\mathbf{81})_6]$); **90b**. Single crystal structure of **90** ($[(Pd)_3(\mathbf{81})_6]$; **81.** terminal pyridyle ligand used as building units for supramolecular structures (**90 b**: Framework: Pd=yellow, C, N=blue; guests in cavity: C=gray, N=blue, O=red, S=yellow. Photocredit: M. Fujita et al. *Angew. Chemie - Int. Ed.*, 2007, **46**, 2878))[116]

3.2.3 Photophysical properties

The absorption spectra of both **Ir-5** and **$[(Ir\text{-}5)_6Pd_3](PF_6)_{12}$** in MeCN were recorded. According to the literature[80], peaks under 340 nm are attributed to ligand-cantered transitions (LC). The bands between 340 and 500 nm are associated with the mixture of metal-to-ligand charge transfer (^{1}MLCT) and ligand-to-ligand charge transfer (^{1}LLCT) between the phenyl rings on C^N ligand and ancillary ligand.[62] As shown in Figure 3.2.2.2, **Ir-5** showed obvious

$\pi-\pi^*$ transitions at 272nm, and the broad peak between 356 nm and 433 nm, 450 nm and 550 nm represented the mixed charge transfer.

By comparing with the absorption of **Ir-5** in MeCN (Figure 3.2.3.1), the absorption spectrum of **[(Ir-5)$_6$Pd$_3$](PF$_6$)$_{12}$** (Figure 3.2.3.1) became broad, and the molar absorptivity of **[(Ir-5)$_6$Pd$_3$](PF$_6$)$_{12}$** was higher compared with **Ir-5** (Table 3.2.3.1). Also, even though **[(Ir-5)$_6$Pd$_3$](PF$_6$)$_{12}$** had LC at 272 nm as **Ir-5**, its signal for ^{1}MLCT and ^{1}LLCT became broader with a blue shift between 370 nm and 500 nm.

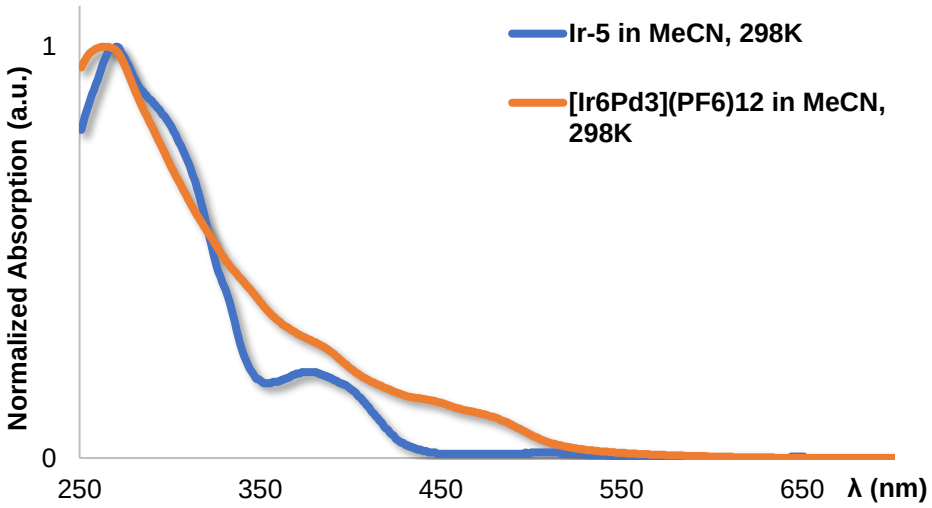

Figure 3.2.3.1 Normalized absorption spectra of **Ir-5** and **[(Ir-5)$_6$Pd$_3$](PF$_6$)$_{12}$** in MeCN

Table 3.2.3.1 Absorption properties of **Ir-5** and **[(Ir-5)$_6$Pd$_3$](BF$_4$)$_{12}$**

	λ_{abs}[a] (nm), [$\varepsilon \times 10^4$ M^{-1} cm^{-1}]
Ir-5	273 [8.65], 296 [7.31], 386 [1.76], 511 [0.1]
[(Ir-5)$_6$Pd$_3$](BF$_4$)$_{12}$	270 [133.50], 391 [33.56], 455 [16.78], 483 [12.27]

[a.] in MeCN at 298 K.

The emission spectra of **Ir-5** (Figure 3.2.3.2) and **[(Ir-5)$_6$Pd$_3$](PF$_6$)$_{12}$** (Figure 3.2.3.3) were similar. **Ir-5** had red emission at 638 nm in degassed MeCN. After forming supramolecular structures, there was a slight red shift to 659 nm because of the coordination Pd (II) which acts as a Lewis acid and lowers the HOMO-LUMO gap of the cage. However, the PLQY of **[(Ir-5)$_6$Pd$_3$](PF$_6$)$_{12}$** was lower in MeCN solution (Table 3.2.3.2) and it was nearly undetectable under UV lamp. The lifetime also decreased from 672 ns to 255 ns after self-assembly.

The differences were more apparent in 10 wt% PMMA doped films. In solid state, both compounds blue shifted compared with the emission wavelengths in solution (Figure 3.2.3.2 and Figure 3.2.3.3), but the emission of **[(Ir-5)$_6$Pd$_3$](PF$_6$)$_{12}$** was still more red-shifted than **Ir-5**. The largest difference was the PLQY (Table 3.2.3.2). In doped film, **Ir-5** had a much higher PLQY than in solution state. The reason could be the reduction of quenching due to vibrational motions. In solid state, compounds have relatively weaker vibrations than in solution, which can decrease the non-radiative decays and improve the PLQY of emitters. Despite this, **[(Ir-5)$_6$Pd$_3$](PF$_6$)$_{12}$** did not highly emit in doped

film, its emission could be detected at 613 nm (Figure 3.2.3.3). Similar of solution state, the formation of Ir-Pd supramolecular cage decreased the lifetime of the Ir (III) chromophores from 809 ns for **Ir-5** to 277 ns for **[(Ir-5)$_6$Pd$_3$](PF$_6$)$_{12}$** (Table 3.2.3.2).

Compared with complex **18**, the extended ancillary ligand stabilized the LUMO of **Ir-5** and as expected promoted a small red shift from 564 nm to 605 nm in 10 wt% PMMA doped film (Table 3.2.3.2).[31] However, the built cage showed a different trend. The emission of **[(Ir-5)$_6$Pd$_3$](PF$_6$)$_{12}$** was blue shifted by 30 nm in doped film compared with **19**. For lifetime, with the addition of alkynyl, the lifetime of both **Ir-5** and **[(Ir-5)$_6$Pd$_3$](PF$_6$)$_{12}$** were relatively shorter than **18** and **19** respectively, but the contributions of components were very similar. Interestingly, the additional alkynyl did not have an effect on their PLQYs in 10 wt% PMMA doped films. Both **Ir-5** and complex **18** had the same PLQY of 28%. However, after the formation of cages, the PLQY of **[(Ir-5)$_6$Pd$_3$](PF$_6$)$_{12}$** decreased dramatically, but cage **19** still kept promising PLQY of 10.9%.

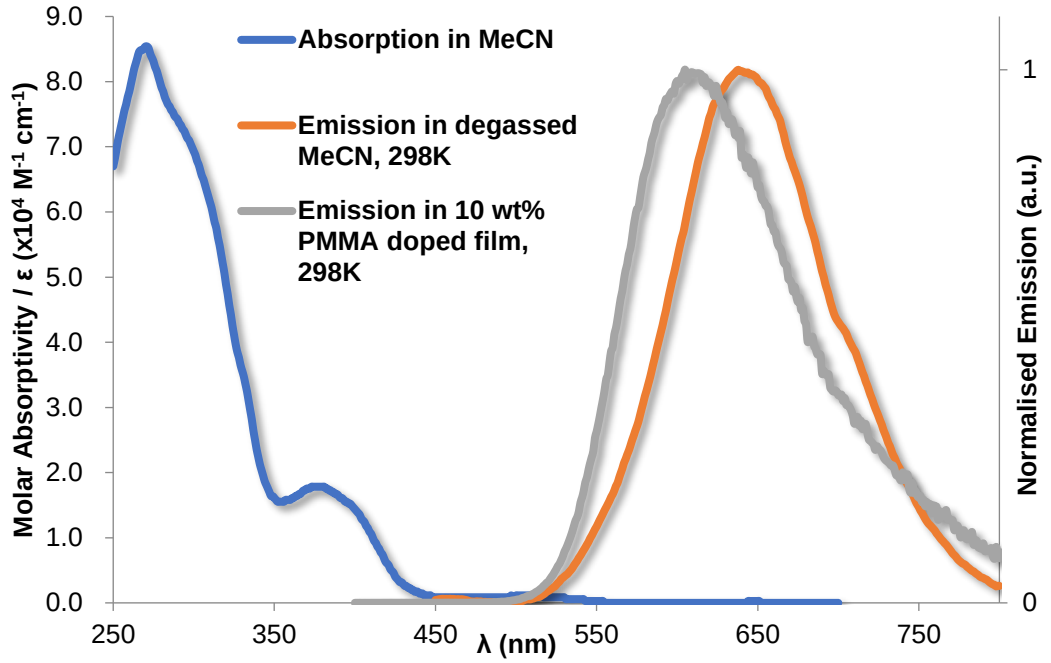

Figure 3.2.3.2 Molar absorptivity and normalised emission spectra of **Ir-5** in MeCN

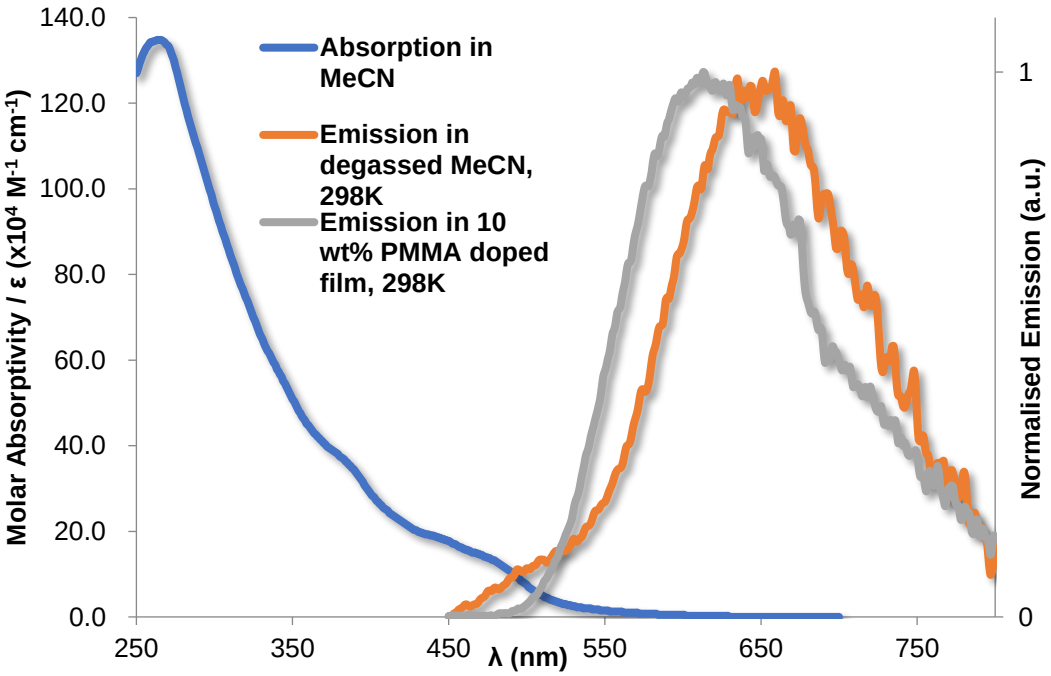

Figure 3.2.3.3 Molar absorptivity and normalised emission spectra of **[(Ir-5)$_6$Pd$_3$](PF$_6$)$_{12}$** in MeCN

Table 3.2.3.2 Emission wavelength, PLQY, and lifetimes of **Ir-5** and **[(Ir-5)$_6$Pd$_3$](PF$_6$)$_{12}$** recorded in degassed MeCN and 10% wt PMMA doped films

	Solution (MeCN 298K, N_2) [a]			Doped film (298K, N_2) [c]		
	Emission λ_{PL}/nm	Lifetime τ_{PL}/ns	PLQY(%)[d]	Emission λ_{PL} /nm [b]	Lifetime τ_{PL}/ns [b]	PLQY(%) [c,e]
Ir-5	638	672	2	605	164 (0.10), 644 (0.89)	28
[(Ir-5)$_6$Pd$_3$](PF$_6$)$_{12}$	659	255	1	613	20 (0.15), 257 (0.84),	1
18 [f,31]	620	300	14	564	300(0.14), 1045(0.86)	28
19 [f,31]	655	204	5	643	49(0.12), 270(0.68), 715 (0.20)	10.9

[a] Measurements in degassed MeCN (HPLC grade) at 298 K (λ_{ex} = 360 nm). [b] Measurements in air at 298 K. [c] 10 wt% of emitter doped in PMMA spin-coated on quartz from DMF solution. [d] Quinine sulfate employed as the external reference (Φ_{PL} = 54.6% in 0.5 M H_2SO_4 at 298 K).[85] [e] Doped thin film values were measured using an integrating sphere under N_2.[f] Measurements in degassed DCM (HPLC grade) at 298 K (λ_{ex} = 360 nm)

3.3 Conclusion

The **Ir-5** and corresponding Ir-Pd cage (**[(Ir-5)$_6$Pd$_3$](PF$_6$)$_{12}$**) were synthesized. Their structures were analysed and characterized by NMR and HR-ESI-MS.

Ligand **82** was designed to obtain a larger supramolecular cage compared to the cage **19** (Figure 3.1.5) reported by Diego Rota Martir in our group.[31] However, this metallo-coordination supramolecular system showed a totally different self-assembly topology. The calculation result exhibits a 3D cage like structure with a triangular shape, in which the Pd (II) acted as the vertices. The photophysical properties of both compounds were explored and compared in MeCN solution and PMMA doped film. The emission wavelengths of both **Ir-5** and **[(Ir-5)$_6$Pd$_3$](PF$_6$)$_{12}$** slightly red shifted compared to the metalloligand **18** and metallocage **19** in MeCN, but **[(Ir-5)$_6$Pd$_3$](PF$_6$)$_{12}$** had much lower PLQY in both solution and 10% wt PMMA doped film.

Although the photophysical properties of this Ir-Pd cage was not exceptional, the extended ancillary ligand still gives some suggestions about designing supramolecular cages with interesting topologies. The extended lengths of metalloligands is not enough to build larger supramolecular cages which contains more building units, the increased angles between edges should also be considered.[21,112] Also, the supramolecular systems can have similar topologies if they are built from ligand scaffolds with similar configurations and linked by meatal cations owing the same coordination structure. For example, because both **Ir-5** and **81** have similar configuration as building blocks and coordinated with Pd (II), it is reasonable to exhibit the same type of combination and configuration after self-assembly. This project is not finished at current

stage, and more research about using the cage for encapsulation of luminescent guest molecules is still ongoing. Because the high-resolution HR-ESI-MS showed some impurity ions during the self-assembling process, improved purification will be done.

Chapter 4. An organic optically active [2+2] Schiff-base macrocyclic system containing luminescent building blocks and its application in metal ion recognition

4.1 Objectives

Macrocycle structures have attracted much attention because of their innate symmetry and tunable cavity sizes. As a popular group of host-guest compounds, macrocycles have wide applications in catalysis,[123] as medicines[124] and in molecular recognition.[125] They can also be used as blocks for building larger 3D and cage-like supramolecular structures, such as rotaxanes[126] and catenanes.[127] Schiff bases are a large family compound with a general structure of $R_2C=NR'$ ($R' \neq H$) (**93,** Scheme 4.1.1).[1] They can be synthesized easily from carbonyl derivatives (**91,** Scheme 4.1.1), such as aldehydes and ketones, and primary amines (**92,** Scheme 4.1.1) under mild conditions.[128] Robson and Pilkington synthesized the first Schiff-base macrocycle (**94,** Figure 4.1.2) in 1970.[129] Since then, these structures have been developed and applied in many areas because the nitrogen atoms in the structures can form strong coordination bonds with numerous metal cations (**95,** Figure 4.1.2).[130,131] Schiff-base macrocycles have been used in a variety of applications including gas storage,[132] simulation of functional proteins[55] and

metal ion recognitions.[130] The macrocycles can be constructed from non-emissive building blocks such as pyridine (**96,** Figure 4.1.2)[133] and biphenyl (**97,** Figure 4.1.2)[134] derivatives that are photophysically inactive or emissive blocks such as substituted phenanthrene (**98,** Figure 4.1.2).[135] However, there are a few examples focussing on the photophysics of luminescent Schiff-base macrocycles. In 2017, compound **97** was published by Olson et al. It is a [3+3] triangle macrocycle synthesized from biphenyl derivatives. This series of macrocycles gave emissions ranging from 369 nm to 470 nm in MeCN. Another example is compound **99** (Figure 4.1.2) reported by Kersting in 2017.[136] This macrocycle compound had 3D structure with a large cavity and emitted at 440 nm in pyridine solution. Compound **99** also showed specific recognition of Zn (II) and was used as ion-sensor. In this project, the synthesis of photoactive Schiff-base macrocycles started from luminescent blocks to explore both their photophysical properties, and their possible applications, ranging from electroluminescent devices to metal ion sensors.

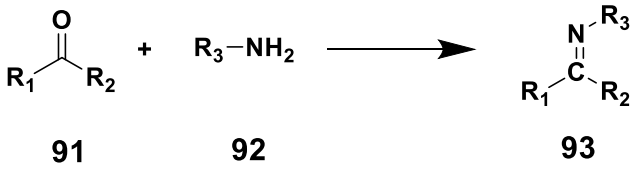

91 **92** **93**

Scheme 4.1.1 Standard synthetic method for Schiff base.[1,128]

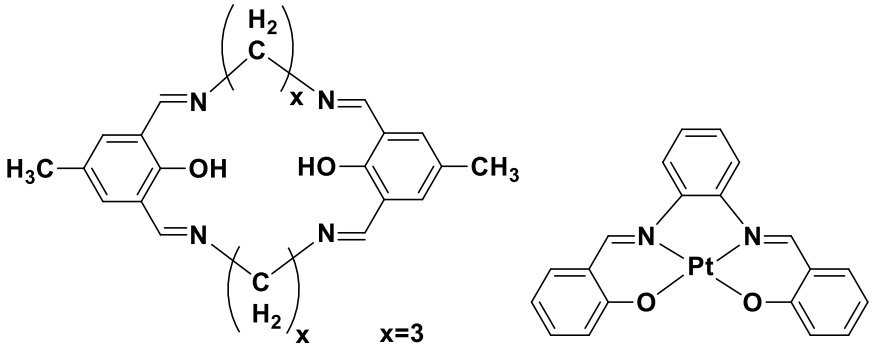

94 **95**

Figure 4.1.1 The first Schiff-base macrocycle (**94**) synthesized by Robson et al. and a monomeric complex based on Schiff-base macrocycle and Pt (II) (**95**).[129,131]

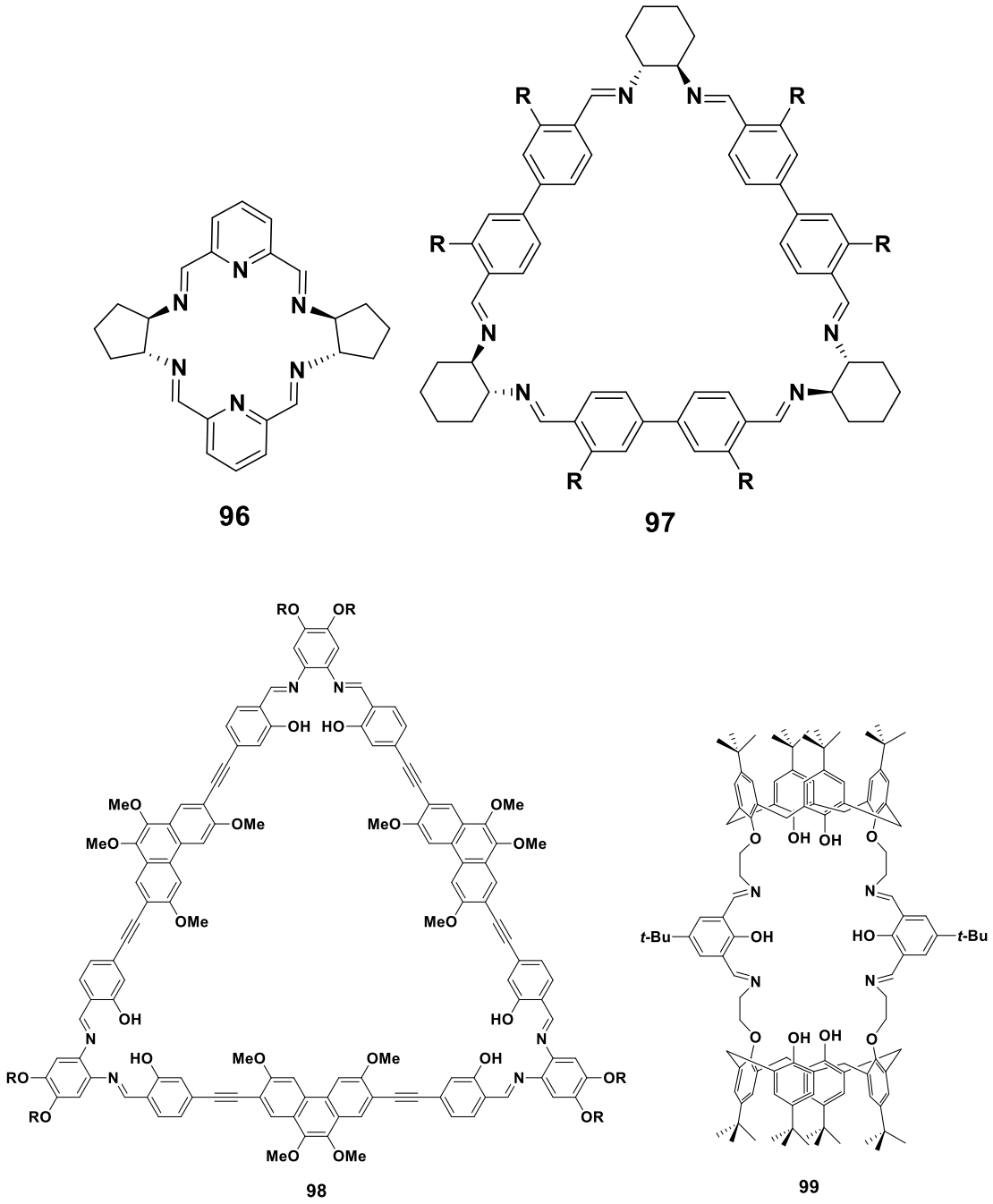

Figure 4.1.2 Photoactive Schiff-base macrocycles synthesized from inactive (**96**, **97**, **99**) and emissive (**98**) blocks (**99** exhibits 3D structure with large cavity and specific recognition to Zn(II)).[133-136]

A group of carbazole-derived dialdehydes (**Mol-0** to **Mol-2,** Figure 4.1.4) were designed and synthesized. By adding different substituents to the carbazole nitrogen, the adjustment from non-emissive (**Mol-0**) to deep blue (**Mol-1**) and yellow (**Mol-2**) emissive molecules was achieved. The nature of the emission (fluorescent, phosphorescent, and thermally activated delayed fluorescent) could be modulated as a function of this substitution. Based on these dialdehyde molecules, their corresponding [2+2] Schiff-base macrocycles were synthesized from the condensation with 1,2-ethylenediamine (**Mac-0** to **Mac-2,** Figure 4.1.4). Their optoelectronic properties were measured both in solution and as powders. Further, thin film photophysical measurements were made with **Mol-1** and **Mol-2**, which were both doped in PMMA (polymethyl methacrylate).

The length of the diamine was also varied as exemplified by **Mac-3**. Longer alkyl chains were expected to improve the solubility of macrocycles in organic solvents.

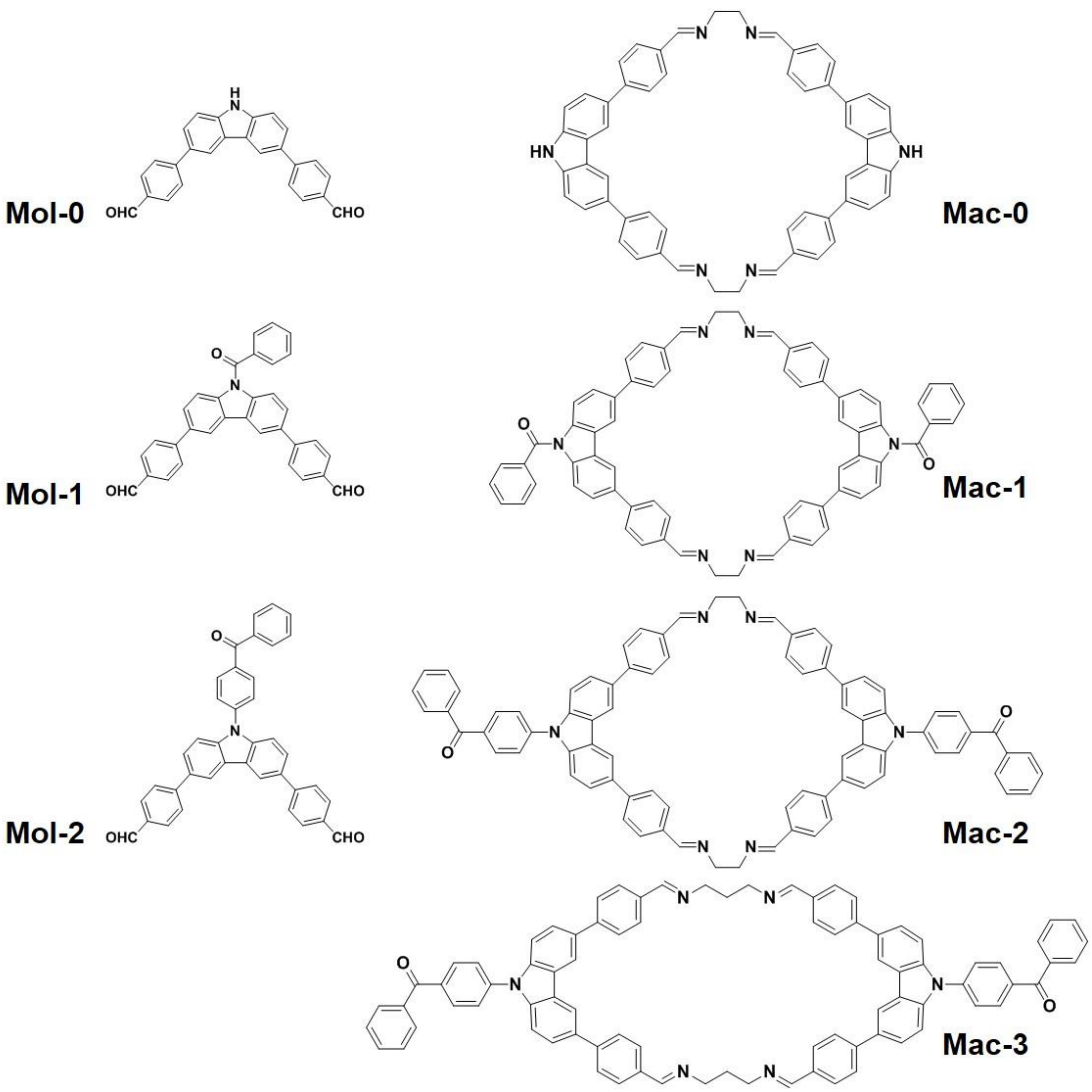

Figure 4.1.3 Chemical structures of dialdehyde carbazole derivatives (left, **Mol-0** to **Mol-2**) and corresponding Schiff-base macrocycles (right, **Mac-0** to **Mac-3**).

Metal ion recognitions were tested using aqueous solutions of inorganic salts. Five metal ions (Fe (III), Co (II), Ag (I), Zn (II), and Cd (II)) were investigated at $1*10^{-4}$ M, and this type of cyclic structure showed selectivity and sensitivity to

Fe (III). According to the literature, Schiff-base macrocycles have shown selectivity to heavy metal ions such as Cu (II),[54] Pb (II),[137] and rare earth ions,[138] but few showed the characteristic recognition of Fe (III). Fe (III) plays an important role in human growth and health, thus developing sensitive probes for qualitative and quantitative measurements of Fe (III) could be important.

4.2 Results and discussion

4.2.1 Synthesis

The **MoI-0** was used as the reference compound for a group of dialdehyde compounds. 9*H*-carbazole was used as the starting material and dissolved in MeCN. 2.5 Equivalents of *N*-bromosuccinimide solution in MeCN was added dropwise in a water bath (Scheme 4.2.1.1). Because this reaction could produce a great quantity of heat, a dropping funnel was necessary for large scale preparation. After 4 h stirring at room temperature, the solvent was removed under reduced pressure and the product was washed with water.

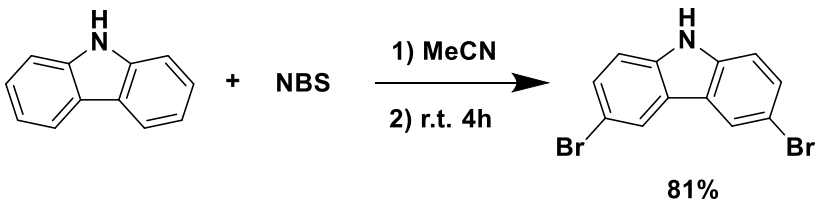

Scheme 4.2.1.1 The bromination of 9*H*-carbazole

Compound **MoI-0** was prepared through the Suzuki-Miyaura palladium catalysed cross-coupling reaction (Scheme 4.2.1.2). $Pd(PPh_3)_4$ was the catalyst, and the reaction system needed to be strictly degassed because $Pd(PPh_3)_4$ is sensitive to oxygen and can decompose to palladium black and lose its activation. This reaction was left overnight under an inert atmosphere at 70 ^oC (Scheme 4.2.1.2). It is better not to use chromatography columns for purification because of its poor solubility in most of solvents including DCM and ethanol, but the other method for purification was provided as follows. Non-polar solvents such as hexane and diethyl ether were used to wash the obtained powder, followed by further washing with water, DCM and cold ethanol to afford the pure product. After being washed several times, the purified product was obtained as a yellow powder. The ^1H NMR showed a resonance at 11.63 ppm corresponding to the *N*-H while the dialdehyde signal was found at 10.07 ppm integrating to 2, all in d_6-DMSO.

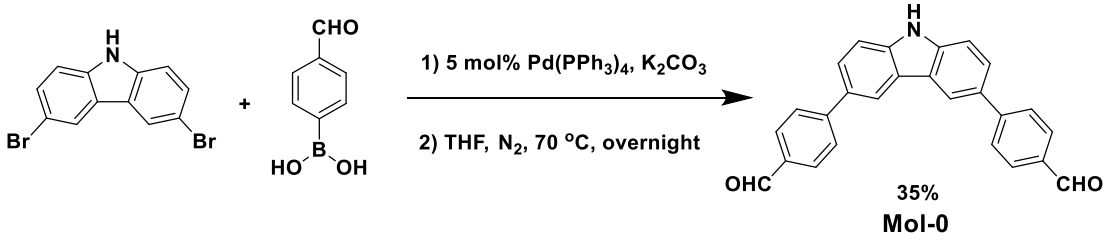

Scheme 4.2.1.2 Suzuki-Miyaura coupling for synthesizing the **MoI-0**

The *N*-group of **Mol-1** was a benzoyl group. According to a series of published structures (Figure 4.2.1.1, **100, 101**), **Mol-1** was expected to be a phosphorescent material.[11,139] The synthesis also started from 3,6-dibromo-9*H*-carbazole. The *N*-H on the carbazole was deprotoned by the sodium hydride in anhydrous THF and the benzoyl was anchored on the nitrogen with the addition of benzoyl chloride (Scheme 4.2.1.3). After removing the solvent, the purification was achieved through washing with water, hexane:ethyl acetate (v/v =10:1) and cold ethanol to afford the **102**. The following step was the Suzuki-Miyaura coupling reaction with (4-formylphenyl)boronic acid under the same reaction conditions as **Mol-0** (Scheme 4.2.1.3). The ^{1}H NMR showed the proton resonance for aldehyde at 10.09 ppm, which was similar to the chemical shift of **Mol-0**.

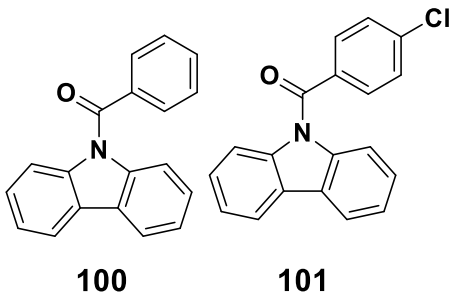

100 **101**

Figure 4.2.1.1 Carbazole based phosphorescent emitters **100**[139] and **101**[11,139] reported in the literature

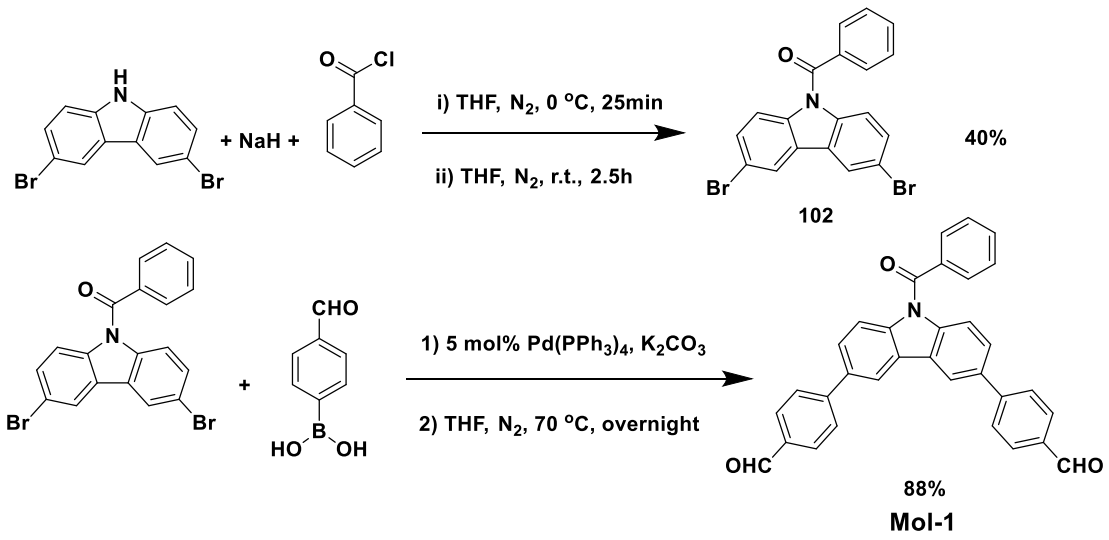

Scheme 4.2.1.3 Synthetic route of **Mol-1**

In the **Mol-2** structure, benzophenone was chosen as the *N*-substituent. This structure was expected to have TADF properties according to the literature (Figure 4.2.1.2, **103**).[140] Mr. Diego Rota Martir in our group also synthesized and showed that two related molecules were TADF (Figure 4.2.1.2, **104**, **105**). 3,6-Dibromo-9*H*-carbazole and (4-fluorophenyl)(phenyl)methanone were dissolved in anhydrous DMF and 1 equivalent of *t*-BuOK was added. This reaction was kept overnight at 150 °C under nitrogen. The purification was achieved through the same method as the compound **102** to afford the **106**, and Suzuki-Miyaura coupling was the final step to prepare the **Mol-2** (Scheme 4.2.1.5).

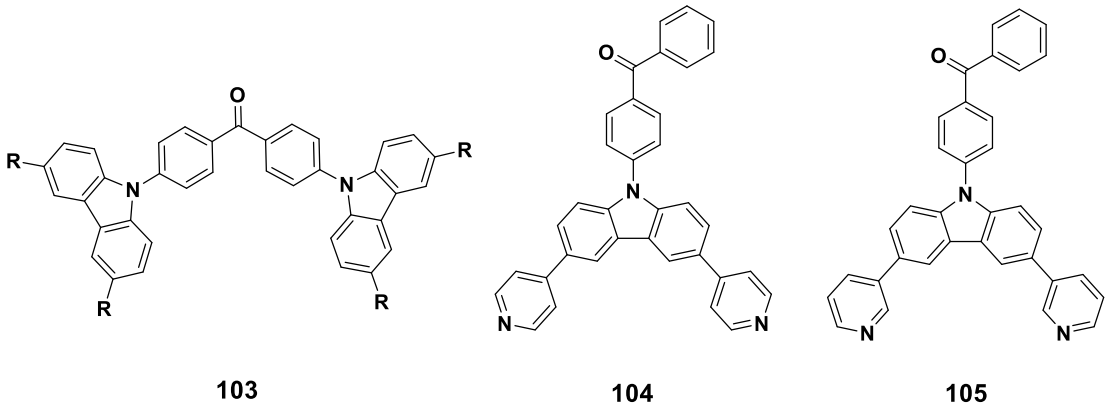

103 104 105

Figure 4.2.1.2 Benzophenone based TADF emitters **103**[140]**, 104** and **105**

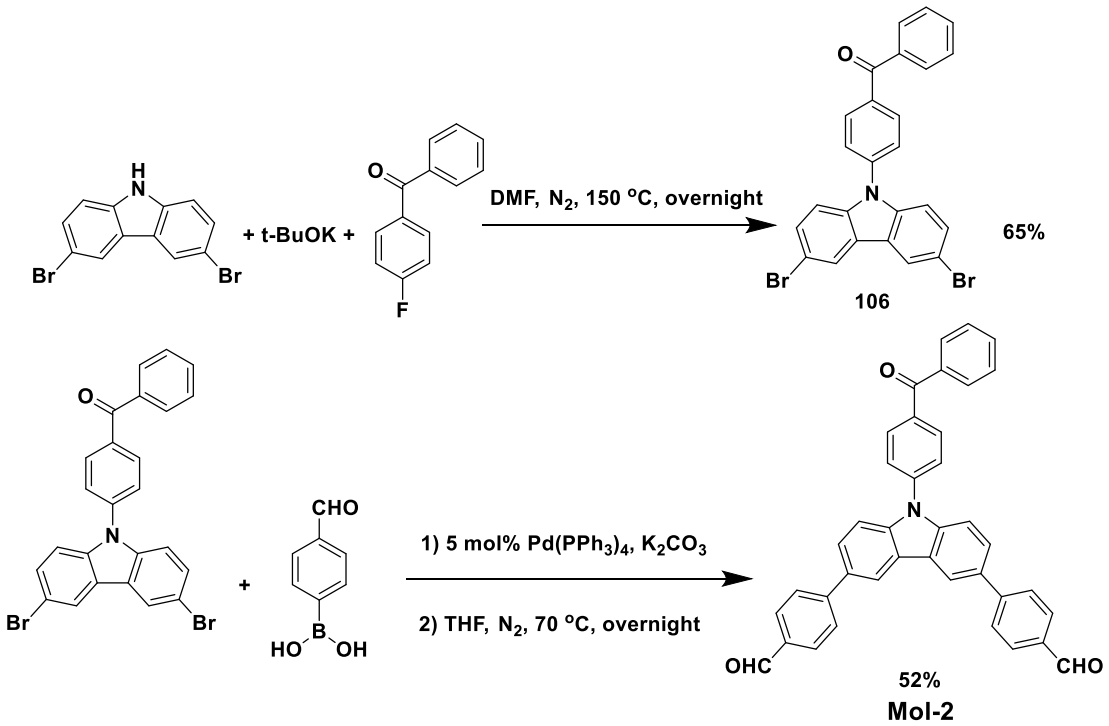

Scheme 4.2.1.4 Synthetic route of **Mol-2**

Both **Mol-1** and **Mol-2** do not have good solubility in most solvents, including DCM, ethyl acetate and MeOH, so high polarity solvents such as DMSO and DMF are the best choice for preparing solutions. Because of their very poor

solubility, it was impossible to purify them using column chromatography directly, proper solvents were chosen to wash and remove impurities in the products. In order to purify **Mol-1** and **Mol-2**, after the removal of the solvents, the residues were washed with water, cold DCM, ethyl acetate and ethanol to afford the pure product. Finally, some cold acetone was used for further purification, because the products, especially **Mol-2**, could hardly be dissolved in acetone as well.

The macrocycles were all synthesized using a general method. The dialdehyde compound and equal equivalent of diamine were added to 1,4-dioxane and ultrasonicated to form a suspension. The mixture was heated to 110 ^{o}C in a sealed heavy wall tube for three days (Scheme 4.2.1.5). The starting material gradually dissolved with increasing temperature, and the product was formed as a precipitate. These macrocycles had very poor solubility in most solvents, including DMSO and DMF, and ^{1}H NMR could not be obtained even in d_6-DMSO. However, the precipitation of the product pushes the reaction equilibrium toward the products. The purification was similar to dialdehyde compounds, and the collected precipitate was stirred in DMSO and heated to 110 ^{o}C for 10 minutes before filtration. The other solvents, such as water, hexane and ethanol, were used for washing after filtration. The residues were collected as products.

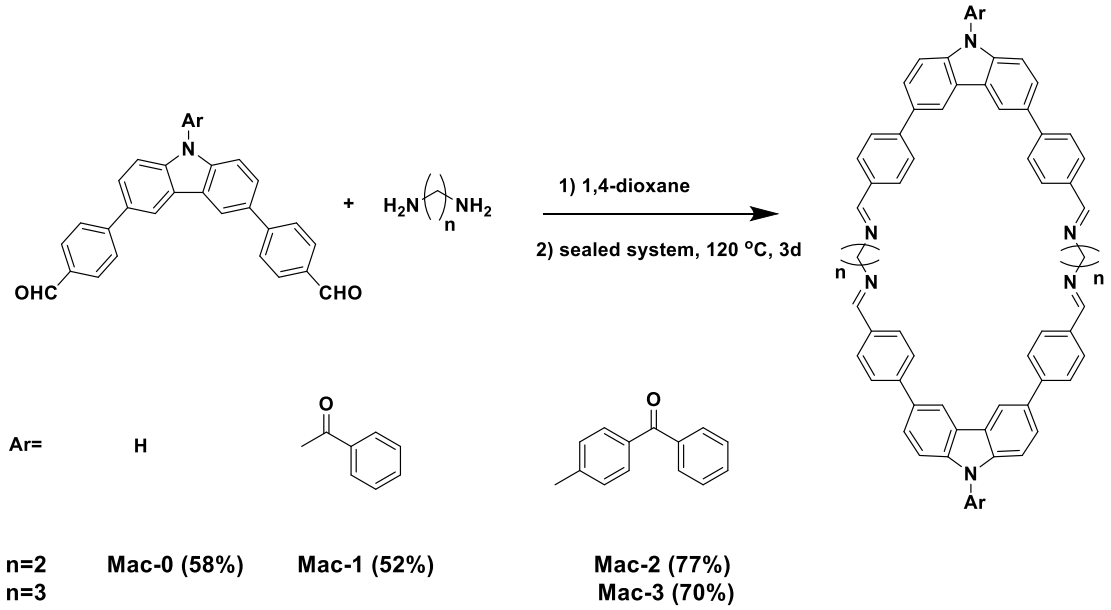

Scheme 4.2.1.5 General synthetic route of Schiff-base macrocycles in the project (**Mac-0** to **Mac-3**)

4.2.2 Characterisation

All these macrocycles had very poor solubility in most solvents, even in d_6-DMSO and therefore we could not obtain satisfactory ^{1}H NMR. FT-IR was chosen as the primary analytical method for monitoring and basic characterization. The MS and elemental analysis (EA) further corroborated their structures.

In Figure 4.2.2.1, **MoI-0** showed a sharp and strong band at 3360 cm^{-1} (**a**), which is the characteristic signal for *N*-H stretching vibration on carbazole.[141]

The other peaks at 2812 cm^{-1} (**b**) and 2727 cm^{-1} (**c**) were the stretching vibration peaks for the C-H on aldehyde, and the peak at 1682 cm^{-1} (**d**) was the overlap of the C=O stretch of the aldehyde and the C=C stretch of benzene and carbazole.[141,142] After the condensation and formation of macrocycles, the peak at 2849 cm^{-1} (**a'**) showed the stretching vibration of C-H of the imine. Another peak at 1641 cm^{-1} (**d'**) was formed corresponding to the imine and became weaker and sharper compared with the broad peak at 1682 cm^{-1} (**d**), which represented the aldehyde. The two signals at 2849 cm^{-1} (**a'**)[142] and 1641 cm^{-1} (**b'**) [143,144] both provided evidence for the formation of the imine while no further signal at 1682 cm^{-1} demonstrated that the aldehyde starting material was completely consumed.

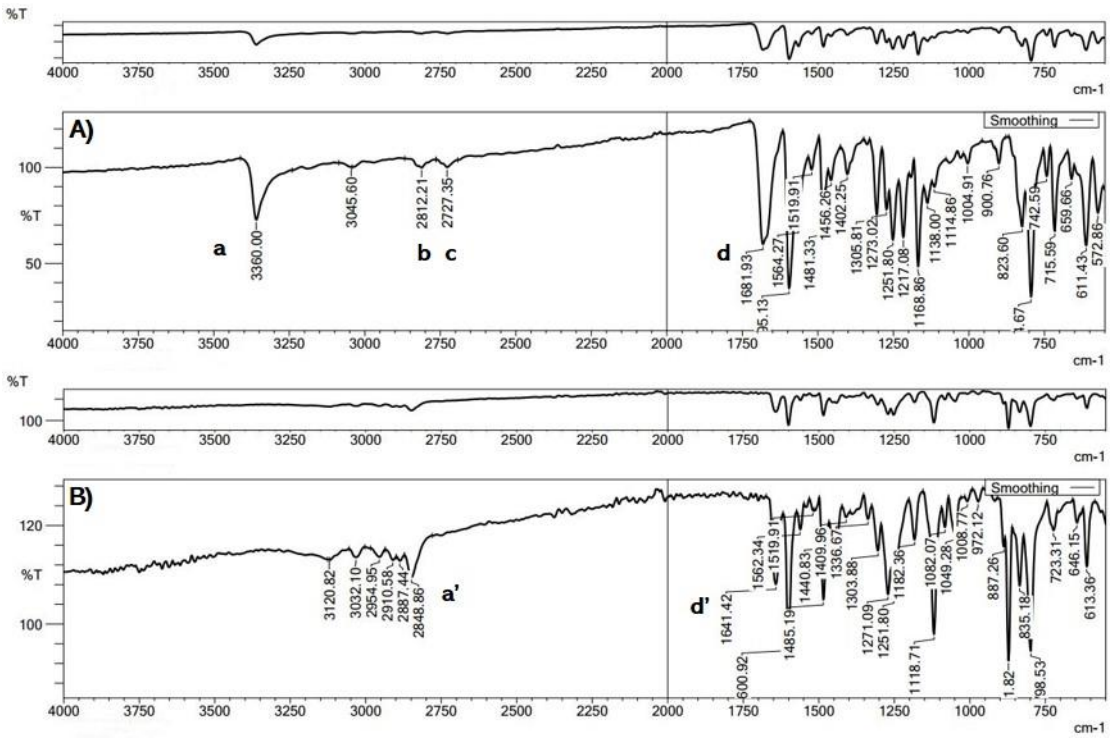

Figure 4.2.2.1 The comparison of FT-IR of **Mol-0** (**A**) and **Mac-0** (**B**)

Mol-1 and **Mol-2** showed similar FT-IR spectra to **Mol-0**, and their carbonyl on *N*-substitutions were characterized as 1666 cm^{-1} (Supporting information, **S-59**)[142] and 1654 cm^{-1} (Supporting information, **S-63**)[142,145], respectively. After the condensation, **Mac-1**, **Mac-2** and **Mac-3** had similar situations on FT-IR. The disappearance of two peaks at 2700-2800 cm^{-1}, and one strong signal at 2710 cm^{-1} represented the reacted aldehyde groups. The new mid-strength peak at 1650 cm^{-1}, and a weak signal at 2835 cm^{-1} proved the formation of Schiff-base. As predicted, the signal of carbonyl on *N*-substituents were not affect by the condensation obviously. In the spectrum of **Mac-1**, its carbonyl on *N*-substituent represented a strong signal at 1676 cm^{-1} (Supporting information, **S-69**), which was very close to the corresponding peak at 1666 cm^{-1} in the spectrum of **Mol-1**. However, in the spectra of **Mac-2** and **Mac-3**, the stretching vibration peaks of carbonyls coupled with the signal of C=N at 1649 cm^{-1} (Supporting information, **S-72**) and 1645 cm^{-1} (Supporting information, **S-75**),[142-145] respectively, which were not easy to be observed but close to the ketone signal at 1654 cm^{-1} in the spectrum of **Mol-2**.

Mass spectrometry (MS) was used to verify the formation of the products. The LTQ Orbitrap was used for **Mac-0** because the proton on the nitrogen of carbazole contributed to its solubility and the concentration was high enough to obtain suitable spectra. **Mac-3** was also measured using the same method. The

longer alkyl chains helped it to dissolve in organic solvents and thus suitable MS could be obtained for this macrocycle as well. The other two macrocycles could not be detected by LTQ Orbitrap and solvent free ASAP-TOF was tried. However, the compounds decomposed using this method. In the MS, only starting material was observed, but FT-IR did not show any aldehyde signals. Finally, ASAP-EI was used to characterize **Mac-1** and **Mac-2**. Although the EI probe could not provide high resolution MS, the observed 1007.4 (*m/z*) showed the molecular ion for **Mac-1** and 1159.4 (*m/z*) was the molecular ion for **Mac-2**. In addition, there was a signal at 1177.4 (*m/z*), and this was the combination of **Mac-2** and one water molecule.

4.2.3 Computational section

The structures were optimized in gas phase with the B3LYP function and 6-31G (d,p) basis set. The TDA (Tamm–Dancoff approximation) calculations were done with the PBE1PBE function and 6-G (d,p) basis set following the established protocol in the group for computing the properties of TADF molecules. From Figure 4.2.3.1, it can be seen that the HOMOs were located on the carbazole and extended onto the benzaldehyde rings. The LUMOs were located on the substituents of the nitrogen atom of carbazoles. However, for **Mol-0**, where there was no functional group on the nitrogen, its LUMO was located towards the aldehydes and their linking phenyl rings.

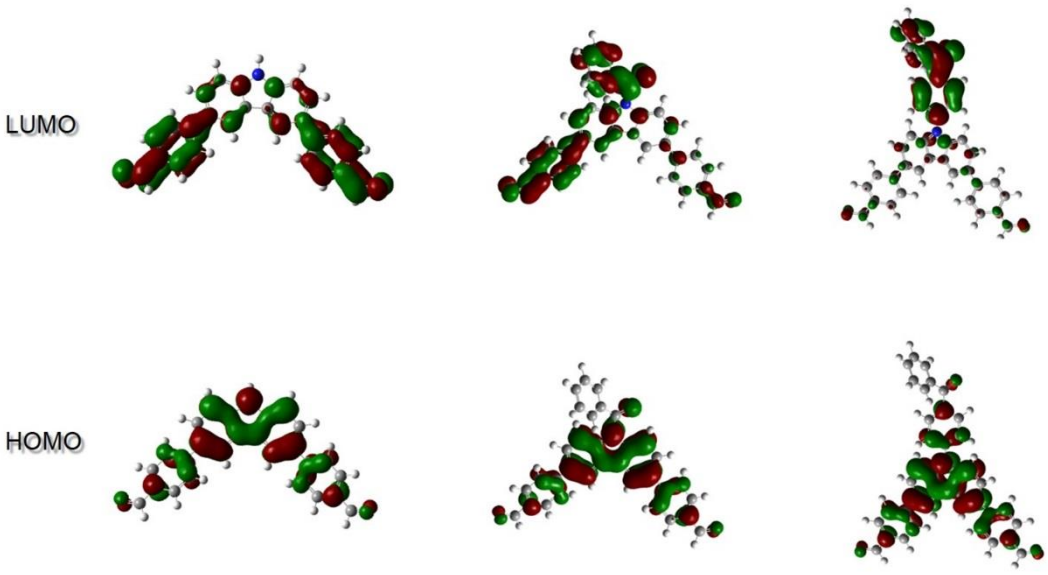

Figure 4.2.3.1 Geometry optimization and HOMO & LUMO localization of **Mol-0**, **Mol-1**, and **Mol-2.**

After forming the macrocyclic structures, the locations of the HOMOs and LUMOs did not change much. Because all macrocyclic structures were pseudo symmetric, two nearly isoenergetic orbitals existed, one with the electron density located on one half of the molecule and the other with the electron density located on the other half of the molecule. From the calculation results (Figure 4.2.3.2), the HOMO and its partner HOMO-1 were located on the carbazoles of **Mac-0**, and its LUMO and LUMO+1 were located on the linking phenyl rings. With the addition of the *N*-benzoyl substituent, **Mac-1** had HOMO and HOMO-1 located on carbazoles. Its LUMO and LUMO+1 were mainly

located on the *N*-benzoyl, and partly located on carbazoles. **Mac-2** and **Mac-3** had similar electron density distributions with respect to each other. The HOMO and HOMO-1 of both **Mac-2** and **Mac-3** were located on carbazoles, and their LUMO and LUMO+1 were located on the *N*-benzophenone.

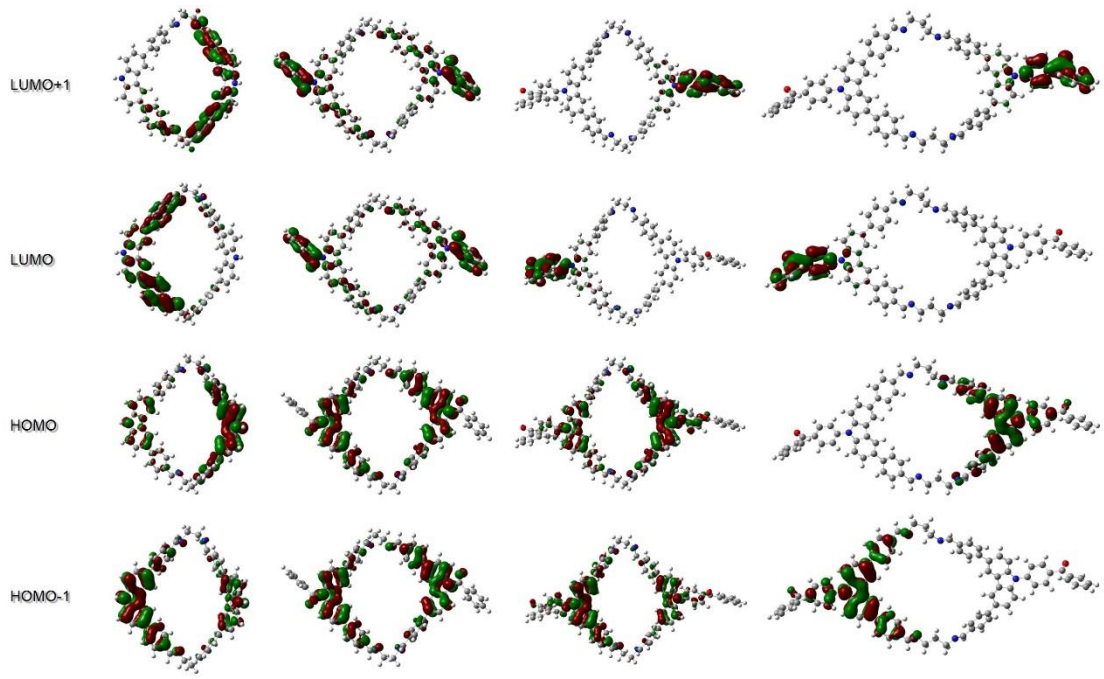

Figure 4.2.3.2 Geometry optimization and HOMO & LUMO localization of **Mac-0**, **Mac-1**, **Mac-2**, and **Mac-3**

By adding *N*-donor to the carbazole, in Table 4.2.3.1, the LUMOs were stabilized, benzophenone contributed more than benzoyl. After forming the cyclic structures, both HOMOs and LUMOs were destabilized, and most of the

band gaps, except **Mac-0**, became smaller. Comparing **Mac-2** and **Mac-3**, their HOMOs, LUMOs and band gaps were almost the same at 3.98 eV, which demonstrated that the linking chain length had little influence on the energy of the system.

Tamm–Dancoff approximation (TDA) is a variant of time-dependent density functional theory (TD-DFT).[146] It has been widely used to calculate the singlet and triplet energy gap especially for small organic molecules because of its relatively simple method and codes.[146,147] Results from TDA also tend to more accurately predict both the nature and the energies of the transitions.[147] The calculation of TDA for organic molecules has been a protocol in our group.

From the TDA calculations (Table 4.2.3.1), the S_1 (lowest singlet state) for **Mol-0** and **Mol-1** were nearly the same at 3.56 eV. However, **Mol-1** had a slightly lower T_1 (lowest triplet state), which led to a larger singlet-triplet energy gap (ΔE_{ST}) at 0.67 eV. When the *N*-group was changed to benzophenone, both singlet and triplet states were stabilized, but the singlet state energy decreased more and led to the smallest ΔE_{ST} at 0.48 eV within this series. There was a much bigger influence on macrocycles for their singlet states, but the triplet states remained essentially the same, especially for **Mac-0**, **Mac-1** and **Mac-2**. The formation of macrocycles also changed ΔE_{ST}. Compared with

corresponding dialdehyde carbazole derivatives, **Mac-0** and **Mac-1** had larger ΔE_{ST}, while **Mac-2** and **Mac-3** were decreased. With a longer alky chain, even though it did not change the energy gap between HOMO and LUMO, the ΔE_{ST} of **Mac-3** decreased by 0.05 eV compared with **Mac-2**.

Table 4.2.3.1 Photophysical data from calculation results

	Mol-0	**Mol-1**	**Mol-2**	**Mac-0**	**Mac-1**	**Mac-2**	**Mac-3**
LUMO+1 (eV) [a]	0.74	0.56	0.56	1.01	0.70	0.51	0.52
LUMO (eV) [a]	0.60	0.47	0.39	0.93	0.69	0.48	0.50
HOMO (eV) [a]	-3.78	-3.91	-3.74	-3.49	-3.62	-3.50	-3.50
HOMO-1 (eV) [a]	-7	-4.09	-4.10	-3.51	-3.64	-3.51	-3.53
(ΔE/eV) [b]	4.38	4.38	4.13	4.42	4.31	3.98	3.99
Singlet state [c] (S_1/eV)	3.56	3.55	3.32	3.63	3.45	3.14	3.17
Triplet state [c] (T_1/eV)	2.92	2.88	2.84	2.74	2.73	2.72	2.79
ΔE_{ST} (eV) [d]	0.64	0.67	0.48	0.89	0.72	0.43	0.38

[a] Used B3LYP/6-31G** for geometry optimization and calculation of HOMO and LUMO. [b] $\Delta E = E_{LUMO} - E_{HOMO}$. [c] Used PBE1PBE/6-31G** for TDA calculation to obtain singlet and triplet state energies. [d] $\Delta E_{ST} = E_{si} - E_{T1}$

4.2.4 Photophysical properties

4.2.4.1 Photophysical properties in solution (anhydrous DMF)

Because this group of compounds had poor solubility in most solvents, all measurements were made in anhydrous DMF. In UV-vis absorption spectra, the higher energy region (300 – 340 nm) was dominated by the π–π^* transition of carbazole of all three molecules (318 nm for **Mol-0**, 325 nm for **Mol-1** and 317 nm for **Mol-2**) (Figure 4.2.4.1.1).[54] The molar absorptivity of **Mol-1** was 66 x 10^3 $M^{-1}cm^{-1}$ between 314 nm and 340 nm, which represented the π–π^* transition of carbazole. However, at the lower energy region, between 340 nm and 415 nm, charge transfer bands could be observed in the absorption spectra of **Mol-0** (ε= 45 x 10^3 $M^{-1}cm^{-1}$) and **Mol-2** (ε=72 x 10^3 $M^{-1}cm^{-1}$). In terms of **Mol-1**, there was virtually no charge transfer from its absorption spectrum. The electron density distributions of the HOMO and LUMO from DFT calculations had a large overlap (Figure 4.2.3.1), which indicated a localized excited state. Furthermore, the HOMOs and LUMOs on **Mol-0** and **Mol-2** were separated, which indicated the presence of a charge transfer state between HOMO and LUMO in these molecules. From the Figure 4.2.3.1, **Mol-0** had a charge transfer from carbazole to benzaldehyde, while **Mol-2** had a charge transfer from carbazole and two phenyls to the *N*-benzophenone.

In the emission spectra (Figure 4.2.4.1.1), with different *N*-groups, the emission maxima were adjusted from 484 nm (**Mol-1**) to 495 nm (**Mol-2**) in degassed DMF solution (Table 4.2.4.1.1). Through the replacement of the proton of *N*-H on carbazole with benzoyl and benzophenone, their emissions in solution were red-shifted by 5 nm and 11 nm, respectively. The prompt components of the emission decays of both **Mol-0** and **Mol-1** contributed the most to their lifetimes, while the three components of **Mol-2** each contributed with similar weighting to the lifetime. With the change of *N*-donors, the PLQYs decreased from **Mol-0** to **Mol-2** in DMF solution. Among this group, **Mol-0** had the highest PLQY at 58%. When the nitrogen on carbazole was decorated with a benzoyl group, **Mol-0** had a bit lower PLQY at 48% compared to **Mol-0**, and **Mol-2** had the lowest PLQY (45%) with *N*-benzophenone substitution. All three materials had high radiative decay rate constants (k_r > 4*10^7 s^{-1}), with **Mol-0** having the largest radiative decay rate constant (k_r = 14.50 *10^7 s^{-1}) of the three. It was also the structure having the highest PLQY within this group. **Mol-1** had the smallest radiative decay rate constant (k_r = 4.54 *10^7 s^{-1}), as well as the smallest non-radiative decay rate constant (k_{nr} = 4.91 *10^7 s^{-1}). From the measurement results, **Mol-2** did not show TADF properties in DMF solution as its lifetime only demonstrated prompt fluorescence (4 ns [0.83], 10 ns [0.12], 121 ns [0.05], contribution of component in brackets). However, because DMF is a very polar solvent, the ^{3}CT was preferentially stabilized, and the TADF phenomenon was expected to be arrested.[148] Variable temperature photophysical measurements

were made to confirm the emission mechanism of **Mol-2** further, which will be discussed in the Chapter 4.2.4.5.

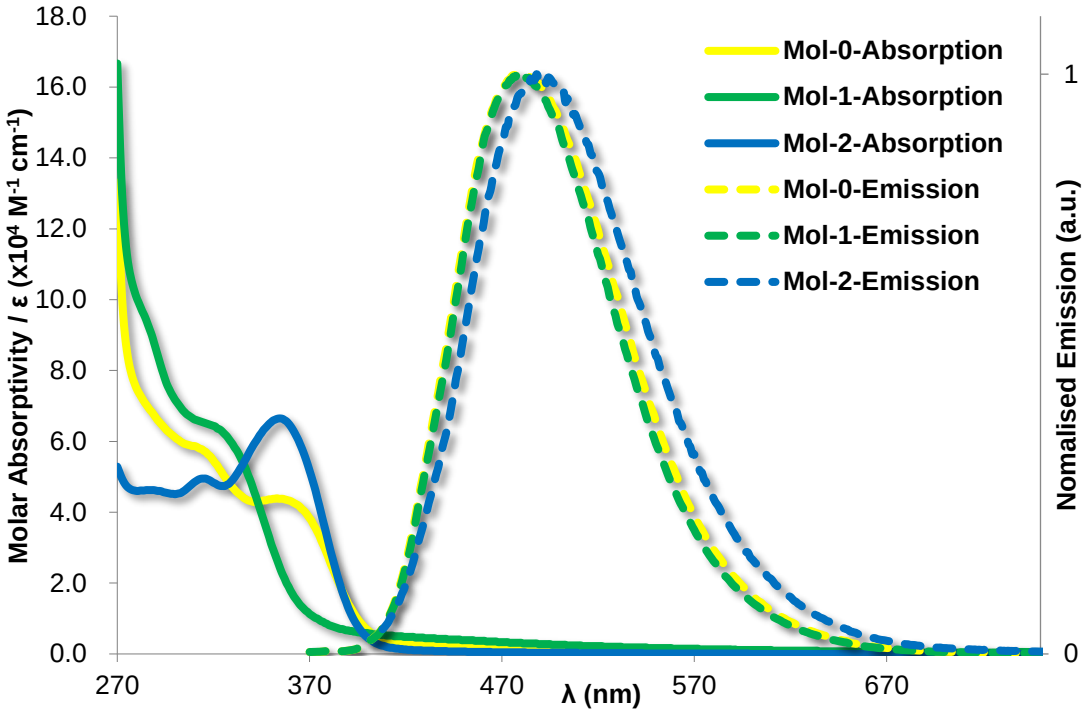

Figure 4.2.4.1.1 Molar absorptivity and emission spectra of **Mol-0** to **Mol-2** in DMF solution (λ_{ex}= 370 nm)

Table 4.2.4.1.1 Photophysical data of **Mol-0** to **Mol-2** in DMF solution

			Mol-0	**Mol-1**	**Mol-2**
Emission λ_{PL} /nm [a]			479	484	495
Lifetime τ_{PL}/ns	Air [b]	1	3 (0.98)	3 (0.97)	6 (1)
		2	8 (0.02)	10 (0.03)	-
		χ^2	1.197	1.166	1.176
	N_2 [a]	1	4 (0.99)	4 (0.83)	2 (0.31)
		2	10 (0.01)	10 (0.12)	4 (0.44)
		3	-	121 (0.05)	9 (0.24)
		χ^2	1.543	1.192	1.183
PLQY (%) [a,c]	N_2		58%	48%	45%
k_r /$10^7 s^{-1}$ [d]	N_2		14.50	4.54	9.91
k_{nr} /$10^7 s^{-1}$ [e]	N_2		10.50	4.91	12.11

[a] Measurements in degassed anhydrous DMF at 298 K, λ_{ex}= 370 nm. [c] Measurements in oxygenerated anhydrous DMF at 298 K. [c] Quinine sulfate employed as the external reference (Φ_{PL} = 54.6% in 0.5 M H_2SO_4 at 298 K).[85] [d] $k_r=\Phi/\tau$. [e] $k_{nr}=1/\tau-k_r$.

After forming macrocyclic structures, there was hardly any difference in emission wavelength between **Mol-1** and **Mac-1** in DMF solution (Figure 4.2.4.1.2). Both **Mol-1** and **Mac-1** emitted at 483 nm, but **Mac-1** had lower PLQY (Table 4.2.4.1.2). By comparing their lifetimes, it could be observed that **Mol-1** had a longer lifetime in solution, but the contribution for each component was very close for both molecules. However, for **Mol-0** and **Mac-0,** which were the reference structures, there was an obvious blue shift from 479 nm to 425 nm after condensation (Figure 4.2.4.1.2). **Mac-0** also had one more lifetime component and higher PLQY compared with **Mol-0** (Table 4.2.4.1.2). Different from the other two groups, **Mac-2** showed a 9 nm red shift compared to **Mol-2** in DMF solution (Figure 4.2.4.1.2). Moreover, **Mac-2** had a slightly shorter lifetime.

The decay constant was also affected by the formation of cyclic structures. Compared with **Mol-0**, **Mac-0** had a higher radiative decay rate constant (k_r=28.57*10^7 s^{-1}), which was also the highest k_r of the whole group, and a lower non-radiative decay rate constant (k_{nr}=6.0*10^7 s^{-1}). The opposite happened with **Mac-2,** which had a lower radiative rate constant (k_r=3.05*10^7 s^{-1}) but a higher non-radiative decay constant (k_{nr}=8.56*10^7 s^{-1}) compared with its precursor. **Mac-1** had an increased radiative rate constant. However, its non-radiative decay rate constant decreased more. In summary, with the formation of

macrocycles, the PLQY decreased on **Mac-1** and **Mac-2** and it is likely due to the increased vibrational quenching which was caused by more flexible structures.

Even though the change of photophysical properties were different in these three sets of compounds after forming macrocyclic structures, the tendency among macrocycles was similar compared to their dialdehyde blocks. From **Mac-0** to **Mac-2**, their charge transfers changed from carbazole-phenyl to carbazole-*N*-groups, and their emission wavelength red shifted in DMF.

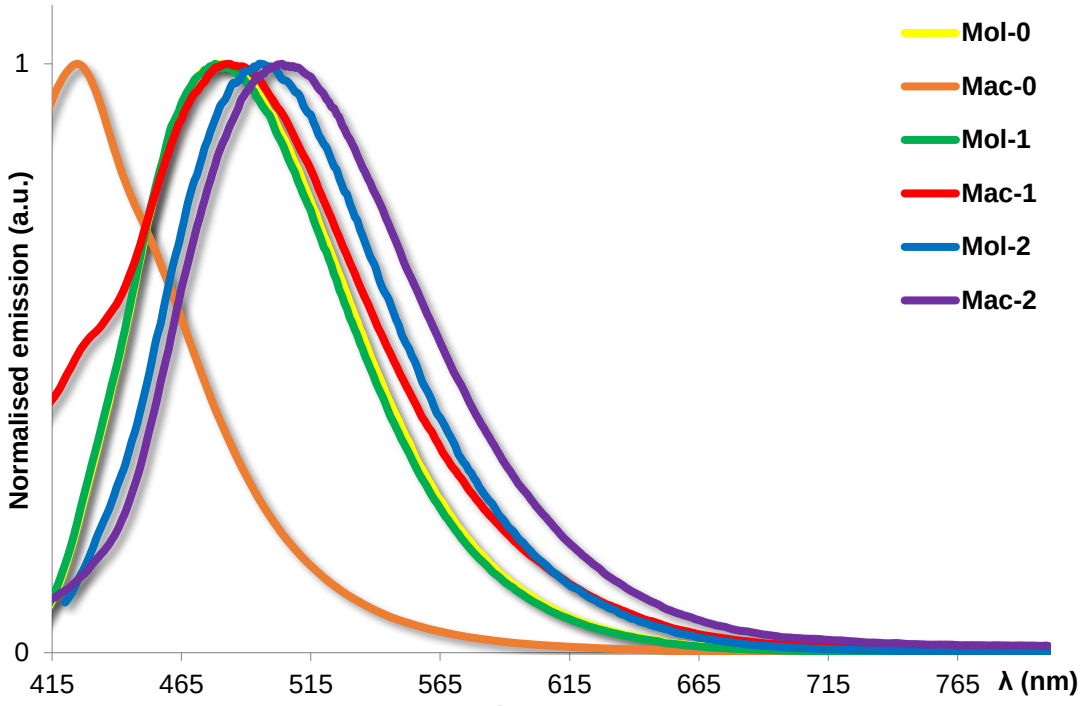

Figure 4.2.4.1.2 Normalized emission spectra of dialdehyde modified carbazoles (**Mol-0** to **Mol-2**) and macrocycles (**Mac-0** to **Mac-2**) in degassed DMF solution (λ_{ex}= 370 nm)

Table 4.2.4.1.2 Photophysical data of **Mol-0** to **Mol-2** and **Mac-0** to **Mac-2** in DMF solution

			Mol-0	**Mac-0**	**Mol-1**	**Mac-1**	**Mol-2**	**Mac-2**
Emission λ_{PL} /nm [a]			479	425	484	483	495	504
Lifetime τ_{PL} /ns	Air [b]	1	3 (0.98)	2 (0.50)	3 (0.97)	2 (0.35)	6 (1)	3 (0.12)
		2	8 (0.02)	4 (0.49)	10 (0.03)	4 (0.58)	-	7 (0.86)
		3	-	12 (0.01)	-	10 (0.07)	-	32 (0.01)
	N_2 [a]	1	4 (0.99)	1 (0.26)	4 (0.83)	3 (0.86)	2 (0.31)	3 (0.23)
		2	10 (0.01)	2 (0.60)	10 (0.12)	8 (0.13)	4 (0.44)	9 (0.76)
		3	-	6 (0.13)	121 (0.05)	54 (0.01)	9 (0.24)	53 (0.01)
PLQY (%) [a,c]	N_2		58%	64%	48%	28%	45%	23%
k_r /$10^7 s^{-1}$ [d]	N_2		14.50	28.57	4.54	7.73	9.91	3.05
k_{nr} /$10^7 s^{-1}$ [e]	N_2		10.50	6.00	4.91	9.00	12.11	8.56

[a] Measurements in degassed anhydrous DMF at 298 K, λ_{ex}= 370 nm. [b] Measurements in oxygenerated anhydrous DMF at 298 K. [c] Quinine sulfate employed as the external reference (Φ_{PL} = 54.6% in 0.5 M H_2SO_4 at 298 K).[85] [d] $k_r=\Phi/\tau$. [e] $k_{nr}=1/\tau-k_r$.

Mac-3 was synthesized from **Mol-2** and propane-1,3-diamine in 1,4-dioxane solution. Theoretically, there should be no difference between **Mac-2** and **Mac-3** in terms of the photophysical properties (Table 4.2.3.1). However, in emission spectra, there was a 7 nm red shift compared with **Mac-2** (Figure 4.2.4.1.3). The lifetime for **Mac-2** was similar to **Mac-3** in the first two components both on lengths and contributions (Table 4.2.4.1.3), and the PLQYs of **Mac-2** and **Mac-3** were close, which were approximately half of the PLQY for **Mol-2** in DMF solution. The vibrational quenching could be the reason for the decrease in PLQY, because the macrocycles had relatively more flexible structures. This result can also be revealed from the kinetic studies. After the condensation, they all had a very high non-radiative decay rate constant (k_{nr}>7*10^7 s^{-1}). Both **Mac-2** (k_r=3.05*10^7 s^{-1}) and **Mac-3** (k_r=3.23*10^7 s^{-1}) had a much lower radiative decay rate constant than **Mol-2** (k_r=9.91*10^7 s^{-1}), which means a slower charge transfer rate, even though their non-radiative decay processes were slightly reduced. However, by comparing the **Mac-2** and **Mac-3**, with the longer alkyl linking chain, **Mac-3** (k_{nr}=7.91*10^7 s^{-1}) had a higher radiative decay constant and a lower non-radiative decay rate compared with **Mac-2** (k_{nr}=10.22*10^7 s^{-1}). This difference could be caused by the different conformations between **Mac-2** and **Mac-3**.

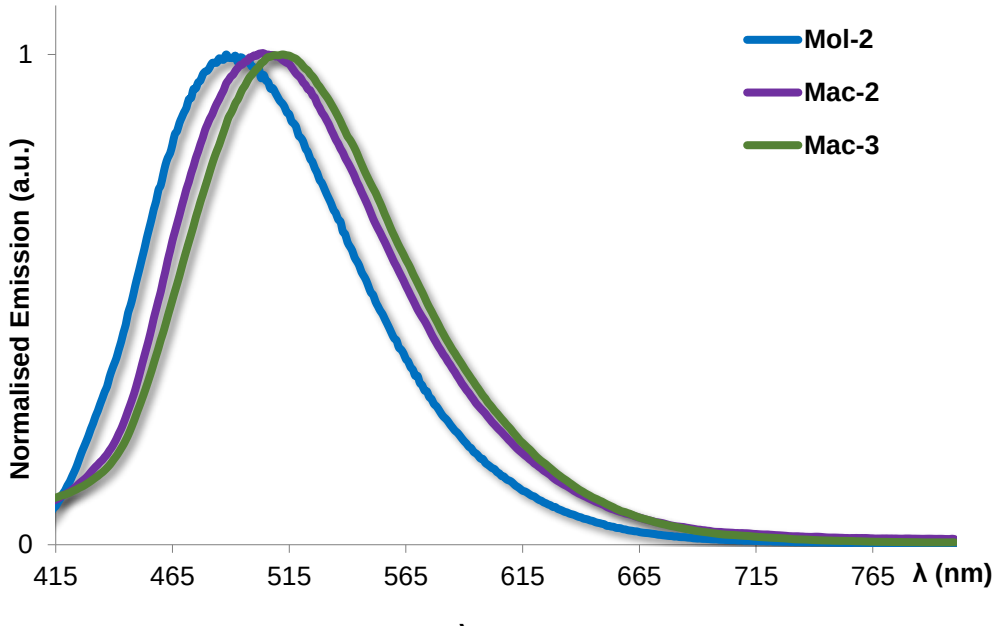

Figure 4.2.4.1.3 Normalized emission spectra of **Mol-2**, **Mac-2** and **Mac-3** in DMF solution (λ_{ex}= 370 nm)

Table 4.2.4.1.3 Photophysical data of **MoI-2, Mac-2** and **Mac-3** in DMF solution

			MoI-2	**Mac-2**	**Mac-3**
Emission λ_{PL} /nm [a]			495	504	511
Lifetime τ_{PL} /ns	Air [b]	1	6 (1)	3 (0.12)	6 (0.98)
		2	-	7 (0.86)	14 (0.02)
		3	-	32 (0.01)	-
	N_2 [a]	1	2 (0.31)	3 (0.23)	7 (0.34)
		2	4 (0.44)	9 (0.76)	10 (0.66)
		3	9 (0.24)	53 (0.01)	-
PLQY (%) [a,c]	N_2		45%	23%	29%
k_r /10^7s^{-1} [d]	N_2		9.91	3.05	3.23
k_{nr} /10^7s^{-1} [e]	N_2		12.11	10.22	7.91

[a] Measurements in degassed anhydrous DMF at 298 K, λ_{ex}= 370 nm. [c] Measurements in oxygenerated anhydrous DMF at 298 K. [c] Quinine sulfate employed as the external reference (Φ_{PL} = 54.6% in 0.5 M H_2SO_4 at 298 K).[85] [d] $k_r=\Phi/\tau$. [e] $k_{nr}=1/\tau-k_r$.

4.2.4.2 Photophysical properties of bulk powder

Mol-0 and **Mac-0** showed promising emission in solution, but they were non-emissive as powders, probably because the aggregation caused quenching. **Mol-1** and **Mol-2** still had promising emission in bulk powder, and their bulky *N*-donors on carbazole could be the reason for decreasing the aggregation caused quenching in solid state. With the decoration of benzoyl, **Mol-1** emitted at 446 nm in powder (Figure 4.2.4.2.1), and there was a red shift to 519 nm for **Mol-2** because of its more pronounced charge transfer (Figure 4.2.3.2). With different *N*-decoration groups on carbazole, their LUMOs moved from the benzaldehyde in **Mol-0** to the *N*-benzophenone group in **Mol-2**. Also, in bulk powder, the emission wavelength of **Mol-2** red-shifted from 495 nm to 519 nm compared to DMF solution.

However, after forming macrocyclic structures, **Mac-1** had 35 nm red shift compared with **Mol-1**, but **Mac-2** had 31 nm blue shift to 488 nm (Figure 4.2.4.2.1). **Mac-1** and **Mac-2** had very close emission wavelengths of 481 nm and 488 nm, respectively. In Table 4.2.4.1.2, **Mac-1** emitted at 481 nm, and **Mac-2** emitted at 504 nm in DMF. Both molecules blue-shifted in bulk powder, and **Mac-2** was more pronounced. This phenomenon is likely due to the lower polarity environment in bulk powder compared with DMF solution.[149,150] There was a shoulder peak on the emission spectra of **Mac-2**. As the holder of powder

measurements are fixing and not presently applicable, these measurements will have to be re-verified at a later date.

Their lifetime in bulk powder also showed different properties compared to the situation in DMF solution (Table 4.2.4.2.1). In bulk powder, all molecules showed much longer lifetimes of up to several microseconds, and their lifetimes were strongly affected by oxygen. By comparing the data in air and vacuum, it was seen that all molecules in air had lifetimes which were hundreds times shorter than the data in vacuum, because their triplet excited states could be seriously quenched by oxygen. Also, in an inert atmosphere, the pre-exponential factor associated with the long delay component increased in importance, especially for **Mol-1** and **Mac-1**. As shown in Table 4.2.4.2.1, after condensation, the lifetime of **Mac-1** increased slightly, but that of **Mac-2** decreased to about half of **Mol-2**. The same situation occurred in DMF (Table 4.2.4.1.2).

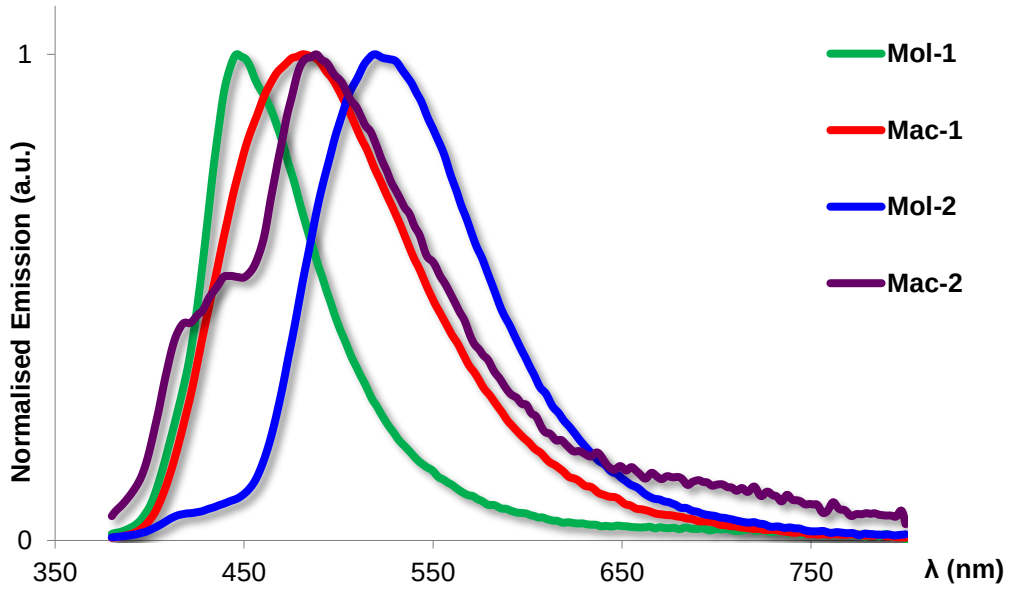

Figure 4.2.4.2.1 Normalized emission spectra of **Mo-1**, **Mol-2**, **Mac-1** and **Mac-2** on bulk powder (λ_{ex}= 370 nm)

Table 4.2.4.2.1 Photophysical data of **Mol-1**, **Mol-2, Mac-1** and **Mac-2** on bulk powder

Powder			**Mol-1**	**Mac-1**	**Mol-2**	**Mac-2**
Emission λ_{PL}/nm [a]			446	481	519	488
Lifetime τ_{PL}/ns	Air [b]	1	2 (55%)	1 (35%)	1 (25%)	1 (59%)
		2	4 (43%)	4 (61%)	7 (64%)	4 (37%)
		3	22 (2%)	19 (3%)	17 (11%)	21 (4%)
	Vacuum [a]	1	15 (22%)	38 (3%)	28 (28%)	19 (46%)
		2	295 (19%)	478 (25%)	314 (25%)	117 (23%)
		3	1917 (59%)	2227 (72%)	2462 (46%)	1412 (31%)

[a] Measurements in high vacuum at 298 K, λ_{ex}= 370 nm. [b] Measurements in air at 298 K.

Not only did N-donor change the photophysical properties, but the length of the alkyl chain between the imines also affected the photophysics. After the condensation, **Mac-2** had 31 nm blue shift in powder compared with **Mol-2** (Figure 4.2.4.2.2). Theoretically, the photophysical properties should not be affected by the length of the bridging alkyl chain between the imines. However, **Mac-3** showed a further blue shift to 438 nm (Figure 4.2.4.2.2). The different inter and intramolecular interactions brought by different conformations and aggregation states could be the reason. According to the calculation results (Figure 4.2.3.3), **Mac-3** was more flexible than **Mac-2** because of the longer alkyl chains. This difference in conformations could cause **Mac-3** to have fewer intermolecular interactions such as π–π stacking, which can lead to the blue-shift.

The emission lifetimes of the molecules were also affected. In Table 4.2.4.2.2, **Mol-2** had the longest lifetime and delayed component of 2462 ns. After the formation of **Mac-2**, the lifetime decreased to 1412 ns, and **Mac-3** only had a lifetime of tens of nanoseconds. Comparing the data, **Mol-2** and **Mac-2** had similar component distributions especially in vacuum. Both of them had the longest lifetime component of 2462 ns and 1412 ns in vacuum, respectively, compared to 17 ns and 21 ns in air. However, **Mac-3** showed the shortest lifetime, lower than 30 ns both in air and vacuum, and the contribution of each

component was similar. There might be a lack of vacuum degree for this measurement, and the triplet state was quenched by oxygen. This measurement will be redone when the instrument is available.

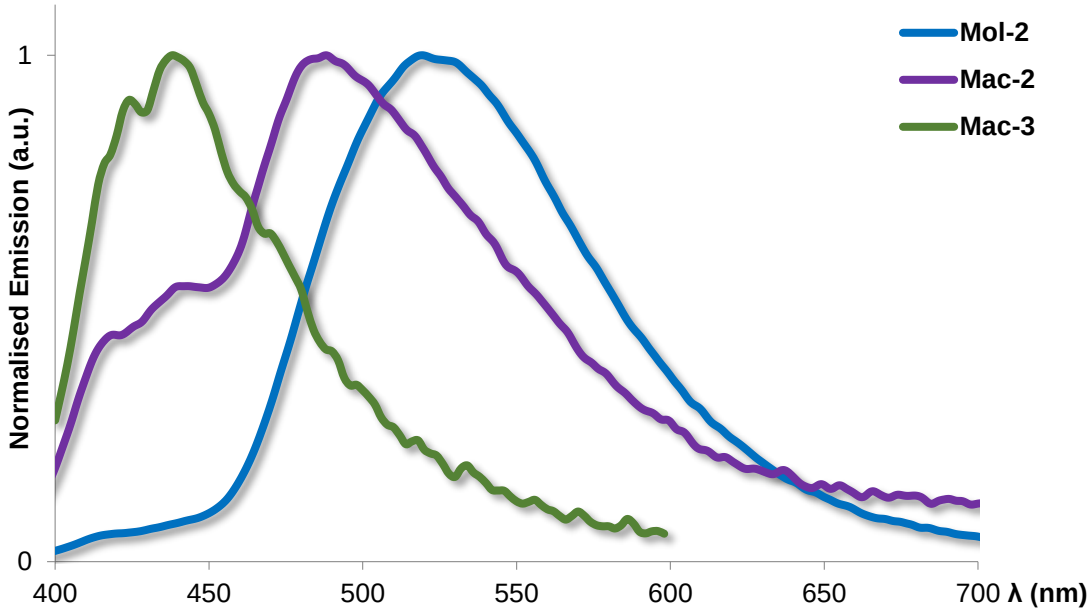

Figure 4.2.4.2.2 Normalized emission spectra of **Mol-2**, **Mac-2** and **Mac-3** on bulk powder (λ_{ex}= 370 nm)

Table 4.2.4.2.2 Photophysical data of **Mol-2, Mac-2** and **Mac-3** on bulk powder

			Mol-2	**Mac-2**	**Mac-3**
Emission λ_{PL}/nm [a]	Powder		519	488	438
Lifetime τ_{PL}/ns	Air [b]	1	1 (25%)	1 (59%)	1 (56%)
		2	7 (64%)	4 (37%)	4 (30%)
		3	17 (11%)	21 (4%)	19 (13%)
	Vacuum [a]	1	28 (28%)	19 (46%)	1 (66%)
		2	314 (25%)	117 (23%)	4 (24%)
		3	2462 (46%)	1412 (31%)	14 (9%)

[a] Measurements in high vacuum at 298 K, λ_{ex}= 370 nm. [b] Measurements in air at 298 K.

4.2.4.3 Photophysical properties on doped film

Not only were solution and bulk powder tested, **Mol-1** and **Mol-2** were also prepared as 10 wt% PMMA (polymethyl methacrylate) doped film to decrease their aggregation and intermolecular interactions in the solid state. As **Mol-0** did not give any emission in solid state, its photophysical properties were only measured in solution state. The emission spectra are shown in Figure 4.2.4.3.1. **Mol-2** had 495 nm emission, which was 11 nm red shift compared with **Mol-1** in DMF. However, in the solid state, both bulk powder and doped film, there was an obvious difference between the two molecules. In doped film, **Mol-1**

was blue shifted to 454 nm compared to 484 nm in DMF solution, while **Mol-2** had red shift to 528 nm from 495 nm. In bulk powder, both molecules showed about 8 nm blue shift compared to the doped film, **Mol-1** emitted at 446 nm and **Mol-2** emitted at 519 nm. These changes of emission maxima in solution and solid state could be explained by different conformations impacting the inter and intramolecular interactions

As shown in Table 4.2.4.3.1, from **Mol-0** to **Mol-2**, the PLQYs in anhydrous DMF solution decreased from 58% to 45%. However, **Mol-0** was non-emissive in solid state, and the PLQYs of **Mol-1** and **Mol-2** in 10 wt% PMMA doped film decreased dramatically to 8% and 7%, respectively.

From the Table 4.2.4.2.1, in an inert atmosphere, **Mol-1** had the longest lifetime of the group in DMF, and the first component contributed the most. **Mol-2** also had three components, but these were much shorter than **Mol-1**. Compared with the solutions, **Mol-1** and **Mol-2** both had longer lifetime in doped film and bulk powder, especially in powder state. These two molecules made similar contributions to each component.

After **Mol-1** and **Mol-2** were doped in 10 wt% PMMA film, their radiative decay rate constant and non-radiative decay rate constant both decreased. In particular, the radiative decay rate constant of **Mol-1** decreased from $4.54*10^7$ s^{-1} to $0.17*10^7 s^{-1}$. Even though its non-radiative decay rate also reduced to $2.00*10^7 s^{-1}$, its PLQY dropped to 8% in PMMA film. A similar situation occurred with **Mol-2**.

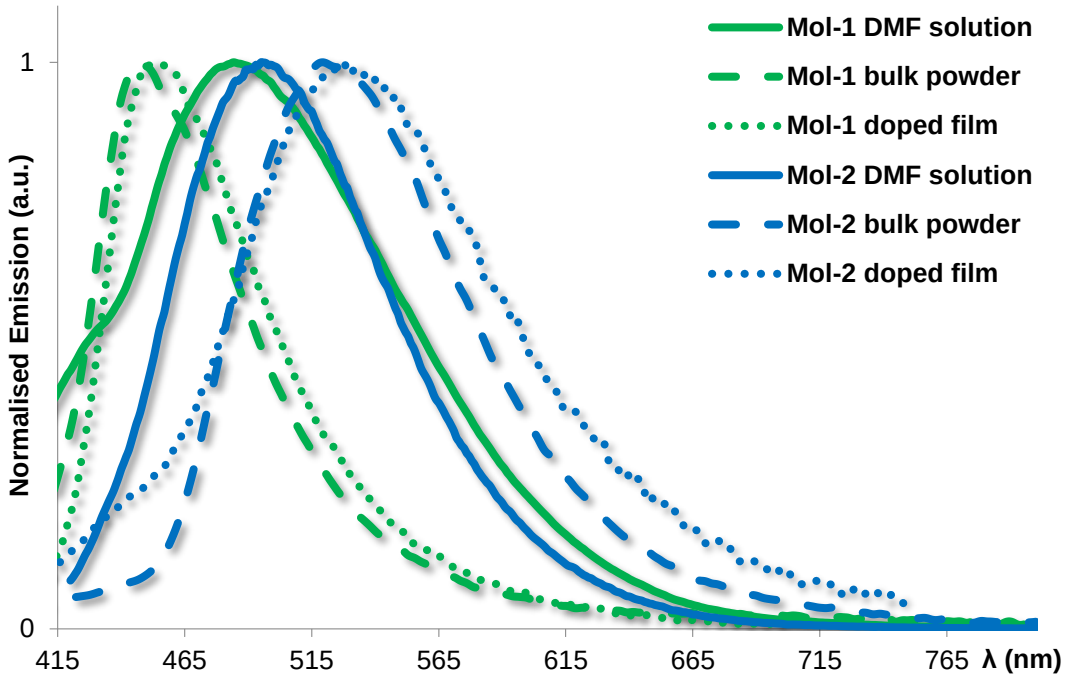

Figure 4.2.4.3.1 Normalized emission spectra of **Mo-1** to **Mol-2** on different states (λ_{ex}= 370 nm)

Table 4.2.4.3.1 Photophysical data of **Mo-0** to **Mol-2** in different media

		Mol-0[1]	**Mol-1**	**Mol-2**
Anhydrous (DMF, 298K, N_2) [a]	Emission λ_{PL}/nm	479	484	495
	Lifetime τ_{PL}/ns	4 (0.99), 10 (0.01)	4 (0.83), 10 (0.12), 121 (0.05)	2 (0.31), 4 (0.44), 9 (0.24)
	PLQY (%) [a,d]	58	48	45
	k_r /10^7s^{-1} [f]	14.50	4.54	9.91
	k_{nr} /10^7s^{-1} [g]	10.50	4.91	12.11
Doped film (298K, vacuum) [b,c]	Emission λ_{PL}/nm	-	454	528
	Lifetime τ_{PL}/ns	-	7 (0.46), 30 (0.35), 169 (0.19)	6 (0.48), 18 (0.42), 146 (0.1)
	PLQY /% [a,e]	-	8	7
	k_r /10^7s^{-1} [f]		0.17	0.67
	k_{nr} /10^7s^{-1} [g]		2.00	8.90
Bulk powder (298K, vacuum) [b]	Emission λ_{PL}/nm	-	446	519
	Lifetime τ_{PL}/ns	-	15 (0.22), 295 (0.19), 1917 (0.59)	28 (0.28), 314 (0.25), 2462 (0.46)

[a] Measurements in degassed anhydrous DMF at 298 K, λ_{ex}= 370 nm. [b] Measurements in high vacuum at 298 K. [c] 10 wt% of emitter doped in PMMA spin-coated on quartz from DMF solution. [d] Quinine sulfate employed as the external reference (Φ_{PL} = 54.6% in 0.5 M H_2SO_4 at 298 K).[85] [e] Doped thin film values were measured using an integrating sphere under N_2. [f] $k_r=\Phi/\tau$. [g] $k_{nr}=1/\tau-k_r$.

[1] **Mol-0** was non-emissive on solid state

4.2.4.4 Variable temperature photophysical measurements

Variable temperature measurements of **Mol-1** and **Mol-2** were also taken in doped film with the aid of a cryostat in order to explore the nature of the emission: phosphorescence or TADF, considering the oxygen sensitivity to the emission previously observed. For fluorescent materials, with the decreasing of temperature, their emission wavelengths would not have any shift and would show similarly short lifetimes (~10 ns) to those at room temperature.[10] Phosphorescent molecules would have enhanced emission intensity under inert atmosphere and low temperature.[11] Also, the lifetime of phosphorescent material is much longer than that of fluorescent, from microseconds to milliseconds.[10,151] Compared with these two mechanisms, TADF molecules would have a decreased lifetime and red-shift emission with the decreasing temperature because of the arrested RISC.[12] This phenomenon could be explained by its emission mechanism (Figure 4.2.4.4.1). Generally, RISC can happen in TADF molecules at room temperature (298K), but this process is relatively slow compared to fluorescence. That is the reason why TADF materials have short prompt component and a long decay up to microseconds.[12] However, under 77K, the RISC will be turned off, from the data, only fluorescent lifetime exists.

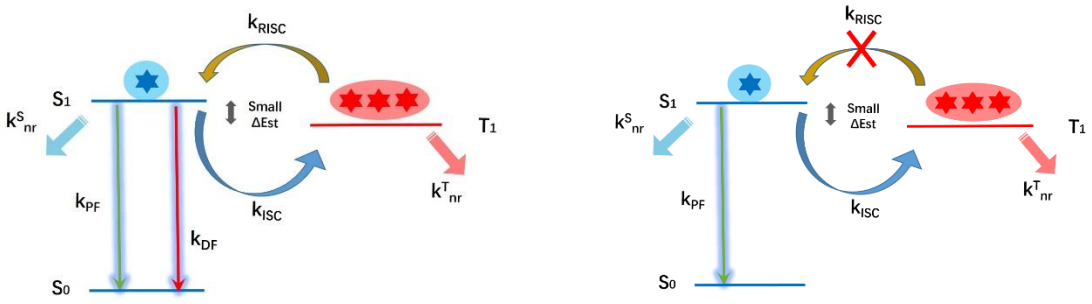

Figure 4.2.4.4.1 Emission mechanism of TADF at 298K and 77K (Left: room temperature; Right: 77K. T_1 = Triplet state; S_1 = singlet state; S_0 = ground state; PF = prompt fluorescence; DF = delayed fluorescence; ISC = intersystem crossing; RISC = reverse intersystem crossing; ΔE_{ST} = the energy difference between the first excited singlet and triplet states; nr = nonradiative.)

In the measured emission spectra (Figure 4.2.4.4.2), there was no shift after the cooling down of the system from room temperature to 77K. Also, the lifetime of **Mol-1** (Figure 4.2.4.4.3) and **Mol-2** (Figure 4.2.4.4.4) were the same during the cooling process. The phenomenon showed neither molecule had TADF properties, and according to the scales of their lifetimes, **Mol-1** and **Mol-2** both emitted fluorescence.

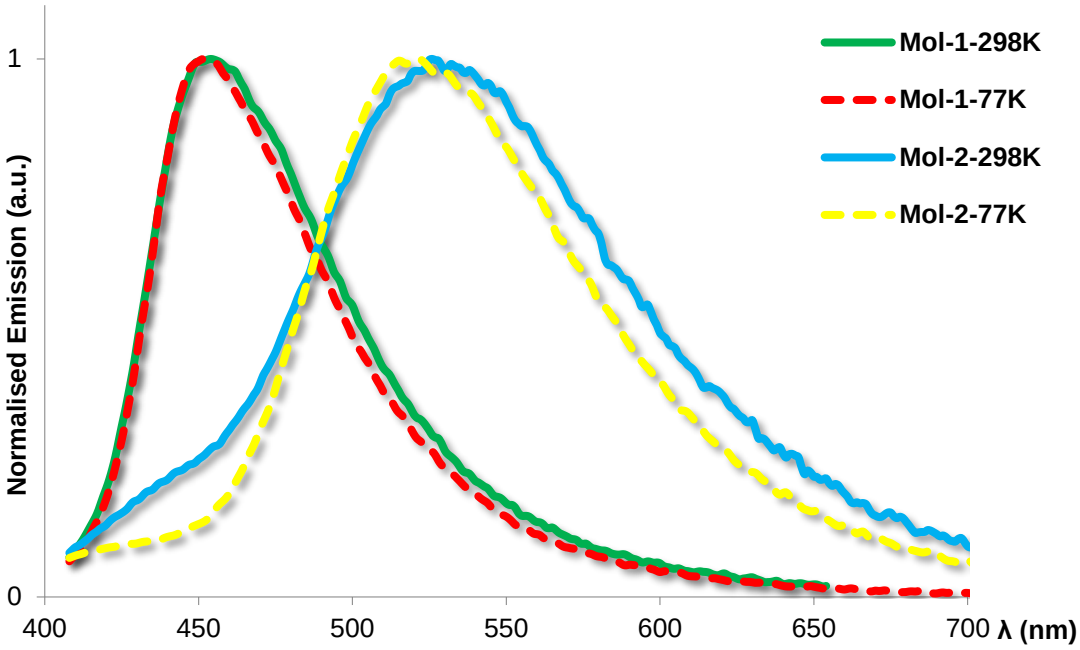

Figure 4.2.4.4.2 Normalized emission spectra of **Mol-1** and **Mol-2** at 298 K and 77 K (10 wt% PMMA doped film) (λ_{ex}= 370 nm)

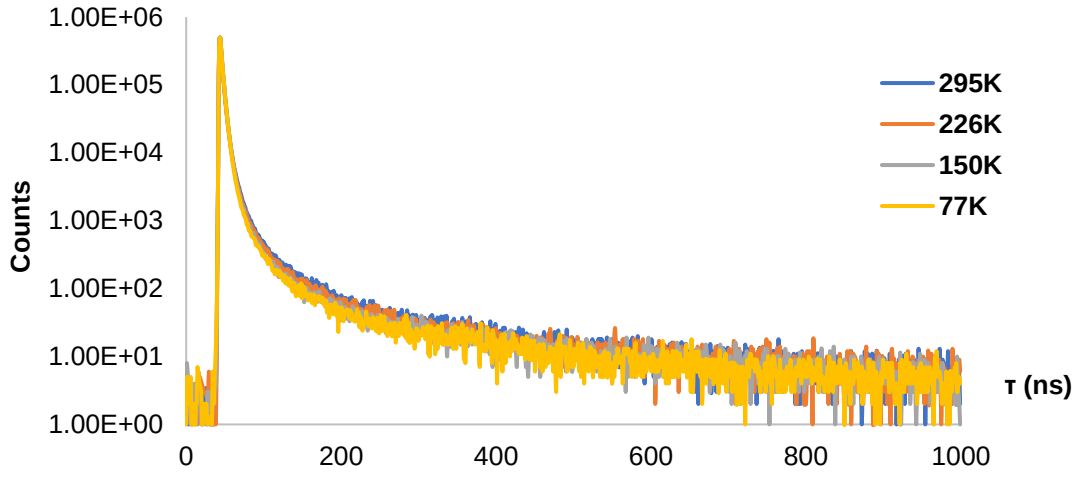

Figure 4.2.4.4.3 Time-resolved spectra of **Mol-1** (in 10 wt% PMMA doped film)

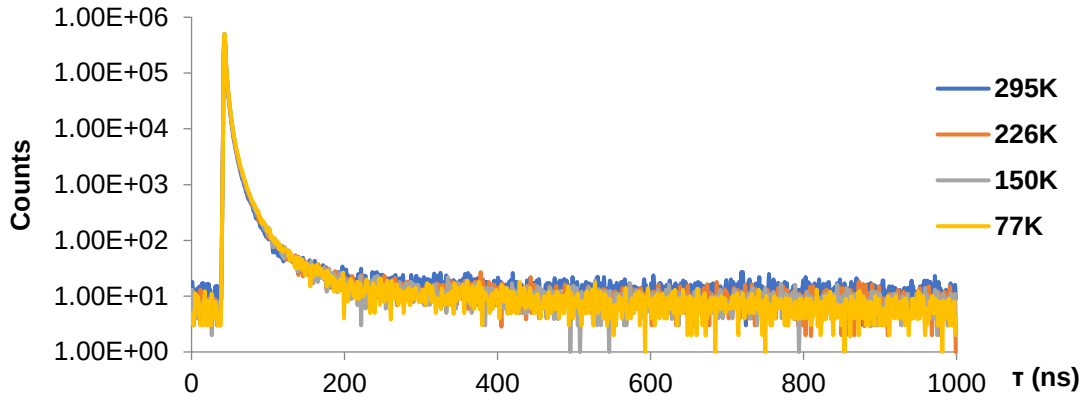

Figure 4.2.4.4.4 Time-resolved spectra of **MoI-2** (in 10 wt% PMMA doped film)

4.3. Potential applications for ion recognition in aqueous solution

Schiff-base macrocycles have potential for metal ion coordination because they have uncoordinated N atoms that can act as donors to coordinate the metal.[130] The coordination ability could be used for metal ion recognition in solvents by measuring the change of the photophysical properties. In general, UV-vis absorbance spectroscopy was used as the main method for testing the ion probes.[130,54] Emission spectroscopy has not been used as widely as UV absorbance because the material needs to be luminescent.

Aqueous systems are the most common and valuable systems in both ionic analysis and biological detection. It is meaningful to design and synthesize low toxicity and high sensitivity probes for ionic and biological recognition in water. A lot of compounds have been published for ion recognition in aqueous solution (Figure 4.3.1, **107**, **108**, **109**).[152,153,154] Most Schiff-base macrocycles have good solubility in high polarity solvents, such as MeOH and MeCN, and these have been favoured as solvents for ion sensing measurements.[130,54,4] However, because of their poor solubility in water, they are seldom applied in aqueous systems.[155].

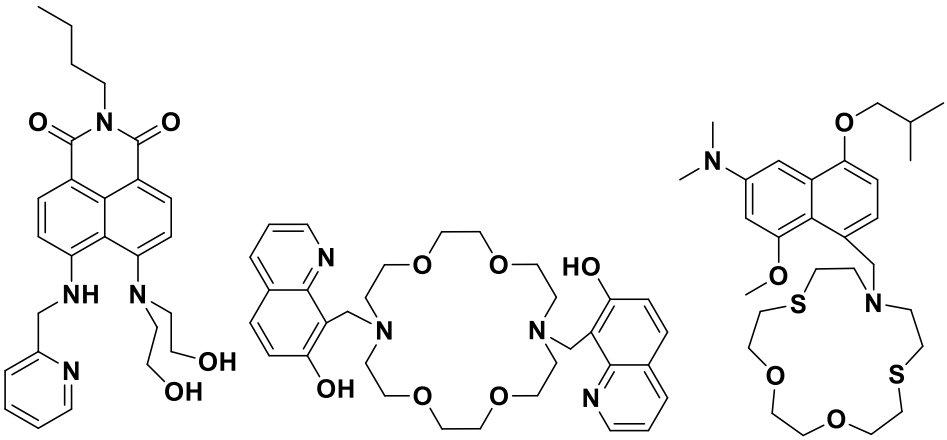

107 **108** **109**

Figure 4.3.1 Ionic probes in aqueous solution (**107**[152] has selectivity to Cu (II), **108**[153] has selectivity to Hg (II), and **109**[154] has selectivity to Ag (I))

Fe (III) plays an important role in human health and growth. Most probes have a characteristic response to heavy metals such as Pb (II) and rare earth

ions.[137,138] A considerable number of siderophores have been published (**110**, **111**, **112**, Figure 4.3.2)[156,157,158], but there are only a few examples using luminescent compounds as sensors. In 2008, Su et al. published a water-soluble polymer (**113**, Figure 4.3.3) as luminescent probe for Fe (III) recognition.[159] The polymer **113** had emission at 518 nm in aqueous solution with a PLQY at 61%. With the addition of metal salt solution, the emission of **113** was quenched, and its relative emission intensity (I/I_0, I represented the emission intensity with salt solution, and I_0 was the initial emission intensity of **113** in solution) showed linear behaviour relative to the logarithm of the concentration of Fe (III) (R^2=0.9827). Another example is the compound **114** (Figure 4.3.3) published by Zheng in 2014.[54] This luminescent Schiff-base macrocycle had emission at 595 nm as a suspension in THF:H2O=1:9 (v/v) system. The emission of this macrocycle could be quenched by Cu (II), and its emission intensity had highly linear correlation to the logarithm of concentration of Fe (III). Even though **Mac-1** to **Mac-3** had poor solubility in all solvents including DMF and DMSO, their aqueous suspensions showed a promising response to Fe (III), and could be quantified according to the change in emission intensities. Two steps were used in metal ion recognition experiments: 1) recognition sensitivity with highly diluted ion solutions; 2) ingredient ion concentration for quantification.

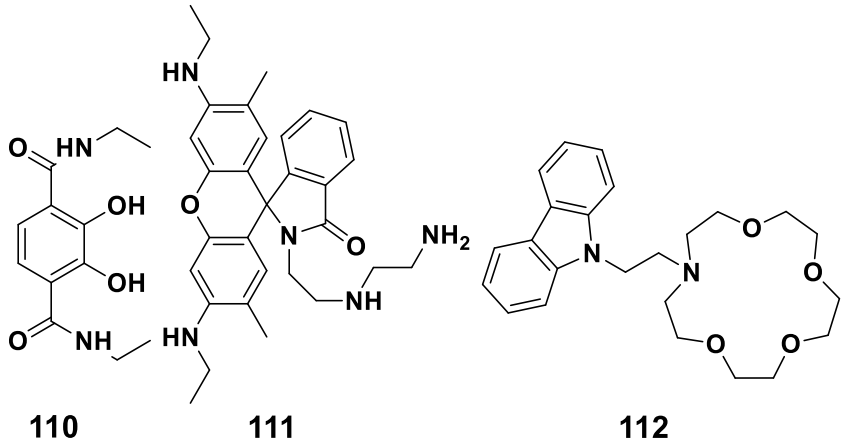

Figure 4.3.2 Published siderophores (**110**, **111**, and **112**)in aqueous solution[156-158]

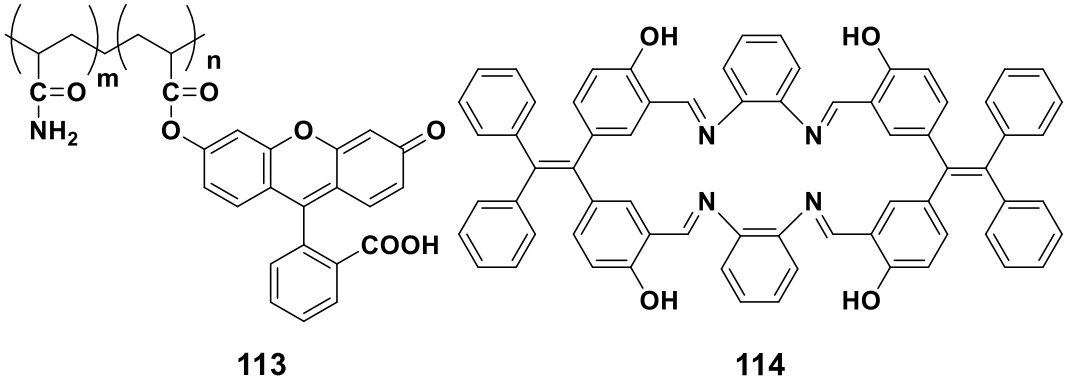

Figure 4.3.3 Luminescent ferric probes applied in aqueous solution[54,159] (water soluble polymer(**113**), and Schiff-base macrocycles (**114**))

4.3.1 Selection of ions

Five metal salts were selected to prepare for standard aqueous solutions, including: $FeCl_3$, $CoCl_2$, $AgNO_3$, $ZnCl_2$, and $CdCl_2$. In order to make the

comparison controllable, all samples were chloride salt with good solubility in water, except Ag (I), and the metal cations had close atomic radius as Fe (III). These solutions had the same concentration as 0.01M in water, and were added to cuvettes with a 10-100 μL micropipette.

Because **Mac-0** did not emit as an aqueous suspension, it could not be used as an emission-based metal ion detector. **Mac-1**, **Mac-2** and **Mac-3** were prepared as aqueous suspensions with theoretical concentration of $1*10^{-4}$M. 2 mL Macrocycle suspension (2 equiv.) was added to the cuvette with 2 mL water and 10 μL standard metal solution (1 equiv.). The mixture was shaken to keep the suspension, steady state and time resolved emission spectra were used to evaluate the recognition process. 2 mL Macrocycle suspension with 2 mL water in the cuvette was used as a template for the blank experiment.

In Figure 4.3.1.1, the emission spectra of the **Mac-1** suspension and its metal salt solution mixtures had similar profiles. Because of the heterogeneous system, the emission spectra had greater noise than the results obtained in homogeneous systems. In addition, there were only minor changes in emission wavelengths, regardless of metal ion additive. It could therefore be concluded that the emission wavelength was not be affected by the addition of metal ions.

All the measurements for ion recognition were processed in air. Because of the high oxygen content in water, all samples of **Mac-1** had very short lifetimes of 5 ns, and no interaction was caused by the metals (Table 4.3.1.1).

As well as emission wavelength and lifetime, emission intensity was an important parameter to be observed. From the spectra (Figure 4.3.1.1), it could be observed that Fe (III) sample had decreased intensity compared with the blank sample. In **Mac-1** system, $FeCl_3$ was used for further measurements with ingredient concentrations to explore the quantification relationship between the emission intensities and the concentrations of Fe (III).

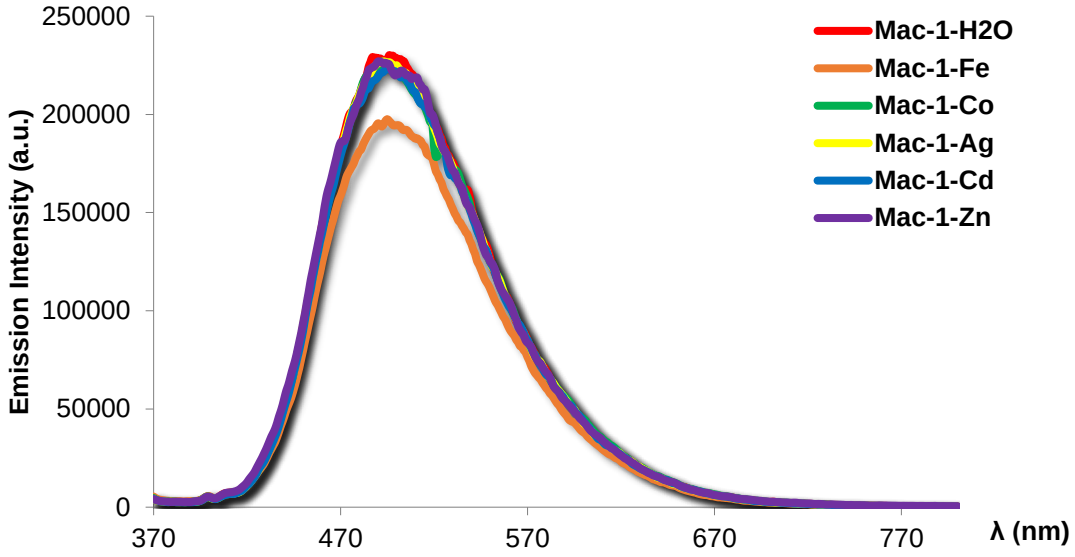

Figure 4.3.1.1 Emission spectra of **Mac-1** suspension with metal salt solutions (Air, at 298K. The theoretic concentration of **Mac-1** was $5*10^{-5}$ M, and the concentration of metal salt was $2.5*10^{-5}$ M in aqueous solution. 2mL **Mac-1** suspension, 2mL H_2O and 10 μL metal salt solution were contained in each cuvette. λ_{ex}= 370 nm)

Table 4.3.1.1 Photophysical data of **Mac-1** suspension with metal salt solutions

Mac-1	H_2O [a,b]	$FeCl_3$ [a,b,c]	$CoCl_2$ [a,b,c]	$AgNO_3$ [a,b,c]	$CdCl_2$ [a,b,c]	$ZnCl_2$ [a,b,c]
Emission λ_{PL}/nm	496	495	496	493	495	490
Lifetime τ_{PL}/ns[d]	5	5	5	5	5	5
Emission intensity	230144	197545	225535	226966	223894	226971

[a] Measurements in air at 298K. [b] Aqueous suspension with theoretic concentration as $5*10^{-5}$ M. [c] Aqueous solution containing metal salt as $2.5*10^{-5}$ M. [d] Lifetime was measured in aqueous solution with 10μL standard metal salt solution.

Mac-2 behaved similarly, but the emission wavelengths of samples located around 484 nm (Figure 4.3.1.2) and their lifetimes were as long as 12 ns (Table 4.3.1.2). By comparing the changes of emission intensities, it was observed that Fe (III), Co (II), and Zn (II) had similar decreased emission intensity, so Mac-2 did not have specific recognition of Fe (III) in aqueous solution system.

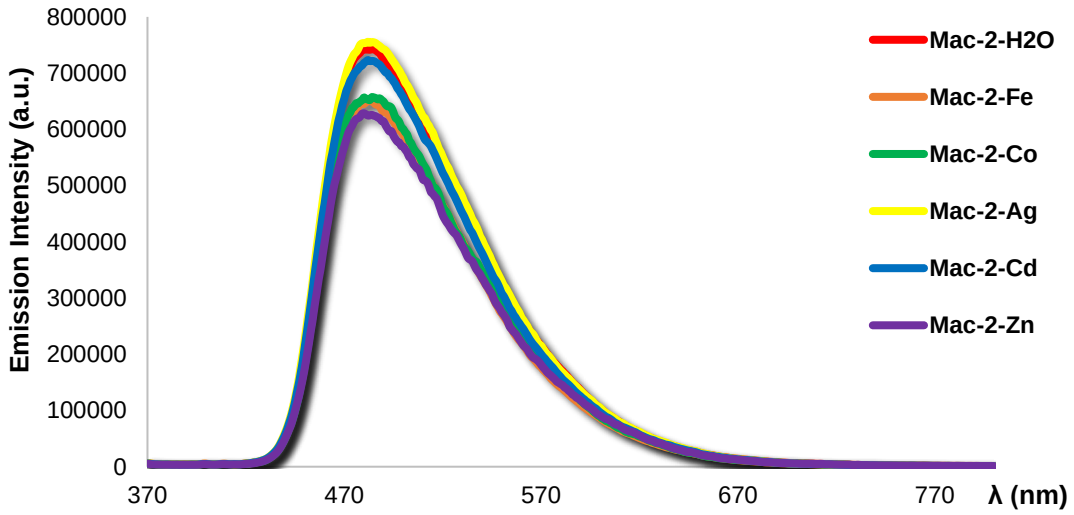

Figure 4.3.1.2 Emission spectra of **Mac-2** suspension with metal salt solutions (Air, at 298K. The theoretic concentration of **Mac-2** was $5*10^{-5}$ M, and the concentration of metal salt was $2.5*10^{-5}$ M in aqueous solution. 2mL **Mac-2** suspension, 2mL H_2O and 10 μL metal salt solution were contained in each cuvette. λ_{ex}= 370 nm)

Table 4.3.1.2 Photophysical data of **Mac-2** suspension with metal salt solutions

Mac-2	H_2O [a,b]	$FeCl_3$ [a,b,c]	$CoCl_2$ [a,b,c]	$AgNO_3$ [a,b,c]	$CdCl_2$ [a,b,c]	$ZnCl_2$ [a,b,c]
Emission λ_{PL}/nm	484	483	484	482	482	480
Lifetime τ_{PL}/ns [d]	12	11	12	11	12	11
Emission intensity	742430	651922	708486	755662	723160	661960

[a] Measurements in air at 298K, λ_{ex}= 370 nm. [b] Aqueous suspension with theoretic concentration as $5*10^{-5}$ M. [c] Aqueous solution containing metal salt as $2.5*10^{-5}$ M. [d] Lifetime was measured in aqueous solution with 10μL standard metal salt solution.

Compared with **Mac-2**, **Mac-3** had a red shift to 505 nm in aqueous suspension (Figure 4.3.1.3). In the **Mac-3** group, all samples emitted as the blank sample at around 505 nm (Table 4.3.1.3). Their lifetimes were the longest compared with **Mac-1** and **Mac-2** groups, up to about 20 ns. Because Zn (II) and Fe (III) decreased the emission intensity of **Mac-3** the most within the group, these two metal cations were used for ingredient concentration experiments.

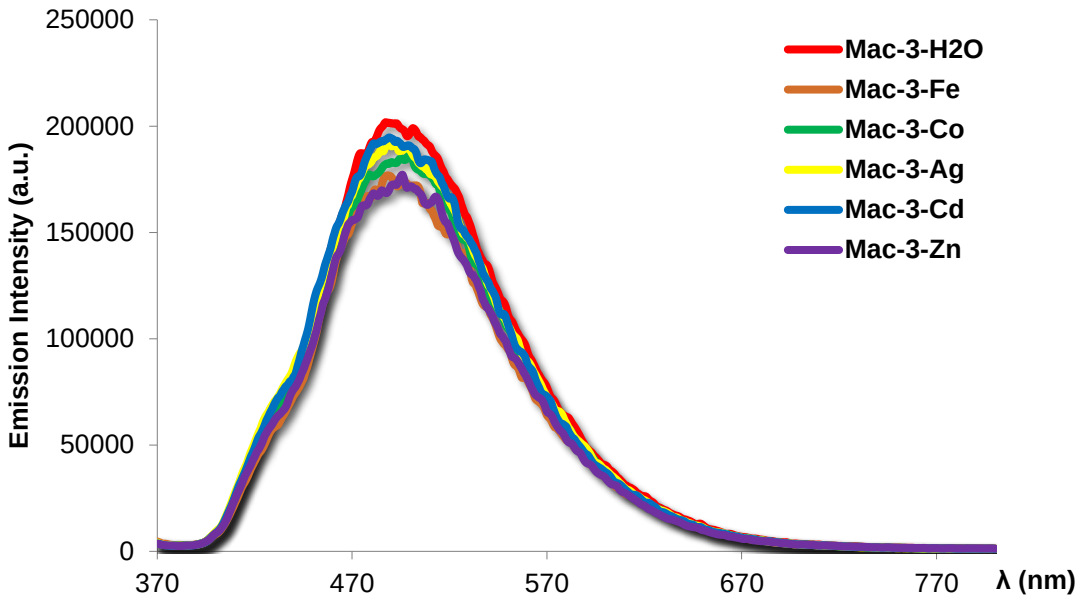

Figure 4.3.1.3 Emission spectra of **Mac-3** suspension with metal salt solutions (Air, at 298K. The theoretic concentration of **Mac-3** was $5*10^{-5}$ M, and the concentration of metal salt was $2.5*10^{-5}$ M in aqueous solution. 2mL **Mac-3** suspension, 2mL H_2O and 10 μL metal salt solution were contained in each cuvette. λ_{ex}= 370 nm)

Table 4.3.1.3 Photophysical data of **Mac-3** suspension with metal salt solutions

Mac-3	H_2O [a,b]	$FeCl_3$ [a,b,c]	$CoCl_2$ [a,b,c]	$AgNO_3$ [a,b,c]	$CdCl_2$ [a,b,c]	$ZnCl_2$ [a,b,c]
Emission λ_{PL}/nm	487	488	489	488	489	493
Lifetime τ_{PL}/ns [d]	17	18	20	18	22	18
Emission intensity	201765	176799	182219	193464	194677	172500

[a] Measurements in air at 298K, λ_{ex}= 370 nm. [b] Aqueous suspension with theoretic concentration as $5*10^{-5}$ M. [c] Aqueous solution containing metal salt as $2.5*10^{-5}$ M. [d] Lifetime was measured in aqueous solution with 10μL standard metal salt solution.

4.3.2 Change of emission intensity with gradient concentration

Mac-1 and **Mac-3** were both prepared as aqueous suspensions with a theoretical concentration of $1*10^{-4}$ M. The standard metal salt solution was prepared as 0.01 M. For each sample, 2 mL suspension and 2 mL H_2O were mixed and transferred to one cuvette. The standard metal salt solutions were added with ingredient amounts of 10 μL, 20 μL, 40 μL, and 80 μL for each sample and their emission spectra were scanned.

For **Mac-1**, with the addition of $FeCl_3$ solution, the emission intensities decreased dramatically by more than 50000 a.u. (Figure 4.3.2.1). The correlation between the logarithmic concentrations of Fe (III) and emission intensities at 495nm was linear, and its R^2 was as high as 0.98 (Figure 4.3.2.2).

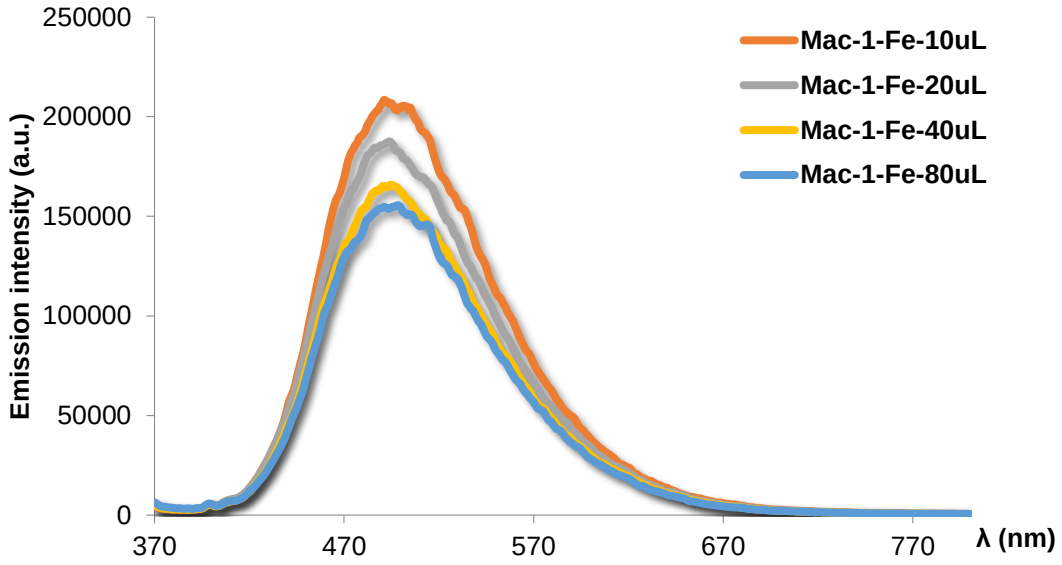

Figure 4.3.2.1 Emission spectra of **Mac-1** suspension with $FeCl_3$ solution in gradient concentrations (Air, at 298K. The theoretic concentration of **Mac-1** was $5*10^{-5}$ M, and the concentration of metal salt was $2.5*10^{-5}$ M in aqueous solution. 2mL **Mac-1** suspension and 2mL H_2O were contained in each cuvette with the gradual addition of metal salt solution. λ_{ex}= 370 nm)

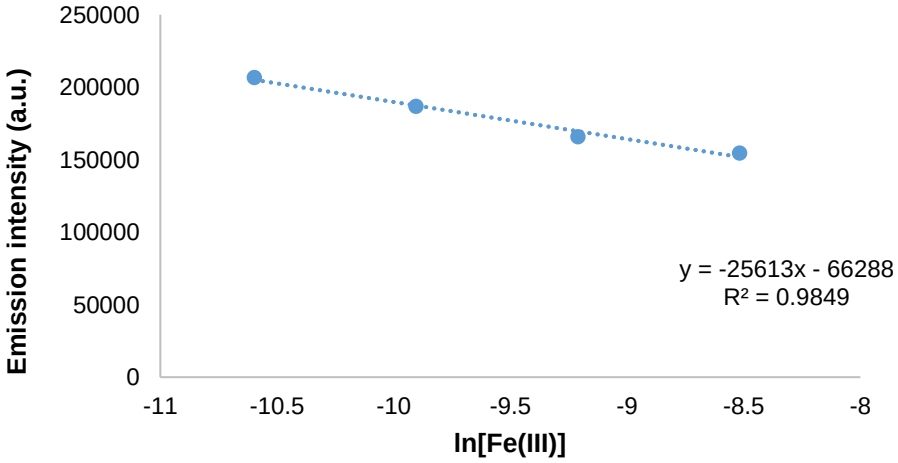

Figure 4.3.2.2 Correlation between the emission intensity of **Mac-1** (λ=495 nm) and the logarithmic concentrations of metal cation (ln[Fe(III)]) in aqueous solution.[54]

In the **Mac-3** group, the emission intensities decreased apparently with the addition of Fe^{3+} and Zn^{2+} (Figure 4.3.1.3). Both metal salt solutions were added gradually to explore the quantitative relations between the emission intensities and the concentrations of metal cations.

Fe (III) samples showed strongly quenched emissions, and the emission intensities of **Mac-3** suspensions decreased from 150000 a.u. to 102600 a.u. (Figure 4.3.2.3). The big change in intensity showed its high sensitivity. The correlation of **Mac-3** was linear with R^2 as 0.99 (Figure 4.3.2.4). The emission spectra for suspension were not as smooth as those for solution, and the emission intensities at 488nm were chosen for quantization.

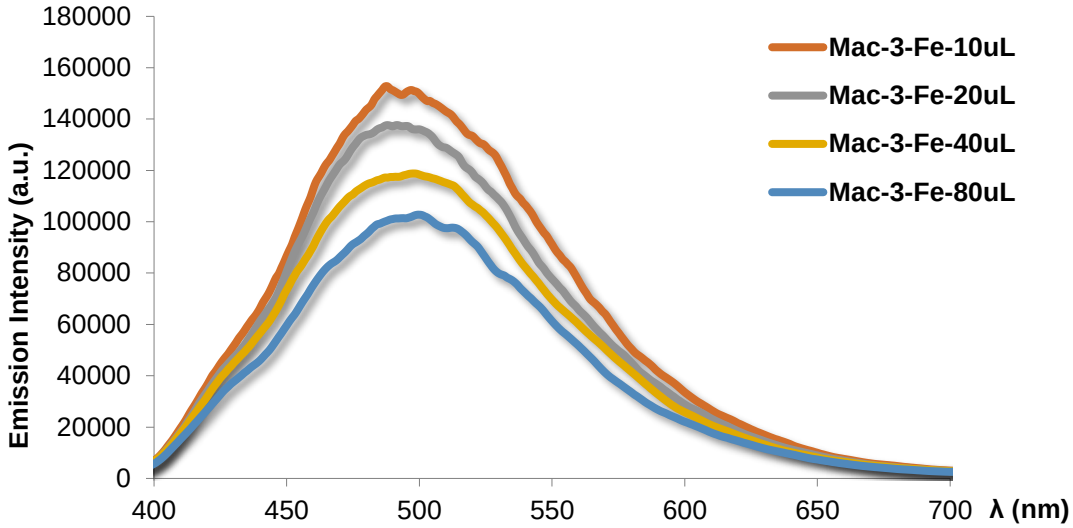

Figure 4.3.2.3 Emission spectra of **Mac-3** suspension with $FeCl_3$ solution in gradient concentrations (Air, at 298K. The theoretic concentration of **Mac-3** was $5*10^{-5}$ M, and the concentration of metal salt was $2.5*10^{-5}$ M in aqueous solution. 2mL **Mac-3** suspension and 2mL H_2O were contained in each cuvette with the gradual addition of metal salt solution. λ_{ex}= 370 nm)

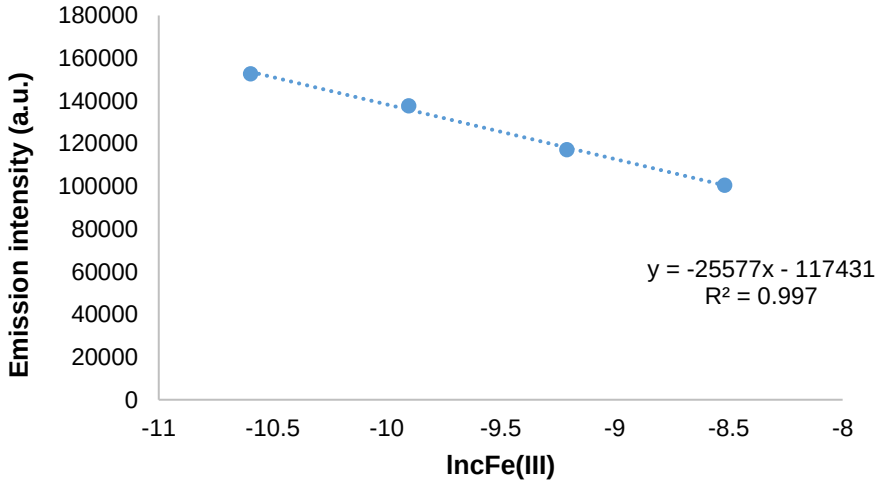

Figure 4.3.2.4 Correlation between the emission intensities of **Mac-3** (λ=488 nm) and the logarithmic concentrations of metal cation (ln[Fe(III)]) in aqueous solution.

The Zn (II) recognition of **Mac-3** showed decreased sensitivity after the addition of one equivalent of salt solution (Figure 4.3.2.5). Even though the emission intensities still decreased, the correlation between the emission intensities and the logarithmic concentrations of Zn (II) in solution was not as good as the group of Fe (III) (Figure 4.3.2.6).

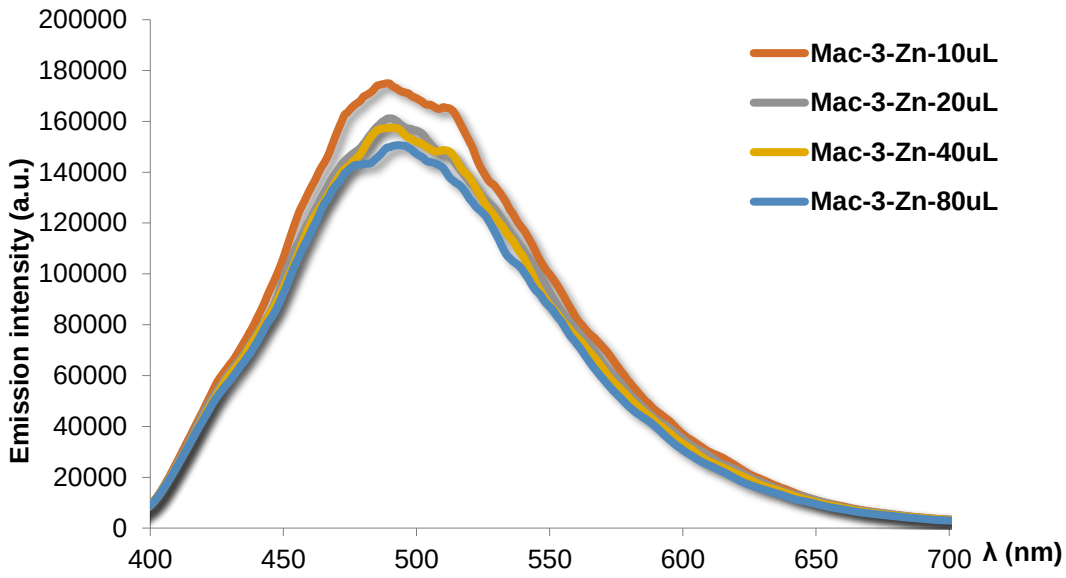

Figure 4.3.2.5 Emission spectra of **Mac-3** suspension with $ZnCl_2$ solution in gradient concentrations (Air, at 298K. The theoretic concentration of **Mac-3** was $5*10^{-5}$ M, and the concentration of metal salt was $2.5*10^{-5}$ M in aqueous solution. 2mL **Mac-3** suspension and 2mL H_2O were contained in each cuvette with the gradual addition of metal salt solution. λ_{ex}= 370 nm)

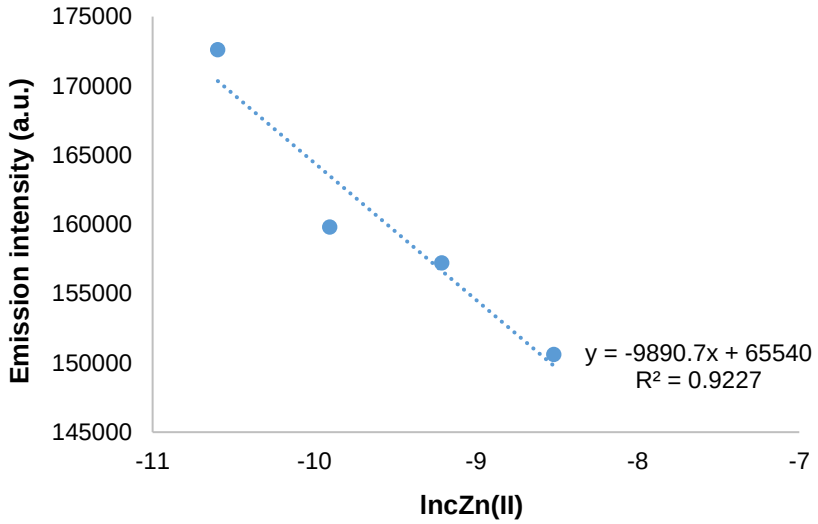

Figure 4.3.2.6 Correlation between the emission intensities of **Mac-3** (λ=493 nm) and the logarithmic concentrations of metal cation (ln[Zn(II)]) in aqueous solution.

Mol-1 and **Mol-2** were used as the blank experiments with ingredient $FeCl_3$ solution. In Figure 4.3.2.7 and Figure 4.3.2.8, both **Mol-1** and **Mol-2** had increased emission intensity with 1.0 equivalent of Fe (III). However, with the addition of more $FeCl_3$ solution (> 1 equiv.), their emission intensities decreased.

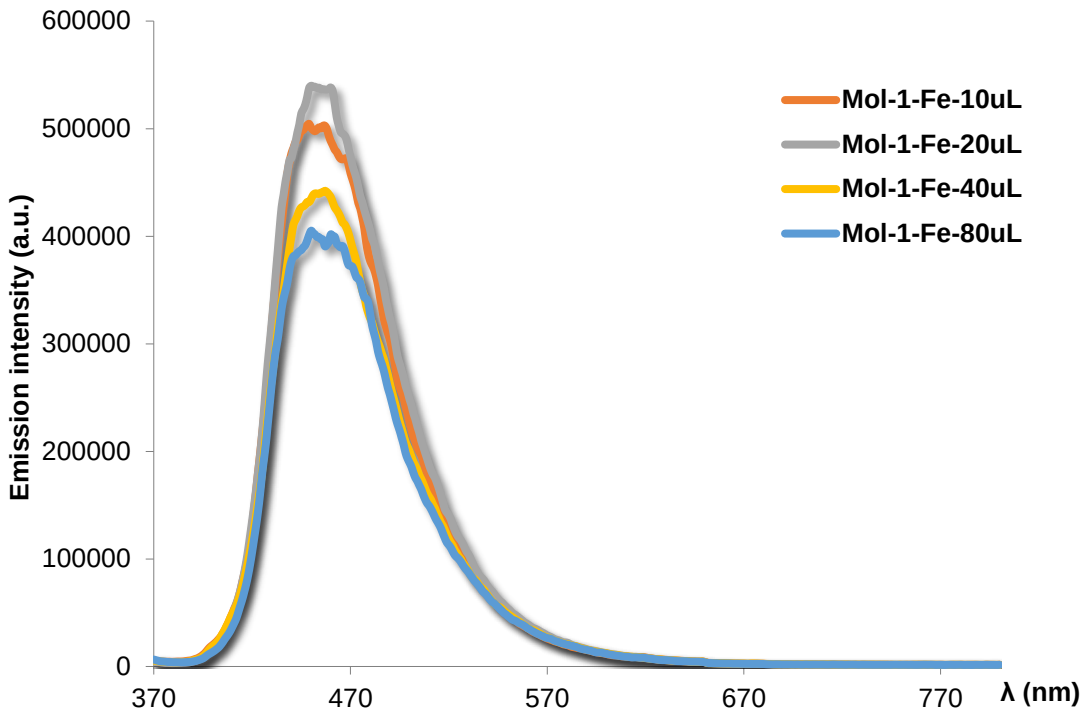

Figure 4.3.2.7 Emission spectra of **Mol-1** suspension with $FeCl_3$ solution in gradient concentrations (Air, at 298K. The theoretic concentration of **Mol-1** was $5*10^{-5}$ M, and the concentration of metal salt was $2.5*10^{-5}$ M in aqueous solution. 2mL **Mol-1** suspension and 2mL H_2O were contained in each cuvette with the gradual addition of metal salt solution. λ_{ex}= 370 nm)

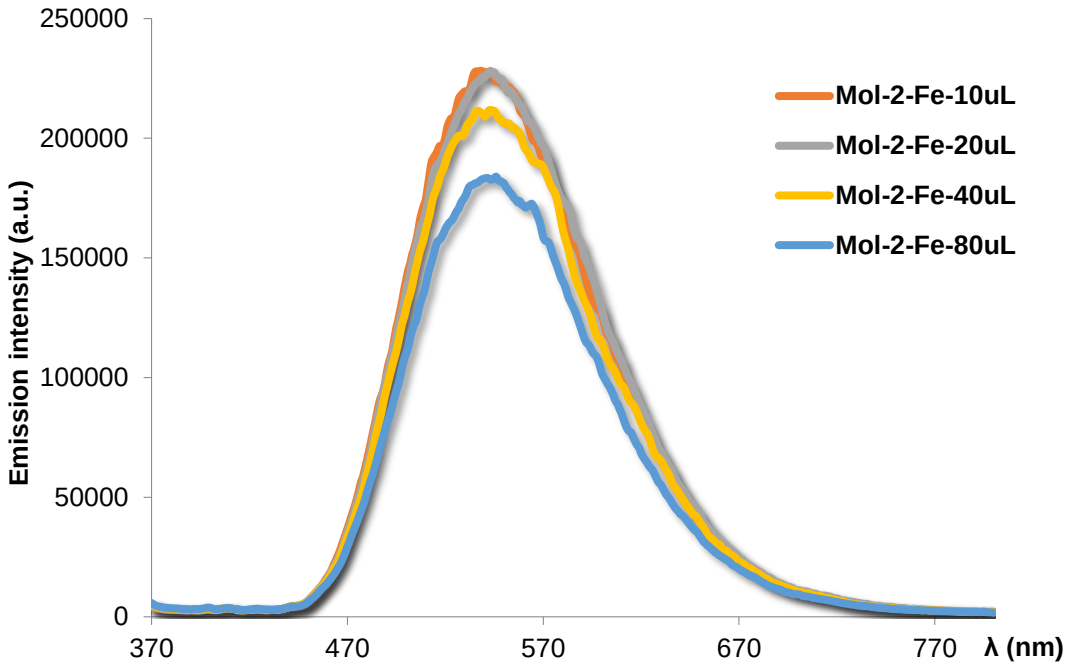

Figure 4.3.2.8 Emission spectra of **Mol-2** suspension with $FeCl_3$ solution in gradient concentrations (Air, at 298K. The theoretic concentration of **Mol-2** was $5*10^{-5}$ M, and the concentration of metal salt was $2.5*10^{-5}$ M in aqueous solution. 2mL **Mol-2** suspension and 2mL H_2O were contained in each cuvette with the gradual addition of metal salt solution. λ_{ex}= 370 nm)

4.4 Conclusion

In this project, a group of dialdehyde modified carbazole-based emitters and corresponding macrocycles were synthesized. Their photophysical properties were measured in different media, including DMF solutions, PMMA doped films and bulk powder. Different *N*-donors were used to regulate the nature of

emission properties. Their emission wavelengths and lifetimes were different in solution and solid state

By changing the length of linking alkyl chains within the diamine, the macrocycle properties were also adjusted, especially in the solid state. The longer linking alkyls between carbazoles blue-shifted the emission and the macrocycle showed relatively shorter lifetime.

By analysing the emission spectra after the addition of different metal salts, **Mac-1** and **Mac-3** showed specific recognitions of Fe (III). More importantly, with the change in concentrations of metal salts, the emission intensities of these macrocycle suspensions decreased exponentially. By comparing with examples from the literature, **Mac-1** and **Mac-3** showed medium sensitivity to Fe (III) in aqueous solution system,[159,160] and relatively high sensitivity within probes used in heterogeneous systems. [54,136] Also, the emission intensities of both **Mac-1** and **Mac-3** showed high linear correlation with the logarithm of concentration of Fe (III) (Figure 4.3.2.2 and Figure 4.3.2.4), which matched the reported titration curves.[54,159] The concentration of Fe (III) can be obtained by calculating the change of emission intensity. A Stern-Volmer analysis will be carried out for further information about their quenching mechanism. If these

macrocycles form a non-emissive Fe (III) complex, the Stern-Volmer plot will be linear, and its slope will decrease when the system is warmed. On the contrary, the slope of Stern-Volmer will increase in heated environment if the luminescent emitters are quenched by collision with Fe (III) in solution. From the different phenomenon, the quenching mechanism between these macrocycles and Fe (III) can be investigated.

Apart from the recognition of Fe (III) in aqueous solutions, these macrocyles will also be researched on detecting toxic metal cations such as Hg (II), Pd (II) etc. Also, these macrocycles have strong π-π stacking in aggregative state, which resulted their poor solubility in most solvents. However, with the supporting of their cavity structure and solvent-thermal synthetic method, these macrocyclic structures are expected to be porous. The gas absorption experiments can be tried to provide the volume of space in these structures. Because they are luminescent materials, it is also interesting to explore how their photophysical properties will be affected by the gas absorption and potential applications on gas pressure sensing.

Chapter 5 Overall Conclusions

With the developing of society, luminescent materials are playing more and more important roles in research area and our daily lives. Compared with the past materials, the new luminescent materials are expected to be more efficient, more colourful, lighter, rollable, etc. The OLEDs can be qualified. Organometallic complexes containing heavy metals such as Ir, Pt, Ru et al. came into the view firstly. These complexes improved the theoretical IQEs of OLED devices to 100% compared with 25% of traditional fluorescent molecules. However, the usage of precious metals limited their applications because of the high cost and toxicity of heavy metals. This problem was solved with the development of TADF molecules, which are small pure organic molecules with low price and toxicity but 100% theoretical IQEs as iTMCs. However, the self-quenching between emitters is a serious barrier limiting the improvement of PLQYs of both iTMCs and TADF molecules.

Supramolecular chemistry has been researched for decades, but still attracts giant attentions because it builds well-defined structures as designed in micro-scale. Also, the mature synthetic route of supramolecules can be applied in industrial producing. In terms of luminescent materials, the supramolecular system makes it possible to research the interactions of emitters within a designed framework. In this thesis, how the photophysical properties of

luminescent molecules were affected by the inter and intramolecular interactions have been discussed, as well as their applications in other areas.

Some luminescent supramolecular systems have been published but still rare, especially for Ir (III) complexes based structures. Two supramolecular systems of Ir (III) complexes have been reported in this thesis built by intramolecular interactions (Chapter 2) and coordination bonds (Chapter 3). Their photophysical properties were measured and compared with luminescent building blocks to explore the effects of self-assembling.

In the Chapter 2, iridium complexes with terminal adamantyls were assembled with CDVs. Their photophysical properties were measured both in MeCN and PB 7.4. Compared with the initial molecules, the supramolecular systems exhibited higher emission intensities and limited changes of emission wavelengths. In other word, their emission colours were kept and PLQYs were improved as being expected. With the help of CDVs, the supramolecular system can be uptaken by cells and aggregated in perinuclear regions with relatively strong emission as bio-imaging probes. It also provides an idea of decorating highly emitting hydrophobic molecules for better luminescent biological probes.

In the Chapter 3, a triangle crown supramolecular cage was built by the iridium complexes and Pd (II) through coordination bonds. This supramolecular system exhibited red-shift emission wavelength compared with its building scaffold. However, its PLQY did not improved because of the quenching by Pd (II) which also acted as the Lewis acid. Even though the extended metalloligand did not provide satisfied results, it represented a different configuration to the published cages which were built from similar metalloligand and reported by our group. By comparing these two systems, it can be confirmed: 1) the increased distance between Ir (III) and Pd (II) did not reduce the quenching brought by Pd (II) linkers; 2) the linearly extended ligand was not enough to build enlarged supramolecular systems without modifying corresponding angles; 3) the similar metallo-coordination cages can be set up by the ligands with similar structures and metal cation linkers with similar coordination configurations. Also, the host-guest experiments will be tried to encapsule small luminescent molecules and explore their interactions in the future.

In the Chapter 4, the synthesis of a group of pure organic luminescent molecules and their corresponding Schiff-base macrocycles were reported. Because of their poor solubility in any common solvent, their structures were characterized by FT-IR, MS and EA. Their photophsyical properties were also measured to verify if them have TADF properties. Even though them did not exhibit desirable properties as TADF materials, their photophysics were

researched in both solution and solid states to explore the effects of condensation, intra and inter molecular interactions. Also, some macrocycles (**Mac-1** and **Mac-3** in Chapter 4) showed specific recognitions of Fe (III) in aqueous solution. Their further applications on toxic metal cation (Hg (II) and Pb (II)) recognitions and gas absorption experiments will be tried in the future.

From the projects in this thesis, three different supramolecular systems were researched, especially focusing on the change of their photophysical properties. By comparing the results and related literatures in the Chapter 1, we can predict that weak interactions such as hydrogen bonds and Von der Waal's force can be better choices to reduce the self-quenching between emitters because they can minimize the effects of the distribution of electrons in molecules and separate the emitters. In comparison, coordination bonds and covalent bonds localize chromophores firmly, but the induction force was also conducted, such as the quenching effect brought by heavy metals in metallo-coordination cages.

From these projects, we can only obtain some primary predictions, but they enriched the examples of luminescent supramolecular systems. With further research, the theory in this area will be completed gradually and provide efficient guidance for designing luminescent supramolecules with better photophysical properties.

Experimental section

General synthetic procedures

Commercial chemicals were used as supplied. All reactions using Schleck flasks were in an inert (N_2) atmosphere with reagent grade solvents. Purification of all compounds was carried out in air. Freshly distilled anhydrous THF was obtained from a Pure Solv^{TM} solvent purification system. Silica gel (Silia-P from Silicycle, 60 Å, 40–63 μm) was used to fill the flash column chromatography. Analytical thin layer chromatography (TLC) was performed with silica plates with aluminum backings (250 μm with indicator F-254). ^{1}H, ^{13}C, ^{19}F NMR, 2D-COSY, 2D-HSQC, 2D-HMBC, ^{1}H-DOSY spectra were recorded on a Bruker Advance spectrometer. Abbreviations have been used to represent multiplet assignments: “s” for singlet, “d” for doublet, “t” for triplet, “m” for multiplet and “br” for broad. Deuterated solvents were used for recording. Melting points (Mp) were recorded using open-end capillaries on an Electrothermal melting point apparatus IA9200 and are uncorrected. FT-IR was measured on a Perkin Elmer Spectrum GX IR spectrometer in air as powder. High-resolution mass spectra were recorded at the EPSRC UK National Mass Spectrometry Facility at Swansea University. Elemental analyses were performed by Mr. Stephen Boyer, London Metropolitan University.

Ligand synthesis

2-(2,4-difluorophenyl)pyridine (67)

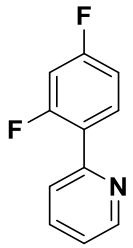

2-bromopyridine (0.62 g, 3.92 mmol, 1 equiv.), (2,4-difluorophenyl)boronic acid (0.86 g, 5.45 mmol, 1.4 equiv.), potassium carbonate (3.25 g, 23.52 mmol, 6 equiv.) were added to a 100 mL round-bottom flask containing 60 mL of a mixture of THF and distilled water (4:1 v/v). The mixture was degassed by N_2 for 15 minutes, and $Pd(PPh_3)_4$ (0.24 g, 5%mol) was added to the flask under positive nitrogen pressure. The mixture was refluxed in a nitrogen atmosphere overnight and then cooled to room temperature. The solvent was removed and the precipitate was extracted by dichloromethane and distilled water for three times. The organic fractions were combined, washed with brine and dried over magnesium sulfate. Filtration and evaporation under reduced pressure gave the crude product. The crude product was purified by flash column chromatography (silica, Hexane: ethyl acetate= 10:1) to produce the pure compound as a light yellow liquid. **Yield**: 75%. **Rf**: 0.48 (10% EA/Hexane) **^{1}H NMR (400 MHz, Chloroform-*d*) δ (ppm)** 8.73 (dt, *J* = 4.8, 1.4 Hz, 1H), 8.02 (td, *J* = 8.8, 6.7 Hz, 1H), 7.80 – 7.75 (m, 2H), 7.31 – 7.25 (m, 1H), 7.03 (tdd, *J* = 7.8, 2.6, 1.0 Hz, 1H), 6.94 (ddd, *J* = 11.3, 8.8, 2.5 Hz, 1H). **^{13}C NMR (126 MHz,**

Chloroform-*d*) δ (ppm) 164.18 (d, *J* = 12.1 Hz), 162.19 (d, *J* = 12.1 Hz), 161.56 (d, *J* = 11.9 Hz), 152.55, 149.79, 136.50, 132.14, 124.28, 122.45, 111.90 (d, *J* = 24.7 Hz), 105.82 – 102.45 (m). **^{19}F NMR (471 MHz, Chloroform-*d*) δ (ppm)** -109.33, -113.03. The characterization matched that previously reported.[161]

2-chloro-4-mesitylpyridine (**88'**)

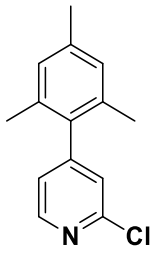

2-Chloro-4-iodopyridine (1.0 g, 4.18 mmol, 1 equiv.), 2,4,6-trimethylphenyl boronic acid (1.0 g, 6.28 mmol, 1.5 equiv.), potassium carbonate (1.75 g, 12.7 mmol, 3 equiv.) were added to a 100mL round-bottom flask containing a 30 mL mixture of 1,4-dioxane and distilled water (4:1 v/v). The mixture was degassed by N_2 for 15 minutes, and $Pd(PPh_3)_4$ (0.24 g, 5%mol) was added to the flask under positive nitrogen pressure. The mixture was refluxed in a nitrogen atmosphere for 48 h and then cooled to room temperature. The solvent was removed, and the residue was extracted using DCM and distilled water for three times. The organic fractions were combined, washed with brine and dried over magnesium sulfate. Filtration and evaporation under reduced pressure gave the crude product. The crude product was purified by flash column chromatography (silica, Hexane: ethyl acetate= 25:1) to give the pure compound as a colourless oil. **Yield**: 62%. **Rf**: 0.4 (20% EA/Hexane) **^{1}H NMR**

(300 MHz, Chloroform-*d*) δ (ppm) 8.47 (dd, *J* = 5.0, 0.8 Hz, 1H), 7.18 (dd, *J* = 1.4, 0.7 Hz, 1H), 7.07 (dd, *J* = 5.0, 1.4 Hz, 1H), 6.98 (s, 2H), 2.36 (s, 3H), 2.03 (s, *J* = 0.7 Hz, 6H). The characterization matches that previously reported.[76]

4-mesityl-2-phenylpyridine (**88**)

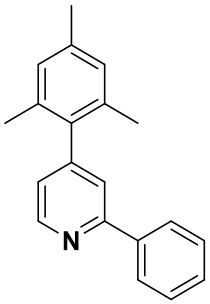

2-Chloro-4-(2,4,6-trimethylphenyl)pyridine (**88'**, 0.6 g, 2.59 mmol, 1 equiv.), phenyl boronic acid (0.5 g, 4.10 mmol, 1.5 equiv.), potassium carbonate (1.1 g, 7.77 mmol, 3 equiv.) were added to a 100mL round-bottom flask containing a 20 mL mixture of 1,2-dimethoxyethane and distilled water (4 : 1 v/v). The reaction mixture was degassed by N_2 for 15 minutes, and $Pd(PPh_3)_4$ (0.05 g, 5% mol) was added to the flask under positive nitrogen pressure. The mixture was refluxed in a nitrogen atmosphere overnight and then cooled to room temperature. The solvent was removed and the precipitate was extracted three times with DCM and water. The organic fractions were combined, washed with a portion of brine and dried over $MgSO_4$. Filtration and evaporation under reduced pressure gave the crude product. The crude product was purified by flash column chromatography (silica, hexane/ethyl acetate gradient 10:1) to give the pure compound as a colourless oil. **Yield**: 49%. **Rf**: 0.38 (10%

EA/Hexane) **^{1}H NMR (400 MHz, Chloroform-*d*) δ (ppm)** 8.77 (dd, *J* = 4.9, 0.9 Hz, 1H), 8.08 – 8.01 (m, 2H), 7.59 (dd, *J* = 1.6, 0.9 Hz, 1H), 7.54 – 7.42 (m, 3H), 7.08 (dd, *J* = 4.9, 1.5 Hz, 1H), 7.01 (dd, *J* = 1.4, 0.7 Hz, 2H), 2.38 (s, 3H), 2.07 (s, 6H). The characterization matched that previously reported.[76]

4-methyl-4'-(4-(trimethylsilyl)but-3-yn-1-yl)-2,2'-bipyridine (**66'**)

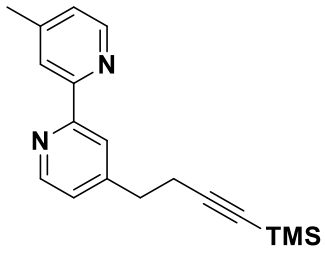

All flasks have to be dried and this reaction was conducted in nitrogen. 4,4'-dimethyl-2,2'-bipyridine (0.46 g, 2.52 mmol, 1 equiv.) was dissolved in dry THF (25 ml) and cooled to -78 ^{o}C for 15 minutes (using dry ice and acetone bath). Another flask containing 5 mL THF and distilled diisopropylamine (0.43 ml, 3.1 mmol, 1.2 equiv.) was cooled to -78 ^{o}C, and *n*-butyllithium (1.58 ml, 2.5 M, 2.54 mmol, 1 equiv.) was added dropwise stirring for 15 minutes to prepare the lithium diisopropylamide (LDA). The freshly prepared LDA solution was added dropwise via a cannula to the THF solution of 4,4'-dimethyl-2,2-bipyridine, and the solution was stirred for 1h. The (3-bromoprop-1-yn-1-yl)trimethylsilane (0.50 mL, 3.53 mmol, 1.4 equiv.) was dissolved in THF (3 mL), cooled to -78^{o}C and added dropwise via a cannula to the 4,4'-dimethyl-2,2-bipyridine solution. The solution was stirred at this temperature for 0.5 h before being allowed to warm up to room temperature, and then stirred overnight. The mixture was

poured into distilled water and extracted three times with DCM. The organic layer was collected and dried with Na_2SO_4, Filtration and evaporation under reduced pressure gave the crude product. The crude product was purified by column chromatography (silica, Hexane/ethyl acetate= 6:1) to give the title product as a colourless oil that solidified upon standing. **Yield**: 50%. **Rf**: 0.38 (30% EA/Hexane on silica). **^{1}H NMR (500 MHz, Chloroform-*d*) (ppm)** δ 8.56 (d, *J* = 15.0 Hz, 2H), 8.27 (d, *J* = 16.3 Hz, 2H), 7.24 – 7.10 (m, 2H), 3.01 – 2.84 (m, 2H), 2.60 (t, *J* = 7.3 Hz, 2H), 2.46 (s, 3H), 0.13 (s, 9H).

4-(but-3-yn-1-yl)-4'-methyl-2,2'-bipyridine (**66**)

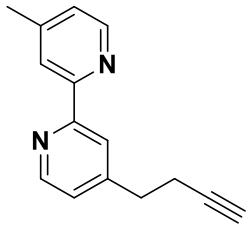

Methanol (20 mL) was added to a 100mL flask containing K_2CO_3 (0.6 g, 4.34 mmol, 5.4 equiv.) and 4-methyl-4'-(4-(trimethylsilyl)but-3-yn-1-yl)-2,2'-bipyridine (**66'**, 0.24 g, 0.80 mmol, 1equiv.). This solution was stirred for 4 h at room temperature. DCM and water were used for three times extraction after removing the methanol. The organic fractions were combined, washed with a portion of brine and dried over Na_2SO_4. Filtration and evaporation under reduced pressure gave the crude product. This solid was kept in vacuum for 1 h to remove remaining TMS and obtain a white solid. **Yield**: 90%. **^{1}H NMR (300 MHz, Chloroform-*d*) δ (ppm)** 8.59 (dd, *J* = 17.3, 5.0 Hz, 2H), 8.27 (d, *J* = 9.7

Hz, 2H), 7.20 (dd, *J* = 21.2, 5.0 Hz, 2H), 2.96 (t, *J* = 7.4 Hz, 2H), 2.61 (td, *J* = 7.4, 2.6 Hz, 2H), 2.47 (s, 3H), 2.02 (t, *J* = 2.6 Hz, 1H). **^{13}C NMR (126 MHz, Methylene Chloride-d_2) δ (ppm)** 156.21, 155.77, 150.10, 149.01, 148.83, 148.11, 124.67, 123.82, 121.72, 120.90, 82.99, 69.16, 34.13, 20.97, 19.31. **HR-MS** (NSI^+): **$[M+H]^+$ Calculated**: ($C_{15}H_{14}N_2H$): 223.1235; **Found**: 223.1230.

4,4'-bis(4-(trimethylsilyl)but-3-yn-1-yl)-2,2'-bipyridine (**70**)

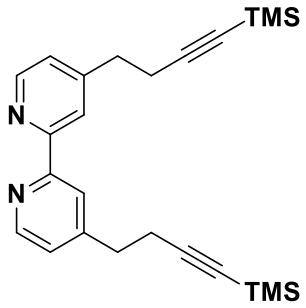

All flasks must be dried, and this reaction was conducted under nitrogen. 4,4'-dimethyl-2,2'-bipyridine (0.43 g, 2.31 mmol, 1 equiv.) was dissolved in dry 25mL dry THF and cooled to -78 ^oC for 15 minutes (in a dry ice and acetone bath). LDA was prepared in another flask containing 5 mL THF and distilled diisopropylamine (1.16 ml, 8.36 mmol, 3.6 equiv.) at -78 ^oC. The *n*-butyllithium (3.44 ml, 1.6 M, 5.50 mmol, 2.4 equiv.) was then added dropwise and stirred for 15minutes to prepare the LDA. The freshly prepared LDA solution was transferred slowly via cannula to the THF solution of 4,4'-dimethyl-2,2-bipyridine. The mixture was stirred for 1 hour. The (3-bromoprop-1-yn-1-yl)trimethylsilane (0.92 mL, 6.47 mmol, 2.8 equiv.) was dissolved in THF (3 mL), cooled to -78 ^oC and added dropwise via a cannula to the 4,4'-dimethyl-2,2-

bipyridine solution. The solution was stirred at -78^{o}C for 0.5 hours before it was allowed to warm up to RT and stirred overnight. The mixture was poured into distilled water and three times extractions with DCM were carried out. The organic layer was collected and dried by Na_2SO_4. The solvent was removed to produce the crude product. The crude product was then purified by column chromatography (silica, Hexane/ethyl acetate= 10:1) to give the target product as a white solid. **Yield**: 61%. **Rf**: 0.57 (5% MeOH/DCM on silica). **Mp**: 102.1-102.8 ^{o}C. **^{1}H NMR (500 MHz, Chloroform-*d*) δ (ppm)** 8.60 (d, *J* = 5.6 Hz, 2H), 8.31 (s, 2H), 7.22 (dd, *J* = 5.0, 1.7 Hz, 2H), 2.93 (t, *J* = 7.3 Hz, 4H), 2.61 (t, *J* = 7.3 Hz, 4H), 0.14 (s, 18H). **^{13}C NMR (126 MHz, Chloroform-*d*) δ (ppm)** 156.12, 150.33, 149.00, 124.10, 121.37, 105.50, 86.15, 34.39, 21.08, 0.01. **HR-MS** (ASAP): **[M+H]$^{+}$ Calculated**: ($C_{24}H_{32}N_2Si_2H$): 405.2182; **Found**: 405.2183. The characterization matched that previously reported.[162] **Anal. Calcd.** for $C_{24}H_{32}N_2Si_2$: C, 71.23; H, 7.97; N, 6.92. Found: C, 69.98; H, 7.76; N, 6.91.

[2,2'-bipyridine] 1,1'-dioxide (**83**)

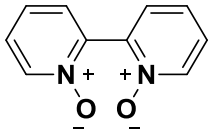

To a solution of 2,2'-bipyridine (15 g, 96.04 mmol, 1 equiv.) in glacial acetic acid (240 ml), H_2O_2 solution (60 mL, 30%, 773 mmol, 8 equiv.) was added in dropwise, and the mixture was heated to 75 ^{o}C. Another portion of 30% H_2O_2 (30 mL, 30%, 386 mmol, 4 equiv.) was added in a similar manner and the

mixture was stirred overnight at 75 ºC. Then the solution was poured into acetone (500 mL) and the white precipitate was collected by filtration and vacuum dried to obtain the crude product as a white powder (14.95g, Yield: 83%). Boiling water and acetone were used for the recrystallization to get the pure product. **Yield**: 73%. **^{1}H NMR (300 MHz, Deuterium Oxide) δ (ppm)** 8.38 – 8.32 (m, 2H), 7.73 (ddd, *J* = 8.4, 7.1, 1.3 Hz, 2H), 7.68 – 7.60 (m, 4H). The characterization matched that previously reported.[120]

4,4'-dinitro-[2,2'-bipyridine] 1,1'-dioxide (**84**)

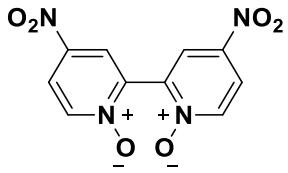

2,2'-bipyridine-1,1'-dioxide (**83**, 13.2 g, 70.2 mmol, 1 equiv.) was added to a 500 mL round-bottom flask. Concentrated sulfuric acid (86 ml, 98%, 1581 mmol, 22.5 equiv.) was added in drops while stirring. This procedure is exothermic and therefore the mixture was kept in an ice bath while sulfuric acid was added. After the addition of the sulfuric acid, the suspension was warmed to room temperature and stirring continued for 0.5 hours until all the 2,2'-bipyridine-1,1'-dioxide was dissolved. Concentrated nitric (36 mL, 70%, 568 mmol, 8 equiv.) acid was added dropwise to the sulfuric acid solution in the water bath. This solution was also stirred for 0.5 hours after being removed from the water bath and then heated to 100 ºC for 3 days. The mixture was poured into a conical flask containing trash ice after cooling to room temperature. Liquid nitrogen was

added to freeze the mixture. After warming the mixture to room temperature, a light yellow powder appeared, if not, more ice and liquid nitrogen needed to be added several times. The yellow precipitate was filtered and dried in vacuum. **Yield**: 50%. **Mp**: 250-255 °C. (lit., 277-278 °C).[163] **^{1}H NMR (500 MHz, DMSO-d_6) δ (ppm)** 8.70 (d, J = 3.2 Hz, 2H), 8.60 (d, J = 7.2 Hz, 2H), 8.38 (dd, J = 7.2, 3.3 Hz, 2H). **^{13}C NMR (126 MHz, DMSO-d_6) δ (ppm)** 142.59, 141.64, 140.93, 124.27, 122.41. The characterization matched that previously reported.[120,164]

4,4'-dibromo-[2,2'-bipyridine] 1,1'-dioxide (**85**)

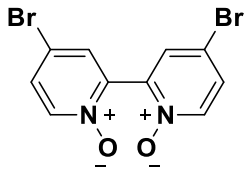

4,4'-dinitro-[2,2'-bipyridine] 1,1'-dioxide (**84**, 5 g, 18.0 mmol, 1 equiv.) was suspended in glacial acetic acid (80 mL, 99%). Acetyl bromide (52 mL, 702 mmol, 39 equiv.) was added dropwise and the suspension gradually became a solution. This solution was heated to 100°C for 8 hours in an inert atmosphere. After cooling to room temperature, the solution was poured onto plenty of trash ice. Saturated sodium hydroxide solution was used for neutralization to obtain a light brown suspension. The solid was filtered and mother liquid was extracted by DCM for three times. The organic layer was collected and evaporated to obtain a light brown solid. These two portions of solids were combined. **Yield**: 80.4%. **Mp**: 223-225 °C (lit., 227-230 °C).[163] **^{1}H NMR (400 MHz, DMSO-d_6) δ (ppm)** 8.31 (d, *J* = 7.0 Hz, 2H), 8.05 (d, *J* = 2.9 Hz, 2H), 7.80 (dd, *J* = 7.0, 2.9

Hz, 2H). Because of its poor solubility, ^{13}C NMR couldn't be obtained. The characterization matched that previously reported. [120]

4,4'-dibromo-2,2'-bipyridine (**86**)

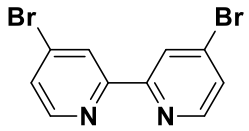

4,4'-dibromo-[2,2'-bipyridine] 1,1'-dioxide (**85**, 4.5 g, 13.0 mmol, 1 equiv.) was suspended in 125 mL MeCN. This suspension became gradually apparent with the addition of phosphorus tribromide (13 mL, 137 mmol, 10.5 equiv.) and the solution was heated to 90^{o}C for 4 hours under nitrogen protection before cooling to room temperature. The cooled solution was poured onto trash ice, and saturated sodium hydroxide was added to neutralize it. DCM was used to extract the neutralized solution for three times, and the organic layers were collected and evaporated to obtain the crude product. Boiling ethanol and water(v/v=1:1) were used to recrystallize and obtain the pure product. **Yield**: 91.8%. **Mp**: 138-139 ^{o}C (lit., 135-136 ^{o}C). **^{1}H NMR (300 MHz, Chloroform-*d*) δ (ppm)** 8.63 (dd, *J* = 2.0, 0.6 Hz, 2H), 8.51 (dd, *J* = 5.2, 0.6 Hz, 2H), 7.53 (dd, *J* = 5.2, 1.9 Hz, 2H). **^{13}C NMR (126 MHz, Chloroform-*d*) δ (ppm)** 155.99, 149.90, 134.07, 127.46, 124.83. The characterization matched that previously reported.[120]

4,4'-bis((trimethylsilyl)ethynyl)-2,2'-bipyridine (**87**)

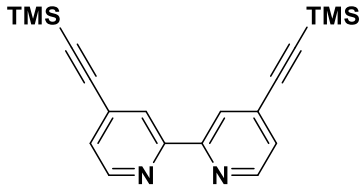

4,4'-dibromo-2,2'-bipyridine (**86**, 0.5 g, 1.59 mmol, 1 equiv.) was dissolved in dry THF (10 mL) and diisopropylamine (2.5 mL). This solution was degassed with nitrogen for 10 minutes before ethynyltrimethylsilane (1.13 mL, 7.95 mmol, 5 equiv.) was added, and degassed for a further 5 minutes. $Pd(PPh_3)_4$ (0.092 g, 5% mol) and CuI (0.030 g, 10% mol) were added to the solution before heating it to 70^{o}C, and kept overnight. After cooling to room temperature, the solvent was rotary evaporated and column chromatography (silica, Hexane: ethyl acetate=8:1) was used for purification. Fractions containing the desired product were combined and evaporated to produce a brown solid which was dried under vacuum. **Yield**: 66%. **Rf**: 0.59 (11% EA/Hexane) **Mp**: 95.0-96 ^{o}C. (lit., 119-121 ^{o}C)[165] **^{1}H NMR (500 MHz, Chloroform-*d*) δ (ppm)** 8.64 (dd, *J* = 4.9, 0.9 Hz, 2H), 8.45 (dd, *J* = 1.6, 0.9 Hz, 2H), 7.35 (dd, *J* = 5.0, 1.6 Hz, 2H), 0.29 (s, 18H). **^{13}C NMR (126 MHz, Chloroform-*d*) δ (ppm)** 155.52, 149.15, 132.30, 125.76, 123.58, 102.16, 100.06, -0.29. The characterization matched that previously reported.[165]

4,4'-bis(pyridin-4-ylethynyl)-2,2'-bipyridine (**82**)

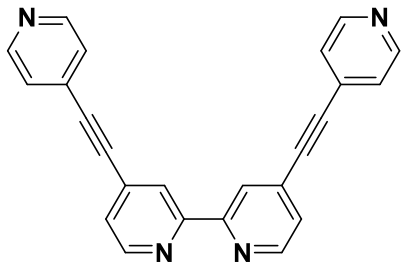

4,4'-bis((trimethylsilyl)ethynyl)-2,2'-bipyridine (**87,** 0.25 g, 0.72 mmol, 1 equiv.) was dissolved in dry THF (5 mL) and tetrabutylammonium fluoride (1.125g, 4.30 mmol, 6 equiv.). This solution was stirred for 0.5 hours before 4-bromopyridine hydrochloride (0.56 g, 2.87 mmol, 4 equiv.) and diisopropylamine (1.25 mL) were added. The mixture was degassed by nitrogen for 15 minutes, then $Pd(PPh_3)_4$ (60 mg, 7% mol) and CuI (22 mg, 15% mol) were added. This reaction was protected by nitrogen and kept at 70^{o}C overnight. TLC was used to monitor this reaction until all 4,4'-bis((trimethylsilyl)ethynyl)-2,2'-bipyridine had reacted. This mixture was dried by rotavapor and the residue was sonicated and washed carefully by water, ethyl acetate, DCM (cold), acetone (cold) and methanol (cold), respectively. The pure product was obtained as an off white solid. **Yield**: 42%. **Mp**: Became grey over 240 ^{o}C. **^{1}H NMR (500 MHz, DMSO-d_6) δ (ppm)** 8.83 (d, *J* = 5.4 Hz, 2H), 8.71 (d, *J* = 4.0 Hz, 4H), 8.55 (s, 2H), 7.75 – 7.70 (m, 2H), 7.66 (d, *J* = 5.9 Hz, 4H). Because of the poor solubility, ^{13}C NMR couldn't be obtained. **HR-MS** (NSI^{+}): **[M+H]$^{+}$ Calculated**: ($C_{24}H_{14}N_4H$): 359.1297; **Found**: 359.1292. **Anal. Calcd.** for $C_{24}H_{14}N_4$ + DMSO: C, 71.54; H, 4.62; N, 12.83. Found: C, 69.91; H, 3.45; N, 13.32. The characterization matched that previously reported.[96]

General procedure for the synthesis of $[(C\hat{}N)_2Ir]_2Cl_2$ dimers

The iridium(III) dimers, including $[(ppy)_2Ir(\mu\text{-}Cl)]_2$, $[(dFppy)_2Ir(\mu\text{-}Cl)]_2$ and $[(mesppy)_2Ir(\mu\text{-}Cl)]_2$, were synthesized according to the literature.[76] To a Schlenk tube containing $IrCl_3 \cdot 3H_2O$ (1.0 equiv.) and C^N ligand (2.2 equiv.) was added 2-ethoxyethanol to theoretically form 0.02M concentration. The suspension was degassed by N_2 for 10 minutes and heated to 120°C and stirred overnight before the solution was cooled and filtered to get a yellow powder. This powder was washed with water, hexane, and cold diethyl ether respectively, and it was dried under vacuum to afford a pure product.

Tetrakis(2-phenyl-pyridinato-N,C$^{2'}$)-bis(μ-chloro)-diiridium(III), $[Ir(ppy)_2(\mu\text{-}Cl)]_2$ (68)

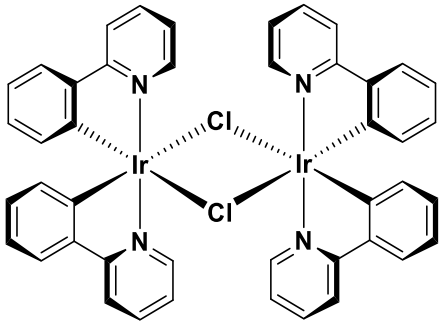

Yield: 77%. **^{1}H NMR (300 MHz, Methylene Chloride-d_2) δ (ppm)** 9.27 (ddd, *J* = 5.8, 1.6, 0.8 Hz, 4H), 7.99 – 7.94 (m, 4H), 7.85 – 7.78 (m, 4H), 7.58 (dd, *J* = 7.8, 1.4 Hz, 4H), 6.89 – 6.80 (m, 8H), 6.62 (td, *J* = 7.5, 1.4 Hz, 4H), 5.89 (dd, *J* = 7.8, 1.2 Hz, 4H). The characterisation matched that previously reported.[76]

Tetrakis[2-(4′,6′-difluorophenyl)-pyridinato-N,C$^{2'}$]-bis(μ-chloro)-diiridium(III), [Ir(dFppy)$_2$(μ-Cl)]$_2$ (69)

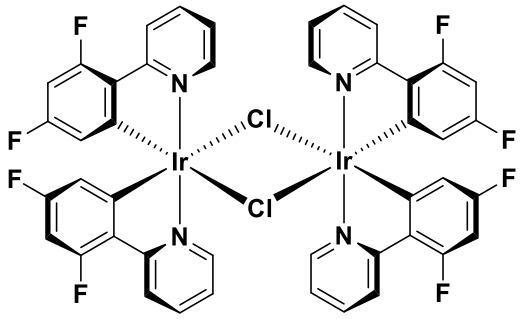

Yield: 91%. **^{1}H NMR (500 MHz, Chloroform-*d*) δ (ppm)** 9.14 (d, *J* = 5.3 Hz, 4H), 8.33 (d, *J* = 8.3 Hz, 4H), 7.85 (t, *J* = 7.6 Hz, 4H), 6.85 (t, *J* = 6.2 Hz, 4H), 6.36 (t, *J* = 11.6 Hz, 4H), 5.31 (d, *J* = 10.5 Hz, 4H). **^{19}F NMR (471 MHz, Chloroform-*d*) δ (ppm)** -107.72 (m), -110.30 (m). The characterization matched that previously reported.[76]

Tetrakis[4-(2,4,6-trimethylphenyl)-pyridinato-N,C$^{2'}$]-bis(μ-chloro)diiridium(III) [Ir(mesppy)$_2$-(μ-Cl)]$_2$ (89)

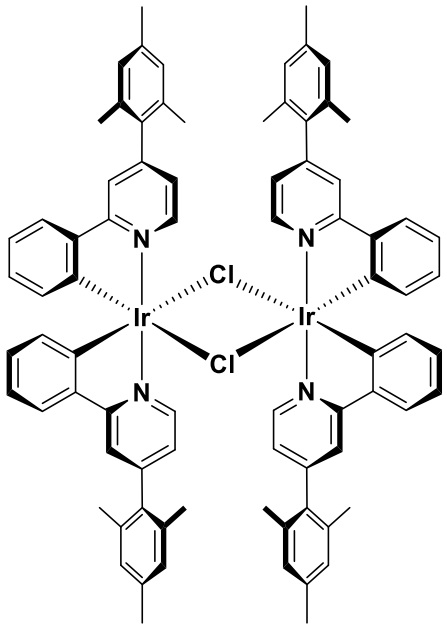

Yield: 65%. **^{1}H NMR (500 MHz, Methylene Chloride-d_2) δ (ppm)** 9.71 (d, *J* = 5.8 Hz, 4H), 7.78 (s, 4H), 7.54 (d, *J* = 7.5 Hz, 4H), 7.06 (d, *J* = 13.8 Hz, 8H), 6.86 (t, *J* = 6.5 Hz, 8H), 6.71 (t, *J* = 7.2 Hz, 4H), 5.95 (d, *J* = 7.8 Hz, 4H), 2.42 (s, 12H), 2.16 (d, *J* = 5.8 Hz, 24H). The characterisation matched that previously reported.[76]

General procedure for the synthesis of [Ir(C^N)$_2$(N^N)]Cl complexes

To a Schlenk tube containing [Ir(C^N)$_2$Cl]$_2$ (1.0 equiv.) and N^N ligand (2.5 equiv.) were added DCM and MeOH (v/v=2:1) to obtain 0.03M concentration. The reaction mixture was degassed by N_2 and the mixture was heated to 55°C overnight in an inert atmosphere. The solution was cooled to room temperature and then rotary evaporated to dryness. This residue was purified by flash column chromatography (silica, DCM/MeOH gradient 20:1 to 10:1). Fractions containing the desired complex were combined and this mixture was then evaporated to dryness, washed vigorously with distilled water and dried to afford a pure material as a chloride salt.

Iridium(III)bis(2-phenyl-pyridinato)-[4-(but-3-yn-1-yl)-4'-methyl-2,2'-bipyridine] Chloride, (Ir-1').

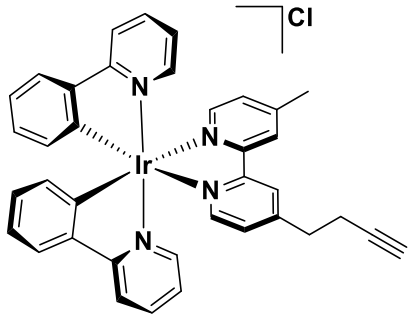

Yellow powder. **Yield**: 96%. **Rf**: 0.29 (5% MeOH/DCM on silica). Purified via flash chromatography (10% MeOH/DCM on silica) **^{1}H NMR (300 MHz, Methylene Chloride-d_2) δ (ppm)** 8.34 (d, *J* = 15.4 Hz, 2H), 7.98 (d, *J* = 8.3 Hz, 2H), 7.92 (d, *J* = 5.7 Hz, 1H), 7.88 – 7.71 (m, 5H), 7.52 (dd, *J* = 11.6, 5.8 Hz, 2H), 7.37 (d, *J* = 5.6 Hz, 1H), 7.27 (d, *J* = 5.8 Hz, 1H), 7.12 – 7.05 (m, 2H), 7.05 – 6.98 (m, 2H), 6.95 (td, *J* = 7.4, 1.3 Hz, 2H), 6.33 (dd, *J* = 7.6, 3.9 Hz, 2H), 3.07 (t, *J* = 6.9 Hz, 2H), 2.66 (td, *J* = 6.9, 2.7 Hz, 2H), 2.61 (s, 3H), 2.08 (t, *J* = 2.6 Hz, 1H). **^{13}C NMR (126 MHz, Methylene Chloride-d_2) δ (ppm)** 167.82, 156.06, 155.75, 154.03, 152.39, 150.73, 149.65, 149.42, 148.57, 148.50, 143.77, 137.95, 131.68, 131.63, 130.53, 128.71, 128.14, 126.92, 126.28, 124.78, 123.16, 122.41, 119.69, 33.74, 21.17, 18.86. **HR** (NSI^+) **MS: $[M-Cl]^+$ Calculated**: ($C_{37}H_{30}IrN_4$): 723.2100; **Found**: 723.2081.

Iridium(III)bis(2-phenyl-pyridinato)-[4,4'-bis(4-(trimethylsilyl)but-3-yn-1-yl)-2,2'-bipyridine]Cl (Ir-3')

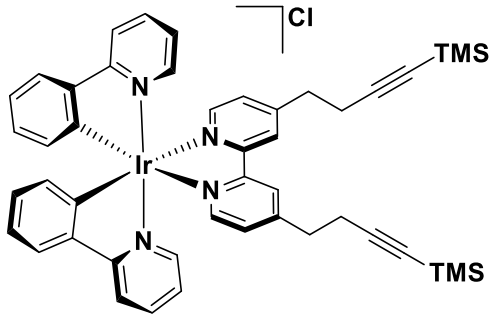

Yellow powder. **Yield**: 76%. **Rf**: 0.51 (10% MeOH/DCM on silica). Purified via flash chromatography (10% MeOH/DCM on silica). **^{1}H NMR (500 MHz, Methylene Chloride-d_2) δ (ppm)** ^{1}H NMR (500 MHz, Methylene Chloride-d_2) δ 9.50 (d, *J* = 7.7 Hz, 2H), 7.98 (d, *J* = 8.2 Hz, 2H), 7.88 – 7.73 (m, 6H), 7.56 (d, *J* = 6.4 Hz, 2H), 7.33 (d, *J* = 5.6 Hz, 2H), 7.09 (t, *J* = 7.5 Hz, 2H), 7.04 – 6.92 (m, 4H), 6.41 – 6.31 (m, 2H), 3.21 – 3.02 (m, 4H), 2.83 (t, *J* = 7.0 Hz, 4H), 0.04 (s, 18H). The data of ^{13}C NMR lacked, which will be completed in the later future.

Iridium(III)bis(2-(4′,6′-difluorophenyl)-pyridinato)-[4,4'-bis(4-(trimethylsilyl)-but-3-yn-1-yl)-2,2'-bipyridine]Cl (Ir-4')

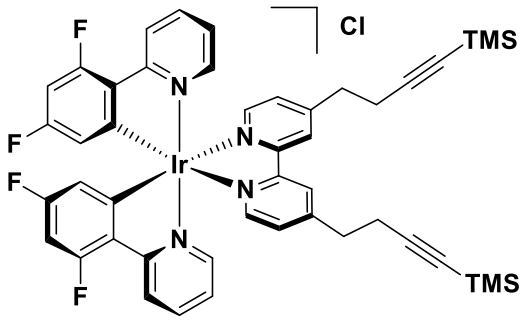

Yellow powder. **Yield**: 94%. **Rf**: 0.46 (17% MeOH/DCM on silica). Purified via flash chromatography (10% MeOH/DCM on silica). **Mp**: 239-240 ^{o}C. **^{1}H NMR**

(500 MHz, Chloroform-*d*) δ (ppm) 10.02 (s, 2H), 8.34 (d, *J* = 8.7 Hz, 2H), 7.87 – 7.80 (m, 2H), 7.74 (d, *J* = 5.6 Hz, 2H), 7.51 (d, *J* = 5.7 Hz, 2H), 7.36 (d, *J* = 5.6 Hz, 2H), 7.08 (t, *J* = 7.2 Hz, 2H), 6.59 (ddd, *J* = 11.6, 9.0, 2.2 Hz, 2H), 5.72 (dd, *J* = 8.3, 2.3 Hz, 2H), 3.21 (ddd, *J* = 39.9, 13.7, 6.9 Hz, 4H), 2.85 (t, *J* = 6.8 Hz, 4H), 0.00 (s, 18H). **^{13}C NMR (126 MHz, Chloroform-*d*) δ (ppm)** 155.83, 155.60, 154.58 (d, *J* = 6.7 Hz), 148.54, 148.37, 138.91, 128.82, 128.30, 123.79, 123.63, 123.48, 113.98, 113.82, 105.69, 99.31, 99.10, 98.89, 86.59, 33.71, 20.64, 0.03. **HR-MS** (NSI$^+$): **[M-Cl]$^+$ Calculated**: ($C_{46}H_{44}F_4IrN_4Si_2$): 977.2670; **Found**: 977.2655.

Iridium(III)bis(2-phenyl-pyridinato)-(2,2'-bipyridine) Chloride, (Ir-0).

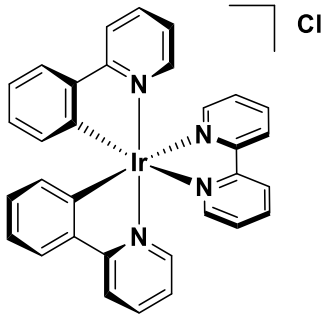

Yellow powder. **Yield**: 42%. **Rf**: 0.53 (5% MeOH/DCM on silica). **Mp**: 305.5-306.5 ^{o}C. Purified via flash chromatography (5% MeOH/DCM on silica) **^{1}H NMR (400 MHz, Methylene Chloride-d_2) δ (ppm)** 9.14 (d, *J* = 8.2 Hz, 2H), 8.23 (dd, *J* = 8.1, 1.6 Hz, 2H), 8.08 – 7.97 (m, 4H), 7.90 – 7.75 (m, 4H), 7.59 – 7.47 (m, 4H), 7.11 (td, *J* = 7.6, 1.2 Hz, 2H), 7.08 – 6.92 (m, 4H), 6.44 – 6.32 (m, 2H). **HR-MS** (NSI$^+$): **[M-Cl]$^+$ Calculated**: ($C_{32}H_{24}IrN_4$): 657.1630; Found: 657.1612. **Anal. Calcd.** for $C_{32}H_{24}ClIrN_4$+$CHCl_3$: C, 48.84; H, 3.10; N, 6.90. Found: C,

48.40; H, 3.03; N, 6.80. The characterization matched that previously reported.[166]

Iridium(III)bis[2-phenyl-4-(2,4,6-trimethylphenyl)pyridinato]-[4,4'-bis-(pyridin-4-ylethynyl)-2,2'-bipyridine]BF_4 (Ir-5)

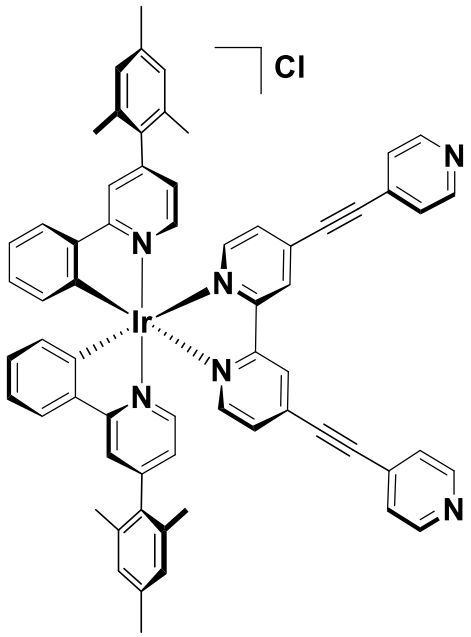

A Schlenk tube containing $[Ir(mesppy)_2\text{-}(\mu\text{-}Cl)]_2$ (**89**, 100mg, 0.06mmol, 1 equiv.) and 4,4'-bis(pyridin-4-ylethynyl)-2,2'-bipyridine (**82**, 48.7 mg, 0.13 mmol, 2.2 equiv.) was set up, and 2-methoxyethanol was used as a solvent to obtain a concentration of 0.03 M. This mixture was degassed by N_2 and heated to 110 ^oC overnight in an inert atmosphere. The dark red solution produced was rotary evaporated to afford the crude products. Silica flash column chromatography was used for purification with DCM:MeOH(v/v)=10:1. The solutions containing the expected portions were collected. After removing the solvent, the pure complex was collected as a red powder.

After obtaining the complex, it (20mg, 0.018mmol, 1 equiv.) was dissolved in DCM:MeOH(v/v)=1:1 solvent and KBF_4 (22mg, 0.18mmol, 10 equiv.) was added. This homogeneous system was stirred for 4 hours before the solvents were removed. Another portion of DCM and water were added to the precipitate and extracted three times, and the organic phases were collected and dried by anhydrous Na_2SO_4. After removing the solvent by rotavapor, an orange powder was obtained, which was the complex charged by tetrafluoroborate.

Orange to red powder. **Yield**: 38%. **Rf**: 0.42 (10% MeOH/DCM on silica). Purified via flash chromatography (10% MeOH/DCM on silica) **Mp**: Became black over 250 ^oC **^{1}H NMR (500 MHz, Methylene Chloride-d_2) δ (ppm)** 9.69 (s, 2H), 8.77 – 8.68 (m, 4H), 8.16 (d, *J* = 5.7 Hz, 2H), 7.83 (d, *J* = 1.4 Hz, 2H), 7.74 (d, *J* = 7.4 Hz, 2H), 7.70 – 7.63 (m, 4H), 7.62 (d, *J* = 5.8 Hz, 4H), 7.15 – 7.10 (m, 2H), 7.07 – 7.03 (m, 4H), 7.01 (s, 2H), 6.92 (dd, *J* = 6.0, 1.7 Hz, 2H), 6.42 (d, *J* = 7.5 Hz, 2H), 2.36 (s, 6H), 2.16 (s, 6H), 2.00 (s, 6H). **^{13}C NMR (126 MHz, Methylene Chloride-d_2) δ (ppm)** 167.62, 155.76, 152.51, 150.77, 150.08, 148.38, 143.78, 138.40, 134.97, 134.89, 134.82, 134.02, 131.47, 130.88, 130.03, 129.01, 128.52, 128.47, 127.54, 125.86, 124.97, 122.94, 121.33, 95.80, 88.33, 20.78, 20.31.**HR-MS** (NSI^+): **$[M\text{-}BF_4]^+$ Calculated**: ($C_{64}H_{50}IrN_6$): 1095.3726; **Found**: 1095.3713.

Iridium(III)bis(2-phenyl-pyridinato)-[4-(2-(1-(2-(2-(2-(2-(((3s,5s,7s)-adamantan-1-yl)oxy)ethoxy)ethoxy)ethoxy)ethyl)-1H-1,2,3-triazol-4-yl)ethyl)-4'-methyl-2,2'-bipyridine] Chloride, (Ir-1).

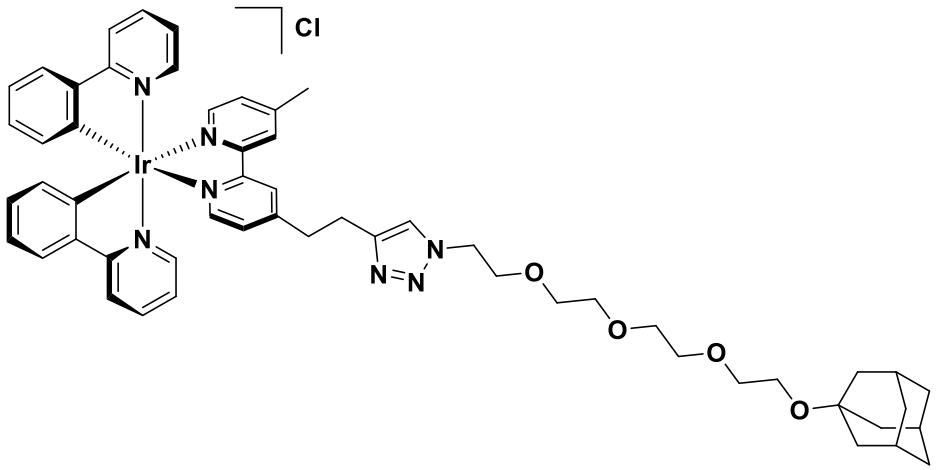

$CuSO_4$ (0.003g, 0.019mmol, 0.2 equiv.) and L-ascorbic acid (0.0067 g, 0.038 mmol, 0.4 equiv.) were added to a round bottomed flask and a mixture of H_2O (8 mL) and MeOH (8 mL) was added. The Iridium(III)bis(2-phenyl-pyridinato)-[4-(but-3-yn-1-yl)-4'-methyl-2,2'-bipyridine] chloride (**Ir-1'**, 0.067 g, 0.095 mmol, 1 equiv.) was added and the solution was vigorously stirred. The desired 1-(2-(2-(2-(2-azidoethoxy)ethoxy)ethoxy)ethoxy)adamantane (0.0355 g, 0.104 mmol, 1.1 equiv.) was added followed by the addition of pyridine (0.037 mL, 0.475 mmol, 5 equiv.). The reaction mixture was stirred for 48 hours at room temperature. Upon completion, the reaction mixture was evaporated to dryness and purified by column chromatography (silica, DCM/MeOH gradient 20:1 to 15:1). Fractions containing the desired complex were combined and this mixture was then evaporated to obtain a yellow oil that solidified in vacuum. **Yield**: 52%, **Rf**: 0.33 (5% MeOH/DCM on silica). **Mp**: 206.6-207.1 ^oC. **^{1}H NMR**

(500 MHz, Methylene Chloride-d_2) δ (ppm) 9.04 (dd, *J* = 6.4, 1.6 Hz, 2H), 8.01 – 7.95 (m, 2H), 7.93 (s, 1H), 7.85 – 7.79 (m, 4H), 7.76 (dt, *J* = 7.9, 1.6 Hz, 2H), 7.56 (dt, *J* = 5.6, 1.2 Hz, 1H), 7.49 (dt, *J* = 5.7, 1.2 Hz, 1H), 7.31 (dd, *J* = 5.7, 1.5 Hz, 1H), 7.25 (dd, *J* = 5.6, 1.5 Hz, 1H), 7.11 – 7.01 (m, 4H), 6.95 (tt, *J* = 7.4, 1.3 Hz, 2H), 6.34 (dd, *J* = 7.7, 1.2 Hz, 2H), 4.52 (t, *J* = 5.3 Hz, 2H), 3.87 (t, *J* = 5.3 Hz, 2H), 3.62 – 3.54 (m, 12H), 3.35 – 3.21 (m, 4H), 2.67 (s, 3H), 2.14 (s, 3H), 1.74 (d, *J* = 2.9 Hz, 6H), 1.70 – 1.58 (m, 6H). **^{13}C NMR (126 MHz, Methylene Chloride-d_2) δ (ppm)** 167.79 (d, *J* = 10.0 Hz), 155.74 (d, *J* = 8.4 Hz), 155.16 , 152.23 , 150.65 (d, *J* = 3.6 Hz), 149.88 , 149.55 , 148.55 , 145.77 , 143.75 (d, *J* = 5.7 Hz), 137.96 , 131.64 (d, *J* = 7.2 Hz), 130.53 (d, *J* = 3.7 Hz), 128.74 , 128.17 , 126.38 , 125.86 , 124.78 (d, *J* = 4.0 Hz), 123.29 , 123.15 , 122.90 , 122.43 , 119.67 (d, *J* = 8.3 Hz), 71.99 , 71.34 , 70.71 – 70.25 (m), 69.44 , 59.16 , 50.01 , 41.44 , 36.41 , 34.85 , 30.63 , 25.84 , 21.21 . **HR-MS** (NSI^+): **$[M-H]^+$ Calculated**: ($C_{55}H_{60}IrN_7O_4$): 1110.4025; Found: 1110.4004. **Anal. Calcd.** for $C_{55}H_{61}ClIrN_7O_4+CH_2Cl_2$: C, 56.20; H, 5.31; N, 8.19. Found: C, 56.00; H, 5.18; N, 8.68.

General procedure for disubstituted Click reaction

Methanol was added to a round-bottom flask containing K_2CO_3 (5 equiv.) and compound with terminal TMS group (1 equiv.). This solution was stirred for 4 hours at room temperature. DCM and water were used for multiple extractions

after removing the methanol. The organic fractions were combined, washed with a portion of brine and dried over Na_2SO_4. Filtration and evaporation under reduced pressure gave the crude product. This solid was kept in vacuum for 1 hour to remove the remaining TMS, and could be used for the next step without further purification.

$CuSO_4$ (0.4 equiv.) and L-ascorbic acid (0.8 equiv.) were added to a round bottomed flask and a mixture of H_2O:MOH(v/v)=1;1 was added to produce a concentration of 0.024M. The Iridium(III)bis(2-phenyl-pyridinato)-[4-(but-3-yn-1-yl)-4'-methyl-2,2'-bipyridine] Chloride (1 equiv.) was added and the solution was vigorously stirred. The desired 1-(2-(2-(2-(2-azidoethoxy)ethoxy)ethoxy) ethoxy)adamantane (2.4 equiv.) was added followed by the addition of pyridine (10 equiv.). The reaction mixture was stirred for 48 hours at room temperature. Upon completion, the reaction mixture was evaporated to dryness and purified by column chromatography (silica, DCM/MeOH gradient 10:1 to 4:1). Fractions containing the desired complex were combined and this mixture was then evaporated to obtain a pure compound under vacuum.

Iridium(III)bis(2-phenyl-pyridinato)-[4,4'-bis-(2-(1-(2-(2-(3-(2-adamantan-1-yl) oxy)ethoxy)propoxy)ethoxy)ethyl)-1H-1,2,3-triazol-4-yl)ethyl)-2,2'-bipyridine]Cl (Ir-3)

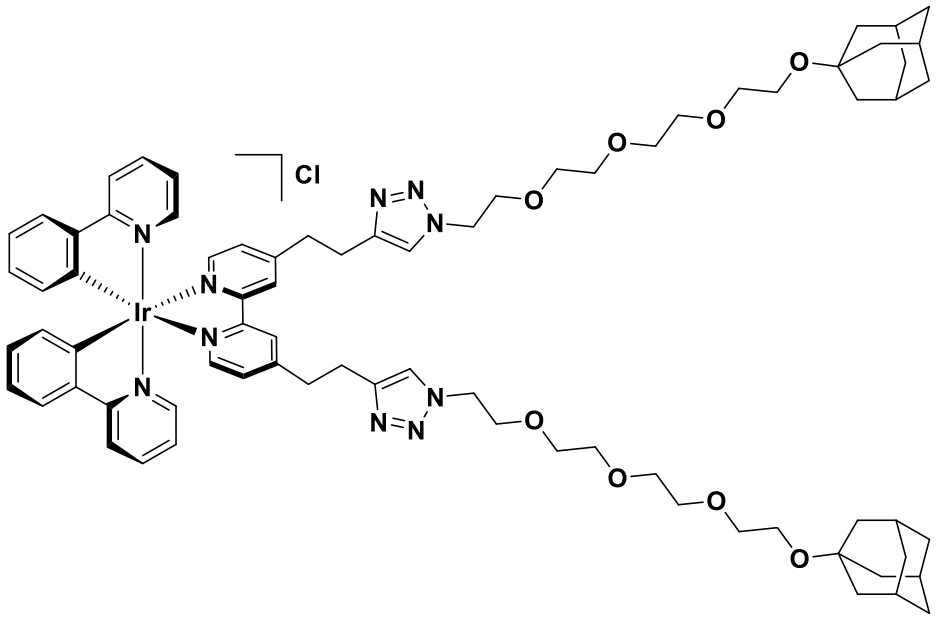

Yellow powder. **Yield**:40%. **Rf**: 0.40 (5% MeOH/DCM on silica). **Mp**: 83-84 ^{o}C. **^{1}H NMR (500 MHz, Methylene Chloride-d_2) δ (ppm)** 9.17 (s, 2H), 7.98 (d, *J* = 8.4 Hz, 4H), 7.87 – 7.78 (m, 4H), 7.76 (d, *J* = 7.5 Hz, 2H), 7.52 (d, *J* = 5.2 Hz, 2H), 7.31 (d, *J* = 5.0 Hz, 2H), 7.07 (d, *J* = 7.0 Hz, 4H), 6.95 (t, *J* = 7.2 Hz, 2H), 6.33 (m, 2H), 4.52 (s, 4H), 3.87 (s, 4H), 3.64 – 3.49 (m, 24H), 3.38 – 3.18 (m, 8H), 2.14 (s, 6H), 1.74 (s, 12H), 1.64 (q, *J* = 11.8 Hz, 12H). **^{13}C NMR (126 MHz, Methylene Chloride-d_2) δ (ppm)** 167.75, 155.89, 155.18, 150.69, 149.81, 148.65, 143.78, 137.98, 131.61, 130.51, 128.15, 126.25, 124.77, 123.32, 122.41, 119.67, 72.05, 71.32, 70.48, 70.46, 70.42, 70.31, 69.45, 59.16, 50.13, 41.42, 36.40, 34.79, 30.63, 25.95. **HR-MS** (NSI^{+}): **[M-Cl]$^{+}$ Calculated**: ($C_{76}H_{94}IrN_{10}O_8$): 1467.6885; Found: 1467.6840. **Anal. Calcd.** for $C_{76}H_{94}ClIrN_{10}O_8$: C, 60.72; H, 6.30; N, 9.32. Found: C, 60.57; H, 6.16; N, 9.40.

Iridium(III)bis(2-(4′,6′-difluorophenyl)-pyridinato)-[4,4'-bis-(2-(1-(2-(2-(3-(2-adamantan-1-yl)oxy)ethoxy)propoxy)ethoxy)ethyl)-1H-1,2,3-triazol-4-yl)ethyl)-2,2'-bipyridine]Cl (Ir-4)

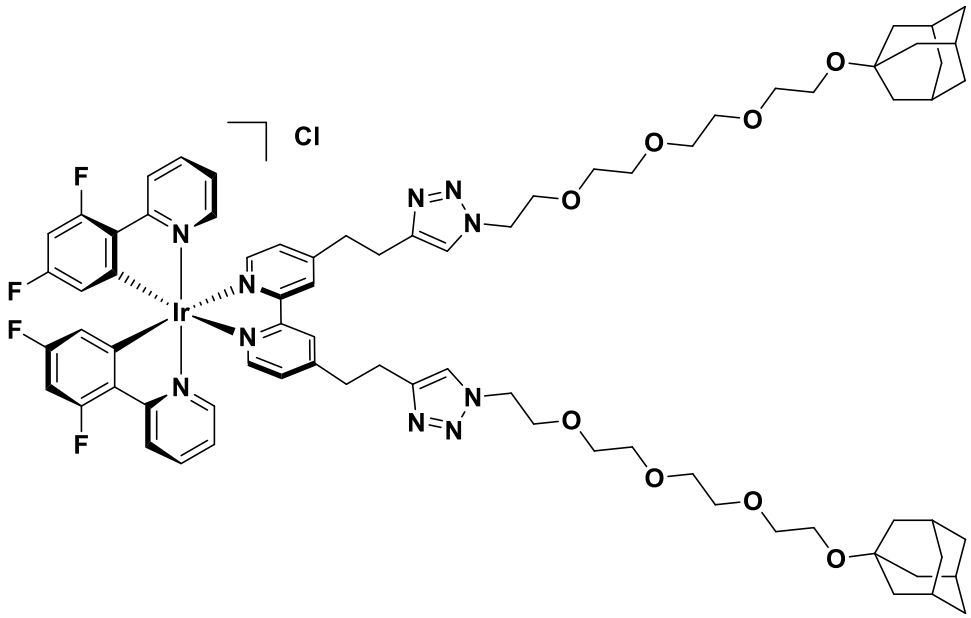

Yield: 30%, **Rf**: 0.37 (5% MeOH/DCM on silica). **Mp**: 97-98 °C. **^{1}H NMR (500 MHz, Chloroform-*d*) δ (ppm)** 9.64 (s, 2H), 8.32 (d, *J* = 8.7 Hz, 2H), 8.04 (s, 2H), 7.83 (t, *J* = 7.8 Hz, 2H), 7.73 (d, *J* = 5.5 Hz, 2H), 7.43 (d, *J* = 5.3 Hz, 2H), 7.34 (d, *J* = 5.5 Hz, 2H), 7.11 (t, *J* = 6.3 Hz, 2H), 6.56 (t, *J* = 10.4 Hz, 2H), 5.67 (d, *J* = 9.8 Hz, 2H), 4.50 (s, 4H), 3.87 (t, *J* = 5.2 Hz, 4H), 3.64 – 3.57 (m, 24H), 3.40 – 3.30 (m, 8H), 2.13 (s, 6H), 1.73 (s, 12H), 1.60 (q, *J* = 12.1 Hz, 12H). **^{13}C NMR (126 MHz, Chloroform-*d*) δ (ppm)** 156.41, 155.68, 154.45, 154.40, 149.17, 148.58, 138.95, 128.40, 127.72, 127.49, 123.80, 123.64, 123.61, 113.95, 113.81, 99.31, 99.10, 98.88, 72.29, 71.25, 70.60, 70.55, 70.53, 70.47, 69.49, 59.22, 50.02, 41.45, 36.44, 34.95, 30.48, 25.92. **HR-MS** (NSI^{+}): **[M-Cl]$^{+}$ Calculated**: ($C_{76}H_{90}F_4IrN_{10}O_8$): 1539.6508; Found: 1539.6450. **Anal. Calcd.** for

$C_{76}H_{90}ClF_4IrN_{10}O_8$ + $CHCl_3$ + MeCN: C, 54.67; H, 5.46; N, 8.88. Found: C, 54.56; H, 4.95; N, 9.06.

$[(Ir\text{-}5)_6Pd_3](BF_4)_{12}$

To a small vial containing **Ir-5** (10mg, 1 equiv.) and $[Pd(NCCH_3)_4]BF_4$ (22.5mg, 0.02 mmol, 5 equiv.), 0.7 mL d_6-DMSO was added. This solution was degassed by N_2 and heated to 80°C overnight and monitored by both ^1H NMR and 2D DOSY NMR. After the signal on ^1H NMR became broad, and 2D DOSY NMR showed another large system had formed, this reaction was stopped and filtered through celite to remove the Pd black. The solution was checked by ESI-MS for further characterisation as **$[(Ir\text{-}5)_6Pd_3](BF_4)_{12}$** . The left portion was added dropwise to saturated NH_4PF_6 aqueous solution at 0°C. The precipitation was collected as **$[(Ir\text{-}5)_6Pd_3](PF_6)_{12}$**. **Yield**: 5%.

HR-MS (**ESI**)**: $[M\text{-}BF_4]^+$ Calculated:** (Figure **S80**-**S83**)

$[(C_{64}H_{50}IrN_6)_6Pd_3(BF_4)_{12}]^{4+}$: 1896.4959 Found: 1896.5511;

$[(C_{64}H_{50}IrN_6)_6Pd_3(BF_4)_{12}]^{5+}$: 1499.7959 Found: 1500.0374;

$[(C_{64}H_{50}IrN_6)_6Pd_3(BF_4)_{12}]^{6+}$: 1235.3292 Found: 1235.3640;

$[(C_{64}H_{50}IrN_6)_6Pd_3(BF_4)_{12}]^{7+}$: 1046.4244 Found: 1046.4565.

3,6-dibromo-9*H*-carbazole

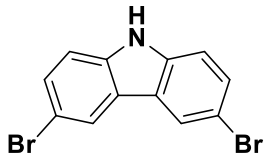

N-bromosuccinimide (4.68 g, 26.31 mmol, 2.2 equiv.) was dissolved in acetonitrile (20 mL) and added in drops to a solution of carbazole (2.00 g,11.96 mmol, 1.0 equiv.) in acetonitrile (40 mL) at room temperature. The reaction mixture was then poured into water (100 mL). The white precipitates were collected and washed with water (3 x 50 mL). The solid was dried in vacuum to obtain the target compound. **Yield**: 74%. **Mp**: 202-203 ^{o}C. (lit., 209-210^{o}C)[167] **^{1}H NMR (500 MHz, DMSO-d_6) δ (ppm)** 11.60 (s, 1H), 8.43 (s, 2H), 7.50 (dd, *J* = 30.1, 7.1 Hz, 4H). The characterization matched that previously reported.[168,169]

(3,6-dibromo-9H-carbazol-9-yl)(phenyl)methanone (**102**)

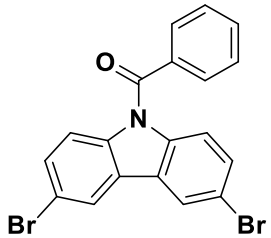

All the flasks had to be dried and this reaction was conducted in nitrogen atmosphere. 3,6-dibromo-9*H*-carbazole (1.00 g, 5 mmol, 1 equiv.) was dissolved in dry THF (15 ml) in a Schlenk flask in an ice-water base. NaH (0.24 g, 10 mmol, 2 equiv.) was added to the solution slowly with nitrogen protect. The solution was stirred at 0 ^{o}C for 0.5 hours before benzoyl chloride (0.654g,

7.5 mmol, 1.5 equiv.) was added drop by drop. The mixture was kept at 0°C for 0.5 hours, and then raised to room temperature for 2.5 hours. 1mL of methanol was added slowly to quench the remaining NaH in solution before the solvent was removed by rotary evaporation. Then, the residue was sonicated and washed carefully with THF, water, Hexane:EA(v/v)=10:1 to obtain a white solid as the expected compound. **Yield**: 40%. **^{1}H NMR (400 MHz, Chloroform-*d*) δ (ppm)** 8.11 (d, *J* = 1.9 Hz, 2H), 7.74 – 7.66 (m, 3H), 7.56 (t, *J* = 7.7 Hz, 2H), 7.47 (dd, *J* = 8.9, 2.0 Hz, 2H), 7.39 (d, *J* = 8.9 Hz, 2H). **^{13}C NMR (101 MHz, Chloroform-*d*) δ (ppm)** 138.15, 134.96, 132.91, 130.24, 129.10, 129.08, 126.57, 122.91, 117.27, 116.83.

(4-(3,6-dibromo-9H-carbazol-9-yl)phenyl)(phenyl)methanone (**106**)

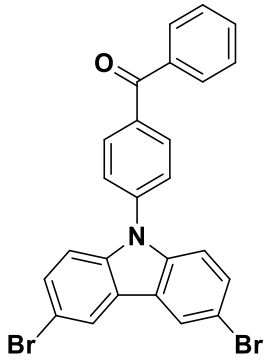

All flasks have to be dried and this reaction was conducted in nitrogen atmosphere. 3,6-dibromo-9H-carbazole (1.00 g, 3.08 mmol, 1 equiv.) was dissolved in dry DMF (20 ml) in a Schlenk flask. The *t*-BuOK (0.35g, 3.08 mmol,1 equiv.) was added to the solution slowly with nitrogen protect. (4-fluorophenyl)(phenyl)methanone (0.62g, 3.08 mmol, 1 equiv.) was dissolved in another Schlenk flask containing 10 mL anhydrous DMF, and the solution was

transferred to the 3,6-dibromo-9*H*-carbazole solution dropwise. The mixture was heated to 150 ^{o}C overnight. This reaction was then cooled to room temperature and poured into 100mL water to produce the precipitate. This suspension was filtrated and washed with water, Hexnae:EA(v/v)= 10:1 for purification. The target product was obtained as a white powder. **Yield**: 65%. **^{1}H NMR (500 MHz, Chloroform-*d*) δ (ppm)** 8.24 (d, *J* = 1.7 Hz, 2H), 8.10 (d, *J* = 8.4 Hz, 2H), 7.92 (d, *J* = 7.2 Hz, 2H), 7.68 (t, *J* = 8.3 Hz, 3H), 7.62 – 7.52 (m, 4H), 7.39 (d, *J* = 8.7 Hz, 2H). **^{13}C NMR (126 MHz, Chloroform-*d*) δ (ppm)** 207.14, 195.47, 140.58, 139.29, 137.17, 136.72, 132.85, 132.03, 130.05, 129.67, 128.53, 126.27, 124.37, 123.41, 113.69, 111.50, 30.97. The characterization matched that previously reported.[170]

General procedure for disubstituted Suzuki coupling

The 3,6-dibromo-carbazole derivatives (1 equiv.), (4-formylphenyl)boronic acid (3 equiv.), potassium carbonate (8 equiv.) were added to a 100mL round-bottom flask containing a mixture of THF and distilled water (4:1 v/v) to a concentration of 0.15 M. The mixture was degassed by N_2 for 15minutes, and $Pd(PPh_3)_4$ (5% mol) was added to the flask under positive nitrogen pressure. The mixture was refluxed in nitrogen atmosphere overnight and then cooled to room temperature. The solvent was removed and the precipitate was washed

with water, Hexane, diethyl ether, ethyl acetate, $CHCl_3$, DCM, ethanol and acetone, respectively.

4,4'-(9H-carbazole-3,6-diyl)dibenzaldehyde (Mol-0)

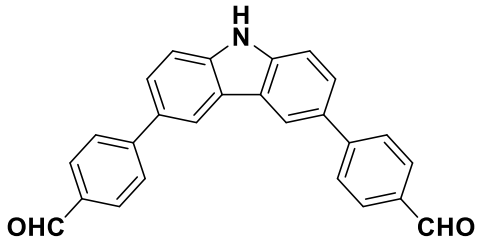

Yield: 35%. **Mp**: 233-234 ^oC. **^{1}H NMR (400 MHz, DMSO-d_6) δ (ppm)** 11.64 (s, 1H), 10.07 (s, 2H), 8.81 (d, *J* = 1.6 Hz, 2H), 8.10 – 8.02 (m, 8H), 7.90 (dd, *J* = 8.5, 1.9 Hz, 2H), 7.65 (d, *J* = 8.5 Hz, 2H). **^{13}C NMR (126 MHz, DMSO-d_6) δ (ppm)** 193.12, 147.40, 141.00, 134.72, 130.71, 130.04, 127.42, 125.71, 123.91, 120.03, 112.29. **HR-MS** (NSI^+): **$[M+H]^+$ Calculated**: ($C_{26}H_{17}NO_2H$): 376.1338; **Found**: 376.1333. **Anal. Calcd.** for $C_{26}H_{18}NO_2$ + 2*CH_2Cl_2: C, 54.76; H, 3.12; N, 2.28. Found: C, 54.41; H, 3.16; N, 2.55.

4,4'-(9-benzoyl-9H-carbazole-3,6-diyl)dibenzaldehyde (Mol-1)

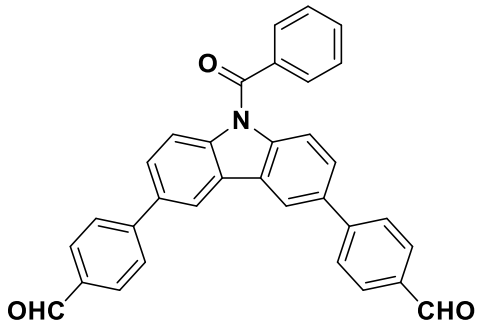

The product was washed by DMSO at room temperature for further purification.

Yield: 88%. **Mp**: 250-251 ^oC. **^{1}H NMR (400 MHz, DMSO-d_6) δ (ppm)** 10.09 (s,

2H), 8.92 (d, *J* = 2.0 Hz, 2H), 8.18 – 8.00 (m, 8H), 7.89 (dd, *J* = 8.8, 1.9 Hz, 2H), 7.85 – 7.73 (m, 3H), 7.66 (t, *J* = 7.6 Hz, 2H), 7.51 (d, *J* = 8.7 Hz, 2H). Because of its poor solubility, ^{13}C NMR couldn't be obtained. **HR-MS** (ASAP): **[M+H]$^+$ Calculated**: ($C_{33}H_{21}NO_3H$): 480.1600; **Found**: 480.1596. **Anal. Calcd.** for $C_{33}H_{22}NO_3$ + Acetone: C, 80.43; H, 5.06; N, 2.61. Found: C, 80.54; H, 3.90; N, 3.18.

4,4'-(9-(4-benzoylphenyl)-9H-carbazole-3,6-diyl)dibenzaldehyde (Mol-2)

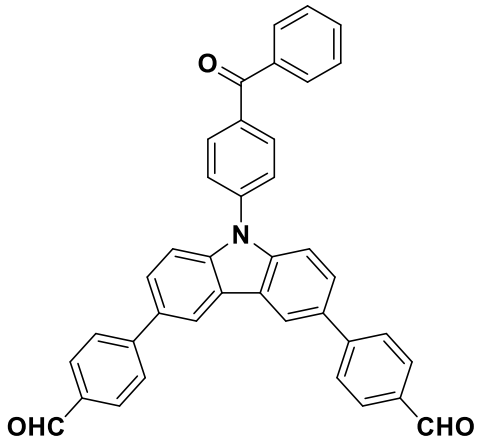

The product was washed by DMSO at room temperature for further purification. **Yield**: 52%. **Mp**: 266-267 ^{o}C **^{1}H NMR (500 MHz, DMSO-*d*$_6$) δ (ppm)** 10.09 (s, 2H), 8.98 (s, 2H), 8.19 – 8.04 (m, 10H), 7.97 (t, *J* = 9.2 Hz, 4H), 7.90 (d, *J* = 7.3 Hz, 2H), 7.75 (t, *J* = 7.4 Hz, 1H), 7.71 (d, *J* = 8.6 Hz, 2H), 7.65 (t, *J* = 7.6 Hz, 2H). Because of its poor solubility, ^{13}C NMR couldn't be obtained. **HR-MS** (ASAP): **[M+H]$^+$ Calculated**: ($C_{39}H_{25}NO_3H$): 556.1913; **Found**: 556.1912. **Anal. Calcd.** for $C_{39}H_{25}NO_3$: C, 84.31; H, 4.54; N, 2.52. Found: C, 84.21; H, 4.44; N, 2.62.

General procedure for synthesizing Schiff-base macrocycles

All flasks must be dried. 4,4'-(9H-carbazole-3,6-diyl)dibenzaldehyde derivatives (1 equiv.) was dissolved in 1,4-dioxane in a heavy wall tube to obtain a concentration of 0.02M. One equivalent of diamine compound (1,2-ethylenediamine or 1,3-propanediamine) was added to the reaction system before it was sealed by a thick Teflon cap and Teflon tapes. The suspension was stirred and heated to 120^{o}C for 3 days and the carbazole was dissolved totally as the temperature rose. After the formation of the precipitate, this reaction was cooled to room temperature and filtered. The residues were washed by hexane, DCM, $CHCl_3$, ethyl acetate, methanol and DMSO respectively.

Mac-0

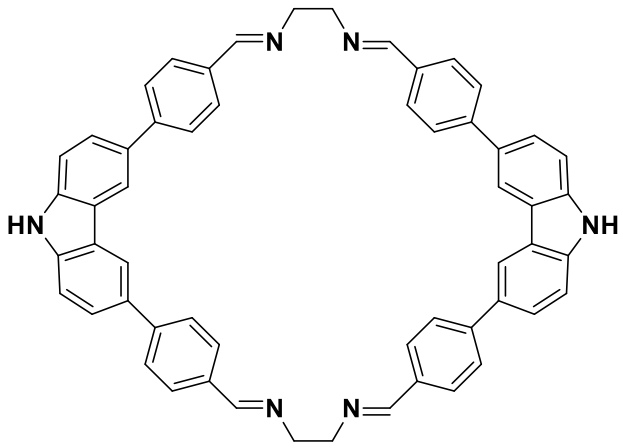

White powder. **Yield**: 58%, **Mp**: Became brown over 250 ^{o}C, and became dark brown over 300 ^{o}C. **HR-MS** (NSI^{+}): **[M+H]$^{+}$ Calculated**: ($C_{56}H_{42}N_6H$): 799.3549;

Found: 799.3540. **Anal. Calcd.** for $C_{56}H_{42}N_6$ + CH_2Cl_2: C, 77.45; H, 5.02; N, 9.51. Found: C, 77.30; H, 5.20; N, 9.80.

Mac-1

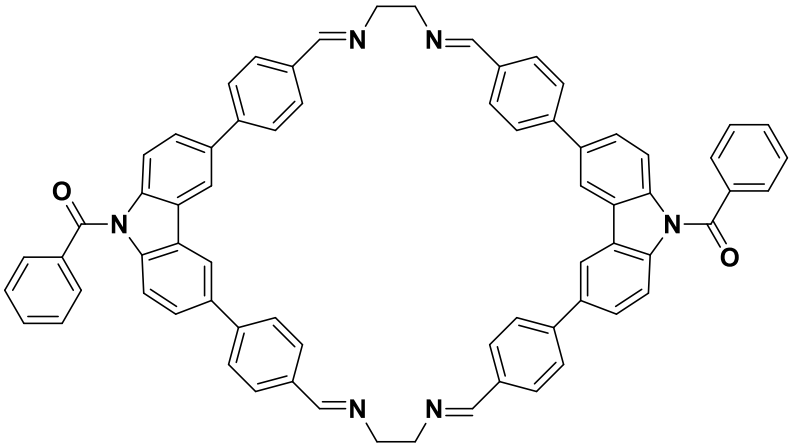

White powder. **Yield**: 52%, Became yellow over 250 ^oC, and became dark brown over 300 ^oC. **MS** (EI): **$[M+H]^+$ Calculated**: ($C_{70}H_{50}N_6O_2H$): 1007.4; **Found**: 1007.4. **Anal. Calcd.** for $C_{70}H_{51}N_6O_2$ + 2*CH_2Cl_2: C, 73.47; H, 4.62; N, 7.14. Found: C, 73.05; H, 4.56; N, 7.20.

Mac-2

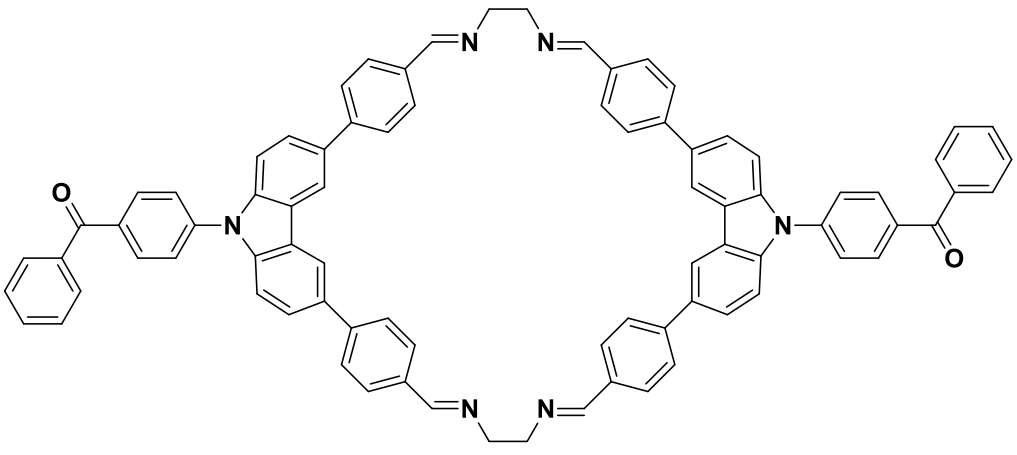

Yellow powder. **Yield**: 77%, Became black over 300 ^{o}C.. **MS** (DCTB matrix): **[M+H]$^{+}$ Calculated**: ($C_{82}H_{58}N_6O_2H$): 1159.5; **Found**: 1159.4. **Anal. Calcd.** for $C_{82}H_{59}N_6O_2$: C, 84.95; H, 5.04; N, 7.25. Found: C, 85.18; H, 5.38; N, 7.40.

Mac-3

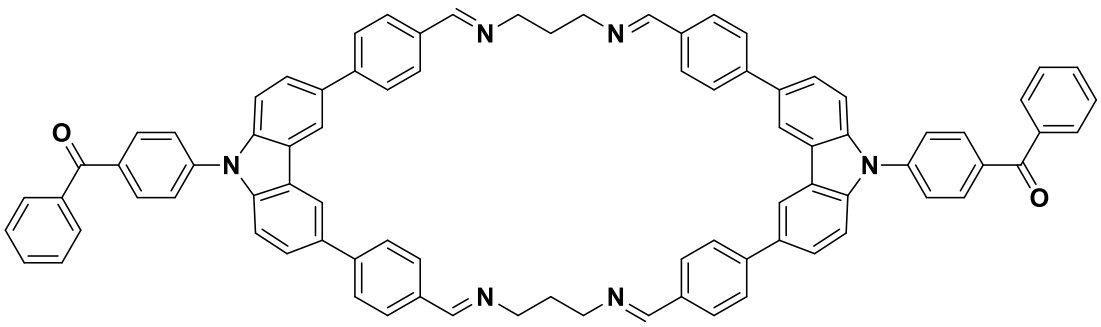

White powder. **Yield**: 37%, Became brown over 300 ^{o}C, and became black over 350 ^{o}C. **HR-MS** (NSI^{+}): **[M+H]$^{+}$ Calculated**: ($C_{84}H_{62}N_6O_2H$): 1187.5013; **Found**: 1187.5020.

Computational details:

All the calculations were performed with the Gaussian09,[171] revision D.018 suite of programs. The geometry of **Mol-0, Mol-1, Mol-2, Mac-0, Mac-1, Mac-2** and **Mac-3** were optimized using a DFT methodology employing the (R)B3LYP[172] functional with the standard Pople[173] 6-31G(d,p) basis set. The Tamm–Dancoff approximation (TDA) was calculated as a variant of Time-dependent density functional theory (TD-DFT) employing the PBE1PBE. The molecular orbitals were visualized using GaussView 5.0 software.[174]

Electrochemistry measurements

Electrochemistry measurements were performed on an Electrochemical Analyzer potentiostat model 600D from CH Instruments. The electrochemistry of complexes were measured in degassed acetonitrile solutions (solution was bubbled by nitrogen for 10 minutes before measurement) with 0.1M [*n*-Bu_4N]PF_6 as supporting electrolyte at room temperature at a sweep rate of 100 mV/s. Glassy carbon was used as the working electrode, spiral Pt as the counter electrode and silver wire electrode as the quasi reference electrode, and the values were converted *vs.* SCE [84] (a correction factor of 0.38 V was added to the redox potentials to report the values *vs.* SCE instead of Fc^+/Fc).

Photophysical measurements

All the samples were prepared in HPLC grade solvents (MeCN and anhydrous DMF) with concentrations at μM grade. Absorption spectra were recorded at room temperature using a Shimadzu UV-1800 double beam spectrophotometer. The linear least-square was used to verify the molar absorptivity determination from at least five independent solutions in gradient concentrations with absorbances from 0.1×10^{-5} to 1×10^{-5} M.

The sample solutions for the emission spectra were prepared in HPLC grade solvents and degassed via three freeze–pump–thaw cycles using an in-house

designed quartz cuvette. Steady state emission and time-resolved emission spectra were recorded at 298 K using an Edinburgh Instruments F980. All samples for the steady state measurements were excited at 360 nm while samples for the time-resolved measurements were excited at 378 nm using a PDL 800-D pulsed diode laser.

Emission quantum yields were determined using the optically dilute method.[175,176] A stock solution with absorbance of ca. 0.5 and four dilutions with dilution factors of between 2 and 20 were prepared. For each sample, linearity between absorption and emission intensity was verified through a linear regression analysis until the Pearson regression factor (R^2) was up to 0.9. Individual relative quantum yield was calculated for each solution and the values reported represent the slope value. A solution of quinine sulfate in 0.5 M H_2SO_4 (Φ_{PL} = 54.6%) was used as the external reference.[85]

Doped films were prepared from DMSO solution, with 10 wt% of compounds in PMMA. Steady state emission and time-resolved emission spectra were recorded at 298 K using an Edinburgh Instruments F980. All the samples for steady state measurements were excited at 360 nm while samples for time-resolved measurements were excited at 378 nm using a PDL 800-D pulsed diode laser, and were recorded in air. Quantum yields were measured using an integrating sphere, in nitrogen atmosphere. Variable temperature photophysical

measurements were tested within cryostat on an Edinburgh Instruments F980 in air and vacuum (10^{-5} mbar). Steady state measurements were recorded at 77K, and time resolved emission spectra were recorded at five temperatures, from 77K to 298K, with the cooling of liquid nitrogen. Powder samples were prepared as thin slices between two pieces of glass and measured both in air and vacuum (10^{-5} mbar) on Edinburgh instruments F980.

NMR spectra, MS spectra, FT-IR spectra and crystal data from XRD measurements of reported compounds are available in the electronic supporting information (ESI).

References

1 A. D. McNaught and A. Wilkinson, *Compendium of Chemical Terminology*, Blackwell Science, Oxford, UK, 2nd edn., 1997.

2 J. Sun, J. Zhao, H. Guo, and W. Wu, *Chem. Commun.*, 2012, **48**, 4169-4171

3 Y. Chen, L. Qiao, L. Ji and H. Chao, *Biomaterials,* 2014, **35**, 2–13.

4 Y. W. Choi, G. J. Park, Y. J. Na, H. Y. Jo, S. A. Lee, G. R. You and C. Kim, *Sensors Actuators, B Chem.*, 2014, **194**, 343–352.

5 L. Flamigni, A. Barbieri, C. Sabatini, B. Ventura and F. Barigelletti, *Top Curr Chem*, 2007,**281**, 143-203.

6 B. Y. M. Kasha, *Discuss. Faraday Soc.*, 1950, **9**, 14–19.

7 A. J. Lees, *Topics in Organometallic Chemistry*, Springer, New York, USA, 2009.

8 H. Yersin, A. F. Rausch, R. Czerwieniec, T. Hofbeck and T. Fischer, *Coord. Chem. Rev.*, 2011, **255**, 2622–2652.

9 R. D. Costa, E. Ortí, H. J. Bolink, F. Monti, G. Accorsi and N. Armaroli, *Angew. Chem. Int. Ed.*, 2012, **51**, 8178–8211.

10 J. R. Lakowicz, *Principles of Fluorescence Spectroscopy*, Springer, New York, USA, 3rd edn, 2006.

11 W. Zhao, Z. He, J. W. Y. Lam, Q. Peng, H. Ma, Z. Shuai, G. Bai, J. Hao and B. Z. Tang, *Chem*, 2016, **1**, 592–602.

12 M. Y. Wong and E. Zysman-Colman, *Adv. Mater.*, 2017, **29**, 1605444.

13 C. A. Parker and T. A. Joyce, *Photochem. Photobiol.*, 1967, **6**, 395–406.

14 H. Yersin, U. Monkowius, DE 10 2008 033 563 A1, 2008.

15 A. Endo, M. Ogasawara, A. Takahashi, D. Yokoyama, Y. Kato and C. Adachi, *Adv. Mater.*, 2009, **21**, 4802–4806.

16 A. Endo, K. Sato, K. Yoshimura, T. Kai, A. Kawada, H. Miyazaki and C. Adachi, *Appl. Phys. Lett.*, 2011, **98**, 10–13.

17 H. Uoyama, K. Goushi, K. Shizu, H. Nomura and C. Adachi, *Nature*, 2012, **492**, 234-238.

18 S. J. Dalgarno, N. P. Power and J. L. Atwood, *Coord. Chem. Rev.*, 2008, **252**, 825–841.

19 S. Zarra, D. M. Wood, D. A. Roberts, and J. R. Nitschke, *Chem. Soc. Rev.*, 2015, **44**, 419–432.

20 R. W. Saalfrank, A. Stark, K. Peters and H. G. von Schnering, *Angew. Chem. Int. Ed.*, 1988, **27**, 851–853.

21 D. Fujita, Y. Ueda, S. Sato, H. Yokoyama, N. Mizuno, T. Kumasaka and M. Fujita, *Chem*, 2016, **1**, 91–101.

22 M. L. Saha, X. Yan and P. J. Stang, *Acc. Chem. Res.*, 2016, **49**, 2527–2539.

23 C. H. M. Amijs, G. P. M. van Klink and G. van Koten, *Dalton. Trans.*, 2006, 308–327.

24 J. Yang, M. Bhadbhade, W. A. Donald, H. Iranmanesh, E. G. Moore, H. Yan and J. E. Beves, *Chem. Commun.*, 2015, **51**, 4465–4468.
25 Z. Li, N. Kishi, K. Hasegawa, M. Akita and M. Yoshizawa, *Chem. Commun.*, 2011, **47**, 8605-8607.
26 V. E. Pritchard, D. Rota Martir, S. Oldknow, S. Kai, S. Hiraoka, N. J. Cookson, E. Zysman-Colman and M. J. Hardie, *Chem. - A Eur. J.*, 2017, **23**, 6290–6294.
27 O. Chepelin, J. Ujma, X. Wu, A. M. Z. Slawin, M. B. Pitak, S. J. Coles, J. Michel, A. C. Jones, P. E. Barran and P. J. Lusby, *J. Am. Chem. Soc.*, 2012, **134**, 19334–19337.
28 W. Sie, G. Lee, K. Y. Tsai, I. Chang and K. Shiu, *J. Mol. Struct.*, 2008, **890**, 198–202.
29 C. Bronner, S. A. Baudron and M. W. Hosseini, *Inorg. Chem.*, 2010, **49**, 8659–8661.
30 C. Xu, A. Guenet, N. Kyritsakas, J.-M. Planeix and M. W. Hosseini, *Chem. Commun.*, 2015, **51**, 14785–14788.
31 D. Rota Martir, D. Escudero, D. Jacquemin, D. Cordes, A. Slawin, H. Fruchtl, S. Warriner and E. Zysman-Colman, *Chem. - A Eur. J.*, 2017, **23**, 14358–14366.
32 X. Li, J. Wu, C. He, R. Zhang and C. Duan, *Chem. Commun.*, 2016, **52**, 5104–5107.
33 X. Li, J. Wu, L. Chen, X. Zhong, C. He, R. Zhang and C. Duan, *Chem. Commun*, 2016, **52**, 9628–9631.
34 M.-L. Ho, Y.-A. Chen, T.-C. Chen, P.-J. Chang, Y.-P. Yu, K.-Y. Cheng, C.-H. Shih, G.-H. Lee and H.-S. Sheu, *Dalton. Trans.*, 2012, **41**, 2592–2600.
35 C.-Y. Sun, X.-L. Wang, X. Zhang, C. Qin, P. Li, Z.-M. Su, D.-X. Zhu, G.-G. Shan, K.-Z. Shao, H. Wu and J. Li, *Nat. Commun.*, 2013, **4**, 1–8.
36 R. D. Costa, E. Ortí, D. Tordera, A. Pertegás, H. J. Bolink, S. Graber, C. E. Housecroft, L. Sachno, M. Neuburger and E. C. Constable, *Adv. Energy Mater.*, 2011, **1**, 282–290.
37 A. S. Polo, M. K. Itokazu, K. M. Frin, A. O. de Toledo Patrocinio and N. Y. M. Iha, *Coord. Chem. Rev.*, 2006, **250**, 1669-1680.
38 S. Horiuchi, H. Tanaka, E. Sakuda, Y. Arikawa and K. Umakoshi, *Chem. - A Eur. J.*, 2016, **22**, 17533–17537.
39 C. Wu, H. F. Chen, K. T. Wong and M. E. Thompson, *J. Am. Chem. Soc.*, 2010, **132**, 3133–3139.
40 M. Sandroni and E. Zysman-Colman, *Dalton Trans.*, 2014, **43**, 3676–80.
41 R. Challa, A. Ahuja, J. Ali and R. K. Khar, *AAPS PharmSciTech*, 2005, **6**, E329–E357.
42 M. Becuwe, F. Cazier, M. Bria, P. Woisel and F. Delattre, *Tetrahedron Lett.*, 2007, **48**, 6186–6188.
43 M. N. Berberan-Santos, P. Choppinet, A. Fedorov, L. Jullien and B. Valeur, *J. Am. Chem. Soc.*, 2000, **122**, 11876–11886.

44 U. Kauscher and B. J. Ravoo, *Beilstein J. Org. Chem.*, 2012, **8**, 1543–1551.
45 B. J. Ravoo and R. Darcy, *Angew. Chem. Int. Ed.*, 2000, **39**, 4324–4326.
46 I. F. Uchegbu, A. G. Schätzlein, L. Tetley, A. I. Gray, J. Sludden, S. Siddique and E. Mosha, *J. Pharm. Pharmacol.*, 1998, **50**, 453–458.
47 P. Falvey, C. W. Lim, R. Darcy, T. Revermann, U. Karst, M. Giesbers, A. T. M. Marcelis, A. Lazar, A. W. Coleman, D. N. Reinhoudt and B. J. Ravoo, *Chem. - A Eur. J.*, 2005, **11**, 1171–1180.
48 J. Voskuhl, M. C. A. Stuart and B. J. Ravoo, *Chem. - A Eur. J.*, 2010, **16**, 2790–2796.
49 M. Paolino, F. Ennen, S. Lamponi, M. Cernescu, B. Voit, A. Cappelli, D. Appelhans and H. Komber, *Macromolecules*, 2013, **46**, 3215–3227.
50 D. A. Uhlenheuer, K. Petkau and L. Brunsveld, *Chem. Soc. Rev.*, 2010, **39**, 2817–2826.
51 V. Alexander, *Chem. Rev.*, 1995, **95**, 273–342.
52 L. Wang, X. Zhu, W. Wong, J. Guo, W. Wong and Z. Li, *Dalton Trans.*, 2005, **0**, 3235–3240.
53 K. Shen, X. Yang, Y. Cheng and C. Zhu, *Tetrahedron*, 2012, **68**, 5719–5723.
54 H.-T. Feng, S. Song, Y.-C. Chen, C.-H. Shen and Y.-S. Zheng, *J. Mater. Chem. C*, 2014, **2**, 2353–2359.
55 N. E. Borisova, M. D. Reshetova and Y. A. Ustynyuk, *Chem. Rev.*, 2007, **107**, 46–79.
56 T. Zhao, Z. Liu, Y. Song, W. Xu, D. Zhang and D. Zhu, *J. Org. Chem.*, 2006, **71**, 7422–7432.
57 S. H. Jung, W. Pisula, A. Rouhanipour, H. J. Räder, J. Jacob and K. Müllen, *Angew. Chem. Int. Ed.*, 2006, **45**, 4685–4690.
58 K. Balakrishnan, A. Datar, W. Zhang, X. Yang, T. Naddo, J. Huang, J. Zuo, M. Yen, J. S. Moore and L. Zang, *J. Am. Chem. Soc.*, 2006, **128**, 6576–6577.
59 L. Huynh, Z. Wang, J. Yang, V. Stoeva, A. Lough, I. Manners and M. A. Winnik, *Chem. Mater.*, 2005, **17**, 4765–4773.
60 S. Lamansky, P. Djurovich, D. Murphy, F. Abdel-Razzaq, H. E. Lee, C. Adachi, P. E. Burrows, S. R. Forrest and M. E. Thompson, *J. Am. Chem. Soc.*, 2001, **123**, 4304–4312.
61 Y. Ma, S. Liu, H. Yang, Y. Wu, C. Yang, X. Liu, Q. Zhao, H. Wu, J. Liang, F. Li and W. Huang, *J. Mater. Chem.*, 2011, **21**, 18974.
62 A. F. Henwood and E. Zysman-Colman, *Chem. Commun.*, 2017, **53**, 807–826.
63 M. G. Colombo, A. Hauser, and H. U. Gudel, *Inorg. Chem.*, 1993, **32**, 3088–3092.
64 C. A. Puckett, R. J. Ernst and J. K. Barton, *Dalton. Trans.*, 2010, **39**, 1159–1170.

65 E. J. New and D. Parker, *Org. Biomol. Chem.*, 2009, **7**, 851–855.
66 F. N. Castellano and J. R. Lakowicz, *Photochem. Photobiol.*, 1998, **67**, 179–83.
67 F. C. M. Leung, A. Y. Y. Tam, V. K. M. Au, M. J. Li and V. W. W. Yam, *ACS Appl. Mater. Interfaces*, 2014, **6**, 6644–6653.
68 K. K. Lo, *Luminescent and Photoactive Transition Metal Complexes as Biomolecular Probes and Cellular Reagents*, Springer, Berlin, Heidelberg, 2015..
69 Y. You, *Curr. Opin. Chem. Biol.*, 2013, **17**, 699–707.
70 Q. Li, Y. Liu, P. Gao, C. Xie, X. Su, X. Li and Q. Zhao, *Sensors Actuators, B*, 2017, **252**, 142–151.
71 T. S.-M. Tang, K.-K. Leung, M.-W. Louie, H.-W. Liu, S. H. Cheng and K. K.-W. Lo, *Dalton. Trans.*, 2015, **44**, 4945–4956.
72 H. Shi, S. Liu, Z. An, H. Yang, J. Geng, Q. Zhao, B. Liu and W. Huang, *Macromol. Biosci.*, 2013, **13**, 1339–1346.
73 A. Harada, Y. Takashima and H. Yamaguchi, *Chem. Soc. Rev.*, 2009, **38**, 875–882.
74 I. Böhm, K. Isenbügel, H. Ritter, R. Branscheid and U. Kolb, *Angew. Chem. Int. Ed.*, 2011, **50**, 7896–7899.
75 W. C. De Vries, D. Grill, M. Tesch, A. Ricker, H. Nüsse, J. Klingauf, A. Studer, V. Gerke and B. J. Ravoo, *Angew. Chem. Int. Ed.*, 2017, **56**, 9603–9607.
76 D. Rota Martir, A. K. Bansal, V. Di Mascio, D. B. Cordes, A. F. Henwood, A. M. Z. Slawin, P. C. J. Kamer, L. Martínez-Sarti, A. Pertegás, H. J. Bolink, I. D. W. Samuel and E. Zysman-Colman, *Inorg. Chem. Front.*, 2016, **3**, 218–235.
77 T. Duan, K. Fan, Y. Fu, C. Zhong, X. Chen, T. Peng and J. Qin, *Dye. Pigment.*, 2012, **94**, 28–33.
78 G. Nagarjuna, S. Yurt, K. G. Jadhav and D. Venkataraman, *Macromolecules*, 2010, **43**, 8045–8050.
79 V. V. Pavlishchuk and A. W. Addison, *Inorganica Chim. Acta*, 2000, **298**, 97–102.
80 C. Adachi, M. A. Baldo, M. E. Thompson and S. R. Forrest, *J. Appl. Phys.*, 2001, **90**, 5048–5051.
81 M. Bixon, J. Jortner, J. Cortes, H. Heitele and M. E. Michel-Beyerle, *J. Phys. Chem.*, 1994, **98**, 7289–7299.
82 J. S. Nam, M. G. Kang, J. Kang, S. Y. Park, S. J. C. Lee, H. T. Kim, J. K. Seo, O. H. Kwon, M. H. Lim, H. W. Rhee and T. H. Kwon, *J. Am. Chem. Soc.*, 2016, **138**, 10968–10977.
83 R. Davidson, Y.-T. Hsu, T. Batchelor, D. Yufit and A. Beeby, *Dalton. Trans.*, 2016, **45**, 11496–11507.
84 V. V. Pavlishchuk and A. W. Addison, *Inorganica Chim. Acta*, 2000, **298**, 97–102.
85 H. Melhuish, *J. Phys. Chem.*, 1961, **65**, 229–235.

86 D. Bruce and M. M. Richter, *Anal. Chem.*, 2002, **74**, 1340–1342.
87 K. K.-W. Lo, S.-K. Leung and C.-Y. Pan, *Inorganica Chim. Acta*, 2012, **380**, 343–349.
88 K. K. Lo, B. T. Chan, H. Liu, K. Y. Zhang, S. P. Li and T. S. Tang, *Chem. Commun.*, 2013, **49**, 4271-4273.
89 M. Ruben, J. Rojo, F. J. Romero-Salguero, L. H. Uppadine and J. M. Lehn, *Angew. Chem. Int. Ed.*, 2004, **43**, 3644–3662.
90 E. Breuning, M. Ruben, J. Lehn, F. Renz, Y. Garcia, V. Ksenofontov, P. Gütlich, E. Wegelius and K. Rissanen, *Angew. Chem. Int. Ed.*, 2000, **39**, 2504–2507.
91 G.-H. Ning, T.-Z. Xie, Y.-J. Pan, Y.-Z. Li and S.-Y. Yu, *Dalton. Trans.*, 2010, **39**, 3203-3211.
92 Q. F. Sun, K. M. C. Wong, L. X. Liu, H. P. Huang, S. Y. Yu, V. W. W. Yam, Y. Z. Li, Y. J. Pan and K. C. Yu, *Inorg. Chem.*, 2008, **47**, 2142–2154.
93 R. Kitaura, G. Onoyama, H. Sakamoto, R. Matsuda, S. I. Noro and S. Kitagawa, *Angew. Chem. Int. Ed.*, 2004, **43**, 2684–2687.
94 T. Sato and M. Higuchi, *Chem. Commun.*, 2012, **48**, 4947-4949.
95 D. L. Caulder and K. N. Raymond, *Angew. Chem. Int. Ed. Engl.*, 1997, **36**, 1440–1442.
96 B. Brusilowskij and C. A. Schalley, *European J. Org. Chem.*, 2011, **2011**, 469–477.
97 H. M. Chawla, P. Goel and P. Munjal, *Tetrahedron Lett.*, 2015, **56**, 682–685.
98 P. P. Neelakandan, A. Jiménez and J. R. Nitschke, *Chem. Sci.*, 2014, **5**, 908–915.
99 I. Bassanetti, F. Mezzadri, A. Comotti, P. Sozzani, M. Gennari, G. Calestani and L. Marchiò, *J. Am. Chem. Soc.*, 2012, **134**, 9142–9145.
100 M. Duriska, S. Neville, J. Lu, S. Iremonger, J. Boas, C. Kepert and S. Batten, *Angew. Chem. Int. Ed.*, 2009, **48**, 8919–8922.
101 A. O. Moughton and R. K. O'Reilly, *Macromol. Rapid Commun.*, 2010, **31**, 37–52.
102 D. Fiedler, H. Van Halbeek, R. G. Bergman and K. N. Raymond, *J. Am. Chem. Soc.*, 2006, **128**, 10240–10252.
103 A. C. Sudik, A. R. Millward, N. W. Ockwig, A. P. Côté, J. Kim and O. M. Yaghi, *J. Am. Chem. Soc.*, 2005, **127**, 7110–7118.
104 Z. Ni, A. Yassar, T. Antoun and O. M. Yaghi, *J. Am. Chem. Soc.*, 2005, **127**, 12752–12753.
105 S. Roche, C. Haslam, S. L. Heath, J. A. Thomas, L. D. Sarson, H.-D. Stachel, J. Lentmaier, K. Peters, E. M. Peters and H. G. von Schneering, *Chem. Commun.*, 1998, **41**, 1681–1682.
106 M. Tominaga, K. Suzuki, M. Kawano, T. Kusukawa, T. Ozeki, S. Sakamoto, K. Yamaguchi and M. Fujita, *Angew. Chem. Int. Ed.*, 2004, **43**, 5621–5625.

107 P. A. Berseth, J. J. Sokol, M. P. Shores, J. L. Heinrich and J. R. Long, *J. Am. Chem. Soc.*, 2000, **122**, 9655–9662.
108 V. Maurizot, M. Yoshizawa, M. Kawano and M. Fujita, *Dalton. Trans.*, 2006, **0**, 2750.
109 J. Y. Yang, M. P. Shores, J. J. Sokol and J. R. Long, *Inorg. Chem.*, 2003, **42**, 1403–1419.
110 D. K. Chand, K. Biradha, M. Fujita, S. Sakamoto, K. Yamaguchi, J. E. Johnson and W. Chiu, *Chem. Commun.*, 2002, **117**, 2486–2487.
111 D. J. Tranchemontagne, Z. Ni, M. O'Keeffe and O. M. Yaghi, *Angew. Chem. Int. Ed.*, 2008, **47**, 5136–5147.
112 Q.-F. Sun, J. Iwasa, D. Ogawa, Y. Ishido, S. Sato, T. Ozeki, Y. Sei, K. Yamaguchi and M. Fujita, *Science .*, 2010, **328**, 1144–1147.
113 M. Fujita, D. Oguro, M. Miyazawa, H. Oka, K. Yamaguchi and K. Ogura, *Nature*, 1995, **378**, 469–471.
114 K. Suzuki, M. Tominaga, M. Kawano and M. Fujita, *Chem. Commun.*, 2009, **0**, 1638-1640.
115 T. Murase, S. Sato and M. Fujita, *Angew. Chem. Int. Ed.*, 2007, **46**, 5133–5136.
116 K. Suzuki, M. Kawano and M. Fujita, *Angew. Chem. Int. Ed.*, 2007, **46**, 2819–2822.
117 H. Z. Xie, M. W. Liu, O. Y. Wang, X. H. Zhang, C. S. Lee, L. S. Hung, S. T. Lee, P. F. Teng, H. L. Kwong, H. Zheng and C. M. Che, *Adv. Mater.*, 2001, **13**, 1245–1248.
118 V. N. Kozhevnikov, Y. Zheng, M. Clough, H. a Al-attar, G. C. Gri, K. Abdullah, S. Raisys, V. Jankus, M. R. Bryce and A. P. Monkman, *Chem. Mater.*, 2013, **25**, 2352–2358.
119 P. Fabbrizzi, B. Cecconi and S. Cicchi, *Synlett*, 2011, 223–226.
120 Ł Skórka, M. Filapek, L. Zur, J. G. Małecki, W. Pisarski, M. Olejnik, W. Danikiewicz and S. Krompiec, *J. Phys. Chem. C*, 2016, **120**, 7284–7294.
121 J. T. Edward, *J. Chem. Educ.*, 1970, **47**, 261-270.
122 Thermopedia: http://www.thermopedia.com/content/1156/. (accessed Augst. 2017)
123 R. R. Fernandes, J. Lasri, A. M. Kirillov, M. F. C. Guedes Da Silva, J. A. L. Da Silva, J. J. R. Fraústo Da Silva and A. J. L. Pombeiro, *Eur. J. Inorg. Chem.*, 2011, **2011**, 3781–3790.
124 K. Ersmark, M. Nervall, H. Gutiérrez-De-Terán, E. Hamelink, L. K. Janka, J. C. Clemente, B. M. Dunn, A. Gogoll, B. Samuelsson, J. Åqvist and A. Hallberg, *Bioorganic Med. Chem.*, 2006, **14**, 2197–2208.
125 Y. Aoyama, Y. Tanaka and S. Sugahara, *J. Am. Chem. Soc.*, 1989, **111**, 5397–5404.
126 P. T. Glink, A. I. Oliva, J. F. Stoddart, A. J. P. White and D. J. Williams, *Angew. Chem. Int. Ed.*, 2001, **40**, 1870–1875.
127 M. Fujita and K. Ogura, *Coord. Chem. Rev.*, 1996, **148**, 249–264.

128 M. J. O'Donnell and R. L. Polt, *J. Org. Chem.*, 1982, **47**, 2663–2666.
129 N. H. Pilkington and R. Robson, *Aust. J. Chem.*, 1970, **23**, 2225–2236.
130 Y. Yao, X. Dong and Y. Zhang, J. Zhao, X. Gou and C. Hua, *Russ J Gen Chem.*, 2015, **85**, 1752–1756.
131 C. M. Che, C. C. Kwok, S. W. Lai, A. F. Rausch, W. J. Finkenzeller, N. Zhu and H. Yersin, *Chem. - A Eur. J.*, 2010, **16**, 233–247.
132 Y. Fan, Q. Wen, T. G. Zhan, Q. Y. Qi, J. Q. Xu and X. Zhao, *Chem. - A Eur. J.*, 2017, **23**, 5668–5672.
133 J. Gregoliński, K. Ślepokura, T. Paćkowski and J. Lisowski, *Org. Lett.*, 2014, **16**, 4372–4375.
134 Z. Wang, H. F. Nour, L. M. Roch, M. Guo, W. Li, K. K. Baldridge, A. C. H. Sue and M. A. Olson, *J. Org. Chem.*, 2017, **82**, 2472–2480.
135 B. N. Boden, J. K. Hui and M. J. Maclachlan, *J. Org. Chem.*, 2008, **73**, 8069–8072.
136 S. Ullmann, R. Schnorr, M. Handke, C. Laube, B. Abel, J. Matysik, M. Findeisen, R. Rüger, T. Heine and B. Kersting, *Chem. - A Eur. J.*, 2017, **23**, 3824–3827.
137 P. A. Vigato and S. Tamburini, *Coord. Chem. Rev.*, 2004, **248**, 1717–2128.
138 F. Faridbod, M. Ganjali, B. Larijani and P. Norouzi, *Sensors*, 2007, **7**, 3119–3135.
139 S. Cai, H. Shi, J. Li, L. Gu, Y. Ni, Z. Cheng, S. Wang, W. wei Xiong, L. Li, Z. An and W. Huang, *Adv. Mater.*, 2017, **29**, 1701244.
140 K. Matsuoka, K. Albrecht, K. Yamamoto and K. Fujita, *Sci. Rep.*, 2017, **7**, 41780.
141 W. Lao, C. Xu, S. Ji, J. You and Q. Ou, *Spectrochim. Acta - Part A Mol. Biomol. Spectrosc.*, 2000, **56**, 2049–2060.
142 B. H. Stuart, *Infrared Spectroscopy: Fundamentals and Applications*, J. Wiley, Chichester, West Sussex, UK; Hoboken, NJ, 2004.
143 X. Chen, M. Addicoat, S. Irle, A. Nagai and D. Jiang, *J. Am. Chem. Soc.* 2013, **135**, 546−549.
144 S. S. Ding and W. Wang, *Chem. Commun.*, 2016, **52**, 7217–7220.
145 T. Kolev, *J. Mol. Struct.*, 1995, **349**, 381–384.
146 C. Adamo and D. Jacquemin, *Chem. Soc. Rev.*, 2013, **42**, 845–856.
147 S. Hirata and M. Head-Gordon, *Chem. Phys. Lett.*, 1999, **314**, 291–299.
148 M. Y. Wong, G. J. Hedley, G. Xie, L. S. Kölln, I. D. W. Samuel, A. Pertegás, H. J. Bolink and E. Zysman-Colman, *Chem. Mater.*, 2015, **27**, 6535–6542.
149 M. Y. Wong, M.-G. La-Placa, A. Pertegas, H. J. Bolink and E. Zysman-Colman, *J. Mater. Chem. C*, 2017, **5**, 1699–1705.
150 D. M. Zink, M. Bächle, T. Baumann, M. Nieger, M. Kühn, C. Wang, W. Klopper, U. Monkowius, T. Hofbeck, H. Yersin and S. Bräse, *Inorg. Chem.*, 2013, **52**, 2292–2305.

151 Z. An, C. Zheng, Y. Tao, R. Chen, H. Shi, T. Chen, Z. Wang, H. Li, R. Deng, X. Liu and W. Huang, *Nat. Mater.*, 2015, **14**, 685–690.
152 J. Huang, Y. Xu and X. Qian, *Org. Biomol. Chem.*, 2009, **7**, 1299-1303.
153 M.-L. Ho, K.-Y. Chen, L.-C. Wu, J.-Y. Shen, G.-H. Lee, M.-J. Ko, C.-C. Wang, J.-F. Lee and P.-T. Chou, *Chem. Commun.*, 2008, **0**, 2438–2440.
154 H. Wang, L. Xue and H. Jiang, *Org. Lett.*, 2011, **13**, 3844–3847.
155 L. Li, Y. Q. Dang, H. W. Li, B. Wang and Y. Wu, *Tetrahedron Lett.*, 2010, **51**, 618–621.
156 T. M. Garrett, P. W. Miller and K. N. Raymond, *Inorg. Chem.*, 1989, **28**, 128–133.
157 J. Mao, Q. He and W. Liu, *Talanta*, 2010, **80**, 2093–2098.
158 P. E. Danjou, J. Lyskawa, F. Delattre, M. Becuwe, P. Woisel, S. Ruellan, S. Fourmentin and F. Cazier-Dennin, *Sensors Actuators, B Chem.*, 2012, **171**–**172**, 1022–1028.
159 B. Wang, X. Guan, Y. Hu and Z. Su, *J. Polym. Res.*, 2008, **15**, 427–433.
160 B. Sui, S. Tang, T. Liu, B. Kim and K. D. Belfield, *ACS Appl. Mater. Interfaces*, 2014, **6**, 18408–18412.
161 V. N. Kozhevnikov, Y. Zheng, M. Clough, H. A. Al-Attar, G. C. Griffiths, K. Abdullah, S. Raisys, V. Jankus, M. R. Bryce and A. P. Monkman, *Chem. Mater.*, 2013, **25**, 2352–2358.
162 M. C. Haberecht, M. Bolte, J. W. Bats and H. Lerner, *Z. Naturforsch. B,* 2005, **60**, 745-752.
163 G. Maerker and F. H. Case, *J. Am. Chem. Soc.*, 1958, **80**, 2745–2748.
164 D. Zhang, P. Telo, C. Liao, S. E. Hightower and E. L. Clennan, *J. Phys. Chem. A*, 2007, **111**, 13567–13574.
165 P. V James, K. Yoosaf, J. Kumar, K. G. Thomas, A. Listorti, G. Accorsi and N. Armaroli, *Photochem. Photobiol. Sci.*, 2009, **8**, 1432–40.
166 R. Cao, J. Jia, X. Ma, M. Zhou and H. Fei, *J. Med. Chem.*, 2013, **56**, 3636–3644.
167 D. Bogdal, M. Lukasiewicz and J. Pielichowski, *Green Chem.*, 2004, **6**, 110–113.
168 E. Zysman-Colman and K. Arias, *Can. J. Chem.,* 2009, **87**, 440-447.
169 Y. N. Polivin, R. A. Karakhanov, V. I. Kelarev, A. A. Bratkov, B. I. Ugrak, G. K. Anashkin and M. E. Panina, *Russ. Chem. Bull.*, 1993, **42**, 214–214.
170 H. Shi, M. Li, L. Fang, X. Dong, X. Zhang, H. Peng, S. Chen and B. Z. Tang, *Synth. Met.*, 2016, **220**, 356–361.
171 M. J. Frisch, G. W. Trucks, H. B. Schlegel, G. E. Scuseria, M. A. Robb, J. R. Cheeseman, G. Scalmani, V. Barone, B. Mennucci, G. A. Petersson, H. Nakatsuji, M. Caricato, X. Li, H. P. Hratchian, A. F. Izmaylov, J. Bloino, G. Zheng, J. L. Sonnenberg, M. Hada, M. Ehara, K. Toyota, R. Fukuda, J. Hasegawa, M. Ishida, T. Nakajima, Y. Honda, O. Kitao, H. Nakai, T. Vreven, J. A. Montgomery Jr., J. E. Peralta, F.

Ogliaro, M. Bearpark, J. J. Heyd, E. Brothers, K. N. Kudin, V. N. Staroverov, R. Kobayashi, J. Normand, K. Raghavachari, A. Rendell, J. C. Burant, S. S. Iyengar, J. Tomasi, M. Cossi, N. Rega, J. M. Millam, M. Klene, J. E. Knox, J. B. Cross, V. Bakken, C. Adamo, J. Jaramillo, R. Gomperts, R. E. Stratmann, O. Yazyev, A. J. Austin, R. Cammi, C. Pomelli, J. W. Ochterski, R. L. Martin, K. Morokuma, V. G. Zakrzewski, G. A. Voth, P. Salvador, J. J. Dannenberg, S. Dapprich, A. D. Daniels, Ö . Farkas, J. B. Foresman, J. V. Ortiz, J. Cioslowski, D. J. Fox, Gaussian Inc., Wallingford, CT, **2013**.

172 C. Lee, W. Yang and R. Parr, *Phys. Rev. B*.,1988, **37**, 785-789.

173 J. A. Pople, J. S. Binkley and R. Seeger, *Int. J. Quantum Chem.*, 2009, **10**, 1–19.

174 M. Moral, L. Muccioli, W.-J. Son, Y. Olivier and J. C. Sancho-García, *J. Chem. Theory Comput.*, 2015, **11**, 168–177.

175 H. Su, F. Fang, T. Hwu and H. Hsieh, H. Chen, G. Lee, S. Peng, K. Wong and C. Wu, *Adv. Funct.*,2007, **17**, 1019-1027.

176 B. C. Rothe, C. Chiang, V. Jankus, K. Abdullah, X. Zeng, R. Jitchati, A. S. Batsanov, M. R. Bryce and A. P. Monkman, *Adv. Funct. Mater.*, 2009, **19**, 2038–2044.